Thèse de Doctorat

Mention: Chimie
Spécialité: Chimie des Solides et Sciences des Matériaux

présentée à l'Ecole Doctorale en Sciences Technologie et Santé (ED 547)

de l'Université de Picardie Jules Verne

par

Matteo BIANCHINI

pour obtenir le grade de Docteur de l'Université de Picardie Jules Verne

In Situ diffraction studies of electrode materials for Li-ion and Na-ion batteries

Soutenue le xx/xx/xxxx après avis des rapporteurs, devant le jury d'examen :

F. Boucher, Directeur de Recherches CNRS, IMN Nantes	**Rapporteur**
K. Kang, Professeur, Seoul National University, South Korea	**Rapporteur**
O. Mentré, Directeur de Recherches CNRS, ENSC Lille	**Examinateur**
S. Whittingham, Professeur, Binghamton University, NY, USA	**Examinateur**
L. Croguennec, Directrice de Recherches CNRS Bordeaux	**Examinatrice**
E. Suard, Scientifique Senior, ILL, Grenoble	**Examinatrice**
C. Masquelier, Professeur, UPJV, Amiens	**Examinateur**

"There is a single
light of science;
and to shine it anywhere
is to shine it everywhere."
I. Asimov

A Camilla,

per aver detto sì.

Publications

The material presented in this thesis is an expanded version of the material that was published in the following papers:

M. Bianchini, F. Fauth, J.B Leriche, E. Suard, C. Masquelier and L. Croguennec, Spinel Materials for Li-ion batteries: New insights obtained by *operando* Neutron and Synchrotron X-Ray diffraction, Accepted: *Acta Cryst. B - Special Issue on Energy Materials* (**2015**).

M. Bianchini, N. Brisset, F. Fauth, F. Weill, E. Suard, C. Masquelier and L. Croguennec, A comprehensive investigation of the $Na_3V_2(PO_4)_2F_3$ - $NaV_2(PO_4)_2F_3$ system by *operando* high resolution synchrotron X-ray diffraction, *Chemistry of Materials* (**2015**), 27(8), 3009-3020.

M. Bianchini, E. Suard, L. Croguennec and C. Masquelier, Li-Rich $Li_{1+x}Mn_{2-x}O_4$ Spinel Electrode Materials: An *Operando* Neutron Diffraction Study during Li^+ Extraction/Insertion, *Journal of Physical Chemistry C* (**2014**), 118(45), 25947-25955.

M. Bianchini, N. Brisset, F. Fauth, E. Elkaim, F. Weill, E. Suard, C. Masquelier and L. Croguennec, $Na_3V_2(PO_4)_2F_3$ Revisited: A High-Resolution Diffraction Study, *Chemistry of Materials* (**2014**), 26 (14), 4238-4247.

M. Bianchini, J.-M. Ateba Mba, P. Dagault, E. Bogdan, D. Carlier, E. Suard, C. Masquelier and L. Croguennec, Multiple phases in the ϵ-VPO_4O - $LiVPO_4O$ - Li_2VPO_4O system: a combined solid state electrochemistry and diffraction structural study, *Journal of Materials Chemistry A* (**2014**), 2, 10182-10192.

M. Bianchini, J. B. Leriche, J.-L. Laborier, L. Gendrin, E. Suard, L. Croguennec and C. Masquelier, A New Null Matrix Electrochemical Cell for Rietveld Refinements of *In Situ* or *Operando* Neutron Powder Diffraction Data, *Journal of The Electrochemical Society* (**2013**), 160 (11), A2176-A2183.

Abstract

Li-ion batteries are the devices that allowed the "wireless revolution". In the last 30 years they brought smartphones in our pockets and laptops in our backpacks by experiencing an amazing improvement in performances. However much work still needs to be done to make this technology competitive for other applications, such as automotive and energy storage for the grid. Other next-generation battery systems are also being developed, as the Na-ion one, a technology analogous to Li-ion but based on a cheaper and more abundant element. The heart of Li- and Na- ion batteries is constituted by the electrodes, materials able to exchange Li^+/Na^+ cations. Their development depends on the discovery of new electrode materials and on a better understanding of the existing ones. This last point in particular is of key importance as it unlocks the full exploitation of an electrode material's capabilities, i.e. obtaining the full theoretical energy density, at sufficiently fast cycling rate and with a long cycle life.

A real comprehension of electrode materials requires a combination of different characterization techniques. Moreover, to understand how they function inside a battery they must be studied *in situ*, or, going a step further, *operando*: that is, the material needs to be studied as the battery functions too. Charge and discharge are in fact processes that can induce profound transformations in the electrodes, since Li^+/Na^+ is extracted and inserted and transition metals are oxidized and reduced. Such transformations often happen out of the equilibrium, in dynamical conditions, this being the reason for the necessity of *operando* studies. In this thesis we mainly make use of diffraction techniques to unravel the crystallographic transformations occurring in electrode materials as they are lithiated and delithiated inside Li-ion and Na-ion batteries. To obtain comprehensive information we combine several probes, sensitive to different atoms in the materials. Neutrons were used extensively because of their peculiar scattering characteristics; this leads to different advantages, the most important of which is that they can shed light on light elements as lithium and oxygen. X-Rays are also much employed as they are cheaper and easier to have at hand, while giving anyway a whole lot of valuable information, for example about transition metals and unit cell parameters. Finally, synchrotron radiation is used in focused studies where high angular, intensity and time resolution are required.

For each one of these probes, we managed to carry out *ex situ*, *in situ* and *operando* studies. To do so, beside electrochemical cells for *in situ* studies using X-Rays and synchrotron radiation that were available in our group, a new cell for *in situ* studies using neutrons was developed. Manufactured with a "neutron-transparent" (Ti,Zr) alloy, and coupled with the use of deuterated electrolytes, the cell combined good electrochemical performances with the ability to obtain neutron powder diffraction patterns of great quality to succeed in Rietveld structural refinements. Thus the whole range of diffraction techniques in real time could be applied. This is a great added value of our approach, as we are able to observe new features revealed upon cycling by several different electrode materials for Li- and Na-ion batteries. The analyzed families of materials range through spinels ($Li_{1+x}Mn_{2-x}O_4$ (x = 0, 0.05, 0.10) and $LiNi_{0.4}Mn_{1.6}O_4$), olivines ($LiFePO_4$), tavorites ($LiVPO_4O$) and fluorophosphates for Na-ion batteries ($Na_3V_2(PO_4)_2F_3$). Among the salient facts that we reported, we mention the phase diagram upon cycling of $Li_{1+x}Mn_{2-x}O_4$, strongly impacted by the presence of the extra lithium in the site of Mn, and the fact that thanks to neutrons we could follow lithium's behavior inside the spinel framework. Sensitive information could be recovered, as site occupancy factors and thermal displacement parameters, giving valuable insight on the long and short range behavior of the atoms in the material (of which $LiNi_{0.4}Mn_{1.6}O_4$ is a meaningful example). On the other hand, thanks to synchrotron radiation we were able to answer the tricky question about the nature of $Li_{0.5}Mn_2O_4$, a long-debated composition found halfway through charge of $LiMn_2O_4$ and that we showed to possess a combined transition metal charge ordering and lithium/vacancy ordering. $LiVPO_4O$ was instead mainly studied with X-Rays, with only complementary help from neutrons and synchrotron radiation. We revealed the impact of particles' size on the material's electrochemical behavior, as well as its phase diagram built by several phase transitions and intermediate phases of previously unknown structure. We were in fact able to describe for the first time the lithiated phases in Li_xVPO_4O (x = 1.5, 1.75, 2). Finally $Na_3V_2(PO_4)_2F_3$, an extremely promising material for the Na-ion technology, was revisited concerning its crystal structure and phase diagram: thanks to synchrotron radiation it was indexed in the new orthorhombic space group Amam and, with the contribution of neutron diffraction, it was assigned an improved crystal structure with redefined position of sodium ions. This allowed a detailed *operando* study of Na^+ extraction until composition $NaV_2(PO_4)_2F_3$, a process rich in several phase transitions induced by sodium and transition metal orderings, that we were able to evidence for the first time. This thesis is

therefore an effort to adopt a comprehensive approach to the use of diffraction techniques, *ex situ*, *in situ* and *operando*, to unravel the crystal structure modifications occurring in electrode materials for Li-ion and Na-ion batteries upon cycling. The obtained insights reveal the interconnections between crystal structures and electrochemical performances in electrode materials, this having key importance to understand and improve them for the next generation of batteries.

Contents

Chapter 1

Introductory concepts and methods

1.1 Background and context

The world's population and energy consumption are steadily increasing. We are an estimated 7.2 billion people, which consumed 104407 TWh of energy in 2012 [1]. This is nearly twice the consumption of 1973 (54326 TWh), when there were almost 4 billion people. It is clear that a society with such a steady and rapid growth should worry about being energy self-sufficient, i.e. it should be able to produce enough electricity to sustain itself without depleting finite resources. However this is not the case. Figure 1.1 shows the world's electricity generation and it is clear that, although increasing, 22668 TWh is quite far from the amount of energy we consume. The biggest difference between the two consists in the oil consumed every year. In 2012 oil still represented more than 40% of the world's energy consumption, clearly showing how our society is heavily dependent on it. However oil is a non-renewable resource, as is coal (still widely used in thermoelectric plants), and at some point (most probably in the next century) they will not suffice anymore. Not to mention the well-known issues of huge CO_2 production and consequent earth-warming and climate changes that oil and coal carry with them. For this reason research has been trying to provide alternatives that are as renewable and "green" as possible. Hydroelectric energy production is one such alternative, exploited for a long time but whose contribution is not likely to increase. Nuclear production is another possible choice but it is not renewable, it

[1] Data taken from the 2014 Key World Energy Statistics published by the IEA (International Energy Agency).

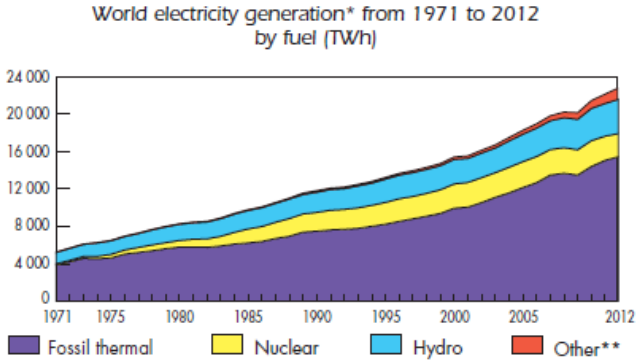

Figure 1.1: World electricity generation (TWh) from 1971 to 2012 by fuel. Data from the International Energy Agency (IEA).

creates hardly-disposable nuclear wastes and it is badly perceived by the population after the incidents of Chernobyl and, more recently, Fukushima. We have reached a point where it is common knowledge that truly renewable sources such as wind and solar energy must be the answer to these issues. Photovoltaics, in particular, is experiencing a new era since the introduction of perovskite-based solar cells, reaching efficiencies already exceeding 20%, a remarkable result for such a young technology [1,2]. However, in 2012 only 5% of the energy produced worldwide came from these sources (actually including also geothermal energy). The biggest limitation to solar and wind energy production is their unsteady nature, meaning that it is highly dependent on the atmospheric conditions and the moment of the day (Figure 1.2).

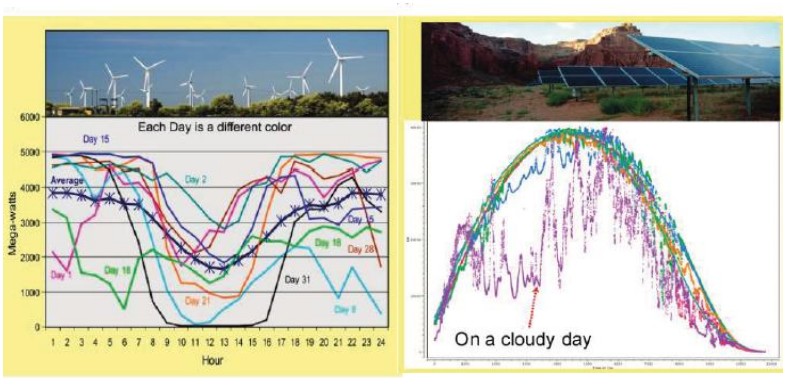

Figure 1.2: Evolution of energy production from wind (left) and solar (right) during several days. Reprinted from [3].

For this reason a reliable energy storage device is required to complement these systems. Such a device must be able to accumulate energy during peak production hours and to

release it when required (at night for example). Being the most advanced electrochemical system available on the market, the Li-ion battery is believed to be the ideal solution to provide these storage capabilities. This battery technology is available on the market since the early 90s, when it started powering the "wireless revolution". By 2002, cell phones, and with them, Li-ion, were everywhere. Thanks to their unprecedented energy and power density (about twice of NiCd and 30% more than NiMH), they allowed electronic devices to be carried around without the need for spare replacement batteries. Besides they have a long cycle life (> 1000 cycles) enabling them to last for years and to dominate the battery market with millions of cells sold every year (Figure 1.3). In 2002 *The Economist* anointed lithium-ion batteries the "foot-soldiers of the digital revolution". For these reasons the

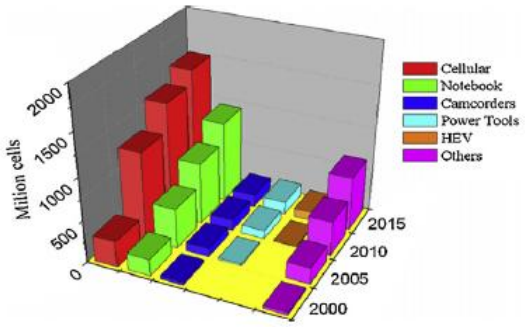

Figure 1.3: Li-ion batteries sold from 2000 to 2015. Reprinted from [4].

applications of Li-ion batteries, initially limited to portable electronics, are now spreading to two major fields: grid-storage and electric vehicles. The former would mean a significant increase in the use of wind and solar power generation, not only at the industrial scale but mostly at the individual one. An important step in this direction was made in 2015 by Tesla Motors, who started commercializing the Tesla Powerwall, a Li-ion-based device to be installed at home (possibly coupled to photovoltaic panels) to turn positive its energy balance (i.e. to sell energy to the grid instead of consuming it). The latter instead has been considered by carmakers since 1990, when General Motors introduced the first all-electric car, the EV1 "impact". However at this time political and economical issues [2] contributed to the failure of the first electric vehicle (technologically immature to rival with traditional cars). Increased awareness of the environmental impact of CO_2 emissions and the ever-increasing price of oil renewed and boosted the interest in electric cars. Real answers were given by Toyota which commercialized the first hybrid vehicles (the Prius, which sold more than 3 million units by 2013). With some delay all carmakers joined

[2] See for example the 2006 documentary *Who killed the electric car?*, Sony Pictures Classic.

the run for better and more performing electric cars, and nowadays they all offer at least one of such vehicles (hybrids, plug-in hybrids or fully-electric). The Nissan Leaf and the Tesla Model S, in particular, are in 2015 the two world's highest selling all-electric vehicles of all times (180000 and 75000 units, respectively). The road to a society dependent on renewable sources only is quite long, but the first important steps have been made and Li-ion batteries (or similar more evolved battery technologies) are going to play a primary role in this evolution.

1.2 What is a battery?

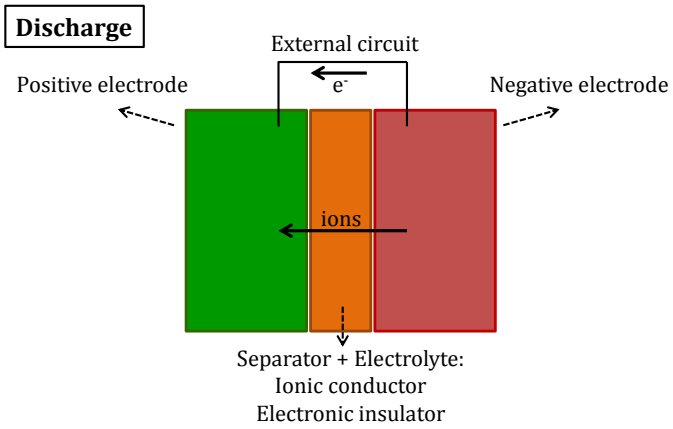

Figure 1.4: Schematic representation of a battery during common use (discharge).

A battery is a device able to convert chemical into electrical energy. It is made by one or more electrochemical cells, which are its fundamental building units. Each of these cells (shown in Figure 1.4) functions exploiting a reduction/oxidation reaction (named "redox") occurring between two main parts called electrodes. Namely, an electron exchange is made at a given potential in each electrode, normally paired with an ion exchange. The third main component of the electrochemical cell is an ionic conductor called electrolyte (usually but not always a liquid). This is in contact with the electrodes, allowing ionic conduction but preventing direct electron exchange. Electrons in fact must flow through an external circuit, so that the electrical energy can be extracted. Figure 1.4 shows a scheme of a generic electrochemical cell. The electromotive force of the cell V_{cell} (defined at open circuit as $V_{cathode}$ - V_{anode}) is governed by the redox reactions involved in the electrodes and it is connected to the thermodynamic difference in Gibbs free energy (J) of the electrodes as:

$$\Delta G_0 = \Delta x \cdot F \cdot V_{cell} \tag{1.1}$$

where F is Faraday's constant (96485 C/mole or 26801 mAh/mole) and Δx is the stoichiometric number of moles of electrons liberated in the reaction. Essentially, the free energy variation during discharge of a battery is given by the work done by the flow of ΔxF electron charges at the potential V_{cell}.

1.2.1 Development of primary batteries

An important distinction should be made when discussing batteries: most of them are built in the charged state and they can provide a single discharge, mainly because the electrodes or the electrolyte are consumed by the reaction. These are called primary batteries. Rechargeable batteries, on the other hand, are called secondary batteries and, obviously, can provide several charge/discharge cycles. The first working (primary) battery continuously powering a circuit was built in 1799 by Alessandro Volta, who invented an electrochemical cell constituted by copper and zinc metals at the electrodes, and brine as the electrolyte. It exploited the oxidation of zinc ($Zn \rightarrow Zn^{2+} + 2e^-$) and the reduction of brine ($2H_3O^+ + 2e^- \rightarrow H_2 + 2H_2O$), to give a potential of 0.76 V, corresponding to the zinc redox potential vs. the standard hydrogen electrode (SHE). Volta's invention built on Luigi Galvani's 1780s discovery of how a circuit of two metals and a frog's leg can cause the frog's leg to respond. For this reason electrochemical cells are also called galvanic cells, while the first battery made by Volta is called voltaic pile. These discoveries opened the way to the invention of several battery systems. The first was an improved version of voltaic pile, called Daniell pile. It still used zinc and copper, but soaked in acid electrolyte solutions of $ZnSO_4$ and $CuSO_4$. This way the same oxidation reaction happens, while copper becomes the reduced element ($Cu^{2+} + 2e^- \rightarrow Cu$). The potential of the pile is now the difference of the two redox potentials, i.e. 0.76 V - (- 0.34 V) = 1.10 V. In 1866 Georges Leclanché invented the zinc-carbon battery, an example of dry cell (in the sense that the electrolyte is a paste and not a liquid), an evolution that made batteries more practical and safe. It works on the redox reactions of zinc and manganese oxide MnO_2, providing 1.5 V, the same potential used also in the alkaline battery. This is an invention by Waldemar Jungner in 1899, and, working independently, Thomas Edison in 1901. These battery systems spread and powered electrical devices throughout the whole 20th century. Lithium-based primary batteries are also available; different chemistries exist for the positive electrode, but they all have in common the use of metallic lithium for the negative one. The most commonly found electrodes are MnO_2-Li, working at a nominal voltage of 3 V, twice that of alkaline

batteries, and having a capacity of 280 Wh/kg.

1.2.2 Secondary (rechargeable) batteries

In 1859 Gaston Planté invented the lead-acid battery, a first example of rechargeable battery of extreme importance and still widely used nowadays (notably in the starter for cars). It exploits the overall reaction $Pb + PbO_2 + 2H_2SO_4 \leftrightarrow 2PbSO_4 + 2H_2O$ (from left to right upon discharge, and vice versa upon charge). Other important rechargeable systems are nickel-cadmium batteries (NiCd, 1898), recently replaced by nickel-metal hydride ones (NiMH, 1967, available for the consumer market since 1989). But the real revolution in rechargeable batteries was made by another technology which saw the light in the same years, the Li-ion battery.

1.3 Li-ion batteries

Li-ion batteries are nowadays the most advanced and diffused rechargeable batteries available. The first example of such batteries was introduced by S. Whittingham in the mid '70s[6]. It was based on the idea of Li^+ cations shuttling through the electrodes, constituted by metallic lithium and TiS_2 (an insertion compound). The term "intercalation" is also very used in the literature; it implies a special case where "insertion" occurs into a host matrix retaining its structural integrity during the intercalation process. These batteries were announced to be commercialized by Exxon. However, the use of metallic

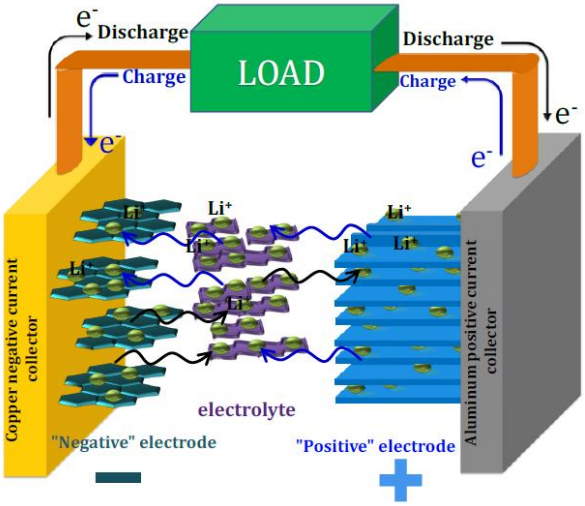

Figure 1.5: Schematic representation of a Li-ion battery, constituted by a $LiCoO_2$ positive electrode and a graphite negative electrode. Reprinted from [5].

lithium for a secondary battery posed several safety issues upon reiterate cycles. It can in fact create dendrites growing on lithium's surface and possibly penetrating the separator and short-circuiting the cell, posing a serious hazard. The commercialization of safe Li-based batteries had to wait for another technology, the Li-ion battery. This was made possible by the work of Mizushima et al.[7] and it was successfully developed by SONY®. John B. Goodenough, with Yoshio Nishi, Rachid Yazami and Akira Yoshino received the 2014 Charles Stark Draper Prize for being the rechargeable battery pioneers who laid the groundwork for today's lithium ion battery.

A simplified scheme of the battery is shown in Figure 1.5. This technology eliminates the dangerous lithium metal while still exploiting Li^+ ions which are present in the positive electrode material and as a salt in the electrolyte. In fact, intercalation materials are used in both electrodes: $LiCoO_2$ at the positive and graphite or amorphous carbon at the negative. Both have layered structures, allowing to accommodate lithium between sheets of CoO_6 octahedra or graphite, respectively. The two are separated by a porous medium called separator, soaked in an electrolyte containing Li salt (usually $LiPF_6$) in organic solvents (ethylene carbonate, dimethyl carbonate and/or propylene carbonate). The reactions involved are the following: Upon charge:

$$Cathode : LiCo^{III}O_2 \rightarrow Co^{IV}O_2 + Li^+ + e^- \tag{1.2}$$

$$Anode : 6C + Li^+ + e^- \rightarrow LiC_6 \tag{1.3}$$

It is thus clear that two parallel reactions take place: in the cathode, lithium deintercalation and cobalt oxidation; in the anode, lithium intercalation and carbon reduction. Li^+ cations travel from $LiCoO_2$ through the electrolyte in the separator until they reach the carbon sheets. As the electrolyte is a poor electronic conductor, electrons flow outside the cell, through a wire closing the circuit. The reactions described above are not spontaneous; they require a power supply to be carried out and thus to store energy in the battery. Once it is fully charged, i.e. when all lithium "travelled" from the positive to the negative electrode, the battery is ready to be used. The arrows in equation 1.2 and 1.3 are reversed upon discharge, as are the involved reactions. Power is now generated from the battery, supplying a spontaneous electrons flow to the external load.

1.3.1 Battery conventions and definitions

Note that in the previous section the terms cathode and anode were used. This might be confusing since a rechargeable battery is both an active (during discharge) and passive

(during charge) electric component. In the battery community, a convention is to use the term cathode for the positive electrode and anode for the negative one. The convention was thus chosen to match the case of Li-ion battery discharge, as the cathode is usually defined as the electrode where a positive current departs or a negative one enters. The

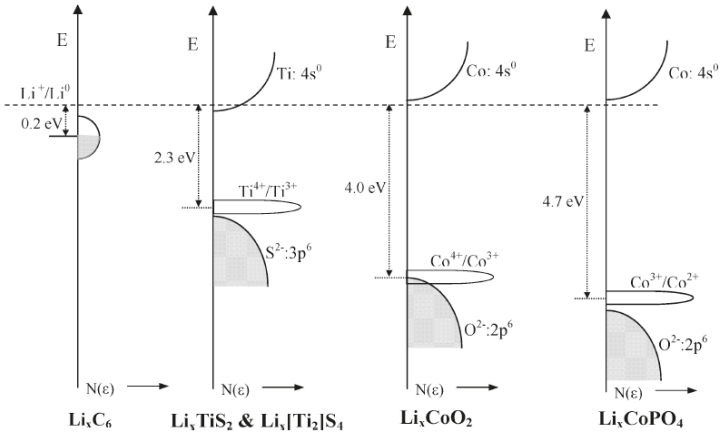

Figure 1.6: Schematic of the energy vs. density of states showing the relative positions of the Fermi energy in an itinerant electron band for Li_xC_6, the Ti^{4+}/Ti^{3+} redox couple for Li_xTiS_2 and $Li_x[Ti_2]S_4$, the Co^{4+}/Co^{3+} redox couple for Li_xCoO_2, and the Co^{3+}/Co^{2+} redox couple for Li_xCoPO_4. Reprinted from [8].

relationship between Gibbs free energy and external voltage of a battery has been already described (equation 1.1). It can be well-visualized in Figure 1.6, where the relative position in energy of the electrons density of states (DOS) determines the potential of the cell. Another key quantity to evaluate battery performance is the theoretical capacity C_{th}. This is the amount of electric charge that can be delivered by the electrode material, per unit of mass. It is then defined as:

$$C_{th} = \frac{\Delta x \cdot F}{M_w} \tag{1.4}$$

where M_w represents the molecular weight of the material. Faraday's constant value is 96485 C/mole, but in the battery community it is more common to discuss capacity in terms of milliAmpere-hour/g; for this the value of F = 26801 mAh/mole is often used, where the difference is a factor 1000/3600. Once the potential V_{cell} and the capacity C_{th} of an electrochemical cell are known, the gravimetric energy density can be simply calculated as:

$$Energy[Wh/kg] = C_{th} \cdot V_{cell} \tag{1.5}$$

Or, introducing the density ρ [kg/l], the volumetric energy density as:

$$Energy[Wh/l] = C_{th} \cdot V_{cell} \cdot \rho \tag{1.6}$$

The quantities described above do not depend on the charging rate of the battery, i.e. they do not account for the time required for electrons to be delivered. However charging/discharging rate capabilities are extremely important factors in evaluating batteries' performance. In a classic galvanostatic experiment, a fixed current I is imposed to the battery for the time t required to complete a charge or discharge. A convention is used for the current rate: the charge/discharge is said to happen at C/n rate when 1 mole of e^- (and of Li^+ ions) is exchanged in n hours. C/2 will then be charge/discharge in 2 hours, while 2C in 30 minutes. The cycling rate relates to the available capacity to give the current I following:

$$I = \frac{C_{th}[mAh/g] \cdot mass[g]}{n[hours]} \tag{1.7}$$

I is then the current delivered through an electrode of mass m during a galvanostatic experiment carried out at C/n rate. Another common way to charge or discharge a battery is a potentiostatic experiment, where instead of providing a fixed current I and recording the evolution of the voltage V_{cell}, the contrary is made. Galvanostatic Intermittent Titration Technique (GITT) is another widely used protocol: it consists at alternating galvanostatic current steps with relaxation times of fixed length (imposing a condition on the duration of the relaxation time or on the value of dV/dt). The technique is useful because it allows to determine the equilibrium potential relaxed after every charging step and the shape of the relaxation curve can also give information on lithium's diffusion. Finally, the fixed-voltage counterpart of GITT is called PITT (Potentiostatic Intermittent Titration Technique) and it works analogously.

1.3.2 Positive electrode materials

In a Li-ion battery the positive electrode is not simply constituted by the electrochemically active material (AM), as for example $LiCoO_2$. In most cases the electrode's electronic conductivity needs to be improved to provide facile electrons transport to the current collectors. Carbon is therefore added to the AM and the two are intimately mixed. Moreover, during battery operation the electrode must face important volume changes due to lithium insertion and extraction; for this reason a polymeric binder (polyvinylidene fluoride, PVDF or polytetrafluoroethylene, PTFE) is added to the mixture, providing elasticity to

the electrode so that good particle connectivity is retained after many cycles. Although $LiCoO_2$ has been a successful positive electrode material, it still leaves room for significant improvements. Therefore the scientific community started looking for better AMs for positive electrodes. The most important families of materials have been reviewed in the literature[9–12] and they are briefly described in the following, classified according to their framework structure (Figure 1.7).

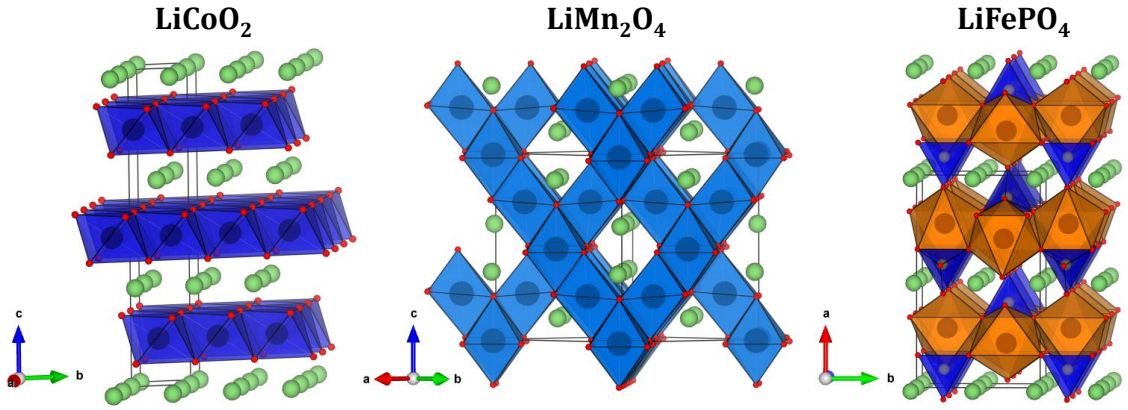

Figure 1.7: Structural frameworks of the most common positive electrode materials: left) layered $LiCoO_2$, middle) spinel $LiMn_2O_4$, right) olivine $LiFePO_4$.

Layered materials

Layered materials have been the first explored compositions, starting from $LiCoO_2$[7], developed by analogy with the previously used TiS_2. They crystallize in the $R\bar{3}m$ space group and their structure is clearly suitable for lithium insertion/extraction, as this is stacked into layers of close-packed transition metal (TM) octahedra. This arrangement allows bidimensional Li^+ transport pathways. They have also the advantage of being rather light, resulting in a high energy density that can reach ≈1.1 kWh/kg (theoretical) at 4 V. On the other hand, $LiCoO_2$ has drawbacks that pushed researchers to find suitable alternatives. Firstly, Co is toxic and expensive. Secondly, $LiCoO_2$ suffers from thermal instability and O_2 loss when more than half lithium is extracted from the framework, limiting the practical capacity to half of the theoretical value[13] (although nowadays modifying the electrode's surface $LiCoO_2$ can be cycled on 0.7 Li^+ [14]). A number of substitutions of Co (or of Ni in the isostructural $LiNiO_2$) with one or more transition metal elements has been proposed, trying to minimize the amount of cobalt and to improve the available capacity. Among this,

important compositions are $LiNi_{1-y-z}Co_yAl_zO_2$ [15,16] and $LiNi_{1/3}Co_{1/3}Mn_{1/3}O_2$ [17], that have reached commercial exploitation. Another route has been to overlithiate manganese-rich layered oxides ($Li_{1+x}(TM)_{1-x}O_2$, TM being one or several transition metals), resulting in materials exhibiting high reversible capacity (> 200 mAh/g) after an activation process during 1^{st} charge at potential > 4.5 V [18,19]. However in this case redox processes involve both the transition metal ions and the oxygen anions. Irreversible structural modifications (TM reorganization and oxygen loss) occur inducing a continuous decrease in discharge voltage and energy, making these Li-rich materials still not mature for applications.

Spinel materials

Spinel materials have been the second family of heavily studied oxides for Li-ion batteries. They are briefly introduced here, since they will be thoroughly discussed in Chapter 3. The spinel framework is cubic, belonging to the $Fd\bar{3}m$ space group. The basic stoichiometry is $LiMn_2O_4$ (Figure 1.7), introduced as a positive electrode for Li-ion batteries by M.M. Thackeray in 1983 [20–22]. The material offers a capacity of ≈150 mAh/g at a very high potential (4.1 V for the Mn^{III}/Mn^{IV} redox couple). Moreover the framework, built by lithium in tetrahedral coordination and Mn in close-packed octahedra, favours tridimensional lithium transport, making it especially suitable for high-rate applications. As $LiMn_2O_4$ suffers of capacity fading upon cycling, over-lithiated ($Li_{1+x}Mn_{2-x}O_4$) and cation-defective ($Li_{1-x}Mn_{2-2x}O_4$) compositions were proposed to improve the cycling life of the material [23]. Although these compositions are nowadays commercialized, research is still done to improve the energy density by substituting Mn with other TMs. Nickel in particular allows to reach high operating potentials (4.7 V for $LiNi_{0.5}Mn_{1.5}O_4$) [24,25], but the lack of stable electrolytes in this window has been the limiting factor for this technology's exploitation.

Polyanionic materials

Polyanionic materials contain more complicated anionic components than the simple O^{2-} present in oxides. These groups $(XO_4)^{n-}$ make materials heavier, which is a limiting factor for electrode materials as it decreases their gravimetric energy density (the so-called "weight penalty"). But they also offer several advantages [10]:

- Stable frameworks providing structural stability (mainly due to the strong covalent bonds in the $(XO_4)^{n-}$), essential for cycling stability and safety.

- The inductive effect, described by Manthiram et al.[26,27], allowing to tune the potential of the materials across a wide range (Figure 1.8) depending on the choice of the counter-anion for a given metal.

- The great amount of possible elements combination and anionic/cationic substitutions, giving these materials unprecedented versatility.

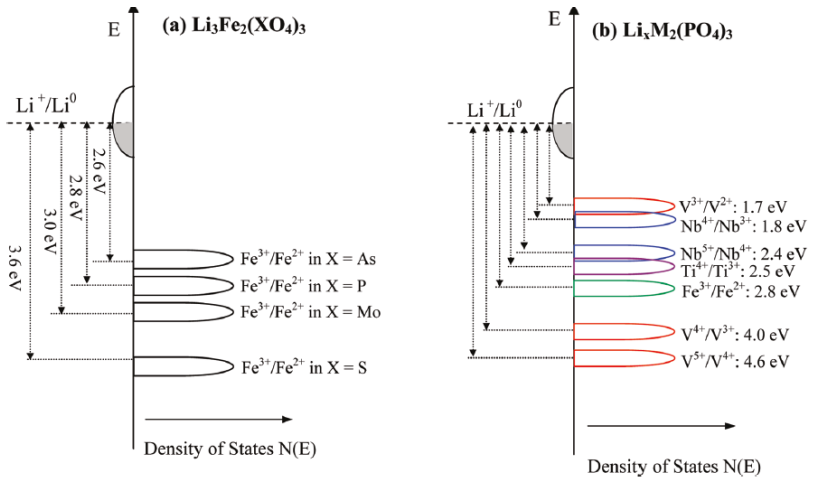

Figure 1.8: (a) Positions of the Fe^{3+}/Fe^{2+} redox couple relative to the Fermi energy of lithium in the NASICON structure with different polyanion countercations. (b) Positions of some M^n/M^{n+1} redox couples in $Li_xM_2(PO_4)_3$. Reprinted from[8].

The interest in polyanionic compositions sparked in 1997, with the discovery of the electrochemical activity of the olivine $LiFePO_4$ by Padhi et al.[28,29] (Figure 1.7). Once the issue of its low electronic conductivity is properly addressed (by carbon coating, nanostructuration or other means) the material shows a constant (i.e. flat) electrochemical voltage-composition profile at 3.45 V, for a high capacity reaching 170 mAh/g (theoretical) and 160 mAh/g (actual)[30]. This capacity was shown to be retained for thousands of cycles, even at high rates[31,32]. Moreover, the material is stable at high-temperatures, environmentally benign and safe. $LiFePO_4$ is also an extremely interesting material for the physics involved in its phase transformation upon delithiation, as it shows a phase diagram dependent upon cycling rate, temperature and particle size[33–36]. All these factors contribute to explain why the publications on $LiFePO_4$ can today be counted in thousands (the original paper by Padhi was cited more than 4000 times [3]). After $LiFePO_4$, several compositions were explored as suitable polyanions with good electrochemical properties. Among these, one should mention other olivines $Li(TM)PO_4$ (TM = Co, Mn...), NASICON structures

[3]Data from Web of Knowledge

(A_x(TM)(TM')(XO_4)$_3$, actually among the first open-framework structures investigated by Goodenough et al.[37], Figure 1.8) and more exotic structures such as silicates, borates, alluaudites, diphosphates and hydrated phosphates...which have recently been thoroughly reviewed[10,38]. A class of polyanionic materials of special interest in this thesis is the Tavorite A(TM)XO_4Y, a promising composition which is the object of Chapter 4.

1.3.3 Li-ion: achievements and limitations

Li-ion batteries have been the main tool that allowed the "wireless revolution". Compared to previous battery technologies, they have a much higher gravimetric energy density, which is the key parameter required to power a portable device. Figure 1.9 compares the Li-ion technology with common commercial alternatives. One quickly notices that Li-ion is superior in terms of gravimetric and volumetric energy density, and in terms of power.

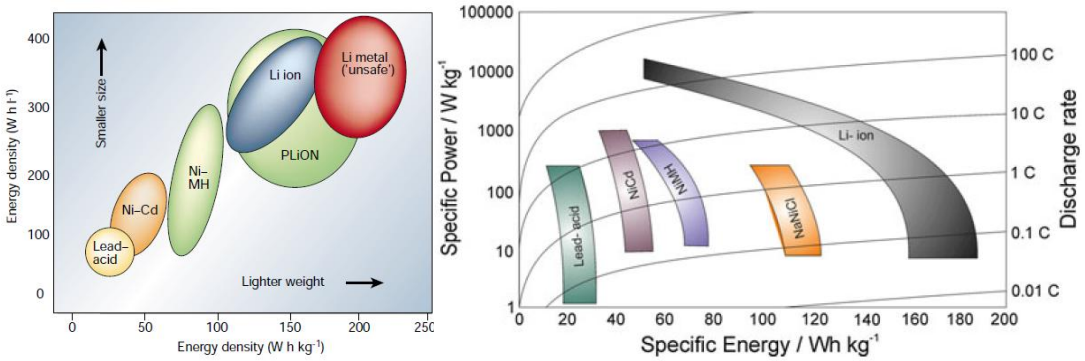

Figure 1.9: Comparison of different battery technologies. Left: in terms of gravimetric and volumetric energy density, taken from[39]. Right: in terms of gravimetric energy and power density, from[40].

The origin of this superiority is twofold:

- lithium is the third lightest element on earth (M_w = 6.94 g/mol).
- the redox couple Li^0/Li^+ has the highest oxidation potential (-3.04 V vs. SHE), meaning that lithium is the element with the strongest tendency to oxidize and release one electron.

Besides energy and power density, Li-ion batteries also have a good cycling life (up to 10000 cycles), adequate safety and cost to power a wide range of applications. Portable electronics has been the first technology to benefit from them, mainly using layered materials as positive electrodes. The advances brought by pouch-cell casings and by the use of polymers

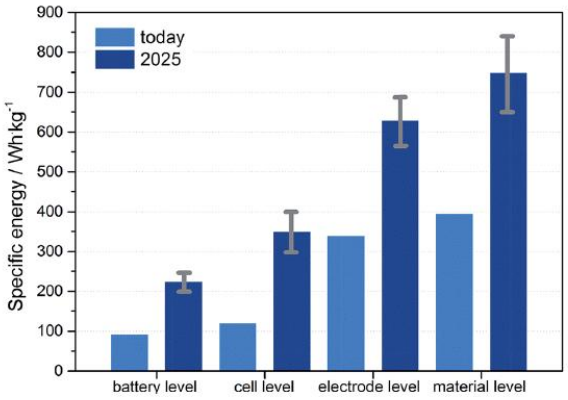

Figure 1.10: Specific energy density of Li-ion batteries at the material, electrode, cell and battery level. Automotive targets for 2025 are also shown. Reprinted from [41].

as electrolytes (either to make standard electrolytes in the form of gels (LiPo) or using actual ionic-conducting polymers (PLiON)) have been the key to pack more energy in smaller and more customizable batteries. The ability to produce them in almost any desired shape further contributed to make Li-ion batteries unrivalled to power portable devices of any kind. As discussed in section 1.1, recently research and industry have been converging on the common goal of extending the use of high energy density technologies to massive transport and storage applications [3,42], even though important challenges have to be overcome. The development of spinels and olivine materials helped speeding up this process and they strongly broadened Li-ion's applications range. Although all major car manufacturers already propose at least one fully electric vehicle and different hybrid possibilities, it is in the automotive market that the Li-ion technology shows its limitation. In fact, it can reach energy densities as high as 170 Wh/kg, but this just falls short when compared to the energy density of gasoline (1700 Wh/kg). Note that the actual energy density of a commercial battery can be as low as 15% of the theoretical value (see Figure 1.10 or simply compare 170 Wh/kg with the theoretical 1.1 kWh/kg of $LiCoO_2$). An interesting automotive perspective on the future of positive electrodes is offered by Andre et al. [41]. Strong improvements are required to bring electric vehicles' range from the actual ≈150-200 km to $>$ 500 km, competitive with the range of standard combustion engines.

1.3.4 Li-ion: perspectives and future developments

It is possible to envisage several improvements for the current generation of Li-ion batteries. Most efforts are done in the search of better positive electrodes. It is not the goal of this thesis to describe the countless materials that have been synthesized and that

show promising properties. Many review papers are available to get a comprehensive view of all investigated materials[8,9,11,12,43–45]. Among the well-known ones described above, only marginal improvements have been done in recent years since they already became as performing as they can possibly be. It is possible that better battery designs will allow to achieve higher energy densities and improve the situation depicted in Figure 1.10, but these will probably be minimal advancements. Research has now evolved towards attempts to achieve two-electron transfer at a single metal redox center, which would improve the capacity twofold. This implies the transfer of 2 Li^+ during every charge and discharge, with the consequently augmented volume change. Many materials are known to be able to accomplish the 2 Li^+/2 e^- reaction ($0 \leq x \leq 2$ in $Li_x(TM)_yMn_{2-y}O_4$, Li_xVPO_4O and $LiVPO_4F$...) but the challenge of achieving long cycle life with such a significant volume expansion (and through a very wide voltage range) has not been satisfactorily solved yet[11]. The improvement of negative electrodes should not be neglected as well, and the same is true for electrolytes stable in a wider range of potentials and temperatures[8]. At the negative electrode side, especially, the ideal configuration would be to use lithium metal, which has virtually infinite capacity and the lowest available potential. However every attempt to safely use lithium metal with liquid electrolytes failed because of its high reactivity and the tendency to grow dendrites, especially at high cycling rate, that can cross the separator and short-circuit the battery, resulting is potentially severe hazards[46,47]. The use of carbon at the negative electrode already reduces the available potential by about 0.3 V, and it limits high-rate applications. Other solutions for negative electrodes are under study (Si, Ge, Sn, SnSb, $LiTi_4O_{12}$...), often involving conversion-type reactions, and they have been described elsewhere[39,48].

1.4 Beyond Li-ion

Although Li-ion will surely be the leading storage technology for many years to come, longer timescale concerns have been raised about the future availability of lithium resources, located in remote and politically sensitive areas[49,50] and about the extent to which Li-ion technology is economically sound[51].

Given the limitations discussed above, a great effort is done to improve the Li-ion technology, but also to go beyond it. For this reason much research has been addressed to lithium's alternatives such as Na-based batteries[52] and more specifically to the Na-ion technology[53]. Sodium has been the obvious material to replace lithium since it is

Table 1.1: Comparison of lithium and sodium properties relevant to the battery technology.

	Cation Radius (Å)	Atomic Weight (g/mol)	V vs. SHE	Cost ($/ton) (carbonates)	Capacity (mAh/g) (metal)	Preferred coordination
Lithium	0.70	6.9	-3.04	5000	3829	Octahedral & Tetrahedral
Sodium	1.20	23.7	-2.71	150	1165	Octahedral & Prismatic

abundant and cheap while possessing the same external electronic structure (valence shell). Nevertheless a few drawbacks (Table 1.1) are present: (i) a standard reduction potential of -2.71 Volts for the Na^+_{aq}/Na redox couple, less negative than that of Li^+_{aq}/Li (-3.04 Volts); (ii) a larger ionic radius (1.20 Å instead of 0.7 Å); (iii) a bigger molecular weight, implying a lower energy density. This last point in particular is the reason for which the Na-ion technology is more promising for storage-grid applications than for portable or automotive ones. Yet materials for Na-ion batteries could develop rapidly because of the essential similarity between Li^+ and Na^+ intercalation chemistry [55], which made possible to build a sodium counterpart for many positive electrode materials of interest for Li-ion batteries ($NaCoO_2$ [56,57], $NaFePO_4$ [58–60], $NaVPO_4F$ [61–63], $Na_3V_2(PO_4)_3$ [64–66]) while candidates for negative electrodes are more scarce [67–69] (Figure 1.11).

A significant fraction of recently proposed electrodes are phosphate-based polyanionic materials [10]. Among them, vanadium-based fluorophosphates [70] are of particular interest, as they exploit the $(PO_4)^{3-}$ polyanion and vanadium's chemical versatility, as for example in the $Na_3V_2O_{2\delta}(PO_4)_2F_{3-2\delta}$ $(0 \leq \delta \leq 1)$ family of compositions [71–75]. Depending on δ, the oxidation state of vanadium varies between 3+ and 4+ with a concomitant modification

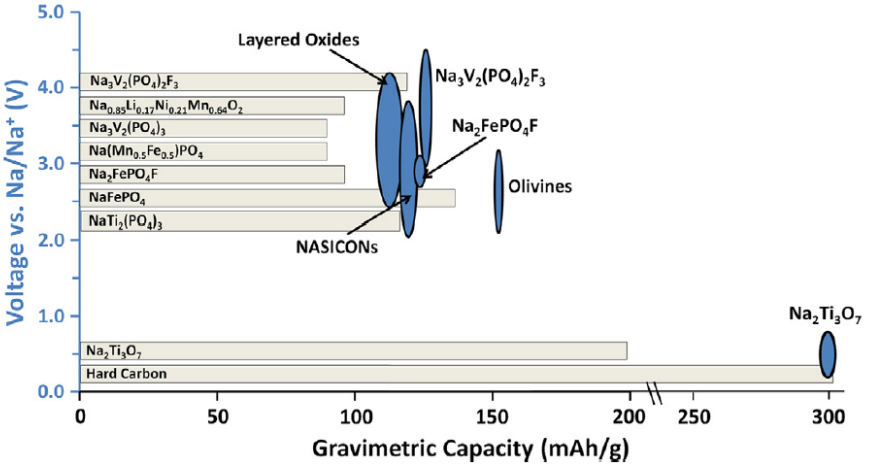

Figure 1.11: Gravimetric capacity and operating potential of the most promising electrodes for Na-ion batteries. Reprinted from [54].

of the physical properties and of the electrochemical signature of the material. The end member $Na_3V_2^{III}(PO_4)_2F_3$ ($\delta = 0$) is the object of Chapter 5 and will be carefully described there. Besides Na-ion, other recent technologies are waiting for the leap that will make them suitable for commercial exploitation. Sticking to intercalation reactions, batteries based on multivalent cations are given great attention (Figure 1.12)[76]. Despite the difficulties at developing suitable stable electrolytes, Mg^{2+} and Ca^{2+} seem promising alternatives as they exchange two electrons for a single metal center (avoiding the problem of excessive volume expansion generated by a 2 Li^+ intercalation). However, the higher charge density poses solid state diffusion challenges. Denser multivalent cations such as aluminum and zinc have also been reported to be able to cycle, but the potentials involved are much lower than those of Li-ion batteries[77,78]. Among completely different chemistries that could replace Li-ion, one should mention rechargeable lithium-sulfur (Li-S)[79] and lithium-air (Li-air) batteries[80], both promising especially in terms of the huge capacity they can provide.

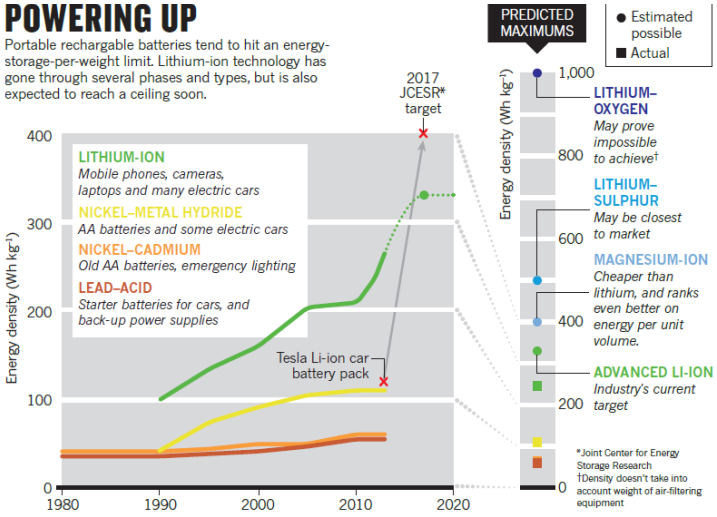

Figure 1.12: Energy density of current and future battery technologies. Reprinted from [81].

1.5 Electrochemical (de)lithiation/(de)sodiation mechanisms

As previously mentioned, intercalation materials are compounds where insertion (of alkali cations in our case) into the material's framework occurs leaving its host structure untouched. This is a simplified view, since on the atomic scale Li^+ (or Na^+) insertion can happen in different ways, significantly impacting the material's physical properties and electrochemical performances. Two main processes can usually be observed, a monophasic or a biphasic reaction (Figure 1.13):

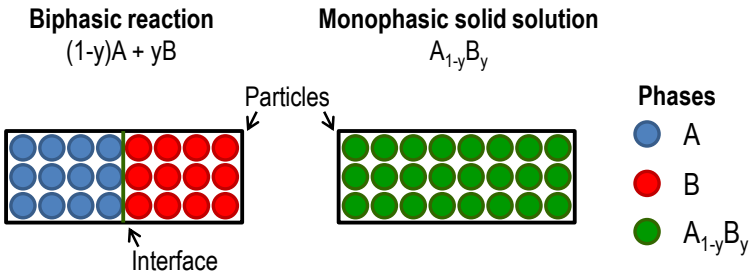

Figure 1.13: Scheme showing particles reacting through a biphasic reaction (left) and a solid solution (right). Phases are represented as circles: blue ones are the A phase, red ones the B phase and green one the intermediate $A_{1-y}B_y$.

- A monophasic reaction, also called solid solution, is a second-order process characterized by a complete miscibility of the lithiated A and delithiated B phases. Therefore, during such a transition only one phase $A_{1-y}B_y$ is present in all particles of the material. As an example, Li_xFePO_4 at high temperature shows a complete solid solution ($0 \leq x \leq 1$) between $LiFePO_4$ and $FePO_4$ [33]. During the transformation, the composition x continuously changes and so do the cell parameters (and possibly all other structural parameters) to allow the volume change induced by Li^+ (de)intercalation.

- A biphasic reaction is a first-order process where the lithiated A and delithiated B phases are not miscible. Therefore during delithiation, for example, the Li-poor phase has to nucleate, overcoming an energy barrier required to create the interface. Once it does so, the phase front propagates and the whole particle has composition (1-y)A + yB while transforming from Li-rich to Li-poor. Again mentioning micrometer-sized $LiFePO_4$, at T_{amb} and under slow cycling conditions, the material is an example of perfect biphasic reaction between $LiFePO_4$ and $FePO_4$. During the transformation from one end-member to the other, the two in principle have constant composition (therefore the crystal structures of A and B do not change, although the two do not have to be the same) and only the relative weight % y is modified (linearly). Different theories exist to model this behaviour, as core-shell models [82] or domino-cascade ones [83]. Their domain of application strongly depends on the considered material, on the morphology of its particles determining phase front's stability, on the thermodynamic (or not) equilibrium situation, etc. This is an interesting domain, which fully showed its complexity in the case of the phase diagram of $LiFePO_4$ [35,84].

The existence of a monophasic "solid solution" reaction or of a biphasic one directly impacts the electrochemical behaviour of an electrode material. Indeed, Gibbs phase rule states that:

$$F = C - P + 2 \tag{1.8}$$

where F is the number of the thermodynamic system's degrees of freedom, C the number of components and P the number of phases in equilibrium with each other. The rule comes from the fact that the equilibrium condition imposes a constraint on the number of intensive variables. This is relevant to Li-ion batteries because during (de)intercalation the system is composed of 2 components (the Li-rich and the Li-poor) and as we discussed P can be either 1 or 2. In the first case (the solid solution) F = 3. Since temperature and pressure are already supposed to be constant, one degree of freedom is left for the voltage. Upon cycling, the voltage-composition curve of a material showing a single-phase reaction will then be sloping. On the other hand, if the reaction is biphasic P = 2 and thus F = 2 too. The two degrees of freedom are taken by temperature and pressure, and therefore the value of the voltage must be fixed. During a two-phase reaction the voltage-composition curve will then be flat or, using the French word, a "plateau".

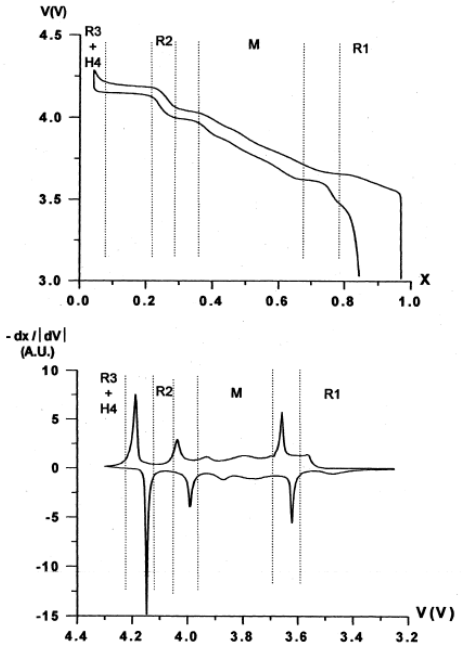

Figure 1.14: Relation of the electrochemical galvanostatic curve V = f(x) (top) with the inverse derivative $(dV/dx)^{-1}$ (bottom) for the layered material $LiNiO_2$. The three most intense peaks close to R1, R2 and R3 indicate biphasic transitions, while M indicate an extended solid solution region. Reprinted from [85].

Note that the two reaction mechanisms described above are not exclusive; a certain material can react in a given composition range through a monophasic reaction and in another through a biphasic one; this actually happens most of the time and several examples will be discussed in this thesis. Distinguishing the two mechanisms is sometimes easy from the voltage-composition curve of a galvanostatic experiment V = f(x) (flat vs. sloping), while sometimes it can be hard. A valuable tool in this case is the inverse derivative curve $(dV/dx)^{-1}$ of the voltage-composition one. As can be seen in Figure 1.14, this representation shows intense narrow peaks for biphasic reactions, at the voltage typical of the considered redox reaction. In contrast, when the (de)intercalation mechanism is a solid solution, it shows broader and weaker peaks.

1.6 Characterization techniques

Several characterization techniques are employed in this thesis to get insight on the behaviour of electrode materials for Li-ion and Na-ion batteries. Besides electrochemical characterizations (mainly galvanostatic cycling and GITT) which have already been described, diffraction is the main technique that we used, thus deserving a detailed discussion.

1.6.1 Powder Diffraction

Diffraction is a phenomenon occurring when a wave (whatever its nature) interact with an obstacle. Among several possible interactions, diffraction dominates when the typical length of the obstacle (for example the dimension of a hole or the distance between two objects) is comparable to the wavelength. The discovery of X-Rays by Röntgen (1895) was the first step that allowed Bragg (father W.H. and son W.L.) to lay the basis for the modern science of crystallography [86]. In fact X-Ray tubes produce radiation having a wavelength of the order of 1 Å, the same of typical inter-atomic distances in crystals. Therefore shining X-Rays on a NaCl crystal allowed the Braggs to observe the first X-Ray diffraction (XRD) pattern in 1913, which earned them the Nobel Prize in 1915. The most basic comprehension of X-Ray diffraction is provided by Bragg's law. When considering an X-Ray beam of wavelength λ incident on a crystal with angle θ with respect to a given set of crystallographic planes (labelled by the Miller indices hkl), the elastic diffraction condition is given by:

$$2d_{hkl}sin\theta = n\lambda \tag{1.9}$$

that essentially imposes constructive interference between the reflected beams. Here d_{hkl} indicates the distance between successive (hkl) crystallographic planes and n the order of diffraction. The same law can be stated in a more general way using Van Laue's vectorial formulation:

$$\vec{Q} = \vec{G} = \frac{n2\pi}{\vec{d}_{hkl}} \tag{1.10}$$

Here $\vec{Q}$ represents the difference of incoming and scattered wavevector (in the common case of elastic scattering $\vec{Q} = 4\pi sin(\theta)/\lambda$) and $\vec{G}$ is a vector of the reciprocal lattice. Hence equation 1.10 states that to have diffracted intensity the momentum transfer from the wave to the crystal lattice must equal a vector of the reciprocal lattice. Every time this condition is matched a so-called Bragg peak appears. The intensity of every one of these peaks depends on the scattering power of the atoms in a given crystallographic plane (hkl) (N.B. X-Rays are scattered by the electrons orbiting the nucleus, so heavier atoms are those who scatter the most). Such intensity can be shown to be proportional to the so-called structure factor F_{hkl} following:

$$I_{hkl} \propto |F_{hkl}|^2 = \sum_{j=1}^{n} O_j f_j e^{i2\pi(hx_j+ky_j+lz_j)} \tag{1.11}$$

where x_j, y_j and z_j represent the atomic positions of the j^{th} atom, f_j its atomic scattering factor and O_j the fraction of sites (x_j, y_j, z_j) occupied by the atom.

X-Ray diffraction is the basic tool of crystallography, and it is worth mentioning that we just celebrated 2014 as the international year dedicated to this science. Several techniques have been developed during the last century to carry out more and more advanced X-Ray diffraction experiments. It is not worth discussing this in too many details here, as several textbooks already did [4]. It is only important to mention that, after the first experiments carried out on single crystals (the so-called single crystal XRD), new techniques dealing with polycrystalline samples and powders have been developed. A powder is a polycrystalline sample where all crystallites have perfectly random orientation. This is of special importance as many materials synthesized by a variety of chemical methods are in the form of powders, and therefore X-Ray Powder Diffraction (XRPD) was established as the technique of choice to characterize the crystal structure of new synthesized materials. Although equation 1.9 only shows one angular dependence, in a monochromatic single crystal XRD experiment one finds Bragg reflections distributed all over the surface of a sphere to account for all possible planar orientations in the crystal (Figure 1.15). Thus two

[4] see for example *X-Ray Diffraction* by B.E. Warren

angular coordinates (θ,ϕ) are required to determine the position of a Bragg spot (once a detector is set at a given distance). Instead, shining monochromatic X-Rays on a powder sample is the same as making an integration over one angular direction, leaving only one (θ) free variable. Then one observes cones diffracting from the sample (instead of spots), drawing characteristic circles on a flat-plate detector. Every circle appears at an angle θ given by Bragg's law (equation 1.9) which relates to the crystallographic planes distance and ultimately to the material's space group and unit cell parameters, while the integrated intensity of every circle is given by the position of the atoms inside the unit cell.

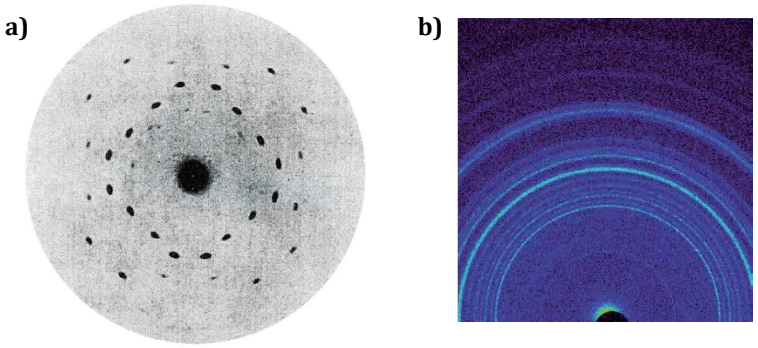

Figure 1.15: a) Max Von Laue's X-ray diffraction pattern from a zinc-blende (ZnS) single crystal, revealing spots of various shape and intensity. b) X-Ray powder diffraction pattern of a sample of the soil of Mars, collected by the Curiosity rover, revealing the classical cones created by the powder averaging. Pictures taken from the Editorial of Nature Milestones in Crystallography, 2014 (doi:10.1038/nature13348).

Note that X-Rays were the first probe to allow diffraction from crystals, but they are definitely not the only ones. Nowadays diffraction experiments can also be carried out using electrons, synchrotron radiation and neutrons. The diffraction of these probes is similar to X-Rays' one (Bragg's law holds) but each probe has specific properties dependent on the different radiation-matter interaction mechanism (in equation 1.11, f_j has a different behaviour for every probe). As a conclusive remark, one should note that the golden age of crystal structures did not start until 1969, when the Rietveld method became available [87]. This is a refinement procedure, developed by Hugo Rietveld, that allows precise determination of a crystal structure starting from an XRPD pattern, provided that an initial model sufficiently close to the actual one is known. The basic idea is that a certain quantity estimating the difference between the calculated and experimental diffraction pattern is minimized, providing a final model closer to reality than the initial one. Reiteration of the

process until convergence usually provides the true crystal structure.

1.6.2 Neutrons

Neutrons are one of the fundamental particles that constitute our universe, since they are among the building blocks of atomic nuclei. Neutrons were discovered in 1932 by James Chadwick, who was bombarding beryllium with α particles ($^4He^{2+}$) and he observed the reaction:

$$^9Be + \alpha \rightarrow {}^{12}C + {}^1n + 5.7MeV \tag{1.12}$$

Because of mass and energy conservation, Chadwick understood that the neutron exists and that it has approximately the same mass of the proton. He won the Nobel prize in Physics for his achievement in 1935.

Nowadays the properties of neutrons are well-known: they are spin 1/2 particles, without electric charge (this was actually measured at ILL in 1987, finding a charge of -0.2(8) $\cdot$ 10^{-21}e) and with a lifetime of 880(1) s (or, more precisely, with a half-life of 611(1) s). Being electrically neutral, neutrons interact weakly with matter; however they still experience gravity, weak nuclear force and strong nuclear force. Since they have a nuclear magnetic moment, they also respond to magnetic fields. These interactions allow the use of neutrons for several important applications, both industrial and scientific. The first use of neutrons is due to Enrico Fermi, who understood the principles of nuclear fission. Neutrons are fundamental to it because they are the key to achieve a chain reaction. In fact, in a nuclear reactor uranium is hit by neutrons and as a consequence it is split in lighter elements, releasing energy. The extra neutrons freed in the process allow the reaction to sustain itself.

While industrial reactors are designed to safely sustain a fission chain reaction to exploit energy in the form of heat, the scientific use of neutrons relies mainly on reactors specifically designed for their extraction. The Institut Laue-Langevin is one example of such reactors, where different tubes exit the reactor's nucleus to bring neutrons to the instruments. Another possible way to produce neutrons is called spallation, which is based on the bombardment of a heavy element target (e.g. Hg) by highly accelerated protons; the impact destabilizes the heavy element and it induces it to release many particles, among which several neutrons that can be collimated for subsequent use.

The interaction of neutrons with matter is a complicated subject, properly described in many works[88,89]. Related to this thesis, three main isotope-dependent processes are

relevant and should be noted here: elastic coherent scattering, elastic incoherent scattering and neutron absorption. In the first case, neutrons are scattered coherently between different atoms, meaning that one can probe correlations among them (such mechanism for example is at the origin of Bragg peaks in diffraction). In the second case, elastic incoherent scattering cause neutrons to be randomly scattered, originating a strong featureless background; this is due to the isotopic distribution of a given element (namely in most cases there is no control on the actual isotope present in the sample, but elements with "natural abundance" are used). Finally, few elements are also strong neutrons absorbers, as for example lithium, boron or cadmium (i.e. they have at least one isotope which is a strong neutron absorber).

Neutrons' scattering length is the key property when considering the diffraction of neutrons. In fact, these are particles but also waves (as clear from the De Broglie principle) and therefore they can diffract. But a strong difference is present with respect to other probes as for example X-rays. Neutrons used for diffraction are in most cases thermal neutrons, i.e. they have an energy of approximately 25 meV. At this energy, their wavelength has an order of magnitude of 1 Å because of their heavy mass. However, neutrons do not interact with the electrons surrounding the nucleus, but with the nucleus itself, which has a typical dimension of 10^{-5} Å. Thus the potential they experience, called the Fermi potential, is a point-like one of the form:

$$V(\vec{r}, \vec{R_0}) = \frac{2\pi\hbar^2}{M} b\delta(\vec{r} - \vec{R_0}) \tag{1.13}$$

where $\delta(\vec{r} - \vec{R_0})$ is a Dirac delta and M is the neutron's mass. In this description, b is called scattering length and it defines the intensity of the potential felt by a neutron when it interacts with a nucleus. Related to powder diffraction, when neutrons are the probe eq.1.11 for the intensity still holds but with the form factor f_j replaced by the scattering length b_j of the j^{th} atom. Note that, although f_j is always positive, b_j can be negative for a few elements. This is due to the fact that the interaction is not always repulsive but, in a few cases, it can be attractive. Neutron scattering lengths and their importance for the study of Li-ion batteries are further discussed in the next chapter (2).

1.6.3 Powder diffraction and electrode materials

In the field of Li-ion batteries, powder diffraction has classically been used to characterize pristine synthesized materials in terms of structure and purity. The study of compositions formed upon electrochemical cycling is also extremely important, as these are usually

unstable in air and cannot be synthesized by standard chemical techniques. These measurements can be done rather easily *ex situ*, i.e. out of the electrochemical cell. This means that a certain composition is prepared via lithium extraction or insertion in the cell, which is subsequently opened in an argon-filled glove-box in order to recover the material, properly wash it and/or grind it, and perform a powder diffraction experiment. This approach, albeit valuable, is very limited because the composition under study might be metastable and evolve once the material is extracted from the cell. Moreover, once this is done the risk of contamination or oxidation from atmospheric agents (O_2, H_2O...) or tools used in the process is significant. Hence it is hard to be sure that the material studied in the diffraction experiment is exactly the same that was prepared upon electrochemical cycling.

1.6.4 *In situ/operando* studies applied to Li-ion batteries

To overcome the limitations of *ex situ* studies, *in situ* and *operando* approaches have been developed. A distinction is made since *in situ* means "in place" (i.e. in the battery in our case), while *operando* means "during operation". In both cases the electrochemically prepared material is studied directly inside the battery. This has the advantage of avoiding exposure to the atmosphere outside it; but an *in situ* (not *operando*) experiment still requires that the battery cycling is stopped, put in relaxation (open circuit voltage OCV) and mounted in the diffractometer (or other experimental setup) to perform the measurement. In an *operando* approach, instead, the battery is in the diffractometer as it is operating, namely the diffraction measurement is done in real time as the battery charges and discharges. The advantage is that metastable phases can be captured, and the real out-of-the-equilibrium battery's behaviour is observed. Note that an *operando* experiment is necessarily *in situ*, while the vice versa is not true.

In situ & *operando* techniques started developing right after the invention of the first Li-ion batteries, and they proved to be exceptionally useful tools to understand the electrodes behavior in Li-ion batteries [90]; these are dynamical in nature and their understanding is limited if they are only looked at through a series of snapshots, such as those we can get from *ex situ* studies. X-ray powder diffraction (XRPD), in particular, has been the leading technique thanks to the possibility to exploit laboratory diffractometers [90–95], as well as more powerful synchrotron sources [36,96–100]. Many studies have been published and their importance is noteworthy. The *in situ* approach to study Li-ion batteries has been applied to almost any other technique, such as Raman spectroscopy [101] XANES (and EX-

AFS)[97,102–104], NMR[105,106], Mössbauer[107–111], Transmission X-Ray microscopy (TXM-STXM)[112,113], TEM[114,115], Neutron reflectometry[116] and X-Ray tomography[117], resulting in a great amount of different perspectives to look at electrochemical reactions in real time. A comprehensive review was recently published by Harks et al.[118].

1.6.5 Electrochemical cells for *in situ* XRPD

Whatever the probe, the first step to carry out *in situ* studies is the development of custom setups to combine the electrochemical needs of the battery with those of the characterization technique of choice. In the field of diffraction studies, setups for laboratory XRPD are common nowadays, while those for Synchrotron Radiation facilities have been developed by several groups (ours included) and have become more readily available[97,103]. The design of an electrochemical cell for *operando* neutron diffraction is a more complicated task, and our own prototype, along with its advantages and drawbacks, is described in the next chapter of this thesis (2).

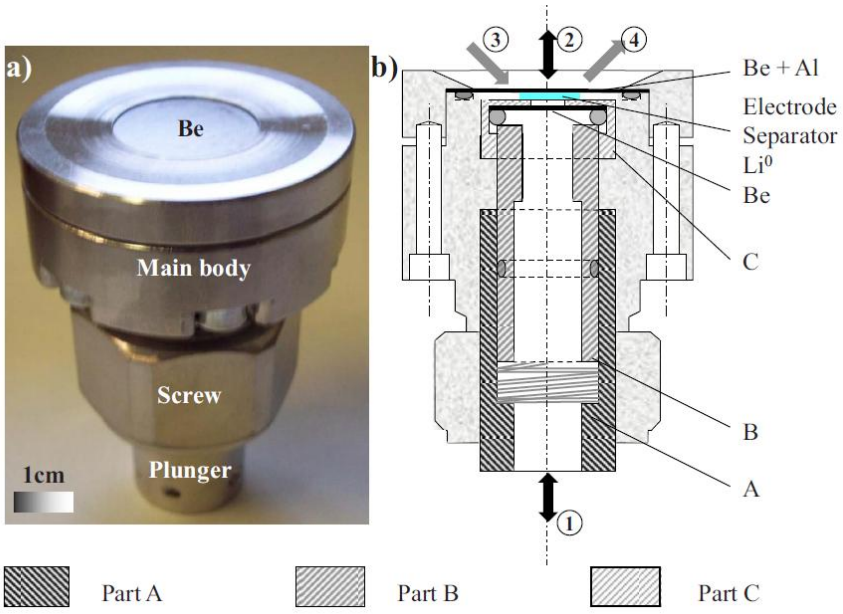

Figure 1.16: Electrochemical cell for *operando* measurements, from[97]. (a) Photo and (b) detailed view of the cell with incoming and outcoming beam paths in transmission geometry.

Here we show the cell for *operando* experiments developed at LRCS in recent years[97] and used in the following for many of the described XRPD measurements. It is reported in Figure 1.16. The design allows for measurements both in reflection (Bragg-Brentano) and transmission geometry. The former is used on the Bruker D8 Advance in-house diffractometer in Amiens (equipped with Cu K$\alpha_{1,2}$ radiation), while the latter is used for experiments

Figure 1.17: Cell for *in situ/operando* XRPD experiments in reflection diffraction on the PANalytical Empirean diffractometer.

in synchrotron radiation facilities such as ALBA or SOLEIL. The stainless steel cell is assembled in an argon-filled glove-box, using Li metal as the negative electrode and Whatman glass fiber separators soaked in commercial LP30 as electrolyte (1M $LiPF_6$ in EC:DMC (1:1 in wt%)). Two metallic beryllium windows are used to seal the cell and to insure at the same time good electronic conductivity and low absorption of the X-Ray beam. Additional details regarding positive electrode's preparation, charge/discharge rate and measurement time of XRPD scans will be provided in the following for each experiment. As a rule of thumb, in-house measurements require ≈1h scans and charge/discharge rates around C/10 or C/20, while synchrotron experiments are faster, taking only a few minutes for a scan and thus allowing (if required) faster charge/discharge rates. The important parameter to preserve is a sufficient resolution in composition Δc; this is given by $\Delta x \cdot t_{scan}/t_{charge}$ (but $\Delta x = 1$ in most experiments). This way no appreciable change in the electrode's structure remains hidden between two scans. Besides the setup described above, a second one was developed at ICMCB for *operando* XRPD experiments. The principle of the electrochemical cell is similar to the one in Figure 1.16; except that it is only suitable for reflection geometry and it is made to be mounted on a PANalytical Empyrean diffractometer (Figure 1.17, having if needed the possibility to isolate Cu Kα_1 radiation for better angular resolution).

1.6.6 Neutron instruments and synchrotron beamlines

The most used instruments and beamlines used in this thesis for neutron powder diffraction and synchrotron X-Ray powder diffraction experiments are described in this section.

D2B and D20 at Institut Laue Langevin

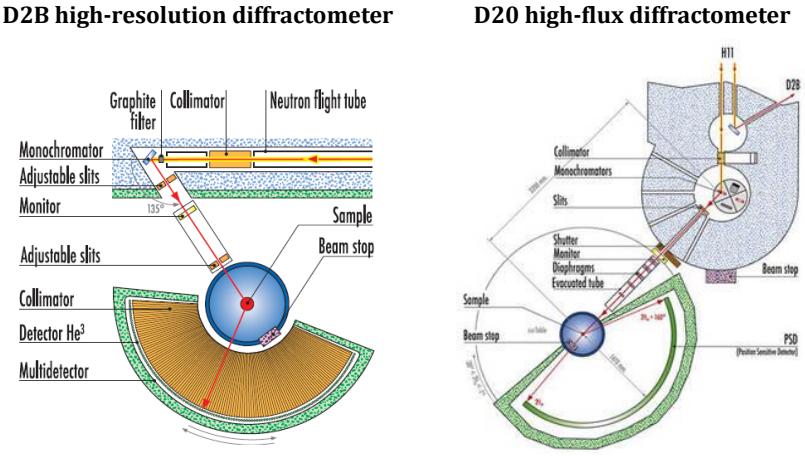

Figure 1.18: D2B (left) and D20 (right) diffractometers at ILL.

The neutron diffractometers used in this work are mainly D2B and D20 at the Institut Laue-Langevin (ILL, Grenoble) (Figure 1.18), both chosen because of their complementary features. D2B is a very high-resolution diffractometer designed to achieve optimal resolution ($\Delta d/d = 5{\cdot}10^{-4}$). We used such an instrument for all standard neutron powder diffraction measurements. The setup of choice involved a Germanium monochromator at reflection (335), resulting in the optimal wavelength for the instrument of $\lambda = 1.594$ Å. In this configuration, a neutron flux of about 10^6 $cm^{-1}s^{-1}$ is obtained. Beam size at sample position is 2x5 cm^2, usually further collimated by slits. The angular range is very wide, measuring $5° < 2\theta < 165°$. A typical room-temperature experiment on the D2B diffractometer is made by filling a vanadium cylindrical container (cans of diameter 6.5 mm or higher) with the powder to be measured. For air-sensitive samples, the containers are filled in an argon-filled glove-box and sealed with an indium wire.

On the other hand, D20 is a very high-intensity diffractometer, especially well-suited for *in situ* measurements due to the ability to collect NPD patterns in short times. The instrument is also very flexible, with different take-off angles and monochromator combinations available to tune intensity and resolution. Neutron flux can thus range between 10^7 $cm^{-1}s^{-1}$ and 10^8 $cm^{-1}s^{-1}$. In our *in situ*/*operando* experiments, we privileged a compromise between the best available flux and resolution, choosing a take-off angle of 90° with a Germanium monochromator either on the (115) reflection ($\lambda = 1.54$ Å) or on the (113) one ($\lambda = 2.4$ Å), depending on the sample. In principle, a wide angular range of 153.6° is available.

MSPD at ALBA

Most of synchrotron radiation XRPD measurements in this thesis were carried out in collaboration with François Fauth at the Materials Science Powder Diffraction (MSPD) beamline at ALBA synchrotron facility[119] in Cerdanyola del Valles, Barcelona. Two main setups of the beamline were interesting in our case:

- A high-angular mode of the station (13 channels Si111 multi-analyzer setup) where data are collected in Debye-Scherrer geometry in the 2° - 50° 2θ angular range. A very high angular resolution (up to $\Delta d/d = 2{\cdot}10^{-4}$) can be reached in this operating mode. The energy can be chosen in a wide range (8-50 KeV); in our case we selected the rather short wavelength of 0.620 Å to avoid absorption issues. Samples were enclosed in 0.7-1 mm diameter borosilicate capillaries and measured at ambient temperature. In case of high temperature measurements, capillaries were heated using a FMB Oxford hot air blower, while for low temperature ones we used a Cryostream Plus nitrogen blower from Oxford Cryosytems.

- A high acquisition-rate mode (but with lower angular resolution). In this case powder diffraction patterns were collected using the one dimensional silicon based position sensitive detector MYTHEN in the 2° - 50° angular 2θ range (d-range: 1.12 - 40 Å). Since MYTHEN detector spans a $\approx 40°$ angular 2θ range, this setup allows fast data acquisition with extremely high statistics and good angular resolution (but lower than the one of a multi-analyzer setup). This mode of the instrument was mainly used for *operando* experiments. In this case batteries were prepared using the cell described in section 1.6.5. Transmission geometry was used, with the beam going through all the layers of the cell. Throughout all the experiments, the operating wavelength was $\lambda = 0.953$ Å. The longer wavelength was specifically chosen in order to minimize peak overlap and in particular to better resolve Bragg reflections. The quality of the data collected in these *operando* conditions allows Rietveld structural refinements of all the identified phases with goodness comparable to refinements performed using the highest angular resolution mode.

CRISTAL at SOLEIL

Synchrotron radiation XRPD experiments were also carried out at room temperature at the CRISTAL beamline of the SOLEIL synchrotron in Saint-Aubin (Paris). CRISTAL is

an undulator-based diffraction beamline, dedicated to single crystals and powders between 4 and 30 keV. In our experiments, data were collected using a 2-circle diffractometer at $\lambda = 0.669$ Å in the 5° - 50° 2θ angular range (energy resolution $\Delta E/E \approx 10^{-4}$). The measurements were performed in Debye-Scherrer geometry, with the powder sealed in a 0.7 mm capillary and the acquisition done with a multi-analyzer (21 Silicon (111) crystals).

1.7 Aim of the thesis

This thesis is the result of the collaboration of three French institutions: the Institut Laue-Langevin (ILL, Grenoble), the Laboratoire de Réactivité et de Chimie des Solides (LRCS, Amiens) and the Institut de Chimie de la Matière Condensée (ICMCB, Bordeaux). It aims at exploiting the potentialities of real-time diffraction experiments for the analysis of electrode materials for Li-ion batteries. Real-time is meant as a synonym of *operando*, i.e. experiments carried out during battery operation. At the material scale, this means during Li^+ extraction or insertion from/into the 3D framework of the intercalation materials constituting the electrodes. We have tried to promote the synergy and take advantage of the complementarities between different probes for diffraction experiments, with a special accent put on neutrons. The first two chapters of this thesis describe in fact the design and development of an electrochemical cell for *operando* neutron diffraction experiments on electrode materials for Li-ion batteries. After building such a cell, we confirmed that it worked as required and we used it to study challenging materials. In particular we analyzed the detailed structural information that neutrons could provide on spinel compositions ($LiMn_2O_4$, $Li_{1+x}Mn_{2-x}O_4$, $LiNi_xMn_{2-x}O_4$), stressing especially the insights that are missed by other characterisation techniques. Chapters 4 and 5 are instead more material-centered and reflect the interest of our research groups on polyanionic compositions. The former deals in fact with the electrochemical transformations of the Tavorite compounds $LiVPO_4O$ and $LiVPO_4F$. These phases were already the object of the thesis work of Jean-Marcel Ateba Mba in our group[5]. They are able to both intercalate and deintercalate lithium; we studied both domains of both materials, looking at the relation between electrochemical and structural properties. We made combined use of XRPD, synchrotron XRPD and NPD techniques, *in situ*/*operando* and *ex situ*, to shade light on the complex phase transformations encountered in these promising compounds. Chapter 5 focuses to a different technology, Na-ion batteries. However the leap is apparent, because the same principles on alkali cation intercalation apply and therefore the same *operando*

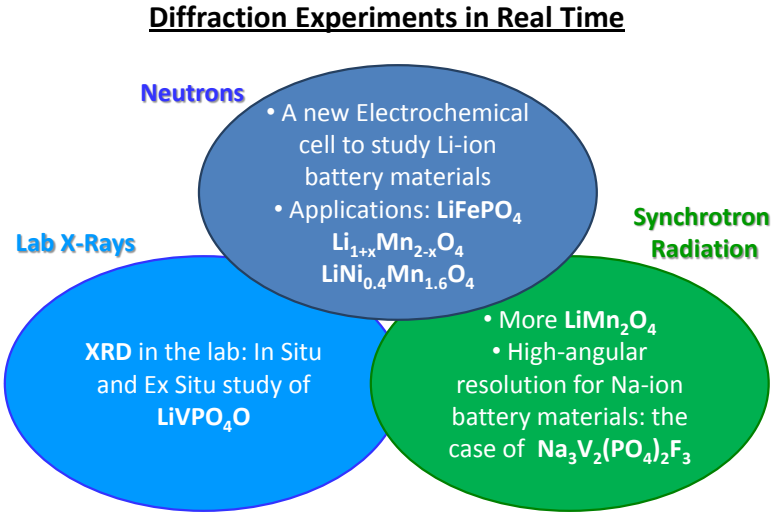

Figure 1.19: Topics treated in this thesis.

characterization techniques are effective for the materials' study. We focused our interest on the polyanionic compound $Na_3V_2(PO_4)_2F_3$ as one of the most promising positive electrode materials for a future generation of Na-ion batteries. During our studies we realized that for this compound the most suitable probe is synchrotron radiation, given the small orthorhombic distortion present in the unit cell and the subtle transformations that we could show to happen during Na^+ extraction and insertion. However, neutrons were still used as a complement for structural determinations. This thesis is therefore an attempt at combining the most advanced diffraction techniques available, using or developing whenever possible an *operando* approach, to shed light on the structural transformations that electrode materials undergo in Li-ion and Na-ion batteries. We chose here a number of materials that we thought are of special interest. However the techniques employed and the tools developed are completely general and can be applied to the study of any of these challenging materials, in the hope to obtain an ever-better comprehension of their working mechanisms and that this will reflect on the betterment of future batteries.

Chapter 2

An electrochemical cell for *in situ/operando* neutron powder diffraction

2.1 Introduction

In the last decade the quest to ameliorate Li-ion and Na-ion batteries followed a great number of different paths, some of which were briefly discussed in the introduction of this thesis. However, the improvement of a given battery technology does not depend solely on the discovery of new chemistries, new materials or new electrode formulations but it also relies on better characterization techniques, allowing to probe chemical reactions in more and more details, until a full comprehension of the mechanisms involved is achieved. In this respect, *in situ* techniques are extremely valuable and their use has been described in the previous chapter. Here we will show how neutrons can be an important probe to study battery materials and how they can be used to carry out *in situ* and *operando* studies.

2.2 Neutrons and Li-ion batteries

Until about 15 years ago, neutron powder diffraction (NPD) was not considered for *in situ* studies on lithium/Li-ion batteries because of the intrinsic difficulties it held, although its advantages should not be neglected. Electrode materials often contain light elements such as lithium and oxygen, almost transparent to X-Rays and lithium in particular is the element whose position, amount and dynamics must be known. These properties can

be probed using neutrons[120] because, although lithium's scattering length is small, it is negative and generates a significant contrast with other elements (most of which have positive scattering lengths, see Figure 2.1). Table 2.1 summarizes the scattering properties of lithium. In all the experiments of this work, natural lithium was used, i.e. $^{6.94}$Li composed of 92.5% ^{7}Li and only 7.5% ^{6}Li. ^{7}Li being the most abundant isotope is certainly an advantage because it is the one having negative scattering length and a relatively small absorption cross section. Isotopic enrichment (the use of a specific isotope instead of the naturally-occurring composition) is sometimes performed in neutron scattering facilities because it can lead to additional experimental information by controlling the element's absorption. In our case this possibility was ruled out because of the different lithium contributions present in a battery (in the positive electrode, in lithium metal and in the lithium salt in the electrolyte) that would have made a proper enrichment very complicated and expensive.

Table 2.1: Neutron scattering properties of ^{6}Li, ^{7}Li and naturally occurring $^{6.94}$Li, obtained from[121]. Columns: nuclide, relative amount, nuclear spin state I. Scattering lengths in fm: bound coherent scattering length (b_c), spin-dependent scattering length for $I+1/2$ (b_+), spin-dependent scattering length for $I-1/2$ (b_-). Cross sections in barns: coherent cross-section σ_{coh}, incoherent cross-section σ_{inc}, total cross-section σ_{scatt}, and absorption cross-section σ_{abs}.

^{A}Symb	%	I	b_c	b_+	b_-	σ_{coh}	σ_{inc}	σ_{scatt}	σ_{abs}
$^{6.94}Li$			-1.90(3)			0.45(1)	0.92(3)	1.37(3)	70.5(3)
^{6}Li	7.5	1	2.0(1)	0.7(1)	4.7(2)	0.51(5)	0.46(5)	0.97(7)	940(4)
^{7}Li	92.5	3/2	-2.22(2)	-4.15(6)	1.00(8)	0.62(1)	0.78(3)	1.40(3)	0.0454(3)

Another advantage of neutrons comes from the fact that many electrode materials contain more than one transition metal element (Mn, Fe, Co, Ni, ...), poorly distinguished using X-Rays diffraction because of their similar scattering powers. Neutrons' scattering lengths, on the other hand, do not vary continuously throughout the periodic table (Figure 2.1): a much higher contrast between such elements may be attained using NPD[122]. Also, neutrons are in general superior to X-Rays and other characterization techniques in terms of their high penetrating power (due to their weak interaction with matter), allowing to probe simultaneously a whole electrode or even a whole battery, depending on the chosen geometry. Finally, another advantage comes from the physics of neutron scattering: X-rays are diffracted by electrons distributed around the nucleus, generating a form factor that decays with Q (the scattering vector $Q = 4\pi sin(\theta)/\lambda$). Neutrons, on the other hand, interact

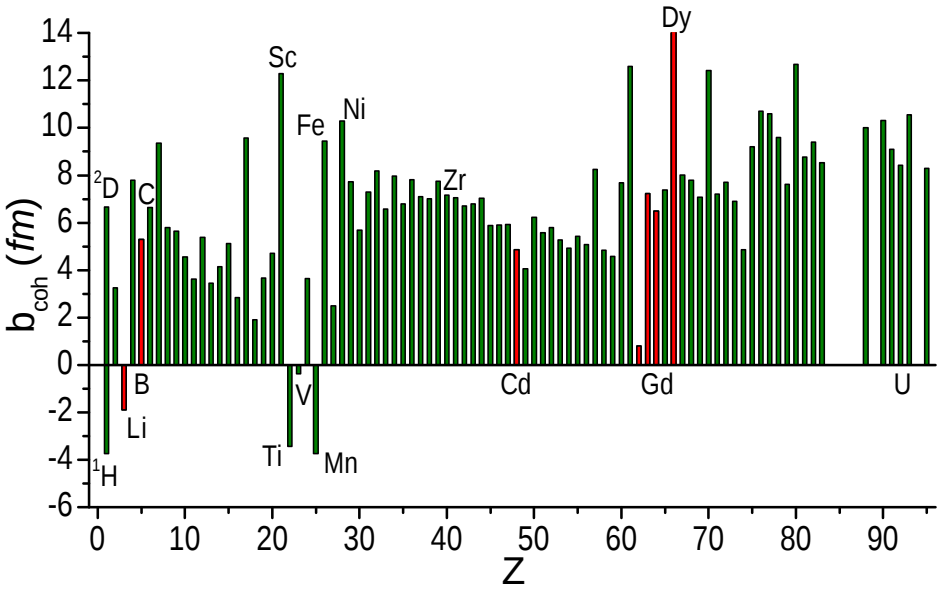

Figure 2.1: Neutron scattering lengths for most elements (natural abundance) in the periodic table. Those in red are strong neutron absorbers.

directly with the nucleus and this point-like potential leads to Q-independent scattering lengths. Therefore, in a NPD experiment one can observe significant intensities at high Q values, leading to important structural information about atomic parameters as site occupancies and Debye-Waller factors. These advantages, which have been the engine to push the development of *in situ* NPD, will be fully illustrated in this thesis. Nevertheless, some obvious drawbacks of neutrons have to be recalled here: first of all, a neutron source is less easy to have at hand. Secondly, Li-batteries include many problematic components such as hydrogen-rich electrolytes that create a strong continuous background, such as natural lithium that absorbs neutrons and such as various other battery parts (aluminum/copper current collectors, steel protective case etc...) that give rise to very intense Bragg peaks. For these reasons *in situ* NPD took more time to be developed. Neutron scattering facilities, worldwide, that can provide the necessary flux and resolution for this kind of investigations are still rare.

2.3 Development of electrochemical cells for *in situ* NPD

The fabrication of custom-made electrochemical cells able to satisfy both the needs of a battery and those of NPD is a mandatory requirement to carry out successful *in situ* experiments and first interesting attempts were reported around 2000 by different researchers

in Uppsala, Sweden [123–125] (Figure 2.2a). The challenge that such cells had to face consisted in combining a good electrochemistry with sufficient statistics for neutron diffraction, knowing that the two requirements often conflict. A big amount of powder for the positive electrode is required for NPD, while this is usually problematic for a homogeneous electrochemical reaction. At that time, the results did not match expectations and improved cell designs were reported by the group of P. Novak at PSI (Switzerland) [126,127] (Figure 2.2b).

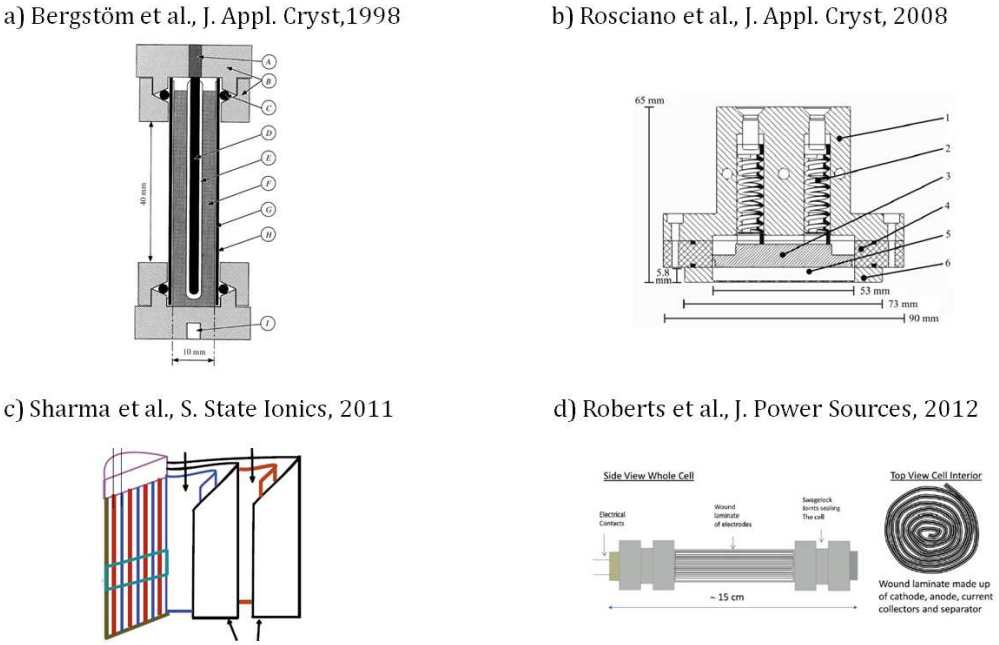

Figure 2.2: Electrochemical cells designed for *in situ* NPD using custom-made geometries (a, b) or traditional roll-over geometries (c, d).

Although these first experiments were important, the results they led to in terms of structural information were quite poor. Qualitative information about the evolution of Bragg reflections was usually found, while the quantitative information was limited to cell parameters and relative amount of crystalline phases, obtained in just a few points ($<$ 10 compositions) during charge. For this reason such early experiments cannot really be regarded as *operando*, in the sense that the resolution in electrode composition (Δx) was not sufficient to follow closely lithium's (de)intercalation reaction. More recently it became clear that even commercially available lithium batteries could be studied with *in situ* NPD [128–136,136–139] giving interesting information on their overall behavior and showing that their diffraction patterns are not worse than those of early custom-made cells. Indeed, a commercial battery possesses quite a significant amount of electrode material (a few grams) illuminated by the beam giving a strong signal and allowing for fast detec-

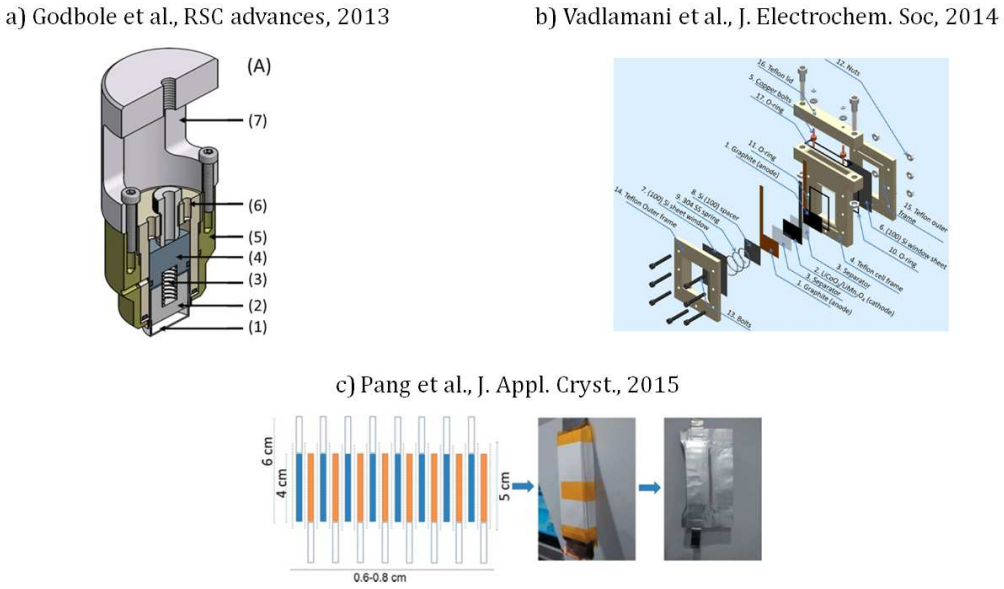

Figure 2.3: Recent electrochemical cells designed for *in situ* NPD using custom-made geometries (a, b) or pouch-cell geometry (c).

tion. The drawback is the presence of at least 5-6 crystalline phases diffracting and once again detailed Rietveld analysis would be extremely challenging. Still, the application to commercial batteries strongly increased the interest of the battery community towards *in situ* neutron diffraction and led to a rather straightforward evolution: the idea to produce custom-made laboratory batteries in a classic roll-over battery design (18650-like) or in a simple but effective pouch-cell design. This approach was undertaken by different groups, as for example by Peterson and Sharma [140–144], Gustaffson and Edstrom [145] and several others [146]. Two of these designs are reported in Figure 2.2c-d. These have the advantage of simplicity, customizability and extremely good electrochemical properties, but still possess all the disadvantages of having a whole battery in the neutron beam. Very recently, another improved cell was designed (Figure 2.3a) by the group of Novak (PSI Switzerland) in such a way to combine most of the required aspects for *in situ* NPD [147]: adequate geometry for diffraction and reliable electrochemistry, able to match most of the expectations. But the design looks over-complicated with respect to what is necessary, and the use of aluminum or titanium metals as current collectors generates strong additional diffraction peaks. After we proposed our own *in situ* electrochemical cell in 2013 [148], discussed in detail in the following, other groups kept pushing cells development. Another complicated design was proposed by Vadlamani et al. [149] (Figure 2.3b), who used silicon (110) single-crystal sheets

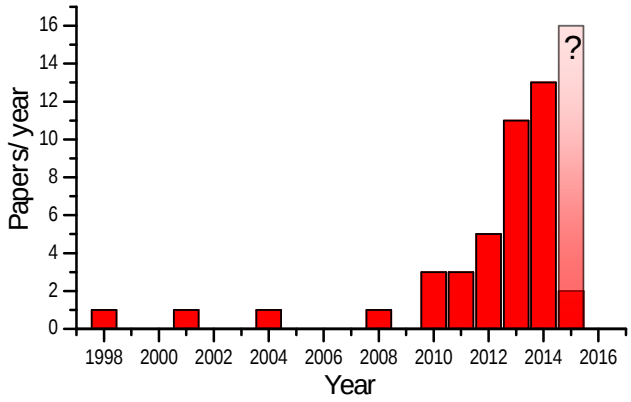

Figure 2.4: Evolution of the amount of publications per year concerning *in situ* neutron powder diffraction on electrode materials in peer-reviewed journals.

for the cell casing, giving a very weak background and very few diffraction peaks. Another idea is the use of modified pouch-cells[150,151] (Figure 2.3c), which can be quite effective as they are simple and allow to place a big amount of electrode material in the neutron beam (but again, the whole battery pack is diffracting and not just one electrode).

Table 2.2 gathers all *in situ* NPD experiments published at present in the literature, while Figure 2.4 represents the evolution of the publications per year on the subject. In spite of all efforts spent up to now and to the best of our knowledge, all the *in situ* NPD data reported until 2012 still suffered from poor reliability of the attempted Rietveld refinements, due to the presence of high background (caused by the electrolyte) and many additional diffraction peaks besides those of the studied electrode material, arising from the cell itself (current collectors, casing, graphite, ...). In such cases, we think that it is almost impossible to perform a good quality multi-phase pattern refinement. For this reason in early 2013 we made a few different design choices for our custom-made setup, which will be described in the next paragraph.

Table 2.2: Summary of all batteries used for in situ neutron powder diffraction studies of Li-ion batteries, adapted from [151].

Year	Reference	Material studied	Cell	Battery Type
1998	Bergstom et al. [123]	$Li_xMn_2O_4$	Half	Pyrex tube-like
2001	Berg et al. [125]	$LiMn_2O_4$	Half	Pyrex tube-like
2004	Rodriguez et al. [129]	$LiCoO_2$, graphite	Full	Commercial 18650-type
2008	Rosciano et al. [126]	$LiNiO_2$	Half	Polyetherketone large coin-type
2010	Colin et al. [127]	$Li_4Ti_5O_{12}$	Half	Polyetherketone large coin-type
2010	Rodriguez et al. [130]	$LiFePO_4$, graphite	Full	Commercial 18650-type
2010	Sharma et al. [131]	$LiCoO_2$, graphite	Full	Commercial 18650-type
2011	Du et al. [142]	$Li_4Ti_5O_{12}$, TiO_2	Half	Roll-over cylindrical vanadium
2011	Sharma, Du et al. [140]	MoS_2	Half	Roll-over cylindrical vanadium
2011	Sharma, Reddy et al. [141]	$LiCo_{0.16}Mn_{1.84}O_4$	Half	Roll-over cylindrical vanadium
2012	Dolotko et al. [135]	$LiCoO_2$, graphite	Full	Commercial 18650-type
2012	Senyshin et al. [133]	$LiCoO_2$, graphite	Full	Commercial 18650-type
2012	Sharma et al. [143]	$LiFePO_4$	Half	Roll-over cylindrical vanadium
2012	Sharma, Peterson [132]	$LiCoO_2$, $LiFePO_4$, $LiMn_2O_4$, graphite, $YFe(CN)_6$, $FeFe(CN)_6$	Half	Roll-over cylindrical vanadium
2012	Wang et al. [134]	graphite	Full	Commercial 18650-type
2013	**Bianchini et al.** [148]	$LiFePO_4$ and $Li_{1.1}Mn_{1.9}O_4$	Half	(Ti,Zr) alloy large cylindrical
2013	Cai, An et al. [136]	$LiMn_2O_4$, graphite	Full	Commercial pouch-type
2013	Godbole et al. [147]	$LiFePO_4$, $Li_4Ti_5O_{12}$, graphite $Li_{1.1}(Ni_{1/3}Co_{1/3}Mn_{1/3})_{0.9}O_2$	Half	Al or Ti alloy large coin cell
2013	Hu et al. [152]	V-doped $LiFePO_4$	Full	Commercial pouch-type
2013	Liu et al. [146]	$xLi_2MnO_3 \cdot (1\text{-}x)LiMO_2$ x=0, 0.5. M = Ni,Mn,Co	Full	Commercial pouch-type
2013	Roberts et al. [145]	$LiFePO_4$	Half	Roll-over cylindrical Swagelock-type
2013	Senyshin et al. [139]	Graphite	Full	Commercial 18650-type
2013	Sharma et Peterson [137,138]	Graphite	Full	Commercial 18650-type
2013	Sharma et al. [144]	$Li_{1+y}Mn_2O_4$	Full	Pouch-type
2014	Alam et al. [153,154]	$LiNi_{1/3}Co_{1/3}Mn_{1/3}O_2$ and Al-doped $LiNi_{1/2}Co_{1/2}O_2$	Full	Commercial 18650-type
2014	**Bianchini et al.** [155]	$Li_{1+x}Mn_{2-x}O_4$ (x = 0, 0.05, 0.10)	Half	(Ti,Zr) alloy large cylindrical
2013	Biendicho et al. [156]	Ni-MH (Li-ion possible)	-	Large coin type
2014	Bobrikov et al. [157]	$LiFePO_4$	Full	Commercial pouch-type
2014	Brant et al. [158]	$Li_{0.18}Sr_{0.66}Ti_{0.5}Nb_{0.5}O_3$	Half	Roll-over cylindrical Vanadium
2014	Dolotko et al. [159]	$LiNi_{1/3}Co_{1/3}Mn_{1/3}O_2$	Full	Commercial 18650-type
2014	Pang, Peterson et al. [150,160]	$Li_4Ti_5O_{12}$	Full	Pouch-type
2014	Pang, Sharma et al. [161]	$LiNi_{0.5}Mn_{1.5}O_4$ and $Li_4Ti_5O_{12}$	Full	Pouch-type
2014	Pang, Kalluri et al. [162]	$LiNi_{1/3}Fe_{1/3}Mn_{1/3}O_2$	Full	Pouch-type
2014	Senyshyn et al. [163]	$LiCoO_2$, graphite	Full	Commercial 18650-type
2014	Vadlamani et al. [149]	$LiCoO_2$, $LiMn_2O_4$, graphite	Full	Planar stacking-type with Si case
2014	Zinth et al. [164]	Graphite	Full	Commercial 18650-type
2015	Pang et al. [151]	review	Full	Pouch-type
2015	Senyshyn et al. [165]	graphite	Full	Commercial 18650-type

2.4 Design of a (Ti,Zr) electrochemical cell at the Institut Laue-Langevin

The design of our custom-made electrochemical cell for *in situ* and *operando* neutron powder diffraction experiments was made combining the experience developed by the scientific community (especially the battery one) during the first 15 years of *in situ* NPD with the knowledge of neutron scattering present at ILL. The cell that we had to develop had to respond to some specific requirements:

- being able to cycle electrochemically for tens of cycles and for loadings of electrode materials comprised between 10 mg and 300 mg,
- at the highest loadings, being able to cycle at rates up to C/5,
- being easy to use, wash and re-use for potential users in large scale facilities,
- provide good quality neutron powder diffraction patterns in 30 min or less with no contributions besides those of the electrode material under study.

Moreover:

- minimize the quantity of battery components probed by the beam,
- focus on one of the battery electrodes only, trying to maximize its contribution to the neutron diffraction pattern.

The idea behind such choices is not to probe the whole battery, which as discussed above, results in many Bragg peaks in the diffraction pattern, but to probe a single electrode instead. This significantly distinguishes our cell design from others present in the literature. The goal is to isolate the electrode from the rest of the electrochemical system, resulting in a maximum of Bragg reflections to succeed in reliable Rietveld structural analysis. The scheme and a picture of the battery designed at ILL (with the participation of Jean-Luc Laborier and Ludovic Gendrin (ILL) and Jean-Bernard Leriche (LRCS)) are reported in Figure 2.5. In the following we will address every battery component and discuss the choices we made.

2.4.1 Cell protective case and positive current collector

Every battery needs a protective case to keep it airtight i.e to isolate it from the external environment. This is problematic since cases are usually made of steel or aluminum,

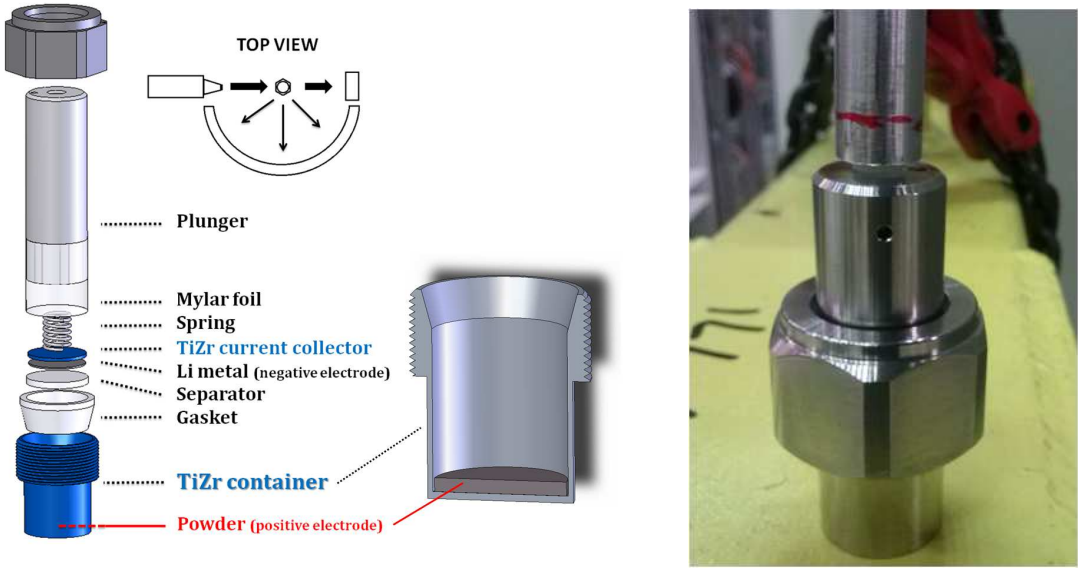

Figure 2.5: Scheme (left) and picture (right) of the electrochemical cell designed for *operando* NPD at ILL.

both generating intense Bragg reflections. To get rid of this problem the battery protective case, that in our design acts as the positive current collector as well, was fabricated using a (Ti,Zr) Null-Matrix alloy[166–170]. This special material, developed for the last 50 years at neutron scattering facilities and well-known at ILL, is neutron "transparent": its coherent contribution to the scattering of neutrons is very weak and in general negligible (on the other hand, incoherent scattering from this material is still present, resulting in a featureless diffused background). Titanium and Zirconium have scattering lengths opposite in sign and in a ≈1:2 ratio (b_{Ti} = -3.37 fm and b_{Zr} = 7.16 fm) and their alloy, prepared with the corresponding necessary stoichiometric amounts of the two elements, has zero overall scattering intensity, thus being a perfect container material for NPD experiments. Calculating the required Ti/Zr ratio is rather trivial, knowing that titanium and zirconium in their pure metallic forms have the same crystal structure, belonging to the hexagonal space group $P6_3/mmc$, and that their alloy does not differ from this. Thus Ti and Zr are both placed in a 2c Wyckoff site of fractional atomic coordinates $x/a = 1/3$, $y/b = 2/3$, $z/c = 1/4$, with a random site occupancy factor respecting the constraint of a full site $O_{Ti} + O_{Zr} = 1$.

Starting from a simple expression for the structure factor for the diffraction of neutrons:

$$F = \sum_{j=1}^{n} O_j b_j exp^{-i2\pi(hx+ky+lz)} = \sum_{Ti,Zn} O_j b_j exp^{-i2\pi(hx+ky+lz)} = \\ (-3.37O_{Ti} + 7.16O_{Zr}) exp^{-i2\pi(hx+ky+lz)} \tag{2.1}$$

Which leads to zero structure factors (for any set of h,k,l, thus for any Bragg reflection) when:

$$-3.37O_{Ti} + 7.16O_{Zr} = 0 \Rightarrow \begin{cases} O_{Ti}/O_{Zr} = 2.1 \\ O_{Ti} + O_{Zr} = 1 \end{cases} \tag{2.2}$$

This results in a formula unit for the null scattering alloy of $Ti_{0.68}Zr_{0.32}$ ($\approx Ti_{2.1}Zr$). As Titanium and Zirconium have atomic weight of 47.867 g/mol and 91.224 g/mol, respectively, the alloy with null coherent scattering length contains 52.2 wt% Ti and 47.8 wt% Zr. These results were already proved in 1956 by Sidhu et al.[169], who measured NPD patterns from metallic Ti, Zr and from an alloy close to the Null-Matrix composition ($Ti_{0.6}Zr_{0.4}$). Their results are shown in Figure 2.6. The fact of being neutron-transparent is not the only requirement needed for a good material acting as current collector and protective case. Such a material must also be a good current conductor, mechanically resistant and should not be easily oxidized, making the cell resistant mechanically and chemically. The Null-matrix (Ti,Zr) alloy used at ILL respond to all these requirements, making it the

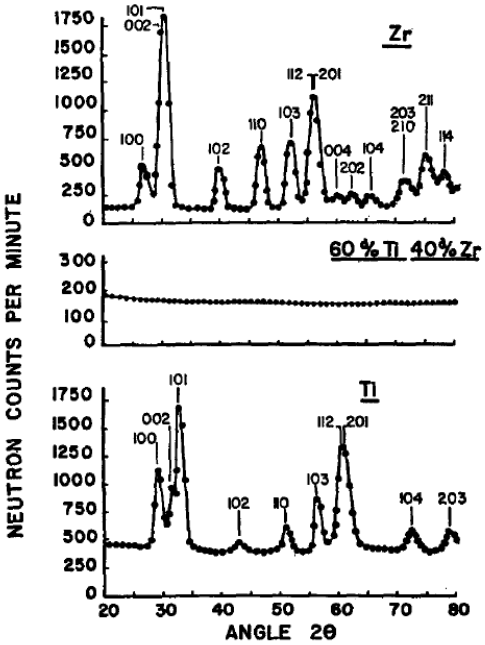

Figure 2.6: Neutron powder diffraction patterns of Zr, $Ti_{0.6}Zr_{0.4}$, and Ti. Neutron wavelength is $\lambda = 1.26$ Å. Reprinted from[169].

material of choice for our cell [170]. The volume of the cylindrical container we designed is approximately 9 cm^3 ($h \cdot \pi \cdot R^2 \approx 3 \cdot \pi \cdot 1^2$). When placed in this container, 200 mg of the powder electrode to be investigated occupy $\approx$ 1 mm in height, to be exposed to the neutron beam.

2.4.2 The Positive Electrode

The positive electrode is usually the battery component under study. It is mainly composed by an electrochemically active material (AM), often having poor electronic conductivity, and by an amorphous carbon, to improve it. In this thesis the positive electrode has always been prepared with commercial Carbon Super P (Csp, unless specified otherwise), intimately mixed with the AM using a mortar. Their relative ratio depends on the specific conductivity of the material, but in general it ranges between 90% AM - 10% Csp (in weight, noted as 90:10 wt%) for good conductors to 80:20 wt% for poorer electronic conductors. The amount used will be specified for every experiment. The contribution of Csp to a NPD experiment can be described as an augmented background that can be observed in Figure 2.7. In this case, $LiFePO_4$ is compared to a mixture of $LiFePO_4$ and Csp in weight ratio 85:15. Csp is amorphous and it does not present any Bragg peak (contrary to graphite for example). However its interaction with neutrons is mainly coherent (σ_{coh} = 5.551(2) barns vs. σ_{inc} = 0.001(4) barns) [121] implying that the scattered intensity does not give a completely flat background, but it rather results in a slowly undulated background, typical of amorphous structures. The maxima of such undulations can be

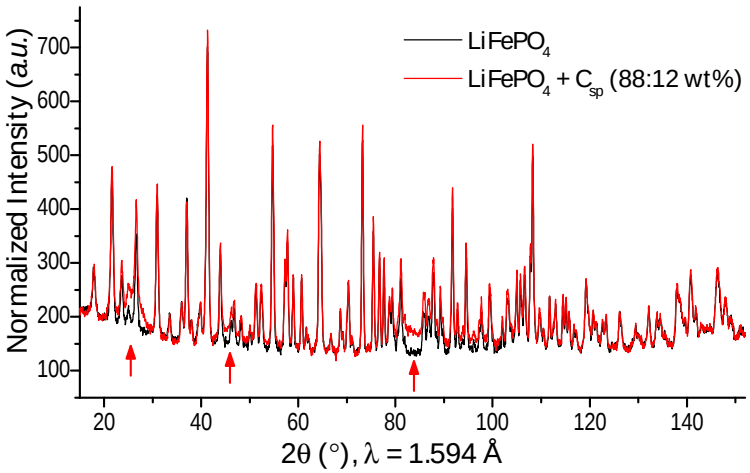

Figure 2.7: Comparison between pure $LiFePO_4$ powder and a mixture of $LiFePO_4$ + Csp, as measured on the D2B diffractometer at ILL.

seen around 25° and 80° at $\lambda = 1.594$ Å (1.76 and 5.28 $Å^{-1}$). The background increase is in general not significant, except for the regions of the maxima. Since this undulating contribution is not straightforward to take into account, the amount of carbon present in the electrode is minimized whenever possible. It is also true, however, that its contribution to the background is poor when compared to other parasitic contributions, particularly the electrolyte's one discussed in the following. For this reason carbon's signal during data analysis is just carefully included in the background, not affecting Bragg peaks' intensities of the material of interest.

After the first studies made with the electrode formulation discussed above, we realized that, due to the big amount of powder used in the electrode, the obtained capacity was good but not optimal (see the studies on spinel materials in the next chapter). A part of the electrode, probably on the sides, did not fully react. Therefore, in the following studies, we adopted an improved formulation for the electrode by adding a binder. This is a polymeric material that, when added to the active material plus carbon mixture, gives as a result a paste (instead of a simple powder). The binder is electrochemically inert, while ensuring a better mechanical strength of the electrode and, more importantly, a better homogeneity. In our case the choice of the binder was relatively easy, since among those used in the battery community only one was completely hydrogen-free, this being a strong advantage in neutron diffraction (see the next paragraph for a discussion on hydrogen's contribution to neutron diffraction). We hence chose polytetrafluoroethylene C_2F_4 (PTFE, or Teflon®) for our electrode formulation. It was mixed in a mortar with active material and Csp, in a variable amount around 6-10% in weight, which will be specified in the following when needed.

2.4.3 Electrolyte and Separator

In a Li-ion battery the separator is a porous medium used to keep the positive and negative electrodes physically separated (avoiding short-circuits) while insuring ionic conductivity between them, thanks to the electrolyte that wets the whole system. This means that there is no way to avoid that the bottom part of the separator and of the electrolyte are exposed to the neutron beam. A wise choice of both components is thus required to minimize their (hydrogen-rich) contribution to the diffracted pattern. Hydrogen is in fact a very strong incoherent scatterer ($\sigma_{coh} = 1.75$ barns vs. $\sigma_{inc} = 80.27$ barns)[121], meaning that in a diffraction experiment it barely affects Bragg peaks, while creating a very intense

background, featureless in the whole angular range, hence reducing the available signal to noise ratio. For the separator material, the most common choices are glass-fiber, PVDF (polyvinylidene difluoride, $[C_2H_2F_2]_n$) or Celgard (polypropylene, $[C_3H_6]_n$). The last one is a polymer made of extremely hydrogen-rich repeating units (H and CH_3) thus clearly being a poor choice for neutron diffraction. PVDF is less hydrogen-rich, but it still contains repeating units of H and F. So our choice was to use glass-fiber separators. They are glass-based (amorphous SiO_2), extremely porous materials. They contain no hydrogen, but on the other hand boron is present in the form of B_2O_3. Naturally-occurring boron ($^{10.8}$B) is a strong neutron absorber because its isotope ^{10}B has a high neutron absorption cross-section (3835 barns, resulting in 767 barns for natural boron)[121]. This could represent a significant problem because of the consequent signal attenuation. However, the amount of boron in glass-fiber separators is just around 3%, thus inducing only a small reduction of the neutrons diffracted. We could readily observe that in fact such material's contribution to the NPD pattern is poor and therefore we retained it as best choice for our studies. Recently, Pang and Peterson[151] measured Celgard, PVDF and glass-fiber separators in a NPD experiment, showing indeed that glass-fiber is the best choice.

Regarding the non-aqueous electrolyte, this is an extremely hydrogen-rich system. It is based on a lithium salt ($LiPF_6$) in a solution of organic solvents (commercial electrolytes mostly use mixtures in different proportion of dimethyl carbonate $(CH_3O)_2CO$, ethylene carbonate $(CH_2O)_2CO$ and propylene carbonate $CH_3C_2H_3O_2CO$). The mixture is chosen to optimize the solution's properties as ionic conductivity, density, viscosity, etc. In the development of *in situ* NPD experiments, it became clear from the very beginning that such organic solvents generated a strong background, coming from the high incoherent cross-section of hydrogen, completely submerging the Bragg peaks of the electrode material of interest. The adopted solution has been the use of a deuterated version of the organic solvents in the electrolyte. Deuterium has an incoherent scattering cross section of 2.05(3) barns, significantly reduced with respect to hydrogen's one of 80.27(6) barns[121]. This solves the electrolyte problem, while significantly increasing the cost of any *in situ* NPD experiment because of the high cost for purchasing deuterated solvents (for example, 20 mL of d-dimethyl carbonate cost about 900 euros, while the normal version costs 43 euros for 100 mL; 5 g of d-ethylene carbonate cost about 1950 euros, while 100 g of the normal version cost 32 euros). One recent attempt of performing *in situ* NPD experiments using standard hydrogenated solvents was carried out by Godbole et al.[147]. Their results clearly

show that the qualitative evolution of Bragg peaks position and intensity can be followed, provided that an extremely high neutron flux is available, but they also show that data quality is not sufficient for any quantitative analysis. Considering that our main goal was to succeed in Rietveld refinement of data collected *operando*, the use of hydrogenated solvents was not satisfactory and we decided to utilize deuterated solvents. The selected electrolyte composition used throughout all *in situ* NPD experiments in this thesis is 1M $LiPF_6$ (Sigma Aldrich) in EC:DMC (1:4 wt%, both from Armar Chemicals). The reason of such proportion choice is both historical (other groups chose this composition in the past, showing that it could properly work [145]) and practical, the price of EC being about four times the one of DMC. Very recently a work by Petibon et al. [171] showed a new possible electrolyte formulation, based on deuterated ethyl acetate, able to give comparable performances at a much lower price.

2.4.4 Other battery components

After the sandwich of positive electrode plus electrolyte-wetted separator, the battery stack is completed by the negative electrode: a lithium foil (Sigma Aldrich) which is put below a negative current collector (this is a 1 mm-thick disk made in $Ti_{2.1}Zr$ to insure that it would not interact with the neutron beam). A spring generates pressure on the whole stack, a plunger closes the cell with a plastic gasket and a screw completes the cell (see again Figure 2.5). It is important to note that a mylar film covers the internal part of the *in situ* cell and together with the gasket assures the electrical insulation between the positive and the negative electrodes and makes the cell air-tight. Once closed, the cell can be mounted (vertically) in the diffractometer as illustrated in Figure 2.8 thanks to a plastic screw entering the top of the plunger, and aligned with slits so that the beam irradiates only the bottom part of the cell where the electrode powder is located.

2.4.5 Mounting of the cell on the D20 diffractometer

The geometry of an *in situ*/*operando* experiment is shown in Figure 2.8. It can be observed that the electrochemical cell is mounted in the center of the diffractometer by means of a plastic screw, which electrically isolates it from the rest of the environment. Cables reach the cell from the top and are connected to a potentiostat (Biologic SP-200) for electrochemical charge and discharge of the battery. The neutron beam size is appositely reduced by means of cadmium masks put on the instrument's final collimating guide (called

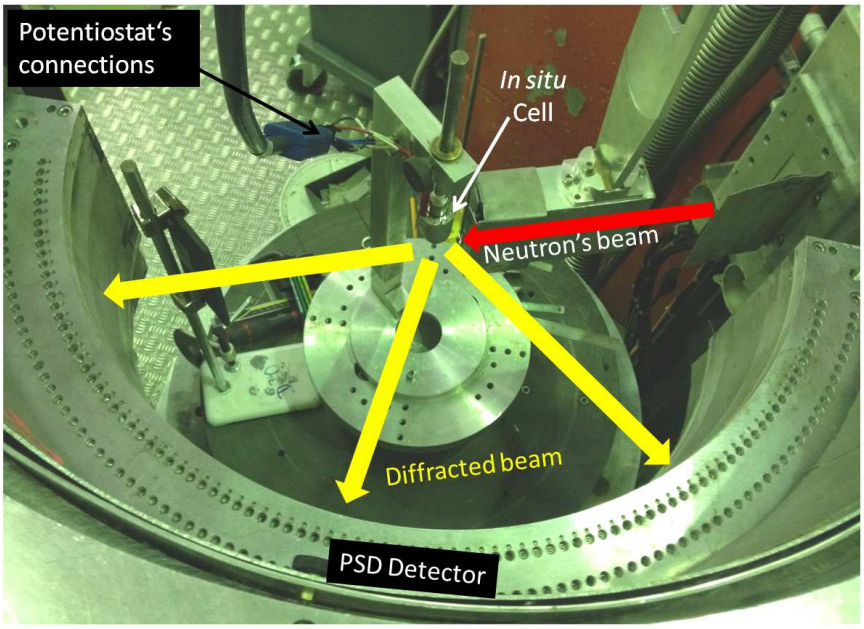

Figure 2.8: Setup of an *operando* NPD experiment with our electrochemical (Ti,Zr) cell on the D20 diffractometer at ILL.

"nose"), that can be placed very close to the cell. The chosen masks have a small dimension of about 10x4 mm^2 to minimize the battery parts in the beam; this setup ensures that the neutron beam illuminates only the bottom part of the (Ti,Zr) cell, where the positive electrode is placed. Neutrons are then scattered and the diffracted cones reach the ^{3}He position sensitive detector (PSD). A second set on cadmium masks are modeled to surround the top part of the cell, to ensure no parasitic diffraction signal reaches the detector. However, due to the dimension of our cell and to our experimental geometry during *in situ* experiments, only 120° out of 156° were fully exploited.

2.5 Cell Validation and testing

The performances of our electrochemical cell were tested with commercially available positive electrode materials. In particular, we report here the data we acquired on an olivine-type phase, $LiFePO_4$ [28]. 18 years after its discovery, this material has now reached industrial exploitation and, although its basic crystal structure is well-known [172,173], it keeps attracting much attention due to the versatility of its electrochemical properties depending for instance on temperature, particle size, carbon coating, etc. [33,34,102,174,175], some of which were already discussed in the introduction. It is worth mentioning that we also tested the cell with a commercial over-stoichiometric spinel-type phase $Li_{1.10}Mn_{1.90}O_4$ [23],

but the results are not shown here since spinel compositions are treated in more detailed studies in the next chapter.

The validation of our cell followed three main steps: first, we conducted electrochemical galvanostatic cycling using different electrolytes and at different rates. Second, we measured $LiFePO_4$ as pure powder in a standard NPD experiment, subsequently comparing the obtained patterns to those recorded in a "full-battery configuration", i.e. with the active material mixed with Csp, mounted in the *in situ* cell with all battery components (electrolyte, lithium, etc.). We then compared the accuracy of the parameters we could obtain from Rietveld refinement in the two cases. Finally, we validated the possibility to conduct a real *operando* experiment measuring NPD patterns upon charge of $LiFePO_4$ and obtaining reliable structural information from Rietveld analysis of the data.

2.5.1 Electrochemical testing

Batteries were assembled in the *in situ* cell described above. The chosen active material was mixed with an appropriate amount of Carbon Super P (12 wt% for $LiFePO_4$) and the electrode mixture was ground in a mortar. No binder was used in these first tests. Batteries were assembled with glass fiber separators and either the commercial LP30 electrolyte (SelectiLyte^{TM}, Merck company, 1M $LiPF_6$ in EC:DMC (1:1) (wt%)) or a home-made deuterated electrolyte (1M $LiPF_6$ (Sigma Aldrich) in d-Ethylene Carbonate : d-Dimethyl Carbonate 1:4 wt% (Armar Chemicals)). Lithium metal was used as anode.

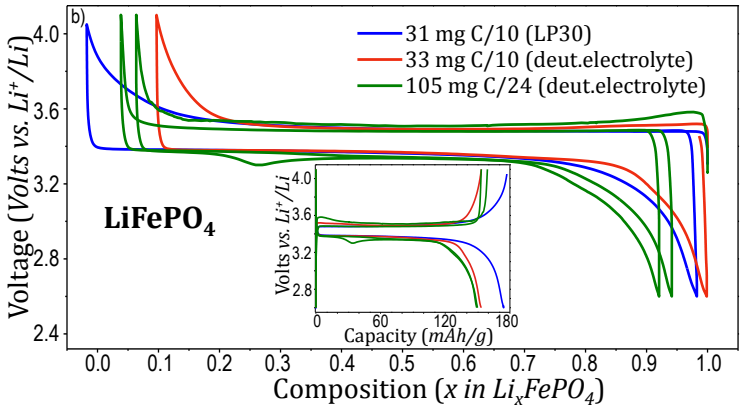

Figure 2.9: Electrochemical galvanostatic data obtained within the *in situ* electrochemical cell with the positive electrode material $LiFePO_4$. Different tests were performed depending on the active mass, the cycling rate and the electrolyte used (LP30 or a deuterated one).

Figure 2.9 illustrates the electrochemical data obtained within the *in situ* electrochemical cell for i) 31 mg of $LiFePO_4$ cycled at C/10, ii) 33 mg at C/10 and iii) 105 mg at C/24.

Only the first cycles are depicted here but subsequent prolonged cycling with good coulombic efficiency was achieved under these conditions. The observed polarization of the cell is quite satisfactory as it does not increase significantly when the mass of the electrode exceeds 100 mg. The voltage plateau observed around 3.45 V vs. Li^+/Li reveals as expected a classical two-phase electrochemical reaction between $Li_{1-\delta}FePO_4$ and $Li_\epsilon FePO_4$ [176]. These data show, additionally, that the deuterated electrolyte we used possessed similar properties than a standard EC:DMC-based one (LP30) at cycling rates as high as C/10. Although it presents slightly lower kinetics, this does not represent a problem for *operando* NPD because of the counting times which are rather long ($\geq$ 10 min/scan). Additionally, only small capacity loss was observed (at slower regime) for higher electrode loadings ($\approx$ 105 mg). The electrochemical cell designed to obtain *in situ* or *operando* neutron diffraction data was thus shown to deliver electrochemical performances comparable to those obtained in classical electrochemical cells, with an active mass that can be rather large and a cycling rate that can be rather fast.

2.5.2 Quality of data and Rietveld refinements obtained for pristine materials within the electrochemical *in situ* TiZr cell

The next challenge was to prove that Rietveld refinement of neutron diffraction data obtained for powders placed within the electrochemical cell and in full-battery configuration was possible and could lead to structural determinations similar to those performed from high-resolution neutron diffraction data obtained on powder alone. Neutron diffraction patterns were collected under various configurations and an illustrative example is reported in Figure 2.10.

- The NPD pattern displayed in the top part of Figure 2.10 was recorded within 4 hours on the high-resolution diffractometer D2B (λ = 1.594 Å) of ILL for pure pristine $LiFePO_4$ powder ($\geq$ 1 g) placed in a vanadium cylindrical container.

- The neutron diffraction pattern displayed in the bottom part of Figure 2.10 was recorded on the high-flux diffractometer D20 (λ = 1.547 Å) of ILL for $\approx$ 200 mg of $LiFePO_4$ (one hour scan) electrode placed within the *in situ* cell together with the deuterated electrolyte, the separator, the negative electrode, the current collector, i.e. in full-operational battery configuration. It should be observed that the raw data were recorded as 10 minutes scans. In Figure 2.10 and in the following, we chose to sum them 6 by 6 so as to obtain better statistics (Table 2.3). However, a 3 by

3 sum was also a possible choice (leading to a diffraction pattern measured in 30 minutes), since reliable refinements could be obtained on 30 minutes scans as well. A comparison between refined parameters for 30 min and 1 hour patterns is reported in Table 2.4.

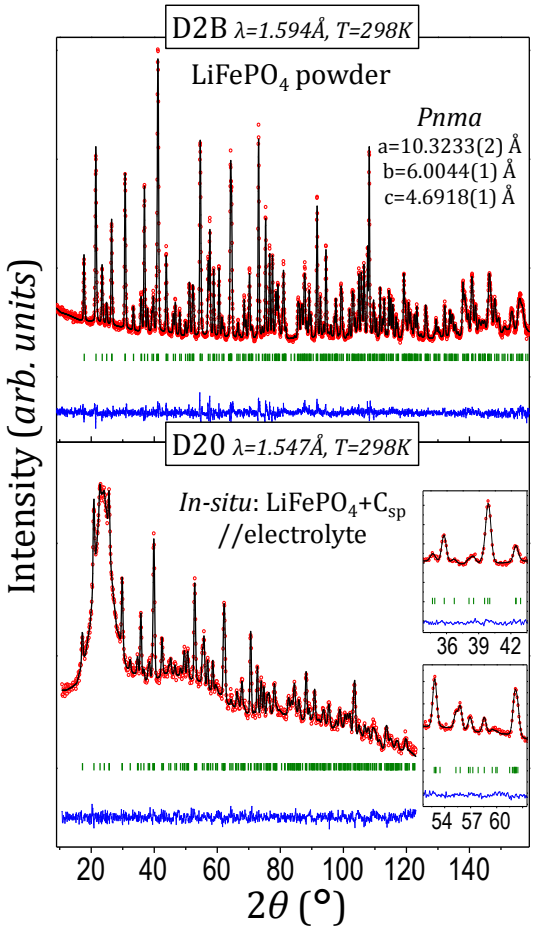

Figure 2.10: Observed (red dots), calculated (black line) and difference (blue line) plots obtained for the Rietveld refinement of neutron powder diffraction data recorded: (top) on the diffractometer D2B for the pure $LiFePO_4$ powder and (bottom) on the diffractometer D20 for the electrode within the *in situ* lithium cell, in a complete battery configuration.

All the diffraction patterns were refined by the Rietveld method [87], i.e. with the determination of cell parameters, atomic positions, occupancy factors and Debye-Waller factors, thanks to the FullProf suite [177]. The similar wavelengths are helpful for a straight comparison of peaks intensities of the collected NPD patterns since they are approximately at the same angular position. The *in situ* pattern shows a large bump in the low-angle region (15-30°) due to the scattering from the deuterated electrolyte (and not from the glass fiber separator) that was taken into account by a point by point background definition. As pre-

Table 2.3: Structural parameters obtained after Rietveld refinement of Neutron diffraction data from phase pure $LiFePO_4$ recorded in the *in situ* lithium cell on the diffractometer D20. For comparison purposes, those obtained for the same powder recorded as pure on the diffractometer D2B are reported in bold. The same parameters were refined in the two cases, except for B_{iso} that was not refined at the same time of Li SOF for the *in situ* cell because of the small angular domain (less than 120°).

$LiFePO_4$

S.G. Pnma; Z=4

a = 10.320(1) Å; b = 6.004(1) Å; c = 4.6907(7) Å;	D20: R_{wp} = 16.7%;
V = 290.68(7) Å^3; V/Z = 72.67 Å^3.	R_B = 6.51%; χ^2 = 1.60
a = 10.3233(2) Å; b = 6.0044(1) Å; c = 4.6918(1) Å;	**D2B: R_{wp} = 11.0%;**
V = 290.83(1) Å^3; V/Z = 72.71 Å^3.	**R_B = 3.98%; χ^2 = 2.54**

Atomic Parameters

Atoms	Wyckoff	Atomic Positions x/a	y/b	z/c	SOF	B_{iso}
Li	4a	0	0	0	1	1.6(4)
Fe	4c	0.282(1) **0.2816(4)**	0.25	0.974(4) **0.9749(8)**	1	0.63 **0.63(5)**
P	4c	0.094(2) **0.0952(6)**	0.25	0.414(4) **0.418(1)**	1	0.43 **0.43(9)**
O(1)	4c	0.097(2) **0.0966(7)**	0.25	0.748(5) **0.743(1)**	1	0.8 **0.8(1)**
O(2)	4c	0.457(2) **0.4566(6)**	0.25	0.204(5) **0.206(1)**	1	0.7 **0.7(1)**
O(3)	8d	0.167(2) **0.1655(4)**	0.045(2) **0.0469(6)**	0.285(3) **0.2836(8)**	1	0.66 **0.66(6)**

viously discussed, we note that neutrons allow obtaining high-intensity diffraction peaks at high angles ($\geq 100°$ in 2θ at $\lambda \approx 1.5$ Å). As shown by the results given in Figure 2.10 (good minimization of the difference between the observed and calculated data) and by the good reliability factors given in Table 2.3 and Table 2.4, single phase data refinements of positive electrode materials can be achieved within a lithium based electrochemical cell. The obtained structural parameters are listed in these tables and match very well with those obtained from high-resolution data.

As already mentioned in the introductory chapter, $LiFePO_4$ belongs to the olivine-type structural family, described in an orthorhombic unit cell (space group Pnma, Figure 2.11) with a = 10.3233(2) Å, b = 6.0044(1) Å and c = 4.6918(1) Å. The structure is built on layers of corner-sharing distorted FeO_6 octahedra linked through PO_4 tetrahedra and with

Table 2.4: Structural parameters obtained after Rietveld refinement of Neutron diffraction data from phase pure $LiFePO_4$ recorded in the *in situ* lithium cell on the diffractometer D20 for one hour and, for comparison purposes, for 30 minutes (bold). The same parameters were refined in the two cases.

$LiFePO_4$

S.G. Pnma; Z=4

a = 10.320(1) Å; b = 6.004(1) Å; c = 4.6907(7) Å;	1h: R_{wp} = 16.7%;
V = 290.68(7) Å^3; V/Z = 72.67 Å^3.	R_B = 6.51%; χ^2 = 1.60
a = 10.320(2) Å; b = 6.004(1) Å; c = 4.6900(7) Å;	**30min: R_{wp} = 21.6%;**
V = 290.61(8) Å^3; V/Z = 72.65 Å^3.	**R_B = 7.15%; χ^2 = 1.39**

Atomic Parameters

Atoms	Wyckoff	Atomic Positions x/a	y/b	z/c	SOF	B_{iso}
Li	4a	0	0	0	1	1.6(4)
Fe	4c	0.282(1) **0.282(2**	0.25	0.974(4) **0.973(5)**	1	0.63
P	4c	0.094(2) **0.094(3)**	0.25	0.414(4) **0.412(6)**	1	0.43
O(1)	4c	0.097(2) **0.098(3)**	0.25	0.748(5) **0.749(7)**	1	0.8
O(2)	4c	0.457(2) **0.457(3)**	0.25	0.204(5) **0.206(7)**	1	0.7
O(3)	8d	0.167(2) **0.168(2)**	0.045(2) **0.045(3)**	0.285(3) **0.287(4)**	1	0.66

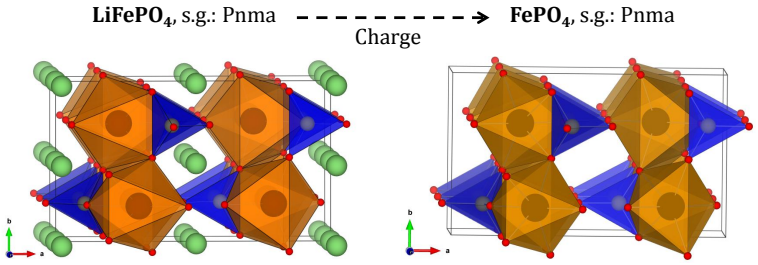

Figure 2.11: Crystal structure of the olivine compound $LiFePO_4$ and of its delithiated form $FePO_4$. PO_4 tetrahedra are shown in blue, FeO_6 octahedra in brown and Li^+ as green spheres.

tunnels along the b and c axes where Li^+ ions occupy octahedral oxygen environments. As shown in Table 2.3, Table 2.4 (and later in Table 2.5), the structural parameters determined for $LiFePO_4$ considering the neutron diffraction data recorded within the *in situ* electrochemical cell on the diffractometer D20 are in very good agreement with those obtained for the pure powder on the high resolution diffractometer D2B: the cell parameters, atomic

positions, distances and distortions of the FeO_6, PO_4 and LiO_6 polyhedra are indeed very similar for the two sets of data. We have thus proved that neutron diffraction data obtained in the electrochemical cell designed for *in situ* experiments are of sufficient quality to determine structures and thus to get more insight into structural changes occurring upon cycling.

2.5.3 *Operando* neutron diffraction upon charge of $LiFePO_4$

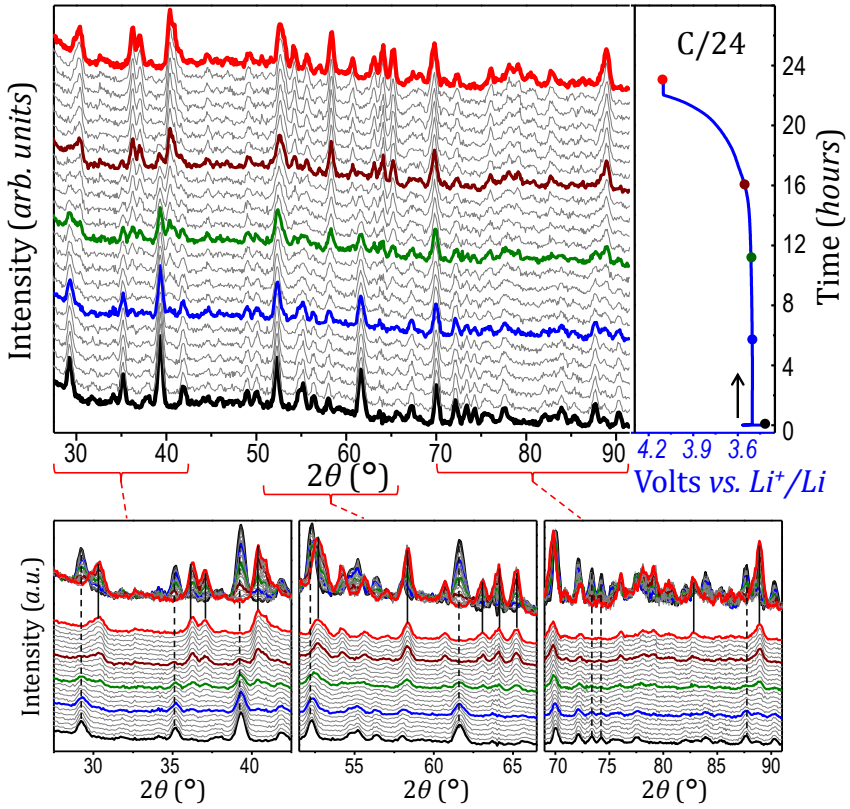

Figure 2.12: 2D View of collected *in situ* NPD patterns for the global electrochemical reaction $LiFePO_4 \Leftrightarrow FePO_4$ (left) and corresponding galvanostatic cycling data (right). Three different angular ranges are given to highlight the changes in the NPD patterns. The NPD patterns given in color refer to global compositions for Li_xFePO_4, with x close to 1 (black), 0.75 (blue), 0.5 (green), 0.25 (brown) and 0 (red).

For this first *operando* experiment, a lithium battery within our (Ti,Zr) cell was prepared using $LiFePO_4$ as follows: 200 mg of $LiFePO_4$ + Csp (88:12 wt%) // deuterated electrolyte (1M $LiPF_6$ in d-EC : d-DEC 1:4 wt%) // lithium metal. The cell was cycled at C/24 rate and then kept for 1 hour at the maximum potential of 4.1 V vs. Li^+/Li; neutron diffraction patterns were recorded every 10 minutes during the charge and the

floating. Figure 2.12 and Figure 2.13 show the *operando* NPD data, i.e. 1 hour patterns corresponding to the sum of 6 successive 10 minutes patterns, and the corresponding galvanostatic curve upon charge. Each 1 hour pattern corresponds to $\Delta x = 1/24 = 0.042$. The electrochemical process can be clearly observed to be a two-phase reaction from the very beginning, with the disappearance of the initial $LiFePO_4$ phase whereas the end member phase $FePO_4$ is forming continuously, in agreement with the obtained electrochemical data, absolutely flat. The initial pattern (black) corresponds to that of Figure 2.10 (bottom), i.e. a 1 hour scan on the pristine material before cycling. The other end member (red) corresponds to $FePO_4$, which appears as a single phase from neutron diffraction despite a global composition for the positive electrode of $\approx Li_{0.08}FePO_4$ at the end of the charge. Its

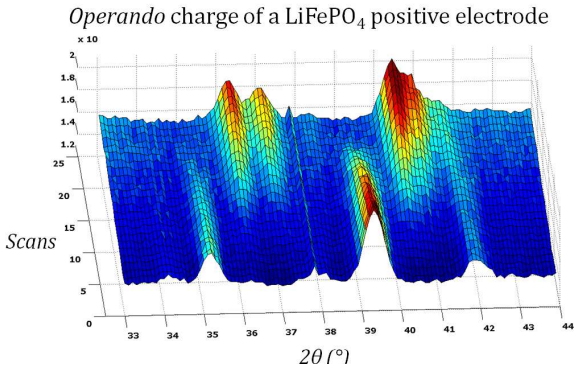

Figure 2.13: Tridimensional visualization of the charge of a $LiFePO_4$ electrode. The biphasic reaction between the two end members can be clearly observed.

neutron diffraction pattern was recorded during 1 hour at a constant potential of 4.1 V vs. Li^+/Li. Between these two end member patterns, the patterns highlighted correspond to global compositions close to 3/4 $LiFePO_4$: 1/4 $FePO_4$ (blue), 1/2 $LiFePO_4$: 1/2 $FePO_4$ (green) and 1/4 $LiFePO_4$: 3/4 $FePO_4$(brown). Rietveld refinements were performed for all the (1-x)·$LiFePO_4$ + x·$FePO_4$ compositions with high quality fittings, as illustrated in Figure 2.14 for these 3 selected compositions and for the two end members $LiFePO_4$ and $FePO_4$. Importantly, note that we closely checked, for the first series of diffraction patterns recorded every 10 min during charge, that the unit cell parameters of $LiFePO_4$ remained absolutely constant and for the last diffraction patterns that the unit-cell parameters of $FePO_4$ remained constant as well. Therefore, the overall reaction may really be regarded as a two phase reaction between $LiFePO_4$ and $FePO_4$, contrary to what observed by Yamada et al.[34] for nano-sized $LiFePO_4$.

For each of the two end members, 15 parameters have been refined: the scale factor, 3

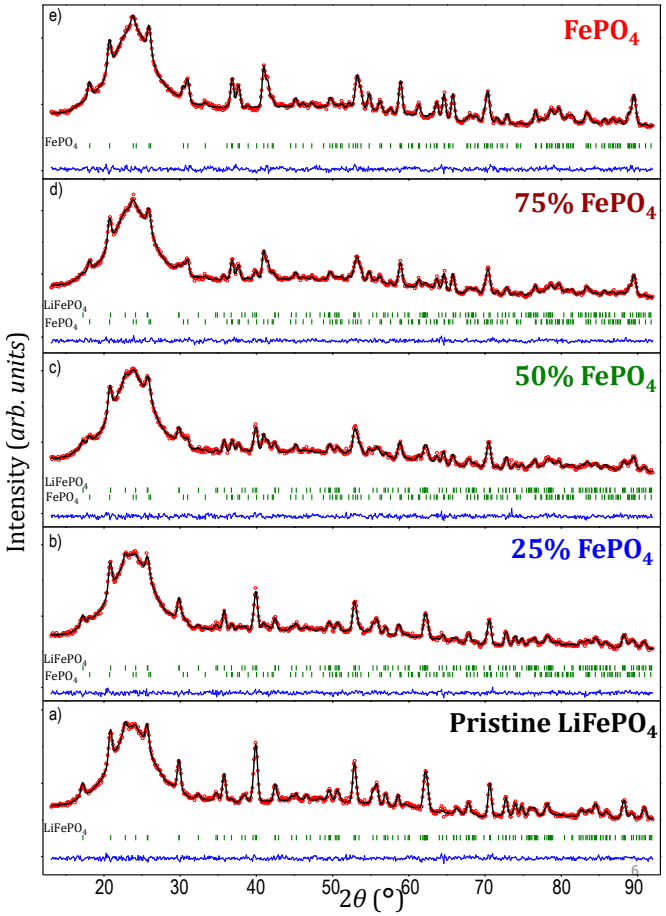

Figure 2.14: Observed (red dots), calculated (black line) and difference (blue line) plots obtained for the Rietveld refinement of neutron powder diffraction data recorded within the *in situ* lithium cell during Li^+ extraction from $LiFePO_4$. Five compositions are given as examples: (a) pristine $LiFePO_4$, (b) 3/4 $LiFePO_4$: 1/4 $FePO_4$, (c) 1/2 $LiFePO_4$: 1/2 $FePO_4$, (d) 1/4 $LiFePO_4$: 3/4 $FePO_4$ and (e) $FePO_4$.

cell parameters and 11 fractional atomic coordinates. Zero shift and wavelength had been previously refined thanks to an internal standard and have been fixed afterwards. Isotropic thermal displacement parameters were instead kept fixed to the values obtained for the pattern measured on D2B for $LiFePO_4$. Besides, the absorption coefficient μR had to be considered due to the presence of lithium. It had thus its maximum value for $LiFePO_4$ (about 0.43) and it was negligible for $FePO_4$. In the case of the three intermediate two-phase compositions, the refined parameters were still 15 for each phase, making a total of 30 for each pattern. The coefficient μR was then reduced according to the weight percent of $LiFePO_4$ remaining in the structure. The main structural results coming from this analysis are reported in Table 2.5, where the good quality of the refinement can be seen from R_{Bragg} parameters, never exceeding 10.6%, and bond length distances in agreement for a

given phase between the different compositions. Refined values are slightly inaccurate only when the crystalline weight of the considered phase is around 25% or less. Moreover, bond length distances for $LiFePO_4$ and $FePO_4$ can be compared to those reported in literature [83] showing a good agreement.

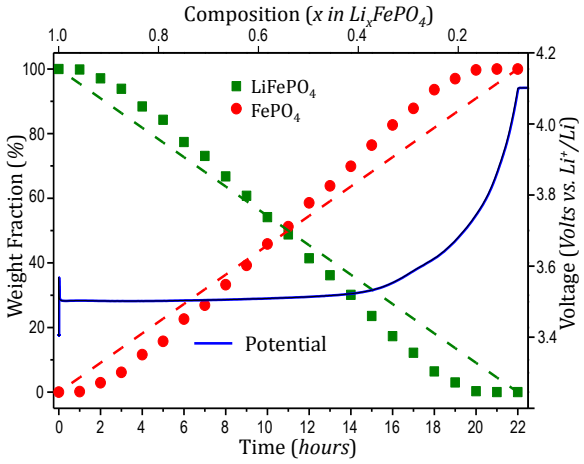

Figure 2.15: Weight fractions for $LiFePO_4$ and $FePO_4$, within the crystalline part of each composition, determined from NPD data recorded *operando* during Li^+ deintercalation from $LiFePO_4$.

A sequential refinement of the *operando* diffraction patterns was also performed, involving all the recorded patterns. In this case the structural parameters were fixed and only scale factors were permitted to vary. This allowed determining weight fractions for $LiFePO_4$ and $FePO_4$, within the crystalline part of all the compositions studied. Indeed, as shown by the results given in Figure 2.15, $FePO_4$ is not detected at the very beginning of the charge, as happens to $LiFePO_4$ at the end of the charge. Note that it does not mean that these minority phases are effectively not present, but their crystalline domains could be small and not extended enough to diffract efficiently. Then, the distribution between $LiFePO_4$ and $FePO_4$ does not follow exactly the theoretical line, although a linear variation is expected for a two-phase reaction. This is well explained by: i) a quantification that is in fact only semi-quantitative due to the absence of an internal standard with a known fraction (versus $LiFePO_4$) in our positive electrode and thus to the impossibility to take into account the possible presence of non-crystalline phases [178] and ii) the strong absorption of Li which is present in one phase, $LiFePO_4$, and not in the other one, $FePO_4$, affecting thus also slightly the ratio between the two weight fractions. Such a deviation from the theoretical behavior had also been observed before by Andersson and Thomas [173]. Despite of that, the change in the weight fractions between $LiFePO_4$ and $FePO_4$ is still close to a linear behavior, as additional proof of the quality of the analysis of these *in situ* NPD data.

Table 2.5: Selected bond lengths (Å) in the structures of $LiFePO_4$ and $FePO_4$ at different key compositions of the phase diagram $xLiFePO_4 \cdot (1\text{-}x)FePO_4$ obtained from NPD data recorded operando in the in situ electrochemical cell on the diffractometer D20. Expected and refined fractions of each phase are reported in red. Polyhedral distortion is calculated as $\Delta = 1/N \sum_i (d_i - \langle d \rangle / \langle d \rangle)^2$.

100 % $LiFePO_4$			**0 % $FePO_4$**		
a = 10.320(1) Å; b = 6.004(1) Å; c = 4.6907(7) Å;			-		
V = 290.68(7) Å^3; R_B = 6.51%			-		
Interatomic distances (Å) / Distortion			Interatomic distances (Å) / Distortion		
Fe-O1=2.19(3)	P-O1 = 1.57(3)	Li-O1(x2) = 2.16(2)			
Fe-O2 = 2.10(3)	P-O2= 1.52(3)	Li-O2(x2) = 2.09(2)			
Fe-O3(x2) = 2.05(2)	P-O3(x2) = 1.56(2)	Li-O3(x2) = 2.20(2)	-	-	-
Fe-O3(x2) = 2.25(2)	-	-			
Δ = 16.1E-04	Δ = 1.3E-04	Δ = 4.2E-04			

75 % $LiFePO_4$ (79(3)%)			**25 % $FePO_4$ (21(2)%)**		
a = 10.316(1) Å; b = 6.003(1) Å; c = 4.6922(7) Å;			a = 9.823(6) Å; b = 5.796(3) Å; c = 4.781(3) Å;		
V = 290.58(8) Å^3; R_B = 4.8%			V = 272.2(3) Å^3; R_B = 9.28%		
Interatomic distances (Å) / Distortion			Interatomic distances (Å) / Distortion		
Fe-O1=2.18(4)	P-O1 = 1.56(4)	Li-O1(x2) = 2.16(2)	Fe-O1=2.0(1)	P-O1 = 1.7(2)	
Fe-O2 = 2.09(4)	P-O2= 1.54(5)	Li-O2(x2) = 2.11(2)	Fe-O2 = 2.0(1)	P-O2= 1.3(2)	
Fe-O3(x2) = 2.08(2)	P-O3(x2) = 1.55(3)	Li-O3(x2) = 2.20(2)	Fe-O3(x2) = 1.8(1)	P-O3(x2) = 1.7(1)	-
Fe-O3(x2) = 2.21(3)	-	-	Fe-O3(x2) = 2.3(1)	-	
Δ = 7.3E-04	Δ = 0.2E-04	Δ = 2.8E-04	Δ = 134.2E-04	Δ = 155.1E-04	

50 % $LiFePO_4$ (50(3)%)			**50 % $FePO_4$ (50(3)%)**		
a = 10.313(3) Å; b = 6.004(2) Å; c = 4.692(1) Å;			a = 9.821(2) Å; b = 5.793(1) Å; c = 4.777(1) Å;		
V = 290.5(1) Å^3; R_B = 7.78%			V = 271.8(1) Å^3; R_B = 7.59%		
Interatomic distances (Å) / Distortion			Interatomic distances (Å) / Distortion		
Fe-O1=2.13(9)	P-O1 = 1.60(9)	Li-O1(x2) = 2.15(4)	Fe-O1=1.94(5)	P-O1 = 1.59(9)	
Fe-O2 = 2.16(6)	P-O2= 1.51(4)	Li-O2(x2) = 2.08(4)	Fe-O2 = 1.89(6)	P-O2= 1.48(9)	
Fe-O3(x2) = 2.05(4)	P-O3(x2) = 1.56(5)	Li-O3(x2) = 2.22(4)	Fe-O3(x2) = 1.93(4)	P-O3(x2) = 1.61(5)	-
Fe-O3(x2) = 2.22(5)	-	-	Fe-O3(x2) = 2.22(5)	-	
Δ = 9.7E-04	Δ = 4.2E-04	Δ = 6.8E-04	Δ = 50.2E-04	Δ = 11.1E-04	

25 % $LiFePO_4$ (18(2)%)			**75 % $FePO_4$ (82(3)%)**		
a = 10.338(7) Å; b = 6.007(4) Å; c = 4.690(3) Å;			a = 9.820(1) Å; b = 5.7891(8) Å; c = 4.7786(7) Å;		
V = 291.3(3) Å^3; R_B = 10.6%			V = 271.65(7) Å^3; R_B = 5.89%		
Interatomic distances (Å) / Distortion			Interatomic distances (Å) / Distortion		
Fe-O1 = 2.2(1)	P-O1 = 1.6(2)	Li-O1(x2) = 2.2(1)	Fe-O1=1.91(3)	P-O1 = 1.54(4)	
Fe-O2 = 2.2(2)	P-O2= 1.2(2)	Li-O2(x2) = 2.1(1)	Fe-O2 = 1.97(3)	P-O2= 1.45(4)	
Fe-O3(x2) = 1.92(9)	P-O3(x2) = 1.6(1)	Li-O3(x2) = 2.28(9)	Fe-O3(x2) = 2.01(2)	P-O3(x2) = 1.58(3)	-
Fe-O3(x2) = 2.5(1)	-	-	Fe-O3(x2) = 2.16(3)	-	
Δ = 104.8E-04	Δ = 193.4E-04	Δ = 17.3E-04	Δ = 21.9E-04	Δ = 11.6E-04	

0 % $LiFePO_4$			**100 % $FePO_4$**		
-			a = 9.820(1) Å; b = 5.7892(6) Å; c = 4.7790(6) Å;		
-			V = 271.69(5) Å^3; R_B = 5.30%		
Interatomic distances (Å) / Distortion			Interatomic distances (Å) / Distortion		
			Fe-O1=1.92(2)	P-O1 = 1.53(3)	
			Fe-O2 = 1.93(2)	P-O2= 1.51(3)	
-	-	-	Fe-O3(x2) = 2.02(2)	P-O3(x2) = 1.58(2)	-
			Fe-O3(x2) = 2.15(2)	-	
			Δ = 20.0E-04	Δ = 3.7E-04	

2.6 Conclusions and perspectives

This chapter recalls the important parameters that have been taken into consideration to successfully develop an electrochemical cell for *in situ* and *operando* neutron powder diffraction. We showed that it could properly function electrochemically, while leading at the same time to NPD patterns of high quality for Rietveld structural refinements. Important choices have been in particular the use of a neutron-transparent material such as the (Ti,Zr) alloy, the use of a deuterated electrolyte and the high neutron flux available on the D20 diffractometer. We showed the satisfactory electrochemical curves obtained for a representative material, $LiFePO_4$. Subsequently, *in situ* NPD measurements were conducted upon charge. For the first time a single- and multi-phase Rietveld refinement could be successfully performed on *in situ* and *operando* patterns, leading to reliable and accurate structural parameters. For these reasons, such a cell can be an extremely useful tool to study new materials of interest for Li-ion and Na-ion batteries, where the understanding of phase transition mechanisms is essential for further improvements and development. The use of our cell to study different classes of materials is described in the following of this thesis. Here it is important to note that *in situ*/*operando* NPD for the study of electrode materials has kept developing ever more rapidly in 2014 and 2015. New cell designs have been proposed [149,151,156] and several new studies undertaken [154,157,159,161,164], making this an extremely rich, challenging and competitive field, as already proved by Table 2.2, Figure 2.3 and Figure 2.4. On our side, future developments mainly regard: i) the use of cheaper deuterated electrolytes, as recently reported [171], ii) the *operando* study of more challenging materials, especially among polyanionic compositions, and iii) the development of similar electrochemical cells for *operando* studies on all-solid-state lithium batteries (i.e. cells able to operate at high temperatures).

Chapter 3

Operando neutron powder diffraction studies of spinel materials for Li-ion batteries

3.1 Introduction

3.1.1 The spinel family

Spinels are a class of minerals of general formulation $A^{2+}B_2^{3+}X_4^{2-}$, crystallizing in the cubic crystal system. They have a close-packed lattice of anions, being in most cases oxygen O^{2-}, while A and B occupy tetrahedral and octahedral sites in the structure[179], respectively. If the anion is not oxygen but another chalcogenide element, the structure is named thiospinel. Although the prototypical spinel $MgAl_2O_4$ contains elements A and B in oxidation states 2+ and 3+, respectively, many other combinations are possible, including monovalent and quadrivalent cations as well. This is of special interest in this thesis, since lithium is monovalent and it is normally the A element in the structure, giving rise to a higher oxidation state for the B element (3.5+). Several minerals in nature are found to crystallize in the spinel crystal structure. "The" Spinel is $MgAl_2O_4$, named in 1779 by Jean Demeste from the latin "spinella", little thorn, alluding to its sharp octahedral crystals[180]. This can be a precious stone, depending on the impurities it may contain. The most abundant member of the spinel family is magnetite Fe_3O_4, where A and B are Fe^{2+} and Fe^{3+} cations, respectively. These two materials, $MgAl_2O_4$ and Fe_3O_4, were used to unravel the general crystal structure of spinels by the co-father of X-Ray diffraction

himself, H. W. Bragg, in parallel with S. Nishikawa, in 1915 [181–183]. Their first discoveries were sustained and complemented by successive works, leading to a good knowledge of the spinels' crystal structure (Figure 3.1) [184]. A very clear description of such structures was given a few years later by M.M. Thackeray, who was working on the composition $LiMn_2O_4$. In his words: "*The cubic spinel possesses prototypic symmetry* $Fd\bar{3}m$ (O_h^7) *and has a general structural formula* $A[B_2]X_4$. *The anions X form a cubic-close-packed array occupying the 32e sites of the space group; the B cations occupy half the octahedral sites, the 16d sites, and the A cations occupy one-eighth of the tetrahedral sites, 8a. The interstitial octahedral sites 16c are interconnected in 3D by sharing common edges with six like near neighbors exactly as the 16d sites, but shifted by half a lattice parameter in space. Each 16c site shares two common faces, on opposite sides, with occupied 8a sites; the other faces are shared with empty, interstitial tetrahedral sites, 48f. The final empty tetrahedral sites, 8b, shares faces with four, occupied 16d octahedral sites; it would require a large energy to insert cations into the 8b sites*" [20].

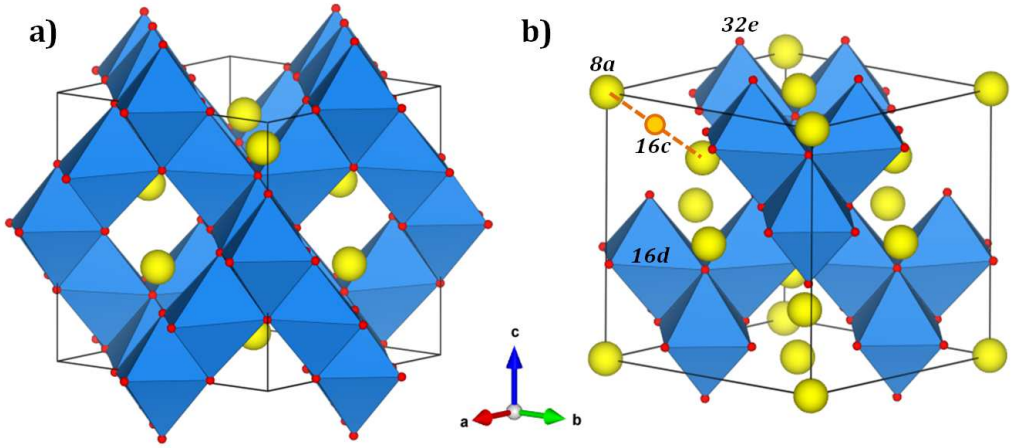

Figure 3.1: Structure of the spinel $MgAl_2O_4$. Small red spheres represent oxygen, blue octahedra represent aluminium and its coordination, yellow spheres 4-coordinated magnesium. One unit cell contains 8 formula units. a) and b) are the two settings reported in the international tables of crystallography, having the origin at -3m and -43m, respectively. b) is obtained from a) via a (1/8, 1/8, 1/8) unit cell translation.

This structure properly describes "normal" spinels. In this picture, tetrahedral sites are in general smaller that octahedral ones, determining a preference based on cation size for the elements that will better fit in these spaces. In fact, it is also possible to observe a spinel inversion [184,185]: a total inversion happens when all the A cations occupy octahedral sites, inducing a displacement of half of the B cations to tetrahedral ones. This is the case

of magnetite, for example. The inversion can also be incomplete, resulting in a crystal structure of the form $[A_{1-x}B_x]^{Td}[A_{x/2}B_{1-x/2}]_2^{Oh}O_4$, where x denotes the degree of inversion. x = 0 represents the normal spinel, x = 1 the inverse one. If A and B are close in the periodic table and thus their scattering powers for X-Rays are similar, it can be difficult to distinguish a normal from an inverse spinel, as it is the case for $MgAl_2O_4$. In such cases, neutron diffraction can usually lift the doubt [186]. The occurrence of inverse spinels has been widely studied; surprisingly, the relative size of s and p atomic orbitals of the two types of atom A and B has been shown to be the leading factor to determine site preference and thus the favourable type of spinel, while the type/size of d orbitals involved only play a secondary role [187].

3.1.2 $LiMn_2O_4$ for Li-ion batteries

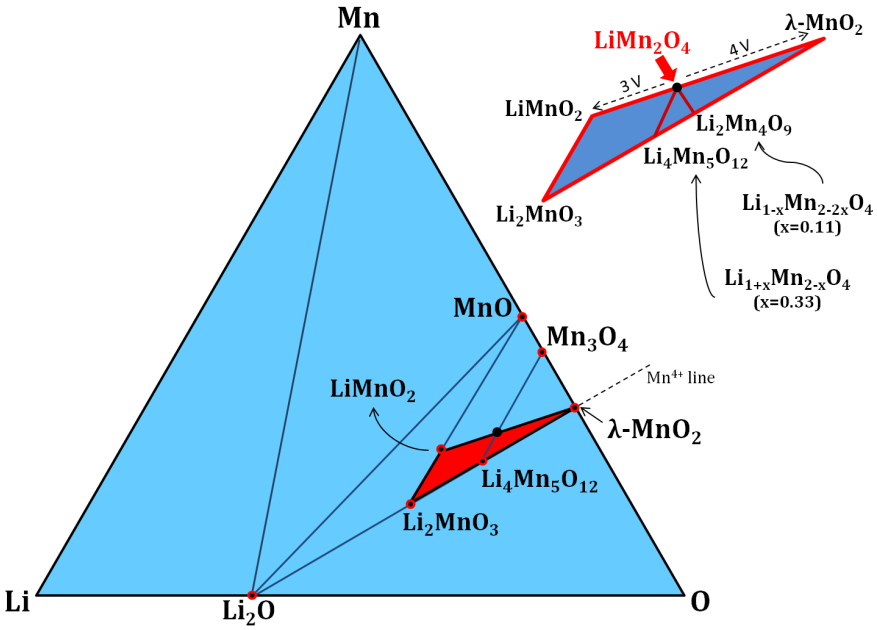

Figure 3.2: Ternary phase diagram of Li-Mn-O at ambient temperature. The highlighted triangle emphasizes the region of highest interest for Li-ion batteries, where Mn^{3+}-containing $LiMn_2O_4$ is shown. Other important compositions are Mn^{3+}-containing $LiMnO_2$ and Mn^{4+}-containing λ-MnO_2, $Li_2Mn_4O_9$, $Li_4Mn_5O_{12}$ and Li_2MnO_3.

The spinel compositions of interest in the field of electrode materials for Li-ion batteries of course contain lithium as the monovalent cation in the A site, and one or more transition metal elements in the B site, where several valence combinations are possible. The most important and widely studied composition is the manganese-containing spinel, i.e. $LiMn_2O_4$.

Its position in the ternary Li-Mn-O phase diagram is reported in Figure 3.2. The pioneering work on such material was carried out by M.M. Thackeray in the early 80s with J.B. Goodenough in Oxford, UK, who had already a wide knowledge of the spinel family due to early works[188]. The first spinel structure Thackeray looked at was magnetite, showing with other iron oxides an interesting electrochemical activity[189,190]. As a consequence of these first studies, he began investigating $LiMn_2O_4$ both in terms of lithium insertion and extraction[20–22]. It is worth mentioning that lithium being placed in the tetrahedral site 8a, as described above, was not an obvious conclusion. It was understood because (220) and (422) reflections, usually present in spinels and therefore allowed by symmetry, are actually extremely weak (almost extinct) in $LiMn_2O_4$ (Figure 3.3). The intensities of these two reflections are chiefly dependent upon the atomic scattering factors of the ions occupying tetrahedral sites. Therefore, the light lithium atoms (Z = 3) with their low scattering power for X-rays were deduced to be the occupants of the tetrahedral sites in the structure of $LiMn_2O_4$[184,191].

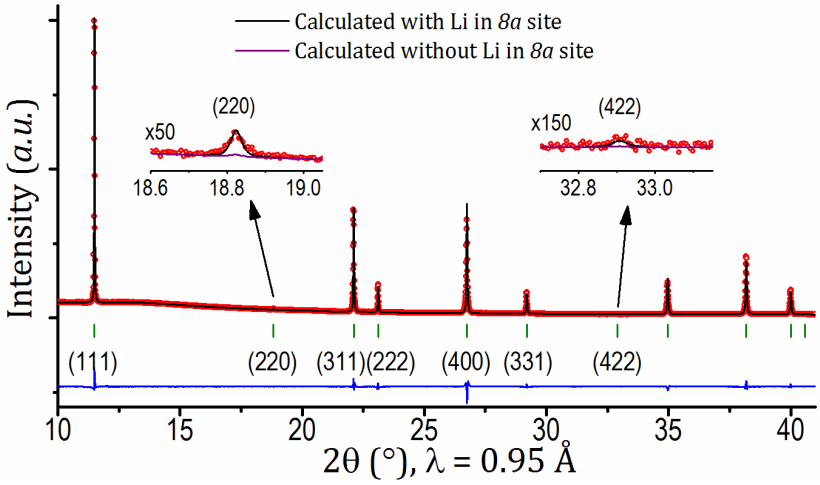

Figure 3.3: Rietveld refinement of a synchrotron XRPD measurement of $LiMn_2O_4$. Observed pattern Yobs in red, calculated Ycalc in black, difference Yobs-Ycalc in blue, Bragg positions as green ticks. In the insets, (220) and (422) reflections are shown, stressing the difference between a model with (black) and without (purple) lithium in the 8a site.

The structure of pristine $LiMn_2O_4$ was already well-known at the beginning of such studies[188,191], so that the investigation could focus on the role of lithium upon intercalation and deintercalation. Figure 3.4 summarizes the electrochemistry of the material in both reactions. Upon Li^+ insertion ($Li_{1+x}Mn_2O_4$), it was found that the cubic symmetry (of cell parameter a = 8.248 Å) is disrupted as a consequence of cooperative Jahn-Teller effect[20],

inducing a tetragonal distortion when lithium content exceeds 1.2 Li/f.u. and thus the ratio of Mn^{3+}/Mn^{4+} increases above ≈3/2. The phase transition between $LiMn_2O_4$ and $Li_2Mn_2O_4$ is first-order and a two-phase region is observed for $0.1 < x < 0.8$ [20,192]. This means that, electrochemically, a flat voltage-composition curve is observed at a potential close to 3.0 V vs. Li^+/Li. The newly inserted Li^+ ions occupy the interstitial 16c sites. These share faces with the 8a tetrahedra, thus electrostatic interactions between the lithium ions on these two sets of sites cause an immediate displacement of the tetrahedral-site lithium ions into neighboring, vacant 16c octahedra. Therefore in the rock salt $Li_2Mn_2O_4$ most of the lithium ions are in 16c sites, although a non-zero occupation of the 8a ones has been demonstrated using neutron diffraction [193]. The actual tetragonal space group becomes $F4_1/ddm$ with a bigger unit cell volume caused by lithium insertion (however, the Jahn-Teller effect causes a to decrease and c to increase, a = 7.994(l) Å, c = 9.329 (1) Å) [20,22].

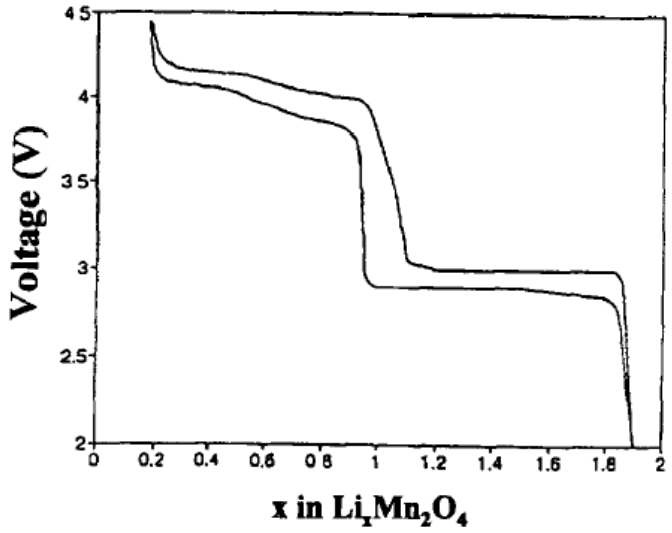

Figure 3.4: The electrochemical profile (voltage-composition galvanostatic curve) of a $LiMn_2O_4$//Li half cell. Both the high-voltage Li deintercalation domain and low-voltage Li intercalation one are displayed. Reprinted from [23].

Upon lithium extraction ($Li_{1-x}Mn_2O_4$), the cubic structure described in space group $Fd\bar{3}m$ is maintained. The completely delithiated end member is λ-MnO_2, a rocksalt compound whose cell parameter is a = 8.03 Å [194], significantly decreased with respect to that of $LiMn_2O_4$ [21,22,193]. The process involves manganese oxidation until 100% Mn^{4+} is obtained. This is electrochemically observed as a sequence of two plateaus in the voltage-composition curve, around 4.05 V and 4.15 V vs. Li^+/Li [21,192,195] (see Figure 3.5 for instance). The ex-

istence of an intermediate phase of composition $Li_{0.5}Mn_2O_4$ has been proposed (although not demonstrated) to explain this feature[196–198] and it will be further discussed in the next paragraphs of this chapter. Such a phase was observed in more recent studies, but it did not seem to involve any change in the crystal structure, i.e. spinel-spinel biphasic transitions were observed[155,197].

$LiMn_2O_4$ has been one of the most widely studied materials in the last 30 years, with thousands of publications reporting synthesis routes and relative electrochemical properties[195,199–208], phase diagram and phase transition as a function of several external parameters[23,196,209–215], nano-fabrications and nano-structurations[216,217]... until finally it led to concrete industrial applications, for example as the positive electrode in the Nissan Leaf vehicle, commercialized from 2010-2011[218]. The interest in the manganese spinel class of materials does not only lie in its industrial potential; it also lies in the fact that it possesses an extremely rich set of physical and chemical properties, at the origin of many debates and doubts in the scientific community, not all clarified yet. Typical examples include the presence of two electrochemical features at 3.3 V and 4.6 V vs. Li^+/Li[219–221], or the role played by a possible oxygen under-stoichiometry[214,215,222–224]. In addition, the crystal chemistry of lithium manganese spinels is extremely varied, with phase transitions at various temperatures[209] and for different composition ranges[20]. Note, however, that the material used for applications is not "stoichiometric" $LiMn_2O_4$. This material was shown to suffer from capacity retention issues[20–23,202,205,224–226], mainly caused by the presence of a significant amount of Mn^{3+} (which is at the origin of cooperative Jahn-Teller distortion and/or disproportionation to yield soluble Mn^{2+} species[227–230]). Thorough control of the synthesis conditions of these apparently simple oxides revealed to be extremely important. Typically, a slight departure from the original oxidation state of manganese (+3.5) towards the value +4 led to better capacity retention, at the expense of the theoretical capacity[202,203,226]. Several routes are possible to solve this problem by reducing the amount of Mn^{3+}. Some of them, rather successful, were already proposed by Thackeray himself and involve the use of lithium in excess or defect to change the properties of $LiMn_2O_4$. Two mains series of compositions were proposed by Thackeray[23,227] and others[202,205,214,222]: Li-rich stoichiometric spinels $Li_{1+x}Mn_{2-x}O_4$ ($0 \leq x \leq 0.33$) and defect spinels $Li_{1-x}Mn_{2-2x}O_4$ ($0 \leq x \leq 0.11$). The first ones change the Li/Mn ratio by adding extra-lithium in the site of manganese, and are described in detail in the next paragraph, as the samples used for our *operando* NPD studies belong to this family. The second ones preserve the Li/Mn = 1/2

ratio, but they are cation-deficient in the sense that vacancies are introduced in the lithium and manganese sublattices in order to increase the average Mn oxidation state.

Research has also evolved towards the substitution of part of the manganese with other transition metal elements (Ti, Fe, Cr, Ni etc...)[25,230–243]. This leads to extremely promising electrode materials because other redox couples than $Mn^{2+}/Mn^{3+}/Mn^{4+}$ are exploited, mostly resulting in much higher electrochemical potentials when used in Li-ion batteries. This could mean a drastic energy increase, once electrolytes stable at such high potentials are fully developed[4,8,39]. $LiNi_xMn_{2-x}O_4$ ($0 \leq x \leq 1/2$) is one of the most promising high-voltage electrode materials, relying mainly on the $Ni^{2+}/Ni^{3+}/Ni^{4+}$ redox couples and operating at a voltage as high as 4.7 V vs. Li^+/Li. More details about these compositions are given in section 3.4, where an *operando* NPD study of $LiNi_{0.4}Mn_{1.6}O_4$[237,238,244,245] is reported.

3.2 *Operando* NPD studies of spinel materials

We decided to exploit our custom-made (Ti,Zr)-alloy cell for *in situ* and *operando* NPD measurements (described in the previous chapter) to get valuable insight into the lithium extraction mechanisms from Li-rich spinels of compositions $Li_{1+x}Mn_{2-x}O_4$ ($0 \leq x \leq 0.10$). In this x range, manganese oxidation state can be increased from 3.5+ to 3.63+ by substituting part of the manganese in the 16d crystallographic sites with lithium. This reduces the usable capacity, but also eliminates significantly capacity fading upon cycling thanks to the lower amount of Mn^{3+} (which as discussed above is at the origin of capacity fading issues). Only few studies have addressed the mechanism of Li^+ extraction from these compositions by means of *ex situ* and *in situ* X-ray diffraction[192,196,197,212], none of them in a systematic way and for comparison purposes for different Li/Mn ratios. We therefore decided to perform an *operando* neutron powder diffraction study during the extraction of lithium from $Li_{1+x}Mn_{2-x}O_4$ spinels, with the goal of giving quantitative information about the different phases involved and with special attention to lithium's site occupancy factors (SOFs). To this end, we synthesized three samples of nominal stoichiometries $LiMn_2O_4$(x = 0), $Li_{1.05}Mn_{1.95}O_4$ (x = 0.05) and $Li_{1.10}Mn_{1.90}O_4$ (x = 0.10).

3.2.1 Experimental

Three samples of the spinel positive electrode material $Li_{1+x}Mn_{2-x}O_4$ were prepared for x = 0 (**Sample S1**), x = 0.05 (**Sample S2**) and x = 0.10 (**Sample S3**). To this end, as

described in [222], stoichiometric amounts of (1+x)/2·Li_2CO_3 and (2-x)·MnOOH were carefully mixed, heated at 400 °C for 2 hours, cooled and mixed at RT prior to being heated for 20 hours at 800 °C in air and rapidly cooled (≤10 °C/min) down to RT. For electrochemical testing, the active materials were mixed with Carbon Super P in 90:10 wt% ratios and ground in a mortar. For these first experiments, no binder was added to the mixture. Swagelok-type cells were used to prepare lithium half cells. Glass fiber separators (Whatman) and LP30 electrolyte (Aldrich) were used. The half cells were cycled at C/20 rate between 3.2 V and 4.5 V vs. Li^+/Li, using small amounts of powders (≤ 20-25 mg) as positive electrodes. Diffraction experiments were initially performed using X-Rays produced within a Bruker D8 diffractometer (Cu K$\alpha_{1,2}$ wavelength, Bragg-Brentano geometry). NPD was subsequently carried out on the D2B high-resolution neutron diffractometer at the Institut Laue-Langevin. Powder samples were put in cylindrical vanadium cans and measured in transmission geometry at $\lambda = 1.5944$ Å (calibrated using $Na_2Ca_3Al_2F_{14}$ as a reference). *In situ* (*operando*) experiments were performed on the D20 high-flux neutron diffractometer at ILL. For each of the three samples, a battery was prepared in our *in situ* cell [148]. The electrode preparation followed the procedure described above, but with high loadings of about 200 mg. Standard electrolytes were replaced by a deuterated version, prepared with 1 M $LiPF_6$ in d-EC:d-DMC (1:4 wt%), which had also been previously tested [148]. No lithium enrichment was performed, i.e. lithium with (nominal) natural isotope abundance was used for all battery components. The batteries were measured *operando* continuously on the D20 diffractometer ($\lambda = 1.5471$ Å) in transmission geometry. Every pattern was acquired for 30 minutes while charging the battery at C/20 rate up to 4.5 V vs. Li^+/Li (4.6 V for the sample x = 0), corresponding to a variation of 0.025 Li/pattern. Data treatment and Rietveld refinements were performed using the FullProf Suite [177]. It is worth emphasizing that for every sample, each *operando* diffraction pattern has been independently treated (i.e. no sequential refinements possible) due to the fact that lithium extraction results both in a decrease of the sample's absorption (lithium is a neutron absorber) and in an increase of the background due to organic components of the battery (deuterated electrolyte) and other scattering elements (separator, carbon). Note that the variable absorption has been dealt with by using a decreasing μR coefficient, starting from about 0.5 for the pristine samples and de-creasing by 0.0125/pattern to reach a value between 0.1 and 0.2 at the end of charge, depending on the sample.

For sample S1 ($LiMn_2O_4$, Table 3.1), which generates different phases upon electro-

Table 3.1: Electrochemical and crystallographic characterization of pristine materials $Li_{1+x}Mn_{2-x}O_4$ (x = 0, 0.05, 0.10) from XRPD, NPD and galvanostatic cycling. Statistical errors are reported (3σ). For sample S1 the refined value of x is different than in Figure 3.5, because in that case oxygen's SOF is also refined.

Pristine Material	**a = b = c (Å)**	**Refined x (ND)**	**Mn oxid. state (calc)**	**Measured/Expected fully oxid. compos.**
S1: $LiMn_2O_4$	XRD: 8.2484(2) ND: 8.2487(1)	0.00(7)	+3.5	$Li_{0.04}Mn_2O_4$ / $Li_{0.0}Mn_2O_4$
S2: $Li_{1.05}Mn_{1.95}O_4$	XRD: 8.2307(4) ND: 8.2355(1)	0.05(8)	+3.56	$Li_{0.19}Mn_{1.95}O_4$ / $Li_{0.20}Mn_{1.95}O_4$
S3: $Li_{1.10}Mn_{1.90}O_4$	XRD: 8.2188(3) ND: 8.2218(1)	0.10(8)	+3.63	$Li_{0.40}Mn_{1.90}O_4$ / $Li_{0.40}Mn_{1.90}O_4$

chemical cycling, Debye-Waller factors (B_{iso}) were refined for the pristine, final and intermediate compositions and then kept constant within the different domains during charge. For samples S2 ($Li_{1.05}Mn_{1.95}O_4$) and S3 ($Li_{1.10}Mn_{1.90}O_4$), which react through significant solid solution regions, a fixed B_{iso} could not take into account the modifications occurring in these domains and thus B_{iso} were refined for every pattern (we used a $B_{overall}$ factor, the same B_{iso} for all atoms). For S2 we observed a decrease of $B_{overall}$ from 1.46 to 0.50, while for S3 from 1.26 to 0.53. One should note that although considering thermal agitation is necessary to account for the data, it is detrimental for the value of the error bars obtained from refinement. This is particularly true for site occupancy factors (SOFs) since the parameters can be correlated. Moreover, lithium and manganese have poor contrast for neutrons (they have both negative scattering lengths, b_{Li} = -1.90 fm and b_{Mn} = -3.75 fm) which explains why error bars for SOFs are far more important than for every other parameter. For this reason such error bars will often be reported with two digits.

3.2.2 Analysis of pristine materials

The three samples were initially characterized in their pristine forms. The neutron powder diffraction patterns collected using the D2B high-resolution neutron diffractometer at ILL are gathered in Figure 3.5. The obtained cell parameters are reported in Table 3.1, in remarkable agreement with those found in the literature [23,214,222] when lithium substitutes part of manganese with concomitant oxidation of the remaining Mn: from X-Ray diffraction we obtain a = 8.2484(2) Å for $LiMn_2O_4$ (Sample S1), a = 8.2307(4) Å for $Li_{1.05}Mn_{1.95}O_4$

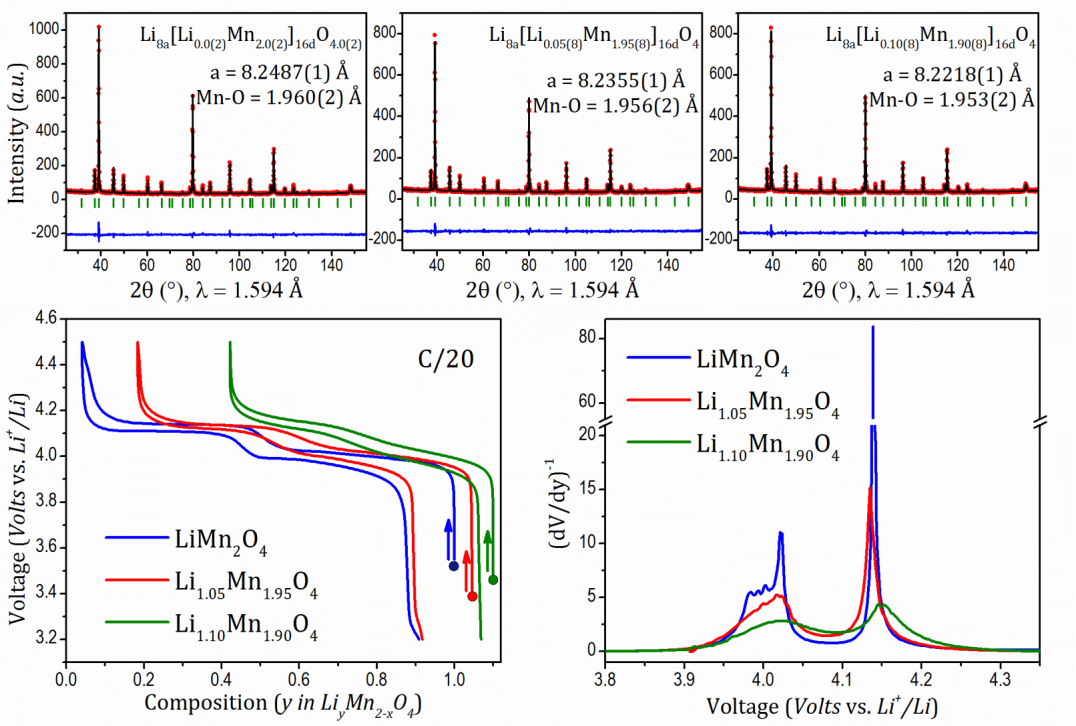

Figure 3.5: Top: Rietveld refinement of neutron powder diffraction data recorded using the D2B high-resolution diffractometer at ILL for $LiMn_2O_4$ (left), $Li_{1.05}Mn_{1.95}O_4$ (center) and $Li_{1.10}Mn_{1.90}O_4$ (right). Bottom: Respective voltage-composition curves recorded vs. Li^+/Li during galvanostatic cycling at C/20 rate (left) and their inverse derivative curves (right), showing the two electrochemical features typical of spinel materials.

(S2) and a = 8.2188(3) Å for $Li_{1.10}Mn_{1.90}O_4$ (S3). It should be kept in mind that since the oxidation state of manganese increases with increasing x in $Li_{1+x}Mn_{2-x}O_4$, the total amount of lithium that can be extracted from the spinel structure decreases accordingly. More precisely, simple calculations show that the total amount of extractable lithium decreases as 1-3x ($0 \leq x \leq 0.33$), and therefore the amount of lithium that remains in the structure at the end of charge increases as 4x (i.e. reaching the fully oxidized Mn^{IV} compositions $Li_0Mn_2O_4$ for sample S1, $Li_{0.2}Mn_{1.95}O_4$ for S2 and $Li_{0.4}Mn_{1.90}O_4$ for S3). The values we observed experimentally from galvanostatic electrochemical Li^+ extraction agree with these considerations and are reported in Table 3.1. The decrease of cell parameters and of Mn-O distances (Figure 3.5) are also in good agreement with an increase in the manganese oxidation state. Rietveld refinements of the crystal structures of the three pristine samples were performed from the NPD data, using the structures reported in literature as initial models (ICSD 40485 and ICSD 166746 [246,247]). As expected, $Li_0Mn_2O_4$ crystallizes in the $Fd\bar{3}m$ space group, with Mn in octahedral 16d sites and oxygen in close-packed

32e sites, building a framework of MnO_6 edge-sharing octahedra. Lithium is confirmed to be in 8a tetrahedral position. The substitution of Li for Mn in $Li_{1+x}Mn_{2-x}O_4$ occurs on the 16d site, therefore generating Li^+ in octahedral oxygen environment [23], written as $Li_{8a}[Li_xMn_{2-x}]_{16d}O_4$. Our Rietveld refinements confirmed that the oxygen's fractional atomic coordinates are close to x = y = z = 0.2368(2) for all the samples. Debye-Waller factors and, more importantly, lithium-manganese exchange ratios on the 16d site were also refined. Table 3.1 reports the obtained values, in excellent agreement with nominal compositions. For sample S1 ($LiMn_2O_4$) we also tried to refine oxygen's site occupancy factors (SOF) together with Li-Mn exchange but this did not result in any significant deviation from the full occupancy of the 32e site, confirming the stoichiometry of the sample. To further prove this, we verified that S1 undergoes a structural transition from cubic to orthorhombic symmetry below 285 K. It was in fact previously demonstrated [209–211] that such a transition is due to charge ordering and it thus happens only for the exact stoichiometry of $LiMn_2O_4$ (Figure 3.6).

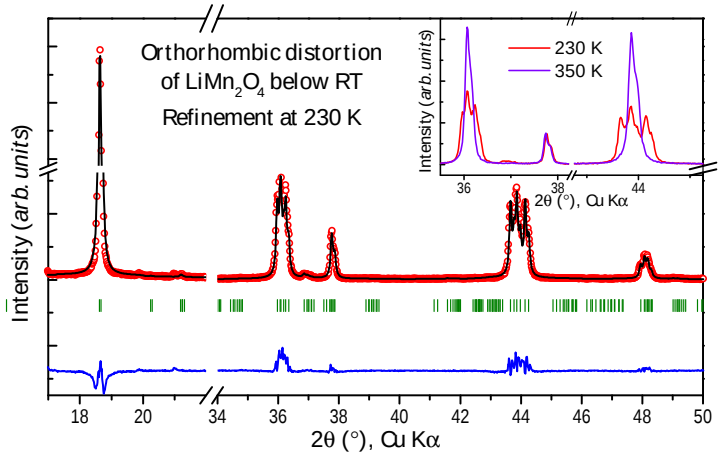

Figure 3.6: $LiMn_2O_4$ after cooling at 230 K. Rietveld refinement is performed using the model published in [211] to account for the observed orthorhombic distortion. The inset shows a comparison with the room-temperature data.

Contrary to what was reported by Berg-Thomas and Sharma [144,248], we did not find any occupation of the 16c site by Li^+. In the case of Sharma et al. in particular, an *in situ* NPD study is reported but comparison with our data is difficult since they provide no information on the sample in its pristine form, received as deintercalated and characterized as $[Li_{0.11(6)}]_{8a}[Li_{0.23(11)}]_{16c}Mn_2O_4$. Inspection of reported cubic cell parameter reveals that upon cycling it never exceeds a = 8.218 Å which is typical of non-stoichiometric spinels as discussed above (Li-Mn exchange for example). The non-stoichiometry of the sample

of Sharma et al. could also explain the fact that they observe the (dis)charge as a solid solution, while on the contrary we observe biphasic domains for the stoichiometric sample S1 (Li/Mn = 1/2). The galvanostatic electrochemical data, gathered in Figure 3.5, show the expected voltage-composition features, i.e. two "plateaus" located around 4.05 V and 4.15 V vs. Li^+/Li. Besides the marked differences in first charge capacities (discussed above), the dissimilarity between the three samples stands in the shape of the derivative curves (Figure 3.5). Both "plateaus" give rise to $(dV/dy)^{-1}$ peaks that are strongly composition-dependent in intensity (as expected from the different capacity) and shape, indicating a possible different lithium extraction mechanism. As a general trend, $(dV/dy)^{-1}$ peaks are sharper for S1 and they become broader from S2 to S3, i.e. as the average oxidation state of Mn in the pristine sample increases, indicating the possible change of the transition nature from first order to second order.

3.2.3 *Operando* NPD studies during Li^+ extraction

After the above-described characterizations of the samples' composition and cation distribution between different sites, *operando* neutron powder diffraction experiments upon charge were performed in a systematic way. A lithium half cell was prepared in our *in situ* cell and charged at C/20 rate, while recording NPD patterns continuously every 30 minutes. Figure 3.7 (for S1) and Figure 3.8 are reported to give an overall idea of the quality of the ND data collected *operando* during charge (Li^+ extraction) from the three

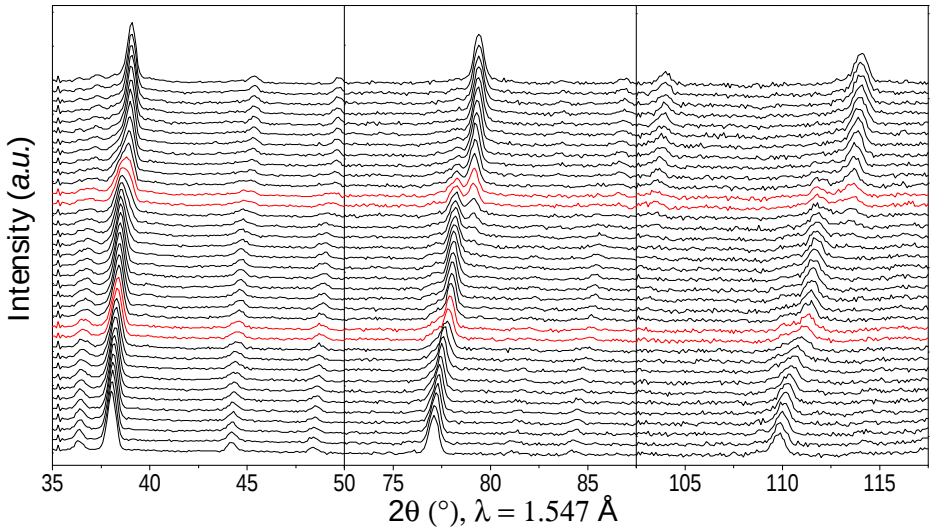

Figure 3.7: *Operando* neutron diffraction patterns recorded upon charge (Li^+ extraction at C/20 rate) for $LiMn_2O_4$. Red patterns indicate the central region of the two biphasic reactions.

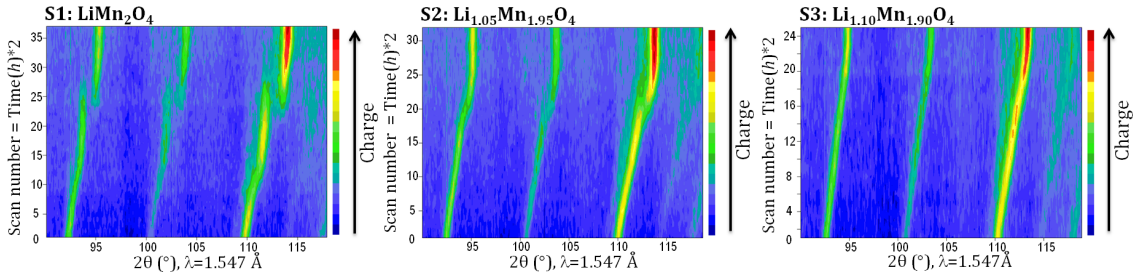

Figure 3.8: Contour plots of neutron powder diffraction patterns recorded *operando* upon charge (Li^+ extraction at C/20 rate) for $LiMn_2O_4$ (left), $Li_{1.05}Mn_{1.95}O_4$ (middle) and $Li_{1.10}Mn_{1.90}O_4$ (right). Focus on the 90°-120° 2θ angular range. Every scan was recorded for 30 minutes; the y axis scale can be read as scan number but also as time (hours), divided by 2.

samples. Keeping in mind the previously discussed advantages of NPD, one is readily obvious from these figures: the possibility to observe high angular range regions (up to 120° at $\lambda \approx 1.54$ Å) that allow clearly separating and visualizing peak shifts. Note however that a drawback was also clear from these measurements: for all samples a fraction of the electrode remained unreacted, as if the electrode was not sufficiently homogeneous and a part of it was passive. This is a consequence of the simple AM+Csp formulation of the electrode in these first experiments, but it was subsequently improved by adding a binder (described in section 3.4). The unreacted part was estimated to be about 10-15% of the electrode by Rietveld refinement (Figure 3.9).

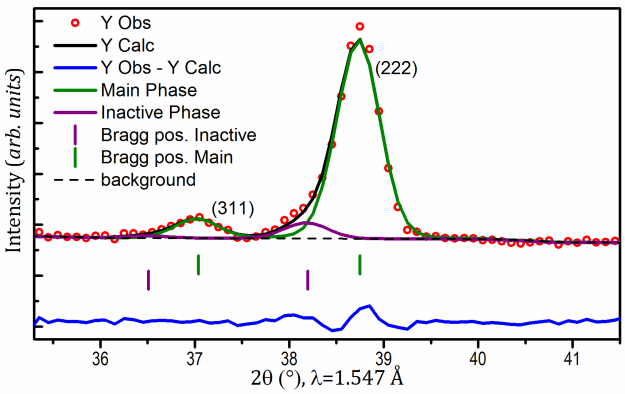

Figure 3.9: Detailed zoom on the 35.5°-41.5° 2θ region in the Rietveld refinement of the end-of-charge phase of Sample S3 $Li_{0.33}[Mn_{1.90}Li_{0.10}]O_4$ (Figure 3.11c) showing the contribution of the unreacted part of the electrode.

The delithiation of sample S3 seems to result in a smooth peak shift from lower to higher angular 2θ values while sample S2 only displays a similar behaviour until the voltage composition plateau at 4.15 V vs. Li^+/Li is reached. There, a biphasic reaction occurs

since the initial peaks disappear and new ones at higher angles concurrently take their place. Sample S1 also shows a two phase reaction associated with the "plateau" at 4.15 V vs. Li^+/Li, as well as a second one at ≈4.05 V, better visualized through the derivative curve of Figure 3.5.

All these "visual" considerations have been carefully analyzed by means of Rietveld refinements. Details about the refinement procedure are given in the Experimental Section 3.2.1 of this chapter. Figure 3.10 summarizes the obtained phase diagrams (vs. y, global Li content) as gathered from Rietveld refinement of our *operando* NPD data, subsequently discussed in more details in the following of this chapter for the three samples. Phase transitions are highlighted and the corresponding miscibility gaps can be evaluated.

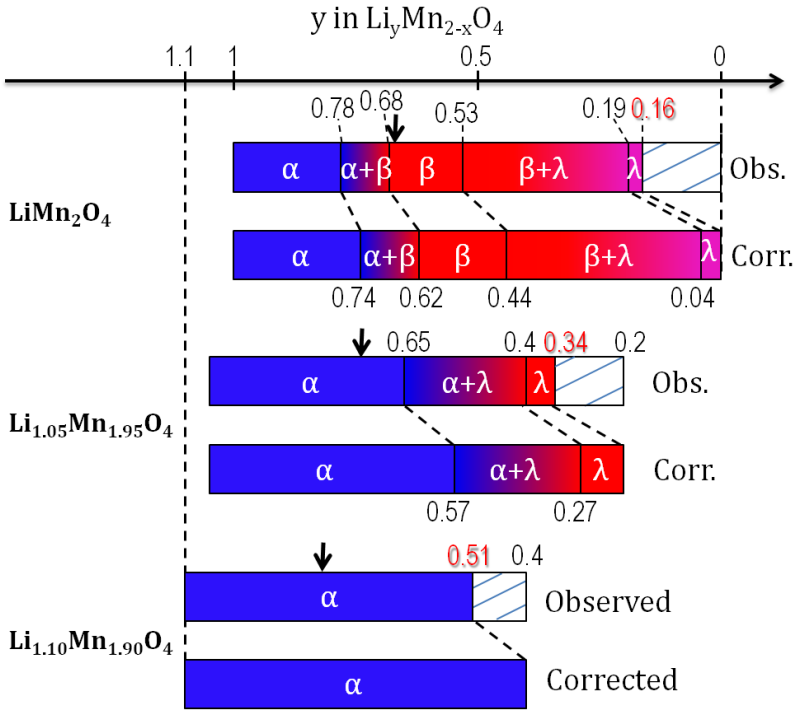

Figure 3.10: Phase diagram and observed miscibility gaps for $LiMn_2O_4$ (top), $Li_{1.05}Mn_{1.95}O_4$ (middle) and $Li_{1.10}Mn_{1.90}O_4$ (bottom). In red is given the y value at the end of the *in situ* charge. For every sample, two bars are reported to account for the bias given by the unreacting part of the electrode. The top bar represents the observed phase diagram and miscibility gaps, while the bottom one represents those corrected considering the full capacity $C_{theor.}$ of the materials (i.e. every observed composition interval is divided by the ratio $C_{obtained}/C_{theor.}$, <1 since obtained capacity < theoretical capacity). Arrows show noteworthy compositions studied in detail in the following.

Mechanism of Li^+ extraction from $Li_{1.10}Mn_{1.90}O_4$ (sample S3)

In $Li_{1.10}Mn_{1.90}O_4$, Mn is in the average oxidation state +3.63 and therefore only 0.7 Li^+ can be theoretically extracted, leading to the final composition $Li_{0.40}Mn_{1.90}O_4$. The use of 200 mg of positive electrode at C/20 rate resulted in the effective extraction of 0.6 Li^+, satisfactory but nonetheless incomplete. As already mentioned, we indeed observed that part of the pristine powder (≈10-15%) did not react; while the main diffraction peaks of the active material were shifting from the original position to higher angular positions a shoulder remained fixed close to the original position (Figure 3.9). All the NPD patterns were therefore refined keeping a "pristine-like" inactive phase. The relative weight ratio of the two phases is shown in Figure 3.11a, with all important refined parameters. It should be mentioned that the phase quantification is possible since the different phases have the same symmetry, contain approximately the same chemical elements and have the same morphology, but it is nonetheless semi-quantitative (no reference material is present in the sample).

The cubic unit-cell parameter of the main phase decreases from the initial value of a = 8.2225(4) Å to a final one of a = 8.0776(3) Å, i.e. a 5% unit cell volume shrinkage from 555.93(4) $Å^3$ to 527.04(4) $Å^3$, in a solid solution manner. The oxygen x = y = z fractional atomic coordinate was also refined, revealing a weak dependence on the state of charge. Indeed, it only increased from 0.2362(6) to 0.2370(5). This will remain in general true for all other samples. As previously discussed, there are two kinds of lithium in the structure: octahedral Li_{16d} that partly substitutes for Mn (0.1 Li_{16d}/formula unit here) and tetrahedral Li_{8a}. One can then write $Li_{1.10}Mn_{1.90}O_4$ as $[Li]_{8a}[Li_{0.10}Mn_{1.90}]_{16d}O_4$. It is generally admitted that only Li_{8a} is electrochemically active, i.e. Li_{16d} cannot be extracted from the structure[230]. The oxidized composition is thus $[Li_{0.30}]_{8a}[Li_{0.10}Mn_{1.90}]_{16d}O_4$. Note that, to the best of our knowledge and due to the lack of sufficiently sensitive experimental techniques, this has never been proved experimentally. We verified this important point by choosing selected compositions (the one in Figure 3.11b, for example) and by refining the lithium content in each site (Li_{8a}, Li_{16d}) with the constraint that Li_{8a}+Li_{16d} shall equal the amount of lithium/f.u. deduced from the electrochemical data. This only resulted in a small variation in the value of Li_{16d} SOF from 0.1 to 0.18(15). Because of the large error bar this increase is not significant; moreover, it is meaningless both because this would force manganese to quit its site and because it is contrary to what is expected for lithium extraction. We hence did not refine the Li_{16d} occupancy, keeping it constant at 0.1 and

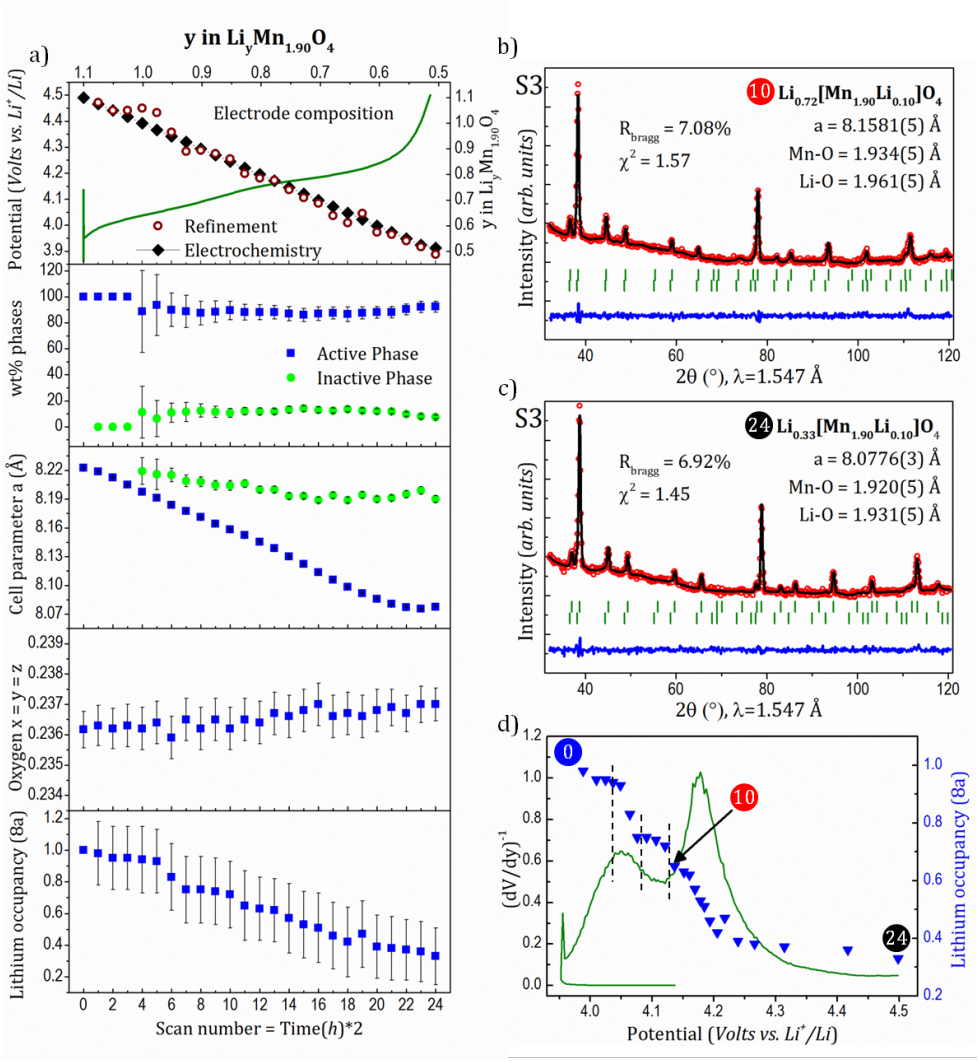

Figure 3.11: a) Refined parameters (Rietveld) from neutron powder diffraction data recorded *operando* during Li^+ extraction from $Li_{1.10}Mn_{1.90}O_4$. A full solid solution is observed with regular monotonous decrease of the cell parameter a. From top to bottom: electrochemical galvanostatic data, total % in weight of the different phases involved, respective cell parameters, oxygen fractional atomic coordinates and 8a lithium site occupancy factor. Top panel also reports the composition of the $Li_{1.10}Mn_{1.90}O_4$ electrode. Values measured during electrochemical cycling and calculated from the results of Rietveld refinement are compared. b)-c) Rietveld refinements of the intermediate phase $Li_{0.72}Mn_{1.90}O_4$ and of the end-of-charge phase $Li_{0.33}Mn_{1.90}O_4$. The second set of Bragg positions represents the unreacted part of the electrode, corresponding to the pristine material (10-15 wt.%). d) Inverse derivative of the voltage-composition curve, plotted with lithium's site occupancy factors for the different phases. The arrow indicates the phase $Li_{0.72}Mn_{1.90}O_4$. Vertical dotted lines help to notice the variation in 8a lithium's SOF decrease.

we further verified *a posteriori* the validity of such a strategy by calculating the electrode composition obtained considering all lithium contributions in the sample: constant Li_{8a}

and Li_{16d} in the side unreacted phase, constant Li_{16d} and refined Li_{8a} in the main active phase. The result is shown in the top panel of Figure 3.11a, where the calculated electrode composition matches very well the one measured during electrochemical cycling. Additionally, examples of Rietveld refinements for specific compositions are given in Figure 3.11b-c. The shrinkage of the unit cell and the one of Mn-O and Li-O bond lengths are highlighted. The variation of the refined occupancy of Li_{8a} is shown in Figure 3.11a-d, revealing a value decreasing from 1 to 0.33(18), just above the 0.3 expected for Li_{8a} (final composition $[Li_{0.30}]_{8a}[Li_{0.10}Mn_{1.90}]_{16d}O_4$). Very interestingly, and revealed for the first time thanks to *operando* neutron powder diffraction, the delithiation does not proceed at "uniform speed". The refinement of Li_{8a} SOF reveals a sharper Li occupancy variation for maximal values of $(dV/dy)^{-1}$, as plotted in Figure 3.11d. This suggests that, although the unit cell shrinkage proceeds at uniform rate, lithium deintercalation does not follow the same linear behavior. We estimate a rate of delithiation of 0.02 Li/(formula unit·hour) in the "slow" regions and of 0.08 Li/(formula unit·hour) in the "fast" regions, i.e. lithium extraction is about 4 times faster on the derivative peaks. This finding relates to an observation recently done on a similar sample by *in situ* Li NMR [249]: during charge, the broad Li_{8a}-related signal at 570 ppm not only shifts, but progressively disappears during charge. However such vanishing was found to be not continuous: it shows a local maximum in the intermediate region of charge (i.e. between the derivative peaks), possibly related to the relaxation time T2 and therefore to lithium's mobility [249]. This relates well with our finding of a slower delithiation in the voltage region between the two derivative peaks. Such observations suggest that the intermediate composition formed could present subtle lithium/vacancy charge ordering slowing down ionic mobility.

Mechanism of Li^+ extraction from $Li_{1.05}Mn_{1.95}O_4$ (sample S2)

In $Li_{1.05}Mn_{1.95}O_4$, Mn is in the average oxidation state +3.56 and therefore only 0.85 Li^+ can be theoretically extracted, leading to the final composition $Li_{0.20}Mn_{1.95}O_4$ (namely $[Li_{0.15}]_{8a}[Li_{0.05}Mn_{1.95}]_{16d}O_4$). The same rate of C/20 was used while charging the battery and the high electrode loading resulted again in the presence of an unreacted phase, estimated at 10-15% from refinements. Figure 3.12a shows all the significant refined parameters extracted from *operando* NPD as a function of the global Li content, y, in $Li_yMn_{1.95}O_4$. Li^+ extraction first proceeds through a solid solution (single phase) mechanism across the first electrochemical feature at 4.05 V vs. Li^+/Li. Concurrently, the unit cell parameter

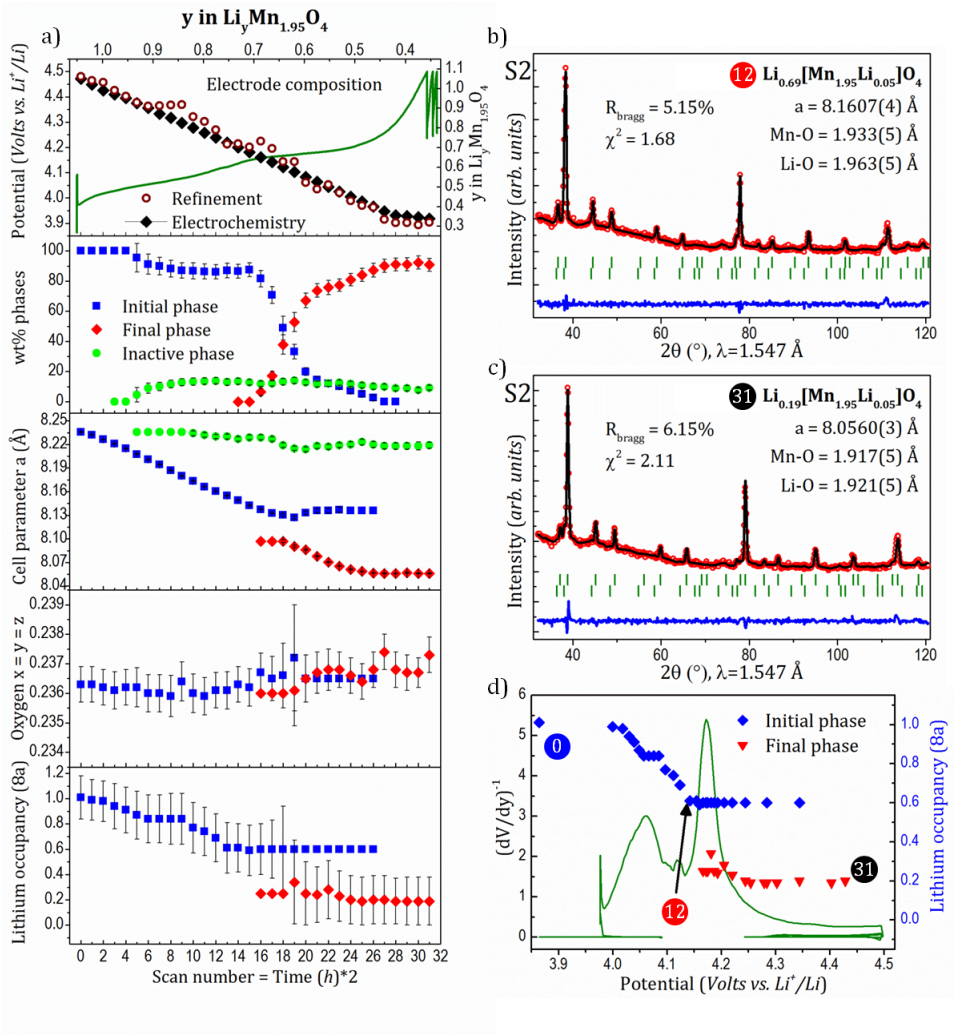

Figure 3.12: a) Refined parameters (Rietveld) from neutron powder diffraction data recorded *operando* during Li^+ extraction from $Li_{1.05}Mn_{1.95}O_4$, where a solid solution followed by a biphasic reaction is observed. From top to bottom: electrochemical galvanostatic data, total % in weight of the different phases involved, respective cell parameters, oxygen fractional atomic coordinates and 8a lithium site occupancy factor. Top panel also reports the composition of the $Li_{1.05}Mn_{1.95}O_4$ electrode. Values measured during electrochemical cycling and calculated from the results of Rietveld refinement are compared. b)-c) Rietveld refinements of the intermediate phase $Li_{0.69}[Mn_{1.95}Li_{0.05}]O_4$ and of the end-of-charge phase $Li_{0.19}[Mn_{1.95}Li_{0.05}]O_4$. The second set of Bragg positions represents the unreacted part of the electrode, corresponding to the pristine material (10-15 wt%). d) Inverse derivative of the voltage-composition curve, plotted with lithium's site occupancy factors for the different phases. The arrow indicates the phase $Li_{0.69}[Mn_{1.95}Li_{0.05}]O_4$.

diminishes from the initial value $a_1 = 8.2358(4)$ Å to $a_1 = 8.1424(4)$ Å i.e. with a unit-cell volume shrinkage of 3.4% from 558.6 Å^3 to 539.8 Å^3. Within the solid solution domain, the lithium's Li_{8a} SOF decreases from 1 to 0.59(21), in a similar fashion as for sample S3, namely a fast delithiation on top of the first derivative peak. When the second electro-

chemical feature at 4.15 V vs. Li^+/Li is reached, the diffraction peaks of the initial phase start to vanish, while a new phase appears characterized by a cubic unit cell parameter a_2 = 8.097(3) Å and a Li_{8a} SOF of 0.25(25). In a matter of about 3 patterns, i.e. 1.5 hours, this new phase overcomes the initial one and in another 3 patterns the initial one has almost completely disappeared (as shown in Figure 3.10, the observed miscibility gap is $\Delta x \approx 0.25$, which becomes $\Delta x \approx 0.3$ when correcting for the inactive phase). We noticed, interestingly, that during this transformation and until the end of charge, the cell parameter a_2 decreases continuously. This result is not expected from thermodynamic equilibrium, but its occurrence has recently been reported by several authors and for several materials in non-equilibrium conditions. In general it can be caused by strains in the phase front during the biphasic transformation [250]. It should also be noted that the biphasic reaction observed here involves a volume change from 539.84(5) $Å^3$ to 530.85(5) $Å^3$, i.e $\Delta V/V$ = 1.6% for $\Delta x \approx 0.3$. Subsequently a small solid solution region is present, leading to the final value a_2 = 8.0560(3) Å and a volume of 522.83(4) $Å^3$. In the same way, Li_{8a} SOF slightly decreases to give a final value of 0.19(19) (compared to the 0.15 expected for Li_{8a}). The occurrence of a one-phase and then of a two-phase reaction mechanisms upon Li^+ extraction from $Li_{1.05}Mn_{1.95}O_4$ electrode is illustrated in Figure 3.12b-c which gathers, as well, Rietveld refined patterns of single phase compositions $Li_{0.74}Mn_{1.95}O_4$ (scan #12) and $Li_{0.24}Mn_{1.95}O_4$ (scan #31).

Mechanism of Li^+ extraction from $LiMn_2O_4$ (sample S1)

For stoichiometric $LiMn_2O_4$ (x = 0) the average oxidation state of Mn is +3.5 and, theoretically, all the lithium ions can be extracted from the tetrahedral position to yield the fully delithiated $Li_0Mn_2O_4$ composition, referred to as λ-MnO_2 in the literature [194]. Previous studies have demonstrated the difficulty of reaching full delithiation (both chemically and electrochemically) [124,125,197]. In our case, from this *operando* NPD experiment (using high electrode loading) we obtained a final global composition of $Li_{0.16}Mn_2O_4$, as a result of the presence of a side unreacted phase (≈ 10-15%) and also of remaining lithium (about 0.1/formula unit) within the tetrahedral 8a site of the main final phase. Refined parameters are shown in Figure 3.13a. As observed from the inverse derivative curve and from the contour plots (Figure 3.5 and Figure 3.8), the reaction can be considered as a sequence of two biphasic reactions, quite different from each other. The pristine $LiMn_2O_4$ phase (1) undergoes, initially, a single phase Li^+ extraction reaction, from the initial value a_1

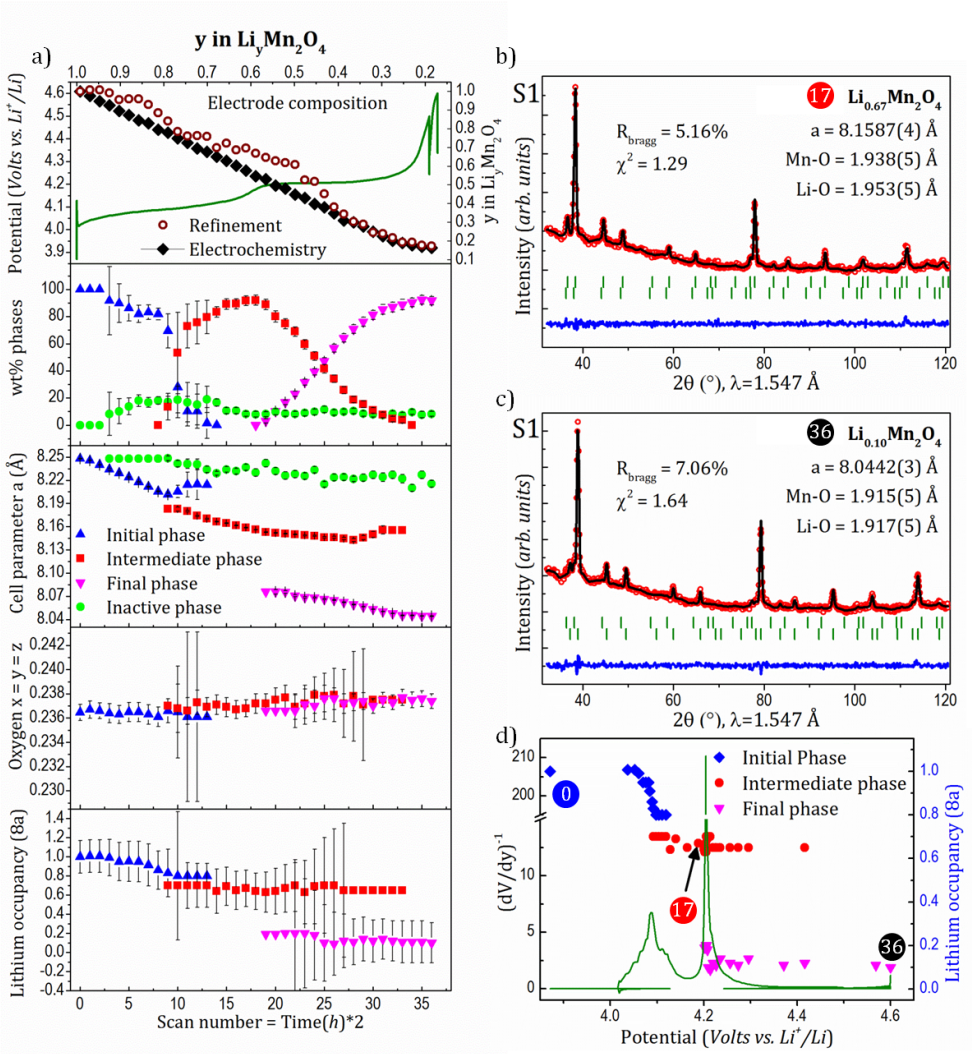

Figure 3.13: a): Refined parameters (Rietveld) from neutron powder diffraction data recorded *operando* during Li^+ extraction from $LiMn_2O_4$, where two biphasic reactions are observed. From top to bottom: Electrochemical galvanostatic data, total % in weight of the different phases involved, respective cell parameters, oxygen fractional atomic coordinates and 8a lithium site occupancy factor. Top panel also reports the composition of the $LiMn_2O_4$ electrode. Values measured during electrochemical cycling and calculated from the results of Rietveld refinement are compared. b)-c) Rietveld refinements of the intermediate phase $Li_{0.67}Mn_2O_4$ and of the end-of-charge phase $Li_{0.1}Mn_2O_4$. The second set of Bragg positions represents the unreacted part of the electrode, corresponding to the pristine material (10-15 wt.%). d) Inverse derivative of the voltage-composition curve, plotted with lithium's site occupancy factors for the different phases. The arrow indicates the phase $Li_{0.67}Mn_2O_4$.

= 8.2480(4) Å to a_1 = 8.2053(5) Å for Li_{8a} SOF = 0.83(25). Then a biphasic reaction takes place, between two phases very close to each other, both in lithium occupancy and cell parameters (the new phase (2) appears having a_2 = 8.183(3) Å and Li_{8a} SOF ≈ 0.7). This reaction happens quickly and is over in a matter of 5 patterns (i.e. 2.5 hours, Δx

$\approx$ 0.10-0.12 as reported in Figure 3.10): this has often been treated as a solid solution domain in the literature[196], until Baehtz et al.[197] showed it to be biphasic thanks to *in situ* synchrotron radiation powder diffraction. We also confirmed this in our own *in situ* synchrotron XRPD study reported in section 3.3.1. This intermediate phase (2) subsequently evolves to final values of a_2 = 8.156(5) Å and Li_{8a} SOF = 0.63(21). As observed for sample S2 at composition $Li_{\approx 0.6}Mn_{1.95}O_4$, we notice that the final composition reached at this stage is not $Li_{0.5}Mn_2O_4$. Figure 3.12b shows the Rietveld refinement of the observed intermediate phase of composition $Li_{0.67}Mn_2O_4$. As previously mentioned, several authors proposed an ordered intermediate phase $Li_{0.5}Mn_2O_4$ to be responsible for the separation of the two electrochemical features at 4.05 V and 4.15 V vs. Li^+/Li[22,198]. However, that phase has not been observed yet and its existence was put in doubt by Liu et al.[196] thanks to *ex situ* NPD that did not reveal any superstructure peak related to Li^+ ordering. This was confirmed later on by Baehtz et al.[197]. However NPD is not the most suited technique to observe superstructure peaks of extremely weak intensity, especially if, as we will discuss later, they mainly rise from cation charge ordering. Based on our *in situ* NPD data, we cannot argue with the existing literature on this point. The fact that we observe an intermediate phase at composition $Li_{0.67}Mn_2O_4$ is largely caused by the inactive part of the electrode. It can be seen in Figure 3.10 that the range where this single-phase intermediate composition is present appears to be $0.68 < x < 0.53$, but when this is corrected for the inactive part of the electrode, it becomes $0.62 < x < 0.44$, consistent with an intermediate phase around Li = 0.5. The presence of this side phase also reduces the precision in the lithium content determination due to peaks' overlap, possibly leading to an overestimation at $Li_{0.67}Mn_2O_4$. A high-angular resolution synchrotron XRPD experiment conducted *operando* is reported in the next paragraph to lift the doubt on such a long-unanswered question.

Lithium deintercalation from $LiMn_2O_4$ proceeds finally through a second well-established biphasic reaction, corresponding to the intense peak in the derivative curve at 4.15 V vs. Li^+/Li. In this case the reaction is clear and much slower than the previous one, involving a final phase with parameters quite different from the initial ones and a large miscibility gap $\Delta x \approx 0.34$ (0.4 when corrected for the unreacted part of the electrode, Figure 3.10). Indeed, the third phase (3) appears with a_3 = 8.076(3) Å and Li_{8a} SOF $\approx$ 0.2 and it evolves to final values a_3 = 8.0442(3) Å and Li_{8a} SOF = 0.10(21). The value of the unit-cell parameter of the final member confirms the presence of remaining lithium in the structure (λ-MnO_2

was reported to be cubic with a = 8.03 Å [194]). For this sample the volume change in the second biphasic reaction is significant, namely from 542.54(5) $Å^3$ to 526.73(5) $Å^3$ ($\Delta V/V$ = 2.9% for $\Delta x \approx 0.34$ - 0.4, approximately twice the one of sample S2). It should be noted that the a_3 value at the end of charge (a_3 = 8.0442(3) Å) is very close to a = 8.03 Å expected for λ-MnO_2; besides, the fact that such value is not exactly reached confirms the presence of some residual lithium in tetrahedral sites, as obtained by Rietveld refinements. The refinement of the final phase is shown in Figure 3.12c.

3.3 Complementing NPD by *operando* synchrotron XRPD

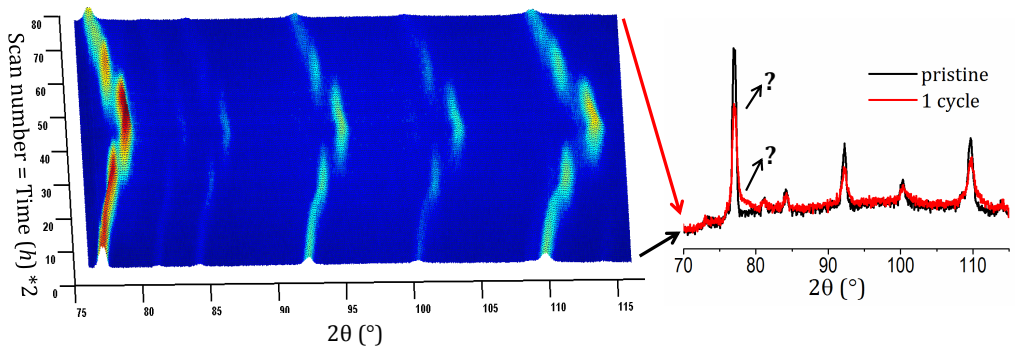

Figure 3.14: 3D representation of a full cycle (charge + discharge) of $LiMn_2O_4$ observed by *operando* NPD. On the right the Bragg peaks' loss of intensity and chenge in shape during the 1^{st} cycle is shown.

As discussed at the beginning of this chapter, it has been widely shown that stoichiometric $LiMn_2O_4$ suffers of capacity fading upon cycling. The reasons for this have been mostly understood and discussed. During the first series of experiments we only looked at Li^+ deintercalation (i.e. the charge, half a cycle) as described above. We then decided, for $LiMn_2O_4$, to measure a full cycle with both NPD and synchrotron XRPD to understand whether we could see any sign pointing towards an irreversible structural modification of the structure already present at the first cycle. Moreover, we hoped that the higher angular and intensity resolution available at synchrotron facilities could help us answer the question of the $Li_{0.5}Mn_2O_4$ phase. For the experiment with neutrons, we basically repeated the one described in paragraph 3.2.3, cycling our battery during charge and discharge at C/20 rate. As we clearly showed there that our electrodes made only with AM + Csp leave a small but significant unreacting part, in this electrode preparation we added PTFE as binder to insure better homogeneity. This allowed us to confirm the results previously obtained

upon charge, in the absence this time of the pristine-like phase. A qualitative view of the experiment can be seen in Figure 3.14. Three observations are striking when looking at the full cycle:

- The phase diagram in terms of position and duration of the biphasic domains presents differences between charge and discharge.
- At the end of discharge all Bragg reflections significantly lose intensity with respect to their initial value. As we will show in the following, this is due to the peaks becoming more lorentzian, but in this *operando* experiment the background is too important to deduce such a behaviour.
- Great difficulty is found while trying to use Rietveld refinement to fit these data of charge+discharge, especially in terms of peaks' shape.

This last point, in particular, prevented us from completing a meaningful quantitative analysis of the full-cycle data.

3.3.1 $LiMn_2O_4$ studied by *operando* synchrotron XRPD

Intrigued by the questions left unanswered during our full-cycle *operando* NPD study, we decided to reinvestigate the same system using the high angular resolution offered by

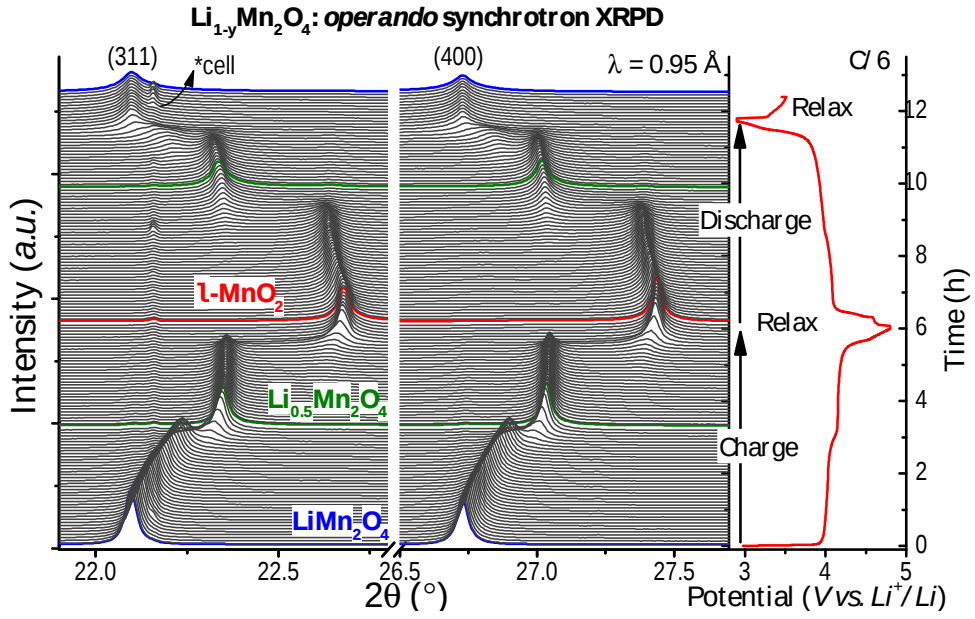

Figure 3.15: Evolution of (311) and (400) Bragg reflections of $LiMn_2O_4$ during a full electrochemical cycle of a $LiMn_2O_4$//Li half cell, observed by *operando* synchrotron XRPD.

operando synchrotron X-Ray powder diffraction at MSPD (ALBA)[119]. The same electrode formulation was used, including the PTFE binder. The battery was mounted in our *in situ* cell for experiments at synchrotron radiation facilities, which was described in the introduction[97]. Galvanostatic cycling was performed at C/6 rate in the extended voltage range between 3 V and 4.8 V vs. Li^+/Li, while measuring XRPD patterns (in transmission) every 5 minutes continuously. The results of this *operando* experiment are shown in Figure 3.15. During charge one clearly notices an initial solid solution region, extending to $Li_{\approx 0.6}Mn_2O_4$, followed by two topotactic biphasic reactions. This allowed us to isolate an intermediate cubic phase of cell parameter a = 8.1529(1) Å (around $Li_{0.5}Mn_2O_4$) and a final one, known as λ-MnO_2, of cell parameter a = 8.0363(1) Å (shown in Figure 3.16). Upon discharge the process is reversed, but not fully reversible. The lithiation, almost complete, could proceed to composition $Li_{0.95}Mn_2O_4$ with a = 8.2435(1) Å, a value extremely close to the pristine one (a = 8.2451(1) Å). However, importantly, the solid solution region is now found to be associated with the Li-poor phase λ-MnO_2 and not with the Li-rich one as was during charge (Figure 3.15).

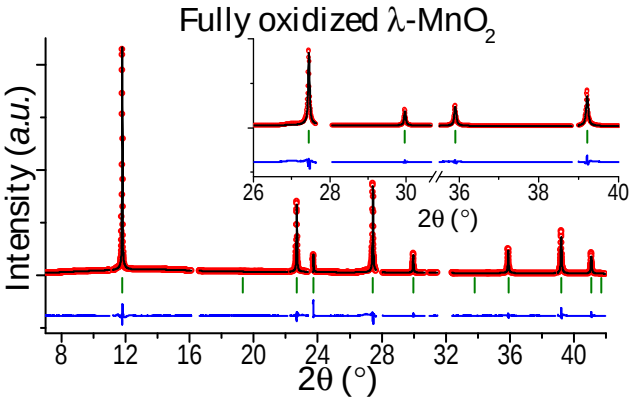

Figure 3.16: Rietveld refinements of *operando* synchrotron XRPD of the end member λ-MnO_2 obtained after a full galvanostatic charge of the $LiMn_2O_4$//Li half cell. Excluded regions account for reflections coming from the cell, metallic Li, PTFE binder, beryllium windows and their protective aluminum layer.

1^{st} cycle irreversibility

Figure 3.17 compares the Bragg peaks in the pristine state with their counterpart after one and two *in situ* cycles had been carried out. One immediately notices a strong peaks' shape evolution upon the first cycle, while almost no evolution is observed between the 1^{st} one and the 2^{nd} one: the shapes of diffracted peaks become significantly more Lorentzian

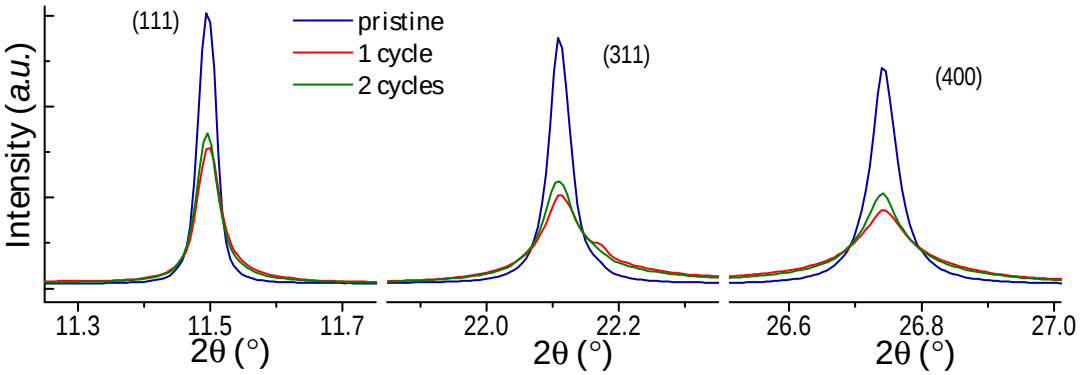

Figure 3.17: (111), (311) and (400) Bragg reflections of $LiMn_2O_4$ in the pristine state and after the 1^{st} and 2^{nd} electrochemical cycle from *operando* synchrotron XRPD data. The curve after 1 cycle (red) shows a shoulder on the right side of the (311) peak, due to a reflection of the experimental setup of variable intensity (also seen in Figure 3.15). Note that the cell rotates on its axis during the measure to obtain a better powder averaging.

and a careful observation of the diffraction scans reveals a continuous broadening, starting from the very first scans. Therefore the phenomenon is not related to some reaction happening at high voltage, but it proceeds continuously throughout charge and discharge. The broadening we observe here, created during the first cycle, is not a simple increase in peak's FWHM. On the contrary, while the FWHM is rather constant, the peak shape after the first electrochemical cycle tends towards a pure Lorentzian function. It is clearly evidenced in Figure 3.17 by the occurrence of extended tails at the base of Bragg reflections and the effect is so significant that the observed peaks can no longer be modelled using a single mathematical function. They have to be described as so-called super-Lorentzian shaped, i.e. two Lorentzian peaks, one narrow and one very broad, centered at the same angular position[251] (Figure 3.18). From the physical point of view this means that we suggest the presence of several "phases", very close in composition (and cell parameters, etc) but with a bimodal distribution of coherent domain sizes. The two Lorentzian peaks will then give the two most representative domain sizes. A slight asymmetry is also observed in Figure 3.17. This indicates that, as a secondary effect, such domains different in size might also have a slightly different composition than the nominal one (of course with a preference for being under-lithiated, since upon cycling Li^+ is extracted and then almost completely reinserted). Note that we say this effect is secondary because it cannot in any way contribute at creating the tails present on the left side of the Bragg peaks, because a different composition in this case would mean that we reached $Li_xMn_2O_4$ with x>1, in contrast with our electrochemical data. For these reasons (and because it proved very

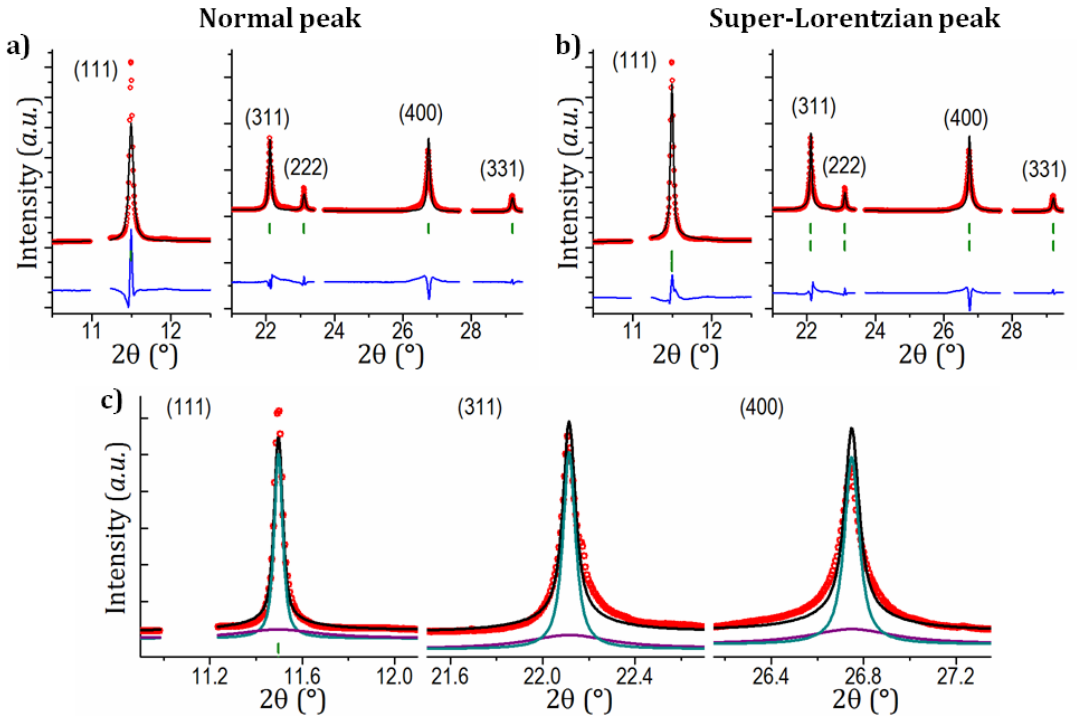

Figure 3.18: Rietveld refinement of synchrotron XRPD data collected *operando* on $LiMn_2O_4$ at the end of the 1^{st} complete galvanostatic cycle. a) Peak shape modeled as a single pseudo-Voigt function. b) Peak shape modeled as super-Lorentzian, i.e. two pseudo-voigdt centered at the same angular position. In this second case the fit improves, especially on the (111) reflection. c)Rietveld refinement of case b) with the highlighted contribution of the narrow and large peaks of the super-Lorentzian.

hard to be included in the data analysis due to limitations in the stability of the Rietveld refinement) this asymmetry was not taken into account.

From a practical point of view, the "two phases" we used in the Rietveld refinements only differ by their isotropic size parameter. One finds that in the pristine state there is essentially no broadening due to size effects (obtained particle size $>$ 100 nm), while after 1 cycle the extremes of the domain size distribution are well identified: one is pristine-like (not broadened) and a second one, from the very broad peaks' tails, corresponds to an apparent domain size of 9.2(1) nm. The "two phases" appear to be in a ≈2:1 ratio and we can conclude that at the end of the 1^{st} cycle about 66% of $LiMn_2O_4$ maintains the same crystallinity, while the other 34% has a significantly reduced coherent domain size, decreasing down to 9.2(1) nm. If the same refinement is performed in the middle of the first cycle, i.e. at the end of charge, one similarly finds that the fraction with reduced domain size is already of 20%, for a domain size which is similar, i.e. 9.9(1) nm. Whether this effect is due to the creation of several small domains within the particles or at the interfacial

region is an issue that cannot be addressed by XRPD, but will be further investigated using TEM. Note also the limits of our analysis in this case, since the complicated peak shapes, combined with peaks asymmetry and additional spurious peaks coming from the setup, made Rietveld refinement only partially satisfactory (Figure 3.18c). A more detailed knowledge of the causes of the peaks becoming Lorentzian will help finding a more suitable model to explain this behaviour.

Li^+ and charge ordering in $Li_{0.5}Mn_2O_4$

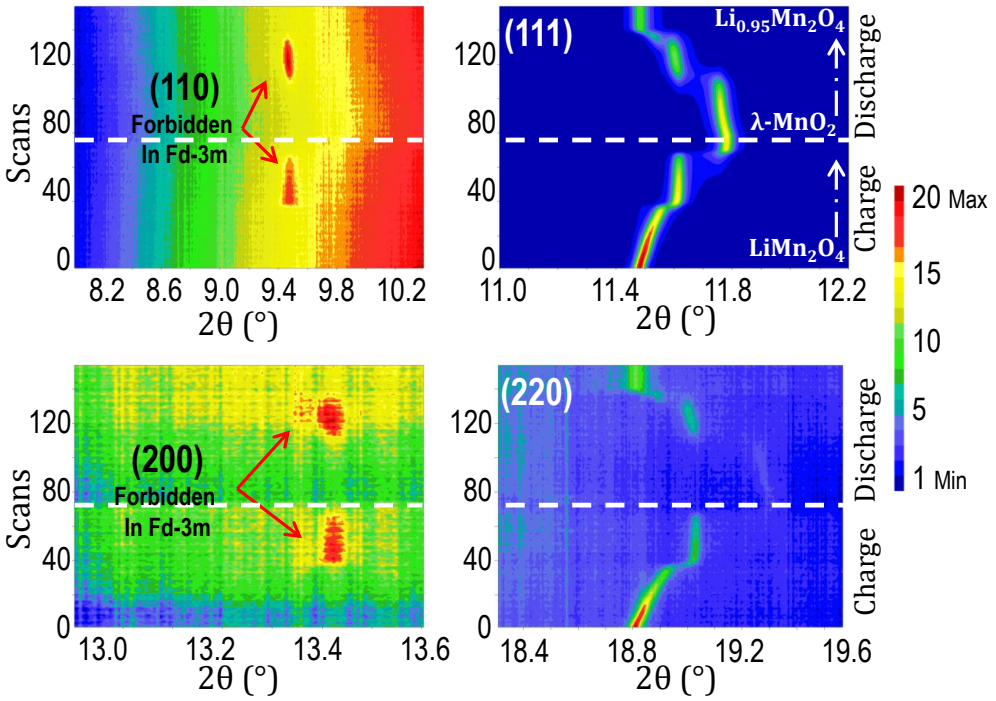

Figure 3.19: Contour plots of significant Bragg reflections observed upon electrochemical cycling of $LiMn_2O_4$ from *operando* synchrotron XRPD. On the right, the evolution of the most intense peak (111) is reported, together with the (220) one, both always present during the experiment (although (220) almost loses all its intensity in the delithiated phase). On the left, (110) and (200) reflections are observed for the intermediate phase only, both during charge and discharge, implying a symmetry reduction.

One matter that can be addressed by our *operando* XRPD experiment is the nature of the intermediate $Li_{0.5}Mn_2O_4$ phase. Two intense Bragg peaks were already shown in Figure 3.15, but even more important clues about the existence of a new phase lie in the observation of weak reflections, as shown in Figure 3.19. Several points deserve to be highlighted:

- The (111) diffracted peak is the most intense one for spinels, due to the high packing

density of Mn cations in this family of planes. It shows the same behaviour already observed for (311) and (400) in Figure 3.15, i.e. only partial reversibility.

- The (220) reflection is interesting as it is strongly correlated in spinels with the scattering power of the atom in the tetrahedral site 8a [184]. In this case this atom is lithium, meaning that the reflection is already very weak in the pristine state and that it totally loses its intensity while approaching the λ-MnO_2 phase, to partially regain it afterwards when lithium is reinserted in the site.

- The most important observation here is the presence of two reflections, (110) and (200), in the middle of charge and discharge, i.e. around the composition $Li_{0.5}Mn_2O_4$.

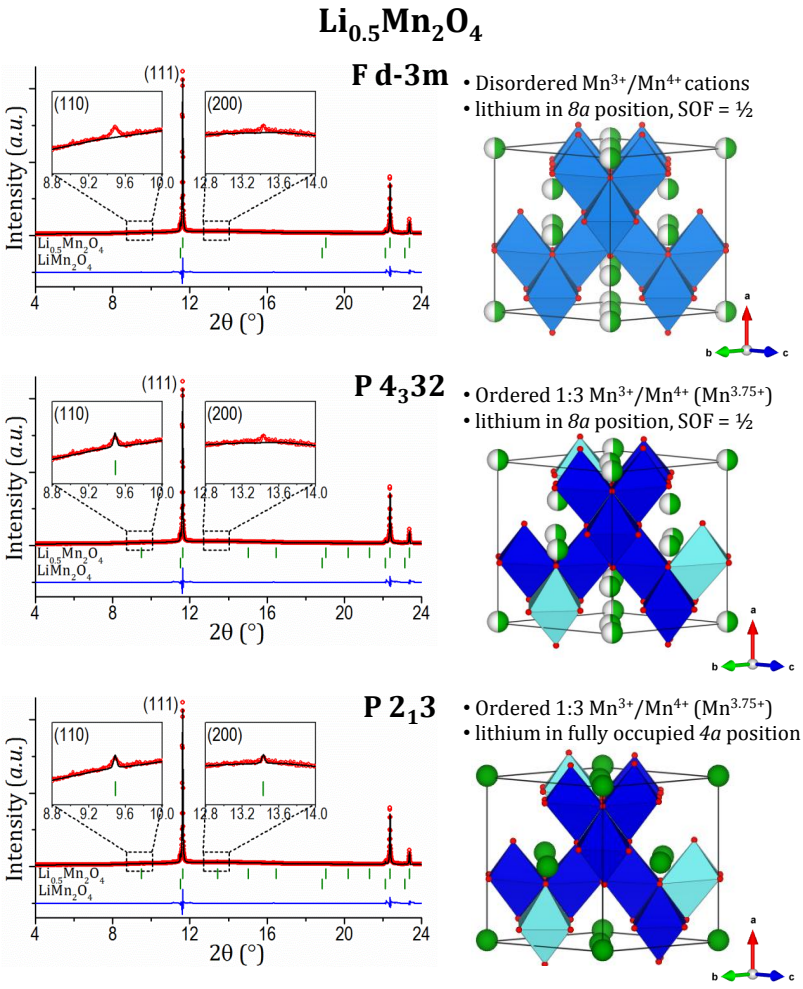

Figure 3.20: Rietveld refinements of *operando* synchrotron XRPD data for the phase $Li_{0.5}Mn_2O_4$ obtained during galvanostatic cycling of $LiMn_2O_4$. Top: pristine-like space group $Fd\bar{3}m$. Middle: Cation-ordered $P4_332$. Bottom: Cation- and lithium/vacancy-ordered $P2_13$. Respective crystal structures are displayed. Insets focus on 8.8°-10.0° and 12.8°-14.0° angular ranges. A secondary pristine-$LiMn_2O_4$-like phase is added in the refinements (≈3 wt%) because of the dynamic *operando* conditions.

These reflections are forbidden in the Fd$\bar{3}$m space group of the pristine spinel. They are observed here for the first time and they are extremely important because they hold the key to reveal and understand the symmetry/ordering within $Li_{0.5}Mn_2O_4$.

The presence of the (110) reflection can be understood by using an analogy with another spinel-based material, $LiNi^{2+}_{0.5}Mn^{4+}_{1.5}O_4$. In this composition, a classical cation-disordered structure can turn into an ordered one where the 1 Ni^{2+} : 3 Mn^{4+} ratio leads to a reduction in space group symmetry, from Fd$\bar{3}$m to $P4_332$, hence allowing the presence of the (110) reflection[239,252,253]. It is interesting to notice that $Li_{0.5}Mn_2O_4$ can indeed be written as $Li_{0.5}Mn^{3+}_{0.5}Mn^{4+}_{1.5}O_4$, showing the same cation ratio (1:3) as in $LiNi_{0.5}Mn_{1.5}O_4$. We applied this space group reduction of $LiNi_{0.5}Mn_{1.5}O_4$ (ICSD 70045[254]) to $Li_{0.5}Mn_2O_4$. The results of the structural Rietveld refinements displayed in Figure 3.20 show how the (110) reflection is nicely fitted taking into account the space group $P4_332$, enlightening for the first time an ordering between Mn^{3+} and Mn^{4+} cations in $Li_{0.5}Mn^{3+}_{0.5}Mn^{4+}_{1.5}O_4$ during charge and discharge of $LiMn_2O_4$, whenever they reach a ratio of 1:3. While these refinements perfectly account for the existence of the (110) Bragg peak, they still maintain the (200) one as forbidden. We hence envisaged possible Li/vacancy ordering at the composition

Table 3.2: Structural parameters obtained from Rietveld refinement of $Li_{0.5}Mn_2O_4$. (-) indicates that a value has not been refined in $P2_13$, but it was kept as refined in the $P4_332$ space group.

$Li_{0.5}Mn_2O_4$

S.G. $P2_13$; Z=8

a = b = c = 8.1529(1) Å; R_{wp} = 18.9%;
V = 541.92(1) Å^3; V/Z = 67.74(1) Å^3. R_B = 8.06%; χ^2 = 60.2
Main $Li_{0.5}Mn_2O_4$ phase = 96(1) wt%;
Secondary $LiMn_2O_4$-like phase = 3.3(2) wt% (Fd$\bar{3}$m, a = 8.2390(4) Å)

Atomic Parameters

Atoms	Wyckoff	Atomic Positions			SOF	B_{iso}
		x/a	y/b	z/c		
Mn1	4a	0.625(7)	0.625(7)	0.625(7)	1	2.6(-)
Mn2	12b	0.128(6)	0.380(4)	-0.127(4)	1	2.6(-)
O(1)	4a	0.387(21)	0.387(21)	0.387(21)	1	2.3(-)
O(2)	12b	0.142(25)	-0.135(16)	0.136(19)	1	2.3(-)
O(3)	4a	0.869(18)	0.869(18)	0.869(18)	1	2.3(-)
O(4)	12b	0.104(19)	0.119(16)	0.396(17)	1	2.3(-)
Li(1)	4a	0.011(-)	0.011(-)	0.011(-)	1	1.0(-)

$Li_{0.5}Mn^{3+}_{0.5}Mn^{4+}_{1.5}O_4$ using a further space group symmetry reduction. In fact, in $P4_332$ all lithium ions are placed in the same 8a site which must therefore be only half occupied to respect the stoichiometry. Among the cubic subgroups of $P4_332$, $P2_13$ allows to maintain the 1:3 cations ratio, while reducing the multiplicity of the tetrahedral lithium site to 4 in such a way that that newly defined lithium site (4a) is full whereas that corresponding to the vacancies is obviously empty. In the $P2_13$ space group, systematic conditions for extinctions allow the presence of both the (110) and (200) reflections, as illustrated in Figure 3.20.

Table 3.3: Significant bond length distances (Å) obtained from Rietveld refinement of $Li_{0.5}Mn_2O_4$ in the $P2_13$ space group, compared to those obtained for the $P4_332$ one. Error bars are reported as 3σ. Polyhedral distortion is calculated as $\Delta = 1/N \sum_i (d_i - \langle d \rangle / \langle d \rangle)^2$, bond valences as reported in [255].

$Li_{0.5}Mn_2O_4$ ($P2_13$ vs. $P4_332$)

		O1	O2	O3	O4	BVS	Distort.
Mn(1)	$P2_13$	-	1.94(15) x3		2.01(15) x3	3.3(6)	2.9E-4
	$P4_332$	-	1.99(4) x6		-	3.2(2)	0.001E-4
Mn(2)	$P2_13$	1.91(18)	1.94(18) x2	1.97(15)	1.90(15) x2	3.8(6)	2E-4
	$P4_332$	1.92(7) x2	1.94(5) x2 1.90(4) x2	-	-	3.8(2)	0.839E-4
Li(1)	$P2_13$	-	1.90(18) x3	2.00(18)	-	1.2(3)	6E-4
	$P4_332$	2.08(7)	1.92(4) x3	-	-	1.07(7)	11E-4

Table 3.2 and Table 3.3 gather and compare the structural informations obtained for $Li_{0.5}Mn_2O_4$ in both the $P4_332$ and $P2_13$ space groups while the arrangements of cations and lithium/vacancy ordered distributions in $Li_{0.5}Mn_2O_4$ are displayed in Figure 3.21. As already well documented in the literature, the oxygen ccp-based spinel structure can be described as a stacking of two types of cations layers, referred to as $[Oh]_3$ (Mn-rich, with 3 octahedral (Oh) sites occupied and 1 Oh empty) and $[Td]_2[Oh]$ (Li-rich, with 2 tetrahedral (Td) sites occupied, 1 Oh occupied and 3 Oh vacant), perpendicular to the $[111]_{cubic}$ direction. Importantly, Mn^{3+} and Mn^{4+} are present in the two types of layers (in an ordered fashion respecting in both cases the 1:3 ratio) and are also ordered along the [111] direction. The red circles in Figure 3.21 show how layers are stacked: a Mn^{3+} cation in the Li-rich layer is always on top of 3 Mn^{4+} cations in the Mn-rich layer. Even though the obtained values of Mn-O bond lengths gathered in Table 3.3 (for $P2_13$) show significant error bars, the environments around Mn(2) (Mn^{4+}, with most Mn-O bonds in the range

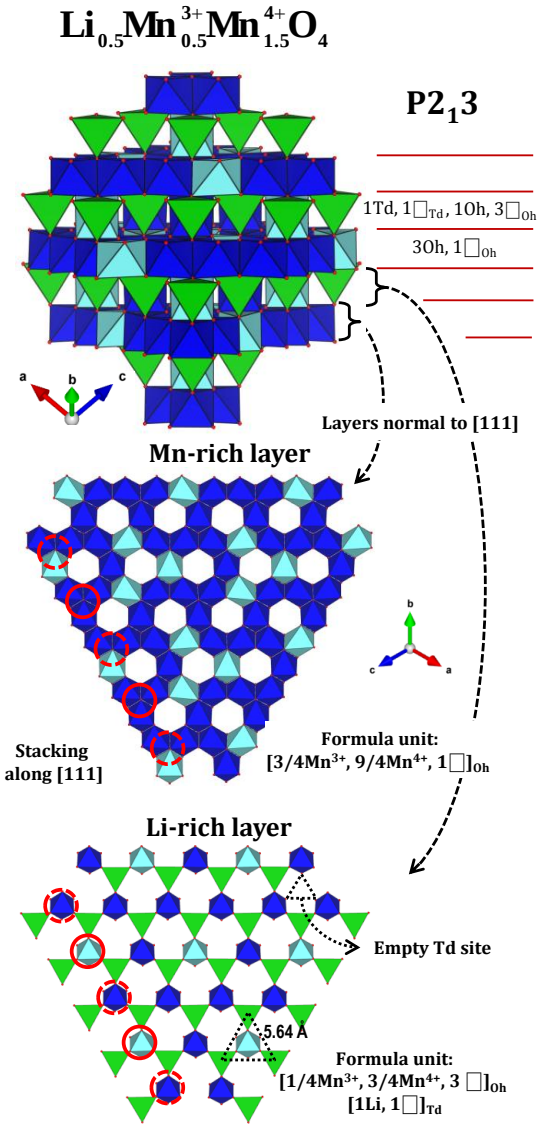

Figure 3.21: Representation of $Li_{0.5}Mn_2O_4$ along the [111] direction, showing oxygen layers and the alternating manganese-rich and lithium-rich layers. Dark blue octahedra represent Mn^{4+}, light blue ones Mn^{3+} and green tetrahedra lithium. At the bottom, isolated Mn-rich and Li-rich layers, seen normal to [111]. The full/dashed red circles are a visual guide for the vertical stacking of layers, namely the Li-rich one can be shifted to the top until the circles coincide.

1.90 - 1.94 Å) and Mn(1) (Mn^{3+}, with longer Mn-O bonds in the range 1.94 - 2.01 Å) clearly enlighten the presence of two Mn environments, further supported by bond valence sum calculations (Figure 3.22). It is noteworthy that this bonds' distribution around Mn(1) (3+3) is not compatible with a "classical" Jahn-Teller distortion of the Mn^{3+} cation (4+2), that one could expect. First-principles calculations (applied to $Li_2Mn_2O_4$)[198] indicated that a compression of the Mn^{3+}-O bond can lead to a favorable low-spin configuration,

where the eg electron is instead placed as the 4th electron in the t_{2g} energy levels (crystal field energy lower than exchange energy). This could be the case here because of the constraints applied by surrounding Mn^{4+} cations on a central Mn^{3+} one, possibly explaining the missing Jahn-Teller distortion. An analogous effect had been for instance observed for Ni^{3+} ($3d^7$) cations in $LiNi^{3+}_{0.3}Co^{3+}_{0.7}O_2$ [256].

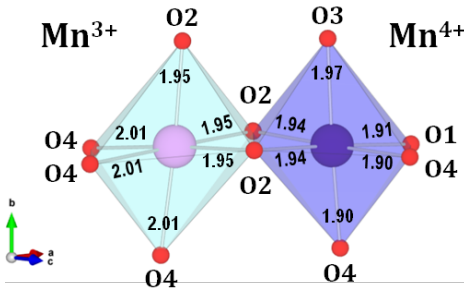

Figure 3.22: Bond-lengths of Mn^{3+}-O and Mn^{4+}-O octahedra.

As previously mentioned, the $P2_13$ space group is well-suited to support lithium/vacancy ordering. Lithium is located in the 8a site in $Fd\bar{3}m$ and $P4_332$ space groups, while it is located in the 4a one in $P2_13$. This site, once filled, represents only half of those partially occupied within the previous space groups, and it satisfies the stoichiometry of $Li_{0.5}Mn_2O_4$. This ordering scheme is the same one that was predicted by Van der Ven et al. through computational methods [198], with lithium and vacancies alternated along the [110] direction (as can be seen at the bottom of Figure 3.20). However, *a priori*, the distribution of lithium and vacancies could be reversed (translation by 3/4, 1/4, 3/4) and we cannot determine yet any preference for one or the other lithium/vacancy ordering. Additional considerations regarding the possible minimization of electrostatic repulsions fail because for both lithium/vacancy distributions lithium ions have in their vicinity (0 - 3.5 Å) 12 manganese cations of which 3 Mn^{3+} and 9 Mn^{4+} with similar bond-lengths. We left the Li position constant to the value reported in the literature for $LiNi_{0.5}Mn_{1.5}O_4$, knowing that x = y = z = 0.011 in $P4_332$ is very close to x = y = z = 0 in $Fd\bar{3}m$ of the classic spinel.

3.4 *Operando* NPD of high-voltage $LiNi_{0.4}Mn_{1.6}O_4$

In the introduction of this chapter it was discussed how the substitution of different transition metals TM for Mn in $Li(TM)_xMn_{2-x}O_4$ is an interesting path to synthesize spinel materials operating as high-voltage positive electrodes (often around 5 V). One of the most common and widely studied choices is TM = Ni, leading to a solid solution of composition

$LiNi_xMn_{2-x}O_4$ in the range $0 \leq x \leq 0.5$. The end member x = 0.5 ($LiNi_{0.5}Mn_{1.5}O_4$) was first synthesized and recognized for its electrochemical and crystallographic properties around 1996[24,25,232]. Manganese is found to be completely oxidized (Mn^{4+}) and the electrochemical activity is thus only brought by the nickel cations, exploiting oxidation states from Ni^{2+} to Ni^{4+}. This gives a gravimetric capacity of 147 mAh/g for $LiNi_{0.5}Mn_{1.5}O_4$ at $\approx$ 5 V potential vs. Li^+/Li, thus delivering a high energy density[24,25,232,233] (Figure 3.23). Also, the fact of avoiding the presence of any Mn^{3+} is an advantage, as previously dis-

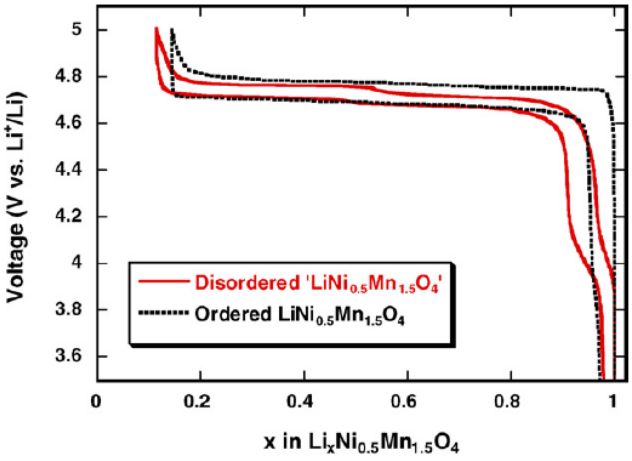

Figure 3.23: Potential-composition profiles of ordered and disordered $LiNi_{0.5}Mn_{1.5}O_4$ spinel oxide vs. metallic lithium, obtained in galvanostatic mode at C/5 rate (for each material, the 10th cycle is reported). Reprinted from[237].

cussed in the case of $LiMn_2O_4$. In principle it is also possible to intercalate a second Li ion, resulting in $Li_2Ni_{0.5}Mn_{1.5}O_4$ through a reaction at 3 V vs. Li^+/Li, but in this case Mn^{3+} is involved. Several studies were published in recent years, dealing with the many aspects of the optimization and understanding of such a material[237,241,257–259]. From the crystallographic point of view $LiNi_{0.5}Mn_{1.5}O_4$ is analogous to $LiMn_2O_4$, crystallizing in the $Fd\bar{3}m$ space group and thus having Ni and Mn randomly distributed in the 16d crystallographic site. For certain synthesis conditions, the Ni/Mn ratio of 1:3 can lead to a reduction in symmetry to the cubic $P4_332$ space group, due to cations charge ordering[254]. This phase has however poorer transport properties than the cation-disordered $Fd\bar{3}m$ one[239,241,252–254] thus showing poorer electrochemical properties and not being interesting for applications (Figure 3.23). Regarding the lithium (de)intercalation reaction at 4.7 V, most studies reported on the presence of two topotactic two-phase transitions involving three cubic phases in the ordered spinels ($P4_332$). In the disordered one, the first of the two biphasic reaction is still present, but on a narrower miscibility gap, revealing a

clear influence of the cations distributions on the phase diagram and electrochemical properties of the material[241]. Note that the ordered spinel $LiNi_{0.5}Mn_{1.5}O_4$ therefore possesses a stable intermediate phase in the middle of (dis)charge, at composition $Li_{0.5}Ni_{0.5}Mn_{1.5}O_4$. This can be seen in the light of the ordering scheme that we showed in paragraph 3.3.1 for composition $Li_{0.5}Mn_2O_4$, found halfway through the charge of $LiMn_2O_4$. It is reasonable to propose an analogy between the two materials at 0.5 Li/f.u. In fact, $Li_{0.5}Mn_2O_4$ could be more properly written as $Li_{0.5}Mn^{3+}_{0.5}Mn^{4+}_{1.5}O_4$; in the same way, $Li_{0.5}Ni_{0.5}Mn_{1.5}O_4$ is $Li_{0.5}Ni^{3+}_{0.5}Mn^{4+}_{1.5}O_4$. Hence we think that the $P2_13$ space group is probably the correct representation also for the composition $Li_{0.5}Ni^{3+}_{0.5}Mn^{4+}_{1.5}O_4$, possessing the same 1:3 cations ratio and the same lithium/vacancy ratio as for $Li_{0.5}Mn_2O_4$, thus having the same ordering scheme and space group belonging. However, to the best of our knowledge this has not been shown yet.

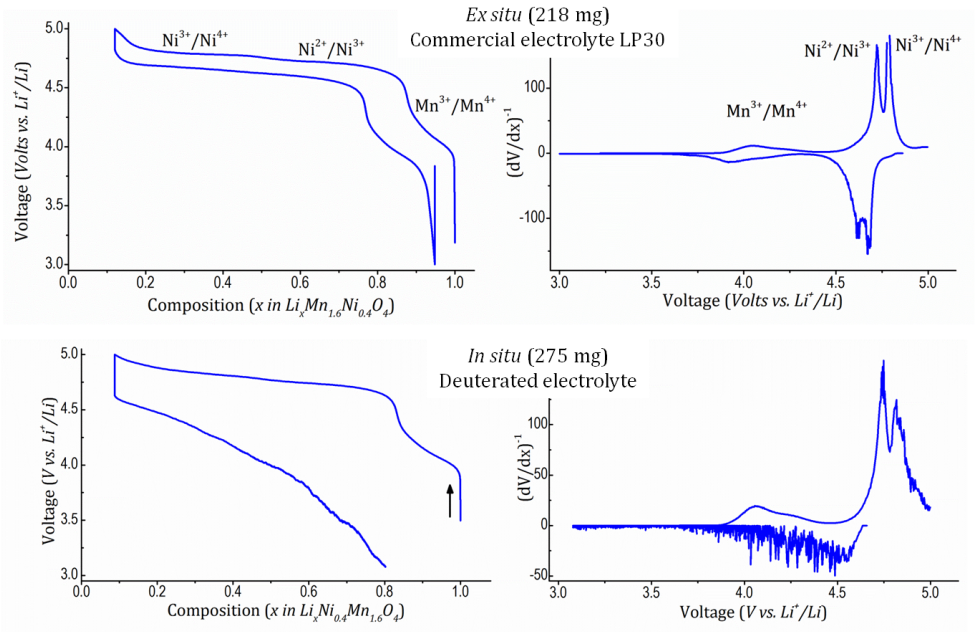

Figure 3.24: Voltage-composition profiles obtained for $LiNi_{0.4}Mn_{1.6}O_4$. Top figures show an *ex situ* galvanostatic cycle using commercial LP30 electrolyte. Bottom ones show galvanostatic cycling during the *operando* experiment. Inverse derivatives are shown on the right.

Compositions within the solid solution $LiNi_xMn_{2-x}O_4$ exhibit an increasing voltage upon lithium extraction when x increases, while the gravimetric capacity is reduced as Ni is heavier than Mn. A good trade-off is found for x = 0.4, i.e. for $LiNi_{0.4}Mn_{1.6}O_4$ (i.e. $LiNi^{2+}_{0.4}Mn^{3+}_{0.2}Mn^{4+}_{1.4}O_4$) now widely studied as a next-generation positive electrode material for Li-ion batteries[237,238,244,245]. The capacity originates for 20% from the Mn^{3+}/Mn^{4+} redox couple (around 4.2 V vs. Li^+/Li), while the remaining 80% is provided by the

Ni^{2+}/Ni^{3+} and Ni^{3+}/Ni^{4+} ones in equal amount at 4.7 V vs. Li^+/Li [237,243,260] (Figure 3.24). $LiNi_{0.4}Mn_{1.6}O_4$ exhibits low capacity fading upon cycling, high energy density and good rate capabilities, making it a more interesting choice than other compositions in the $LiNi_xMn_{2-x}O_4$ solid solution [12]. The mechanism of Li^+ deintercalation from $LiNi_{0.4}Mn_{1.6}O_4$ is described as a solid solution, followed by a biphasic reaction corresponding to the Ni^{3+}/Ni^{4+} redox couple. Namely it behaves as a cation-disordered $LiNi_{0.5}Mn_{1.5}O_4$ spinel where the first biphasic reaction has been completely suppressed [241]. To understand the mechanism behind such phase diagram and to get insight into the deintercalation reaction, we decided to observe it in real time using *operando* NPD. We studied a sample prepared at CEA-Liten (Grenoble) and our (Ti,Zr) electrochemical cell was used to cycle the material (a first charge followed by a discharge at C/20 rate) versus a lithium metal negative electrode, while NPD patterns were continuously acquired for 30 minutes each. Charging the material up to 5 V was challenging: normal electrolytes already tend to decompose/oxidize at such high potentials, and this is even clearer for our deuterated electrolyte which is not optimized for this purpose. The electrochemical data obtained during our experiment is showed in Figure 3.24. Upon charge we could obtain 91% of the theoretical capacity but the electrolyte was likely significantly damaged, indeed the voltage-composition profile upon subsequent discharge was badly impacted. The abundance of electrolyte allowed the reaction to proceed nonetheless and we could recover the composition $Li_{0.8}Ni_{0.4}Mn_{1.6}O_4$ at the end of the next discharge, giving meaningful results on the overall cycle. Figure 3.25 shows a complete representation of the experiment.

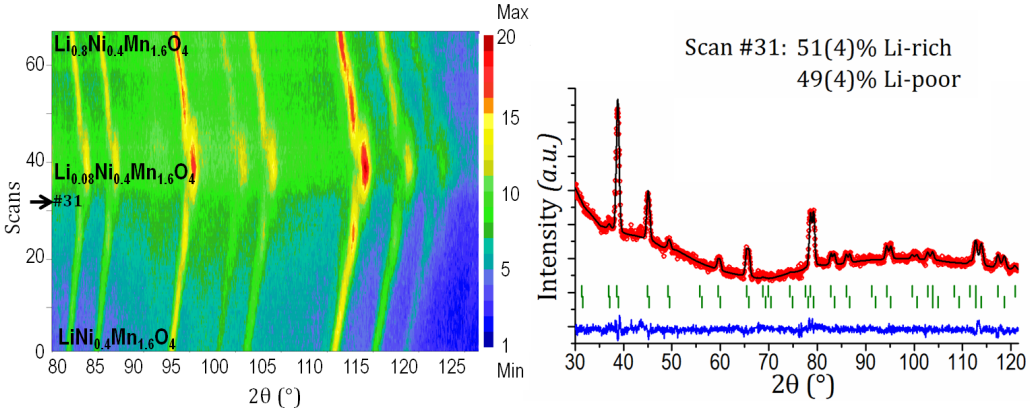

Figure 3.25: Left: Contour view on the 1^{st} cycle of the $LiNi_{0.4}Mn_{1.6}O_4$//Li cell observed by *operando* NPD in the 80°-130° angular range. Wavelength is $\lambda = 1.54$ Å. Right: Rietveld refinement of scan #31 during the biphasic reaction leading to Li-poor $Li_{0.08}Ni_{0.4}Mn_{1.6}O_4$.

Figure 3.26 gathers the evolution of the main structural parameters and features ob-

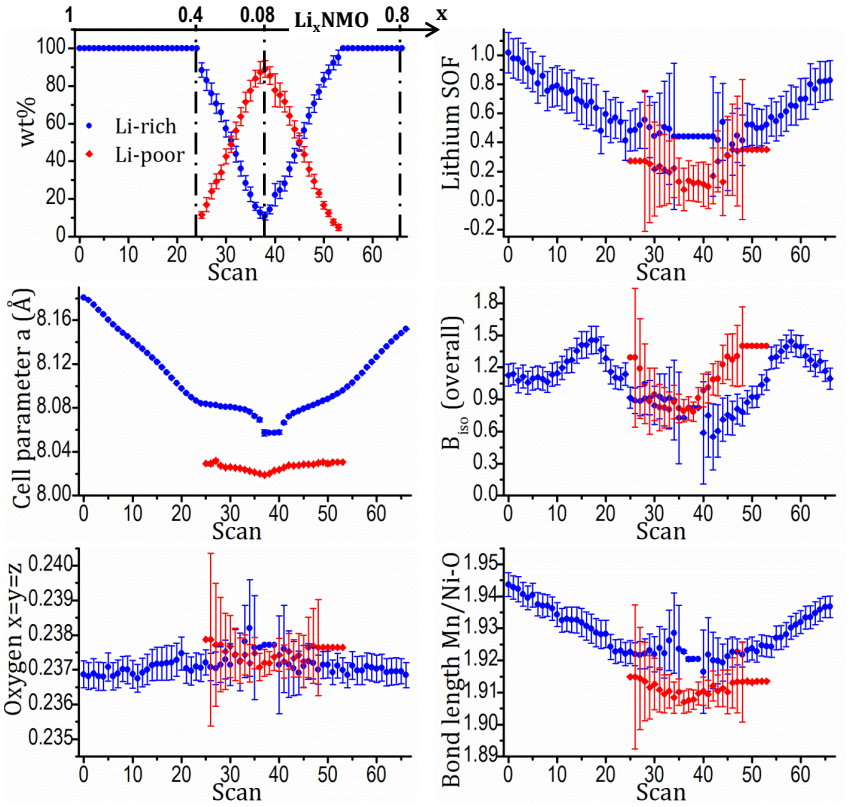

Figure 3.26: Structural parameters obtained from Rietveld refinements upon one cycle of Li^+ extraction/reinsertion from/into $LiNi_{0.4}Mn_{1.6}O_4$. Parameters that had been fixed do not show error bars.

served through the full electrochemical cycle, summarized as follows:

- We confirm the existence of a solid solution region followed by a biphasic reaction upon charge. The single-phase reaction proceeds up to the composition $Li_{0.40}Ni_{0.4}Mn_{1.6}O_4$ ($Li_{0.42(14)}Ni_{0.4}Mn_{1.6}O_4$ from Rietveld refinement), corresponding to the full oxidation of Mn^{3+} to Mn^{4+} and Ni^{2+} to Ni^{3+}. From this composition, Li^+ extraction occurs through a two-phase reaction involving the oxidized composition $Li_{0.08}Ni_{0.4}Mn_{1.6}O_4$ ($Li_{0.12(12)}Ni_{0.4}Mn_{1.6}O_4$ from Rietveld refinement). The two processes are reversible upon discharge.

- The Mn/Ni-O average bond lengths significantly decrease upon charge, consistent with the TM oxidation. Similarly to the case of $Li_{1+x}Mn_{2-x}O_4$ spinels, this results mainly from the decrease of the unit cell parameter value, while the oxygen fractional atomic coordinate inside the unit cell is poorly affected. The unit cell parameter contracts from 8.1807(7) Å to 8.057(3) Å in the Li-rich phase ($\Delta a/a = 1.5\%$), and from 8.029(2) Å to 8.0200(3) Å in the Li-poor phase ($\Delta a/a = 0.1\%$). This induces

Mn/Ni - O bonds to decrease from 1.944(4) Å to 1.923(14) Å in the Li-rich phase ($\Delta B/B$ = 1.0%), and from 1.915(22) Å to 1.908(3) Å in the Li-poor one ($\Delta B/B$ = 0.3%). Error bars fluctuate significantly, becoming large when phases are in minority (< 20 wt%).

- Lithium's SOF is observed to decrease. In the Li-rich solid solution it decreases down to 0.42(14) Li/f.u.. The Li-poor phase contains instead 0.12(12) Li/f.u. at the end of charge. About 10% of lithium seems thus to remain in the structure, consistent with the fact that 91% of the theoretical capacity is measured to be obtained from the electrochemical cycling. Thanks to the use of a PTFE binder in the electrode formulation the whole amount of spinel is electrochemically active (no residue of the pristine material is observed). Note thus that the unexploited capacity is simply due to the already encountered [197,261] difficulty in extracting the whole amount of lithium from spinels.

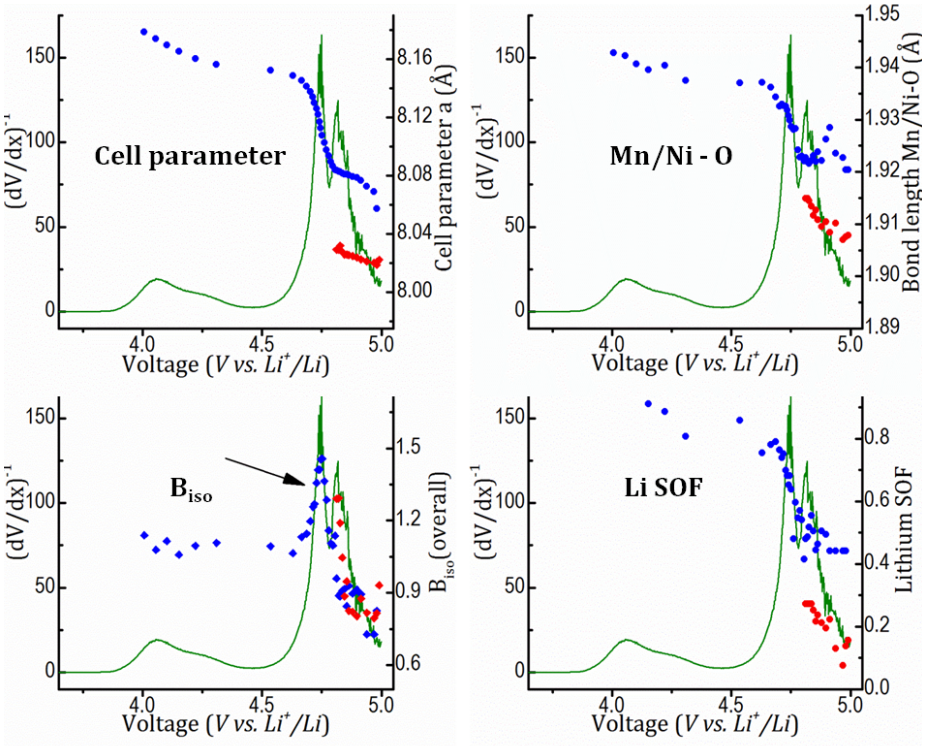

Figure 3.27: Structural parameters obtained from Rietveld refinements upon the charge of $LiNi_{0.4}Mn_{1.6}O_4$, plotted against Voltage and matched with the inverse derivative $(dV/dx)^{-1}$ of the electrochemical curve.

An interesting behaviour was observed upon close inspection of the Debye-Waller thermal parameters. In a first step, we considered B_{iso} to be the same for all atoms (refining

$B_{overall}$ in FullProf) to reduce the amount of free parameters. We observed that it remained almost constant during the electrochemical reaction of the Mn^{3+}/Mn^{4+} redox couple while a substantial and somehow unexpected increase (more than 50%) of $B_{overall}$ was found upon oxidation of Ni^{2+} into Ni^{3+}. During the Ni^{3+}/Ni^{4+} reaction, which is biphasic, $B_{overall}$ recovers a value that is for both phases similar but slightly lower than the initial one.

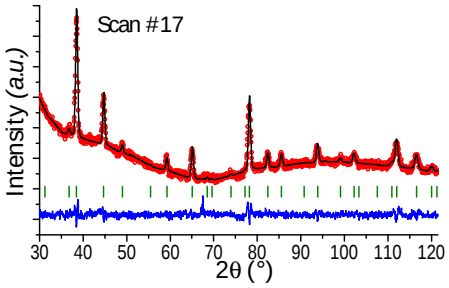

Figure 3.28: Rietveld refinement of scan #17 corresponding to the maximum value of the refined B_{iso}. Wavelength is λ = 1.54 Å. Composition is $Li_{0.68}Ni_{0.4}Mn_{1.6}O_4$ and the respective structural parameters are in Table 3.4.

Figure 3.27 shows the correlation between $B_{overall}$ and electrochemistry in this experiment, i.e. with the inverse differential curve $(dV/dx)^{-1}$: $B_{overall}$ increases exactly as Ni cations oxidize from 2+ to 3+. To understand the reason for such an unexpected observation, we subsequently refined the Debye-Waller factors separately, while leaving other parameters fixed. We could notice that the atom responsible for this increase is oxygen, and not lithium or the TMs. For example, for pattern #17 (showing the maximum value for $B_{overall}$ = 1.42(9)) the refinement led to B_{iso}(O) = 1.5(1) while B_{iso}(Ni/Mn) = 0.2(2) and B_{iso}(Li) = 0.9(5) (Figure 3.28). Ni^{3+} is a $4s^0 3d^7$ cation prone to Jahn-Teller distortion (low spin state $t_{2g}^6\ e_g^1$) but too diluted by Mn in this sample to create a cooperative effect and cause a cubic-to-tetragonal transition. The distortion of the $Ni^{3+}O_6$ octahedra occurs nonetheless at the local scale, with two long and four short Ni-O bonds (typically around 2.09 Å and 1.91 Å as observed in $LiNiO_2$ and in $LiNi_{1/2}Mn_{1/2}O_2$, vs. 1.90 Å for the six Mn-O bonds in $Mn^{4+}O_6$ [262,263]). As Ni and Mn occupy the same crystallographic site and are sitting at the centre of a regular octahedral MO_6 environment (as imposed by the cell description), the oxygen's B_{iso} hence provides an alternative to describe how the M-O distances are distributed at the local scale. Upon further lithium deintercalation from $LiNi_{0.4}Mn_{1.6}O_4$ the most oxidized composition is formed with all the transition metal ions at the Ni^{4+} or Mn^{4+} states and, as expected, with the smaller value observed for oxygen's B_{iso}. Indeed, Ni^{4+} and Mn^{4+} are $4s^0 3d^6$ and $4s^0 3d^3$ cations stable in regular

MO_6 octahedra with M-O bonds close to 1.90 Å: for that specific composition, the average M-O distance calculated from the Rietveld refinement is fully representative for the homogeneity of the M-O bonds formed at the local scale. We have thus shown that through the inspection of $B_{overall}$ (first) and oxygen's B_{iso} (afterwards) in the spinel structure, *operando* NPD during electrochemical cycling can be very sensitive to subtle changes in structural parameters and enlighten local structural features.

Table 3.4: Structural parameters obtained from Rietveld refinement of $Li_{0.68}Ni_{0.4}Mn_{1.6}O_4$ (scan #17).

$Li_{0.68}Ni_{0.4}Mn_{1.6}O_4$

S.G. $Fd\bar{3}m$; Z=8

a = b = c = 8.11124(4) Å;	R_{wp} = 23.7%;
V = 533.88(4) Å^3; V/Z = 66.74(4) Å^3.	R_B = 7.63%; χ^2 = 2.02

Atomic Parameters

Atoms	Wyckoff	Atomic Positions			SOF*	B_{iso}
		x/a	y/b	z/c		
Ni	16d	0	0	0	1	0.2(2)
Mn	16d	0	0	0	1	0.2(2)
O	32e	0.2373(5)	0.2373(5)	0.2373(5)	1	1.5(1)
Li	8a	3/8	3/8	3/8	0.68(15)	0.9(5)

*Occupancy and B_{iso} refined separately

3.5 Conclusions and perspectives

In this chapter we described how we used *operando* neutron powder diffraction (combined with synchrotron XRPD) to elucidate the deintercalation mechanism occurring in manganese spinels. We mainly dealt with $Li_{1+x}Mn_{2-x}O_4$ having different Li/Mn ratio. The three considered compositions are x = 0, x = 0.05 and x = 0.10. Upon charge, the general observed behavior is the expected shrinkage of the unit-cell during Li^+ extraction, but the involved mechanisms are highly dependent on the value of x. While the $Li_{1.10}Mn_{1.90}O_4$ sample follows a full solid solution between the beginning and the end of charge, stoichiometric $LiMn_2O_4$ shows a series of two biphasic processes, happening with different kinetics throughout charge. $Li_{1.05}Mn_{1.95}O_4$ shows an intermediate behavior between the two. Figure 3.29 summarizes these results, that further underline how the presence of lithium in the manganese crystallographic site deeply affects the nature of the deintercalation process. The parameters describing all involved phases have been analyzed by Rietveld refinement

with special attention to lithium's site occupancy factors and dynamics. Thanks to the quantitative nature of the obtained information, the relation of such parameters with the electrochemical features of spinel materials could be highlighted. These results complement others present in the literature to explain why $Li_{1.10}Mn_{1.90}O_4$ is a good candidate for long-lasting commercial Li-ion batteries, while $LiMn_2O_4$ is not. In fact, the former has a smaller volume change and a monophasic deintercalation mechanism, both resulting in less stress for the material upon cycling. Moreover, it contains less Mn^{3+}, which can lead to undesired disproportionation and formation of Mn^{2+} soluble species. We com-

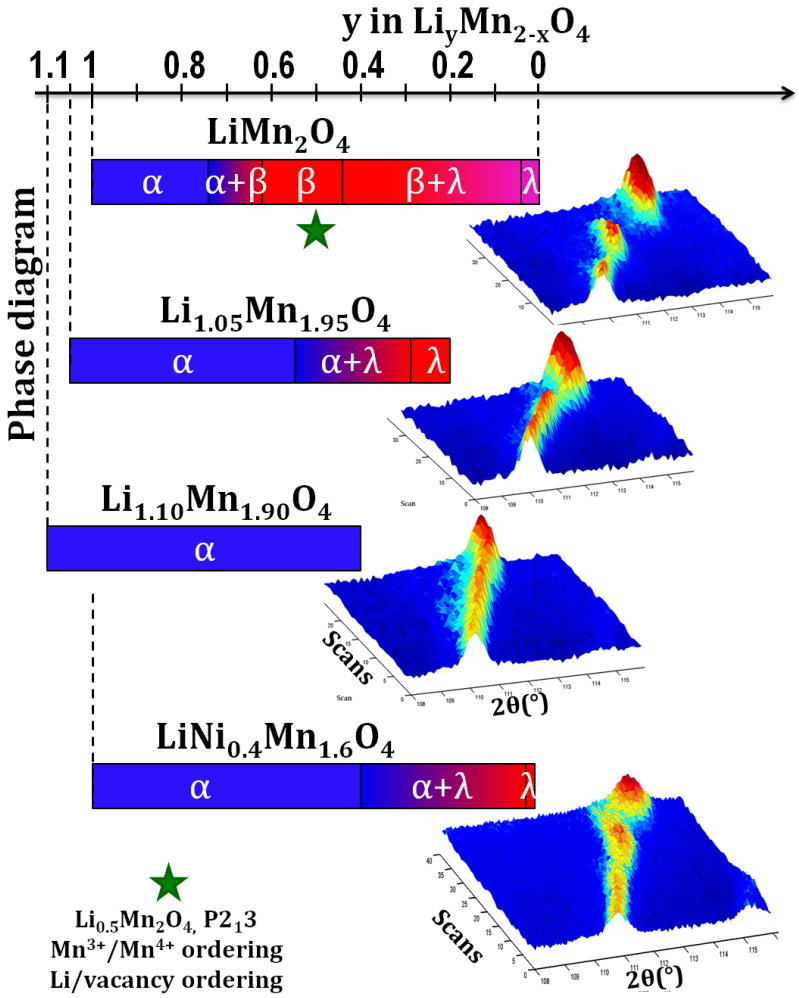

Figure 3.29: Summary of phase diagrams and neutron powder diffraction patterns obtained for $Li_{1+x}Mn_{2-x}O_4$ and $LiNi_{0.4}Mn_{1.6}O_4$.

plemented this *operando* NPD study using *operando* synchrotron XRPD, aiming for new insights brought by high-intensity and high-resolution measurements. We found indeed a 1^{st} cycle irreversibility present upon the cycling of $LiMn_2O_4$, further showing its inadequacy for industrial applications. On the other hand it is an extremely interesting material

from the crystallographic point of view, and we reported for the first time the structure of the phase $Li_{0.5}Mn_2O_4$. This composition observed in the middle of charge and discharge has been thought to possess lithium/vacancy ordering, responsible for the 0.1 V jump in the electrochemical curve of the material. However no proof of this had been found yet. We demonstrate here that $Li_{0.5}Mn_2O_4$ is more correctly written as $Li_{0.5}Mn^{3+}_{0.5}Mn^{4+}_{1.5}O_4$ because a charge ordering of Mn cations is present, as well as the Li/vacancy one. The cations ratio of 1:3 Mn^{3+}:Mn^{4+} leads to a first symmetry reduction from $Fd\bar{3}m$ to $P4_332$. Li/vacancy ordering along the [110] direction gives the final representation in the $P2_13$ space group, allowing to explain all weak Bragg reflections observed at this composition only. These observations open the door to a number of interesting questions, as to indentify the magnetic behaviour of Mn^{3+} (HS or LS?) or, importantly, to detail using SEM and TEM the irreversibility observed upon the 1^{st} electrochemical cycle. Finally, we studied one example among high-voltage spinels, namely the nickel-substituted $LiNi_{0.4}Mn_{1.6}O_4$. A full cycle was observed by *operando* NPD, giving insightful information about lithium extraction/reinsertion process, bond-lengths variations and, unexpectedly, Ni^{3+} Jahn-Teller distortion that could be observed because it correlates to the Debye-Waller factor of oxygen in the structure. This study is further proof that NPD allows us to be sensitive to all structural parameters of interest for electrode materials, and that it can be effective not only on the long (crystallographic) range, but on the local scale as well. The careful (and often tricky) analysis of SOFs and B_{iso} is a powerful tool, distinguishing neutrons from other techniques, and it will certainly be the key for future studies of electrode materials using *operando* NPD. One could imagine also other applications, as measuring the materials *in situ* (but not *operando*) in order to make longer acquisition with better statistics and then analyze the anisotropic Debye-Waller factors B_{aniso}. An electrochemical cell for NPD experiments at high temperature is also under development, as we envisage pushing forward our studies on thermal parameters, but also because we hope to extend our studies to all-solid-state lithium batteries, which cycle above 100 °C.

Chapter 4

Phase Diagram and Electrochemistry of Tavorite Li_xVPO_4O and Li_xVPO_4F $(0 \leq x \leq 2)$

4.1 Introduction

Polyanionic materials were already mentioned in the general introduction of this thesis as important positive electrodes for Li-ion batteries. The reasons that lead many researchers to investigate them despite their "weight penalty" have been already detailed. Within this wide family, some compositions are more promising than others : not only they offer very good energy densities during the exchange of 1 Li^+/f.u. (thus one electron/f.u., Figure 4.1), but they also pledge the exchange of a second Li^+/f.u.[10,11]. This would double the theoretical capacity and energy density, making a revolutionary material for the Li-ion battery technology. Several challenges must be faced to electrochemically cycle a material on 2 Li^+ cations per transition metal but the result would fully repay the effort. Compositions like $LiVPO_4O$ and $LiVPO_4F$ belong to these promising materials, and for this reason they have been studied at ICMCB and LRCS since 2011 (PhD thesis of J.M. Ateba Mba[5]). They are homeotypic, namely they belong to the same structural family, the Tavorite one, described in the next section. This chapter aims at reviewing most of Ateba Mba's work on the subject, to subsequently introduce the *ex situ*, *in situ* and *operando* X-Ray powder diffrac-

tion (XRPD) and neutron powder diffraction (NPD) studies we undertook to unravel the phase diagram of these fascinating materials. We used these techniques, often combined, to better understand lithium's (de)intercalation, hoping that this could lead in the near future to the possibility of exploiting the full potentialities of $LiVPO_4F$ and $LiVPO_4O$.

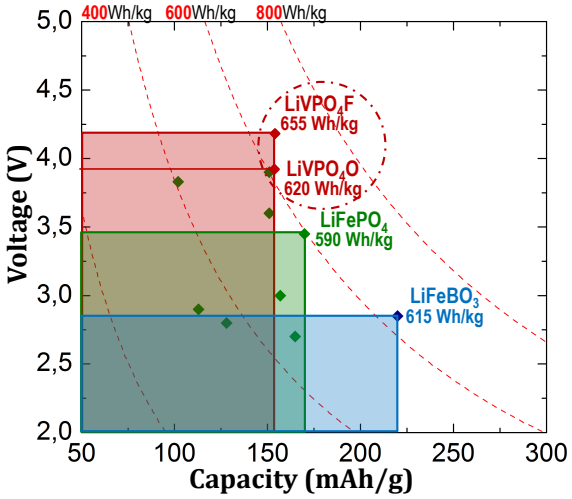

Figure 4.1: Voltage and theoretical capacity of $LiVPO_4O$ and $LiVPO_4F$, both exhibiting high gravimetric energy density. The plot only accounts for the extraction of 1 electron/f.u.. The energy density is double considering also the insertion of 1 Li^+ in their structure, leading to 2 electrons exchanged per f.u..

4.1.1 Tavorite compositions among polyanionic materials

The name Tavorite was introduced 67 years ago by Dr. Elysiário Távora Filho who first discovered it as a mineral[264]. The first study of the Tavorite mineral was performed by M.L. Lindberg et al.[265] who proposed the chemical formula of $LiFePO_4OH$, similar to the already known Montebrasite $LiAlPO_4OH$[266]. Note that the description of the Tavorite structure ($LiFePO_4OH$) is exactly the same as that of the Amblygonite structure, of chemical formula $LiAlPO_4F$. Amblygonite and Tavorite are therefore isostructural and both differ from the Montebrasite structure. Indeed the latter crystallizes in the monoclinic system with the space group of C2/c, while the Tavorite structure crystallizes in the triclinic system with the space group $P\bar{1}$.

The general chemical formula of the Tavorite family is $AMXO_4Y$ with A as the alkaline ion, M as a transition metal or earth-alkaline metal, X as phosphorus or sulfur and Y as halide, hydroxide, oxygen, or a mixed halide/hydroxide (Figure 4.2). V.I. Simonov and N.V. Belov[268] first described the Tavorite's crystal structure, built on MO_4Y_2 octahe-

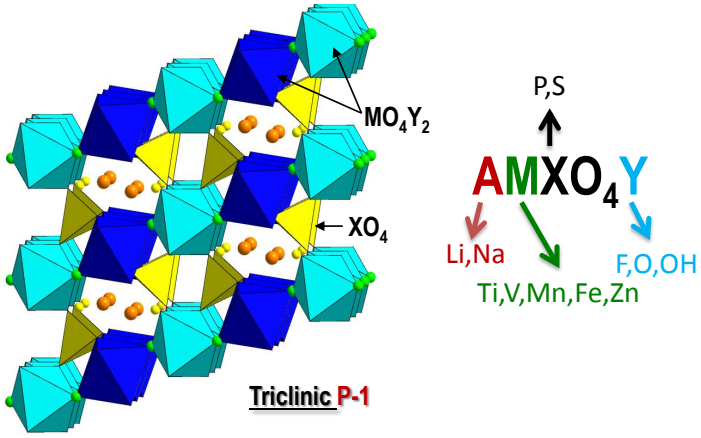

Figure 4.2: Crystal structure of a generic member of the Tavorite family. Adapted from [267].

dra and XO_4 tetrahedra connected to each other through their corners by oxygen atoms. The octahedral MO_4Y_2 units are connected through the ligand Y along -YO_4MY-YO_4MY- chains connected to each other through XO_4 tetrahedra by oxygen atoms. Two crystallographic sites were observed for the transition metal M (both at special Wyckoff positions) and one crystallographic site for X. Although sulphate tavorite materials are interesting because of the possibility to exploit the Fe^{2+}/Fe^{3+} redox couple at 3.6 V [269], they are also chemically unstable in air. Hence in the following we will mainly focus on phosphate structures, where X = P. The Tavorite structure generates 3 tunnels (in three directions), two of which containing the A atom. The number of Li/Na sites and their precise localization were hypothetical in the work of Simonov et al. [268]: through their studies of the $LiAlPO_4(F_xOH_{1-x})$ series, they reported a large and extremely anisotropic displacement parameter for the Li atom and suggested that the site was split into two fractionally occupied positions. Later, during the study of the same series (performed using single crystals), L.A. Groat et al. [270] confirmed the distribution of Li between two sites, highly dependent on the amount of fluorine in the sample. In the following we will stress how such considerations are better addressed using neutron diffraction. Note, as a final remark, that four models of triclinic unit cells describing the Tavorite structure are reported in literature. As this can be quite confusing, they can be found in [271] where the relationship between different descriptions is discussed.

In this chapter we limit our study to $LiVPO_4Y$ (Y = F, O). However, the Tavorite family is a large one, born from the combination of several alkali, anions and transition metals. Figure 4.3 gathers some significant fluorophosphate compositions. Note the great amount of different redox potentials vs Li^+/Li that these materials can attain when used

as battery electrodes, which can in principle be tuned to match a specific requirement. Vanadium, in particular, is the only transition metal able to exploit 3 redox couples, from V^{2+} to V^{5+}, making it extremely versatile. It is then easy to understand the reason for the great attention given to Tavorite materials in the battery community, and to vanadium phosphates in particular in our group.

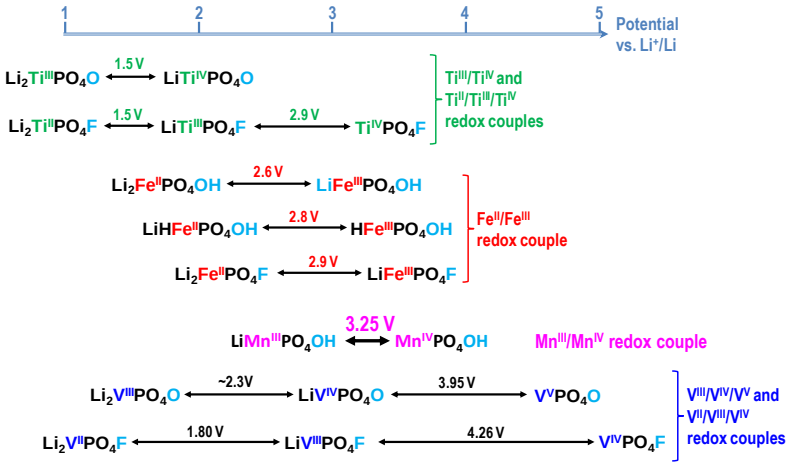

Figure 4.3: Several compounds among Tavorite phosphates in the wide range of available potentials.

4.2 $LiVPO_4O$ and $LiVPO_4F$ as promising electrode materials for Li-ion batteries

4.2.1 Synthesis

The synthesis of $LiVPO_4O$ and $LiVPO_4F$ has been thoroughly described by Ateba Mba et al. in [5,271]. Here we summarize the most important steps. $LiVPO_4F$ was first synthesized by Barker et al. [272,273] using a two-step ceramic method. It is based on the formation of the intermediate phase VPO_4, prepared by carbothermal reduction (CTR), which subsequently reacts to form $LiVPO_4F$. The synthesis procedure has been improved during Ateba Mba's PhD work [5], constituting a precious know-how for ICMCB and LRCS. The materials used in this thesis were in fact sinthesized by Ateba Mba and Philippe Dagault (ICMCB). In more details, the involved reactions are:

$$V_2O_5 + 2NH_4H_2PO_4 + 2C_{sp} \rightarrow 2VPO_4 + 2NH_3 + 3H_2O + 2CO \quad (4.1)$$

$$VPO_4 + LiF \rightarrow LiVPO_4F \quad (4.2)$$

Reaction 4.1 represents the first step where vanadium is introduced in the form of $V_2^{5+}O_5$ and reduced through CTR to form $V^{3+}PO_4$. The highly divided carbon is used in slight excess (about 5 wt%) to ensure a complete reduction. The precursors are SPEX ball-milled for 90 minutes (12 hours in case of planetary ball-milling machine), then pressed into a pellet subsequently heated at 350 °C during 8 hours under argon flow (pre-treatment) prior to a grinding and a final treatment at 800 °C during 10 hours, again under argon flow. The intermediate phase VPO_4 is then obtained coated by carbon (estimated around 7-8% by TGA or gas chromatograpy). Reaction 4.2 describes the second step, where VPO_4 is mixed with lithium fluoride LiF. The mixture is pressed as a pellet, put in a gold tube sealed inside an argon-filled glovebox and heated at 750 °C for 1h. Alternatively, for high purity the pellet can be put in a gold boat and heated in the oven under argon flow. Then the pellet is quenched in liquid nitrogen. This process can possibly leave impurities in the product (α-$Li_3V_2(PO_4)_3$ for example), but these were found to be soluble in water and could thus be eliminated by stirring in water, filtering and drying. Regarding the synthesis of $LiVPO_4O$, it follows a simpler one-step ceramic route procedure. This uses V_2O_3 as a vanadium precursor, together with $NH_4H_2PO_4$ and Li_3PO_4. The detailed reaction is:

$$\frac{1}{2}V_2O_3 + \frac{1}{3}Li_3PO_4 + \frac{2}{3}NH_4H_2PO_4 + \frac{1}{2}O_2 \rightarrow LiVPO_4O + \frac{2}{3}NH_3 + H_2O \qquad (4.3)$$

Instead of Li_3PO_4, LiF can also be used. The procedure is as follows: the precursors are mixed in a planetary ball milling machine (or SPEX, conditions??) and then pressed as a pellet. A first thermal treatment at 300 °C for 5 hours is followed by grinding, making a new pellet and then a second thermal treatment at 800 °C for 10 h under argon flow. The pellet is then quenched and the powder recovered. It is worth mentioning that we do not put any prefix before $LiVPO_4O$, for homogeneity with $LiVPO_4F$. However the product we obtain is one among different polymorphs. Here the material we synthesize is the Tavorite composition crystallizing in the $P\bar{1}$ space group, sometimes referred to as α-$LiVPO_4O$[274–276]. Other polymorphs are tetragonal α_1-$LiVPO_4O$ ($P4/nmm$[277]) and orthorhombic β-$LiVPO_4O$ ($Pnma$[278]), not considered in this thesis.

4.2.2 Crystal Structures

Phase pure $LiVPO_4O$ and $LiVPO_4F$ can be reproducibly obtained using the procedure described above. As already discussed, they both crystallize in the Tavorite crystal structure. Typical XRPD diffraction patterns of the two materials are reported in Figure 4.4. Bragg

positions are calculated in the $P\bar{1}$ space group, with the reported cell parameters [271]. One notices that, although the two materials are homeotypic, the unit cell of $LiVPO_4O$ is twice the one of $LiVPO_4F$. This fact originates additional reflections in the XRPD pattern of $LiVPO_4O$ (at 25° for example) and it is the result of structural differences (vanadium's oxidation state and lithium's position) that will be detailed below. It is also immediately clear that the value of V/Z for $LiVPO_4O$ (85.8 $Å^3$) is significantly smaller than in $LiVPO_4F$ (87.2 $Å^3$), as a result of the higher oxidation state of vanadium in the first case. Similar observations will be done in the following regarding different members of the phase diagrams of Li_xVPO_4O and Li_xVPO_4F ($0 \leq x \leq 2$).

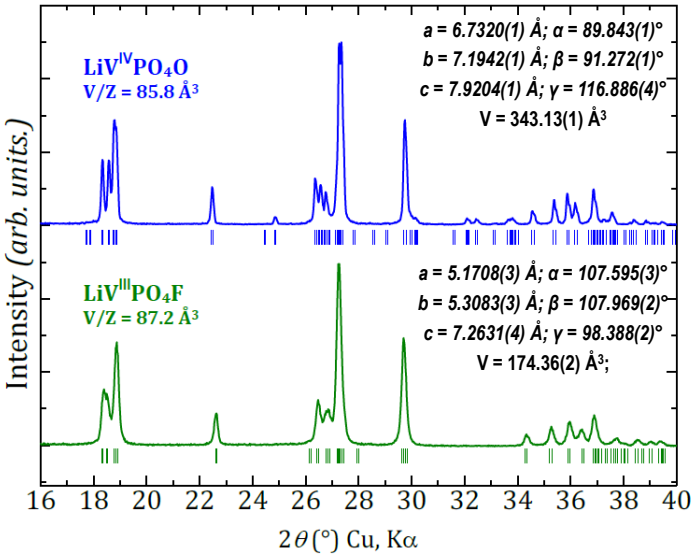

Figure 4.4: XRPD patterns of phase pure $LiVPO_4O$ and $LiVPO_4F$ with calculated Bragg positions and cell parameters. Reprinted from [271].

$LiVPO_4F$

Knowing that $LiVPO_4F$ belongs to the Tavorite family, a complete structural determination aims at precisely refining the various atomic coordinates (which are already approximately known) and most importantly at localizing Li^+ cations within the tunnels of the structure. Simonov et al. [268] had previously published the crystal structure of $LiAlPO_4F$ where two sites of lithium were proposed, each site being occupied at 50% and separated from the other by a distance of 0.5 Å. Based on this work, Ellis et al. [279] carried out a structural determination using synchrotron XRPD. Their proposed model confirms the presence of two lithium sites, although X-Rays are not an effective probe for light elements such as lithium.

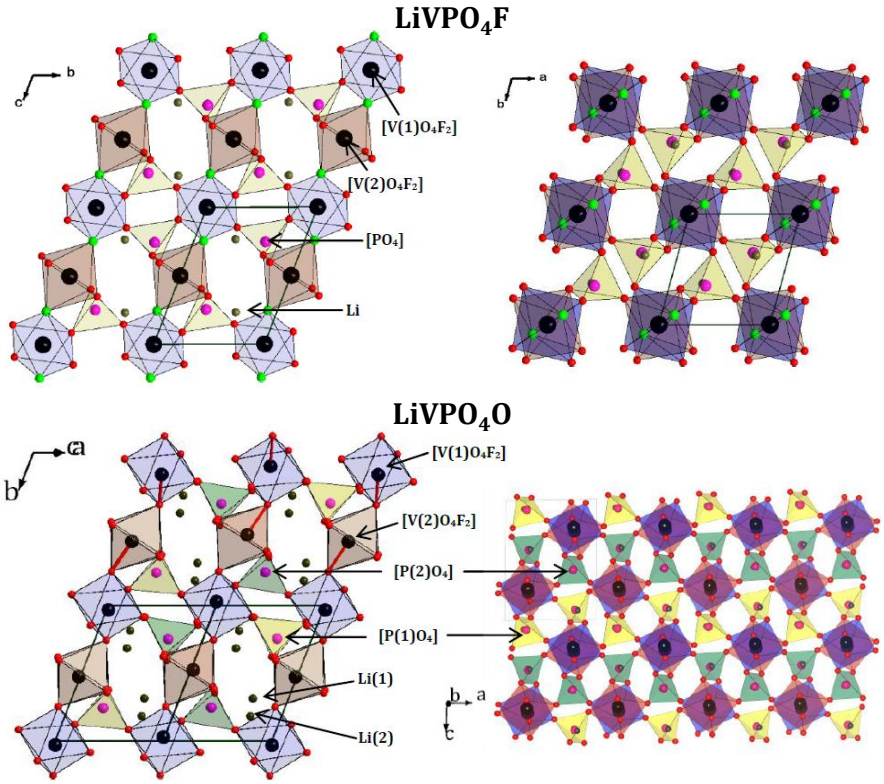

Figure 4.5: Representation of the crystal structures of $LiVPO_4F$ and $LiVPO_4O$, adapted from [5].

A more insightful approach was undertaken by Ateba Mba et al. [271], who made combined used of XRPD (high-angular resolution Cu Kα_1) and neutron powder diffraction (NPD) to characterize the structure and the position of lithium sites (thanks to Fourier difference maps). Interestingly, only one lithium site was found, whose fractional coordinates are at the barycentre of the two Li sites proposed for $LiAlPO_4F$. The crystal structure of $LiVPO_4F$ is shown in Figure 4.5, while detailed atomic parameters are reported in [5,271]. Briefly, the structure is built on VO_4F_2 octahedra which share common fluorine atoms so as to form -F-V-F-V- infinite chains running along the $[001]_{P\bar{1}}$ direction (Figure 4.6). The chains are connected to each other via PO_4 tetrahedra through -V-O-P-O-V- sequences. Vanadium lies in two octahedral sites with a very narrow range of V-O distances, 1.96-1.99 Å. The V-F distances along the -F-V-F-V- chain are very homogeneous (constrained by symmetry) with a value of 1.98 Å.

$LiVPO_4O$

Regarding $LiVPO_4O$, the only structural determination published until 2012 was that of Lavrov et al. [280]. Ateba Mba et al. [271] recently carried out a new structural study, taking

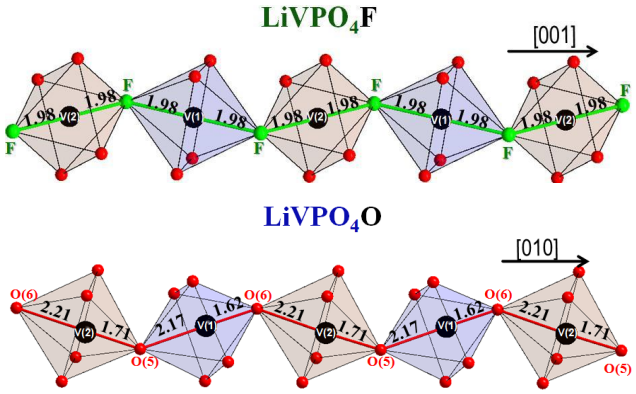

Figure 4.6: Octahedral chains of $LiVPO_4F$ (top) and $LiVPO_4O$ (bottom), revealing regular bond length distances in the first case (V^{3+}) and long-short alternated bonds in the second one (V^{4+}). Adapted from [5].

advantage of XRPD (again Cu Kα_1) and NPD, to verify the older one and to further address the similarity with $LiVPO_4F$. Detailed atomic parameters are reported in [5,271]. The 3D structure of $LiVPO_4O$ is shown in Figure 4.5. Similar to $LiVPO_4F$, it is built on chains of $V(1)O_6$ and $V(2)O_6$ octahedra (V(1) and V(2) are two independent vanadium sites) connected alternatively through their corners by oxygen. These chains run along $[010]_{P\bar{1}}$ (Figure 4.5) and are connected to each other by PO_4 tetrahedra characterized by P-O distances between 1.50 and 1.58 Å. The vanadium cations lie within two octahedral sites with a wide range of V-O distances: 1.62-2.17 Å for V(1) and of 1.71-2.21 Å for V(2), as a typical example of alternate short and long distances in vanadyl-containing compounds [5,95,281]. The short and long V-O distances in VO_4O_2 octahedral chains are alternated along the $[010]_{P\bar{1}}$ direction. The lithium ions are distributed over two fully occupied distinct crystallographic sites, Li(1) and Li(2), due to the doubling of the unit-cell, at a distance of 3.44 Å from each other. They lie in two distorted pentahedral sites.

4.2.3 Electrochemistry

The electrochemical response of $LiVPO_4Y$ (Y = F, O) towards Li^+ insertion / extraction has been well studied by Ateba Mba in his PhD thesis [5], following the pioneering work of Barker [273,282]. We report here the salient results, stressing the similarities and most importantly the differences between the two materials. Figure 4.7 gathers their behaviour upon galvanostatic cycling in Li-ion batteries (coin cells) made as $LiVPO_4Y$ // LP30 // Li metal. Detailed battery preparation procedures can be found in [5]. Here we recall that the electrodes, in the form of a cast film, are composed by active material (> 73 wt.%),

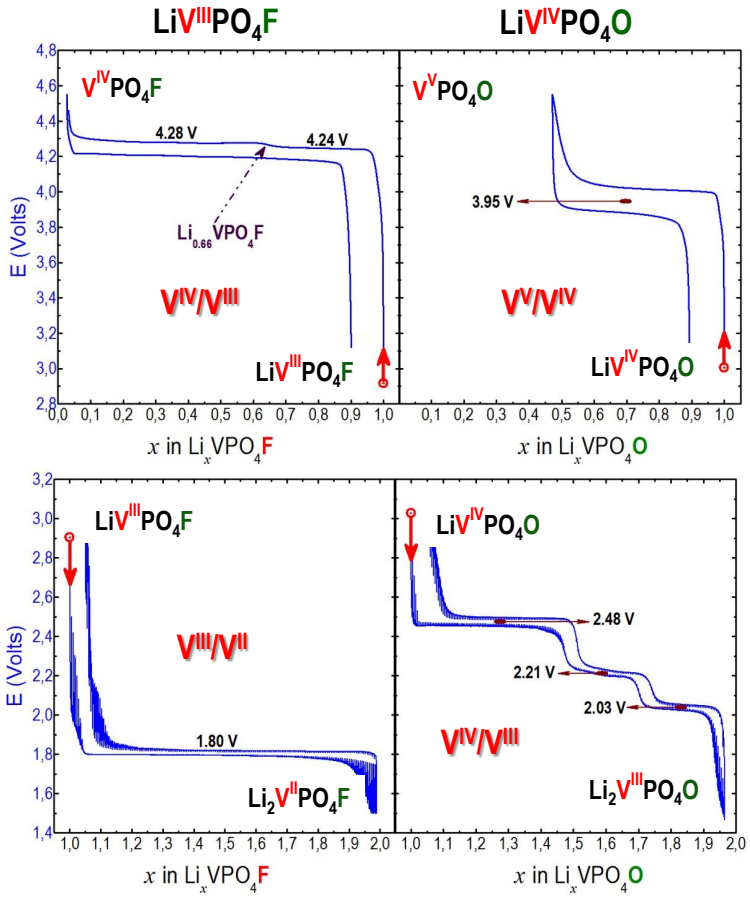

Figure 4.7: Top: Lithium extraction from the structure of $LiVPO_4F$ (left) and $LiVPO_4O$ (right) upon galvanostatic cycling between 3 V and 4.55 V vs Li^+/Li. Bottom: Lithium insertion into the structure of $LiVPO_4F$ (left) and $LiVPO_4O$ (right) upon cycling (GITT: galvanostatic intermittent titration technique) between 3 V and 1.50 V vs Li^+/Li. Adapted from [271].

carbon Csp (12-15 wt.%) and PVdF binder (12 wt.%). In the case of $LiVPO_4F$ we notice immediately a very flat voltage-composition plateau at 1.80 V vs. Li^+/Li that occurs upon insertion of lithium into the structure, with concurrent reduction of V^{3+} to V^{2+}. The absolutely flat shape of the profile is indicative of a biphasic reaction between the end members $LiVPO_4F$ and Li_2VPO_4F. In the high-voltage region, where lithium is extracted from $LiVPO_4F$, we notice instead a different behaviour. Although at a first glance it seems that the reaction proceeds as a plateau around 4.2 V, a closer inspection reveals a sequence of two flat regions, at 4.24 V and 4.28 V vs. Li^+/Li. These two electrochemical features are well-separated and they suggest the presence of an intermediate phase of composition $Li_{0.67}VPO_4F$, before reaching the fully delithiated $V^{4+}PO_4F$. In both domains, $LiVPO_4F$ electrodes reach a capacity very close to the theoretical one.

Despite the structural similarity between $LiVPO_4F$ and $LiVPO_4O$, the latter shows a

significantly different electrochemical behavior. It can be clearly observed in the right part of Figure 4.7. The extraction of Li^+ occurs at an average potential of 3.95 V versus Li^+/Li at C/50 regime: this leads upon 1^{st} charge to a global composition of "$Li_{0.5}VPO_4O$", raising the question whether (i) such a composition is actually the stable one obtained upon oxidation or (ii) the reaction could not be completed because of the poor electrochemical reactivity of $LiVPO_4O$. Given the strict relation with its phase diagram, this matter will be addressed in the next section. Note that $LiVPO_4O$'s ability to deintercalate lithium ions by exploiting the vanadium V^{4+}/V^{5+} redox couple has been addressed in the past by Azmi et al. focusing mainly on the orthorhombic β-$LiVPO_4O$ phase[283,284]. The triclinic Tavorite form of $LiVPO_4O$ has been thought to possess poor electrochemical properties instead, mainly attributed to the fact that it is a wide bandgap semiconductor with low intrinsic electrical conductivity[271,283,285]. In the low voltage domain, the electrochemical behavior of $LiVPO_4O$ is extremely interesting and complicated, in contrast with the simplicity of $LiVPO_4F$'s plateau. The insertion of lithium into $LiVPO_4O$ was first reported by Allen et al.[274], who reported on both the tavorite and the orthorhombic (β-$LiVPO_4O$) polymorphs. They reached compositions $Li_{1.76}VPO_4O$ (and β-$Li_{1.47}VPO_4O$). This suggested that the Tavorite polymorph of $LiVPO_4O$ can accommodate more lithium than the orthorhombic one. In their study, Allen et al. also showed a significantly modified XANES signal between the pristine $LiVPO_4O$ and the lithiated $Li_{1.76}VPO_4O$, both in the pre-edge and edge features. They notice how the vanadium's environment is modified, namely losing the shortest V-O bond present in $LiVPO_4O$ as a result of vanadium's reduction.

In our GITT measurement (Figure 4.7), we observe 3 peculiar features similar to those reported by Allen et al.: the 1^{st} long voltage-composition plateau at 2.45 V vs. Li^+/Li between $LiVPO_4O$ and $Li_{1.5}VPO_4O$, the second "pseudo-plateau" at 2.21 V vs. Li^+/Li, from $Li_{1.5}VPO_4O$ to $Li_{1.75}VPO_4O$ and the final short plateau at 2.04 V vs. Li^+/Li to reach the end member Li_2VPO_4O. The detailed mechanisms associated with these reactions as well as the description of the crystal structures involved is made in paragraph 3.4.4. Note the drastic voltage difference experienced by Li_xVPO_4Y, for the "same" V^{3+}/V^{4+} redox couple, when Y is changed from O to the more electronegative F: this is partly due to the inductive effect of the Y cation, but also to the fact that in Li_xVPO_4O the electrochemically active reaction is done on the vanadyl bond VO^{2+}, absent in Li_xVPO_4F, and finally to the fact that $0 \leq x \leq 1$ for Li_xVPO_4F while $1 \leq x \leq 2$ for Li_xVPO_4O.

Regarding the electrochemical response, it is important to note that it strongly depends

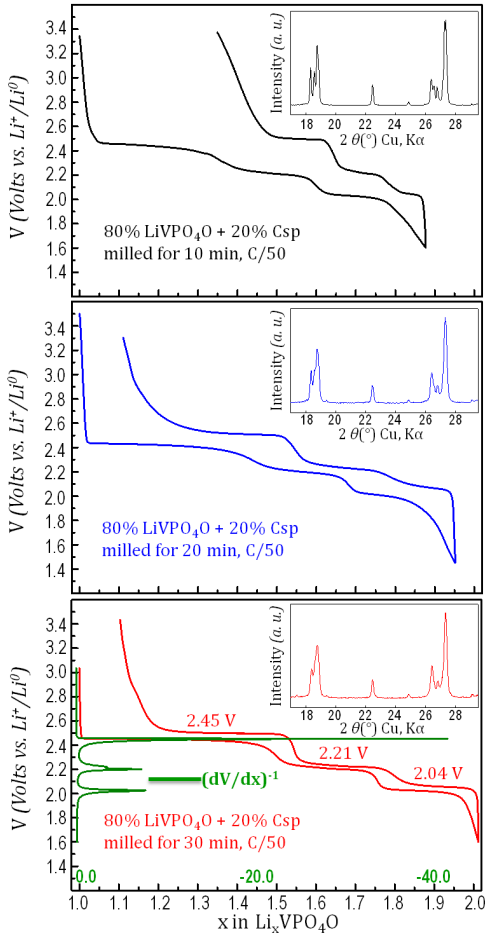

Figure 4.8: Galvanostatic cycling for three different SPEX ball-milling durations of a mixture of 80 wt% $LiVPO_4O$ and 20 wt% Csp. The cycle at the bottom is shown with the respective derivative curve (green). Diffractograms (insets) of the respective crystalline powders obtained after milling are reported.

on the particle size of $LiVPO_4O$. As reported in [5,95,271], the synthesis procedure leads to the formation of 1-2 μm particles, highly agglomerated (5-6 μm). We performed SPEX ball-milling to decrease the particle size and, as illustrated in Figure 4.8 (for similar electrode masses ($\approx$4 mg)), the longer the grinding process, the higher the electrochemical reactivity. This significant improvement is achieved thanks to the smaller size of the obtained particles, which also reflects on the broadening of the X-Ray diffraction peaks (Figure 4.8, insets). Therefore, for a sample milled for a long time (30 minutes here), a discharge capacity close to the theoretical one can be achieved together with good reversibility, while for shorter milling times the capacity decreases and a strong irreversibility is observed, probably due to limited diffusion within the large particles. As we will discuss in the following, this is also a hint to understand the limited reactivity of $LiVPO_4O$ at high potential.

4.3 Phase diagram of $LiVPO_4F$ ($0 \leq x \leq 2$)

In this section the phase diagram and the crystal structures observed by Ateba Mba [5,271,286] upon lithium insertion and extraction into/from $LiVPO_4F$ are briefly reviewed.

4.3.1 Lithium extraction from $LiVPO_4F$ - High voltage domain

Li^+ extraction from $LiVPO_4F$ proceeds through 2 voltage-composition plateaus at 4.24 V and 4.28 V vs. Li^+/Li. This observation (Figure 4.7) was verified for the first time by Ateba Mba et al. using *in situ* XRPD [286]. Upon charge a sequence of two first-order transitions was discovered, the first one between $LiVPO_4F$ and $Li_{0.67}VPO_4F$, the second one between $Li_{0.67}VPO_4F$ and VPO_4F. The two reactions are clearly correlated with the two electrochemical plateaus. The structure of the end member VPO_4F was previously reported by Ellis et al. [279] In good agreement with this, Ateba Mba reported a monoclinic unit cell of a = 7.164(4) Å, b = 7.119(7) Å, c = 7.121(5) Å, β = 118.09(7)° and a volume V = 320.46(4) Å^3 (Table 4.1). This corresponds to a volume change $\Delta V/V$ of more than 8% when all lithium is extracted from $LiVPO_4F$ (Figure 4.9). Thus it is not entirely surprising that an intermediate phase forms upon charge, in order to avoid such an important volume change, which would induce significant stress in the material [59]. The intermediate phase is observed to form around the composition $Li_{0.67}VPO_4F$. This particular stoichiometry immediately suggests lithium/vacancy and/or charge ordering, since it can be written as $Li_{2/3}V^{3+}_{2/3}V^{4+}_{1/3}PO_4F$. The exact nature of this phase, however, has not been determined yet. Its unit cell parameters were reported in triclinic $P\bar{1}$ setting, being a = 5.171(9) Å, b = 5.222(9) Å, c = 7.256(3) Å, α = 109.40(2)°, β = 107.10(1)° and γ = 97.04(6)°. The unit cell volume is V = 171.34(6) Å^3, intermediate between those of $LiVPO_4F$ and VPO_4F. The charge is thus divided into two transitions showing volume changes of 2% and 6%, instead of a single transition of $\Delta V/V$ = 8% (Figure 4.9). Although this seems to

Table 4.1: Cell parameters of Li_xVPO_4F (x = 0, 0.67, 1, 2).

Composition	S.G.	a (Å)	b (Å)	c (Å)	α (°)	β (°)	γ (°)	Vol. (Å^3)	V/Z (Å^3)
VPO_4F	C2/c	7.164	7.119	7.121	90	118.09	90	321.03	80.25
$Li_{0.67}VPO_4F$	$P\bar{1}$	5.173	5.226	7.253	109.41	107.07	97.01	171.48	85.74
$LiVPO_4F$	$P\bar{1}$	5.170	5.308	7.263	107.59	107.97	98.39	174.37	87.18
Li_2VPO_4F	C2/c	7.227	7.949	7.316	90	116.81	90	375.16	93.79

be energetically favourable, a remarkable fact is that the composition $Li_{0.67}VPO_4F$ is not stabilized reversibly upon charge and discharge: during the latter no intermediate phase was observed[286]. Further studies are required to fully understand the structure of this interesting phenomenon.

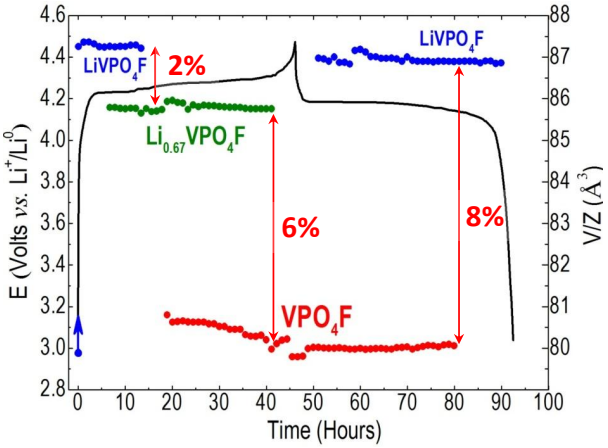

Figure 4.9: Unit-cell volume changes during the global electrochemical reaction $LiVPO_4F$ - VPO_4F involving successive two-phase reactions. Reprinted from[286].

4.3.2 Lithium insertion into $LiVPO_4F$ - Low voltage domain

As we observed from the electrochemical GITT profile presented in Figure 4.7, the lithium insertion into $LiVPO_4F$ proceeds through an extremely flat voltage-composition plateau at exactly 1.81 V vs. Li^+/Li. This is usually the signature of a first order transition. Ateba Mba verified this by means of *in situ* XRPD[286]: he indeed observed a biphasic reaction where $LiVPO_4F$ gradually disappeared while the end member phase Li_2VPO_4F forms. This composition was already reported by Ellis et al.[279], crystallizing in the monoclinic C2/c space group. The cell parameters retrieved from Le Bail fitting by Ateba Mba are a = 7.227(4) Å, b = 7.949(4) Å, c = 7.316(5) Å and β = 116.81(6)° (Table 4.1), in excellent agreement with those reported by Ellis et al. The volume is V = 375.16(1) $Å^3$ (V/Z = 93.79 $Å^3$), bigger (as expected) than that of $LiVPO_4F$ as a result of the V^{2+} ionic radius (0.088 nm) bigger than that of V^{3+} (0.074 nm).

4.4 Phase diagram of $LiVPO_4O$ ($0 \leq x \leq 2$)

In this section the study of lithium extraction and insertion from/into $LiVPO_4O$ is described in details, with special attention to the crystallographic transitions involved and to the new

structures determined.

4.4.1 Experimental

Electrodes were prepared by ball-milling (SPEX, 30 minutes) $LiVPO_4O$ with Carbon Super P (85:15 wt% when not specified otherwise). For batteries cycled in coin cells, PVdF was added as a binder (12 wt%) according to the Bellcore protocol (described in [287]), while *in situ* measurements were carried out using directly a mixture of $LiVPO_4O$ and Carbon Super P. 1M $LiPF_6$ in EC:DMC (1:1) was used as the electrolyte (LP30). *In situ* measurements were performed using a Bruker D8 diffractometer with Cu-K$\alpha_{1,2}$ wavelengths or a PANalytical Empyrean diffractometer with a Cu-Kα_1 setting. In the first case, lithium batteries were prepared in our *in situ* cell [97,98], able to perform both in reflection and transmission geometry. Reflection was used in this case. The same geometry but with a custom modified *in situ* cell was used in the second case. Both cells were described in section 1.6.5. The end members VPO_4O and Li_2VPO_4O were chemically prepared from $LiVPO_4O$. In the first case, it was oxidized with a strong oxidizing agent, nitronium tetrafluoroborate (NO_2BF_4) in acetonitrile medium. The resulting yellow powder was then sealed in a 0.2 mm diameter capillary and X-Ray diffraction was performed on a PANalytical diffractometer (Empyrean, Cu K$\alpha_{1,2}$) in Debye-Sherrer geometry. In the second case, $LiVPO_4O$ was reduced with $LiAlH_4$ in tetrahydrofurane. The resulting dark gray powder was then sealed in a 0.3 mm diameter capillary and X-Ray diffraction was performed on the same diffractometer. Inductively coupled plasma atomic emission spectroscopy (ICP-AES) was used to check the resulting stoichiometry. Neutron diffraction was also carried out on Li_2VPO_4O. The powder was put in a 6.5 mm diameter cylindrical vanadium sample holder and measured at $\lambda = 1.594$ Å on the high-resolution powder diffractometer D2B at Institut Laue-Langevin. Data analysis and structural refinements through the Rietveld method [87] were performed thanks to the FullProf suite [177]. As part of a collaboration with Dany Carlier and Elena Bogdan (ICMCB), we calculated the total energies with the GGA (PBE) [288] and GGA + U method, using the Projector Augmented Wave (PAW) method [289] as implemented in the Vienna Ab Initio Simulation Package (VASP, [290]). The DFT+U method (LDA+U or GGA+U) allows to treat more accurately strongly correlated systems, such as transition metals or rare earth-based materials [291,292]. In our study, the Dudarev's approach was used to perform the GGA + U. The effective on site Coulomb (U) and exchange (J) parameters were not input separately as only the difference U_{eff} =

(U-J) is meaningful. Here U_{eff} values of 0, 3, 4 and 4.5 eV were used. A plane wave cutoff energy of 600 meV and a 6x6x6 k-point grid were used to let the total energies converge by less than 5 meV/unit cell.

4.4.2 Lithium extraction from $LiVPO_4O$ - High voltage domain

We have previously described the limited electrochemical activity of $LiVPO_4O$ at high potential (3.95 V vs. Li^+/Li). Only half of the theoretical capacity was achieved, the question to be answered being "$Li_{0.5}VPO_4O$ or (1/2 $LiVPO_4O$ + 1/2 VPO_4O)?". To address the problem, *in situ* X-Ray powder diffraction was performed during lithium deintercalation from $LiVPO_4O$ at a C/50 rate. Diffraction patterns were recorded for 70 minutes each in the angular domain [13° - 44°] during galvanostatic cycling. The result of such a measurement is reported in Figure 4.10. The phase diagram clearly shows that when the

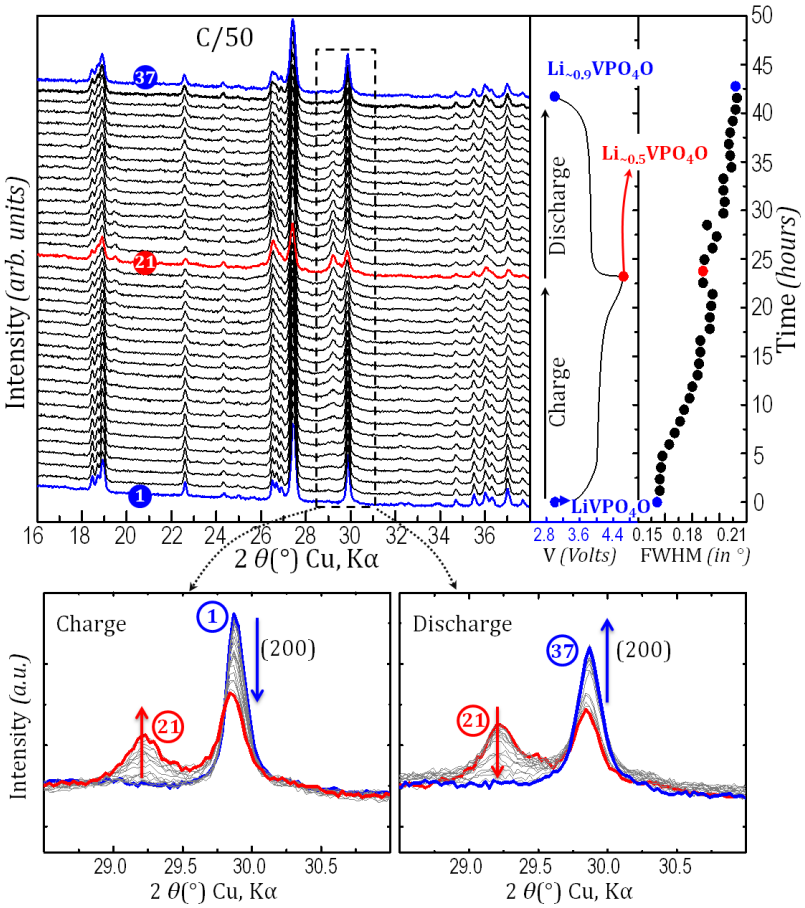

Figure 4.10: *In situ* XRPD patterns (left) of a Li//LP30//$LiVPO_4O$ cell upon galvanostatic charge and discharge (middle) at C/50 up to 4.5 V. The evolution of the FWHM of the (200) peak (30°) is shown on the top right part of the figure. An enlarged view of the 28.5°-31° region is also given at the bottom.

global composition "$Li_{0.5}VPO_4O$" is reached at 4.5 V vs. Li^+/Li, the initial phase has not completely disappeared. Indeed, the diffraction peak in the 30°-2θ region loses intensity to about half of its original value. Upon discharge, the same battery shows a reversible behavior, with the peaks' intensities of the $LiVPO_4O$ phase returning to values very close to the initial ones.

This first observation was a strong hint suggesting that the intermediate composition $Li_{0.5}VPO_4O$ did not exist as a stable single phase. Besides, DFT calculations (described further down) showed that the $Li_{0.5}VPO_4O$ phase is not stable versus $LiVPO_4O$ and VPO_4O, indicating that full extraction of Li^+ from $LiVPO_4O$ was possible (see Figure 4.13 in the following). A close look at the (200) diffraction peak reveals additional important information. In fact its FWHM grows continuously during charge and it broadens also during subsequent discharge, reaching a value about 40% larger than the initial one after the first electrochemical cycle. The growth of the peak's FWHM indicates the shrinkage of the crystallites coherent domain size, that can be linked to a decrease of particles' size and therefore to a possible enhancement of the electrochemical reactivity of $LiVPO_4O$. Unfortunately we could not verify the presence of possible anisotropic broadenings because of the limited resolution and angular domain. To get a better insight into this behavior, subsequent $LiVPO_4O$ charge/discharge cycles were recorded and the results are shown in Figure 4.11. From cycle 1 to cycle 30 a continuous increase of the delivered capacity is observed, from the initial value of 78 mAh/g to about 135 mAh/g (in comparison to a theoretical capacity of 159 mAh/g), corresponding also to a drastic decrease of the battery polarization. This supports the hypothesis that big agglomerated particles of $LiVPO_4O$ do

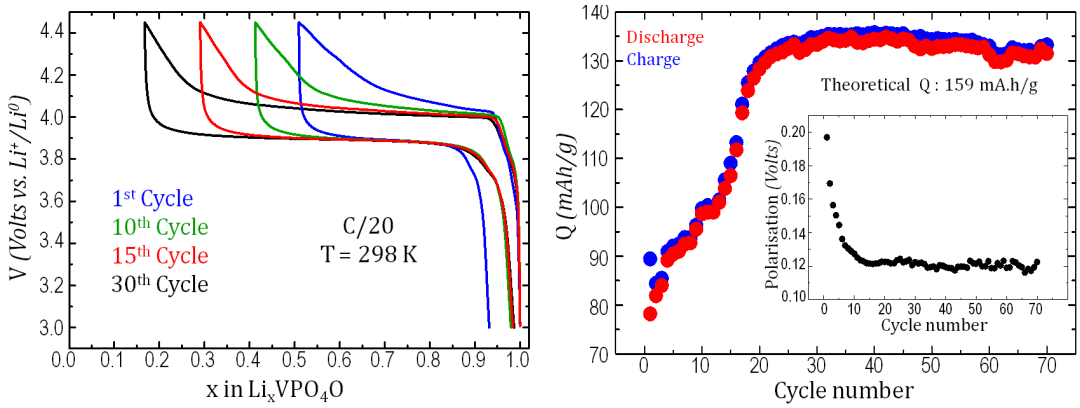

Figure 4.11: (Left) Different cycles (rate C/20) for a Li//LP30//$LiVPO_4O$ cell. The electrode active mass is 3.8 mg. (Right) Charge and discharge capacities of the cell versus number of cycles and respective polarization (inset).

not fully contribute to the electrochemical reaction but also shows that the kinetics can be significantly improved. Such an improvement in electrochemical properties agrees with our previous observations of an increased capacity of $LiVPO_4O$ in the low-voltage region when ball milled (also observed for orthorhombic β-$LiVPO_4O$ [284]).

4.4.3 The crystal structure of ϵ-VPO_4O

Table 4.2: Structural data for different polymorphs of VPO_4O. Space groups and Vanadium-Oxygen bond lengths are reported.

Polymorph	Symmetry	Space group	V=O (Å)	V-O (Å)
ϵ-VPO_4O (this work)	Monoclinic	Cc	1.59	2.51
ϵ-VPO_4O (this work)	Monoclinic	$P2_1/n$	1.59	2.51
ϵ-VPO_4O (ICSD 415924 [293])	Monoclinic	Cc	1.57	2.56
δ-VPO_4O (ICSD 420073 [294])	Tetragonal	$P4_2/mbc$	1.62	1.81
γ-VPO_4O (ICSD 415213 [295])	Orthorhombic	Pbam	1.50	2.70
			1.62	1.81
β-VPO_4O (ICSD 9413 [296])	Orthorhombic	Pnma	1.56	2.59
α_I-VPO_4O (ICSD 108983 [297])	Tetragonal	P4/n	1.63	2.48
α_{II}-VPO_4O (ICSD 2889 [298])	Tetragonal	P4/n	1.58	2.86

The study of the end reaction member VPO_4O has also been carried out, since it is a material with a rich crystal chemistry as witnessed by the existence of many different polymorphs reported in the literature (Table 4.2). Among these, the preparation of VPO_4O from $LiVPO_4O$, both chemically and electrochemically, results in the monoclinic ϵ-VPO_4O phase. Interestingly, a recent study by Ling et al. [276] showed that, energetically, the β-VPO_4O polymorph should be the most favourable one, although this has never been observed experimentally. This anomaly is explained by means of geometric considerations, showing that the transition from $LiVPO_4O$ to ϵ-VPO_4O is preferred as it induces smaller structural deformations. The structure of ϵ-VPO_4O has been already reported in literature with contradictory results since different authors propose different space groups and crystal structures. Indeed, the ϵ-VPO_4O polymorph had first been indexed in the monoclinic $P2_1/n$ space group and its structure determined [299,300]. More recently, a second indexation was performed in the Cc space group [293] and the two structures were compared, demonstrating a less distorted Cc structure. For this reason we performed careful X-Ray diffraction experiments on a VPO_4O powder, chemically obtained from the oxidation of $LiVPO_4O$ and sealed in a capillary. The measured XRPD pattern is shown in Figure 4.12.

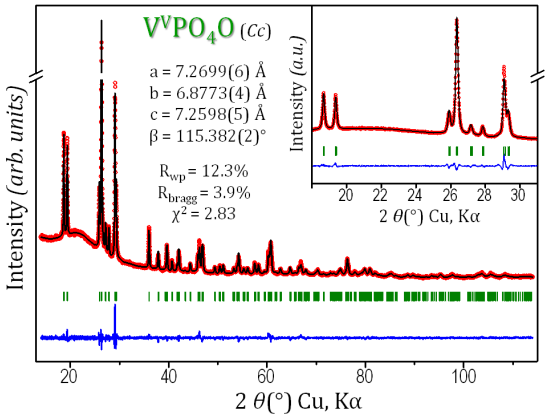

Figure 4.12: XRPD measurement and Rietveld refinement of a ϵ-VPO_4O powder sealed in a 0.2 mm capillary.

The possible space groups found from the automatic indexation of XRPD data are Cc, C2/c and $P2_1/n$. In order to investigate theoretically the phase stability of the different structural hypotheses we compared the total energies resulting from DFT calculations using GGA and GGA+U methods. For VPO_4O with the $P2_1/n$ and Cc space groups, we used as initial structures those reported in [293,299]. For VPO_4O with the C2/c space group, we used as initial structure the one of VPO_4F [279] replacing F by O. We also considered a cell with a $P\bar{1}$ space group using the cell of $LiVPO_4O$ and removing all Li^+ ions. All structures were fully relaxed and the corresponding structural parameters are given in Table 4.4. The lower energy was obtained for VPO_4O in Cc in both GGA and GGA+U calculations. In Table 4.3 we give the formation energy per formula unit for each case versus this most stable phase. It appears that VPO_4O described in $P2_1/n$ is only slightly less stable than the one described in Cc by only about 7 meV/Formula unit (which is lower than kT at ambient temperature (25 meV)). VPO_4O described in $P\bar{1}$ is less stable by about 27 meV/Formula unit. The largest energy difference is obtained for VPO_4O described in C2/c where all

Table 4.3: Formation energies calculated in meV/f.u. for the different structural hypothesis for VPO_4O with GGA and GGA + U vs. the most stable phase (the one described in Cc).

VPO_4O	**GGA**	**GGA+U**			
		U = 3 eV	U = 4 eV	U = 4.5 eV	
Cc	0	0	0	0	most stable
$P2_1/n$	7	7	7	8	
$P\bar{1}$	33	28	27	27	
P2/c	420	361	343	334	

Table 4.4: Cell parameters and V-O bonds distances resulting from the structural optimization using GGA + U (U = 4eV) with the VASP code.

	GGA+U (U = 4 eV)			
VPO$_4$O	Cc	$P2_1/n$	$P\bar{1}$	C2/c
a (Å)	7.326	7.311	6.962	7.221
b (Å)	7.07	7.135	7.705	7.304
c (Å)	7.371	7.408	7.598	7.24
α (°)	90	90	90.78	90
β (°)	115.19	115.02	90.23	121.54
γ (°)	90	90	119.61	90
	distance V-O (Å)			
V(1)-O	1.609	1.609	1.612	1.819 x2
	1.884	1.887	1.892	1.903 x2
	1.917	1.905	1.895	1.929 x2
	1.919	1.909	1.912	
	1.919	1.917	1.922	
	2.574	2.585	2.524	
V(2)-O	-	-	1.611	-
			1.891	
			1.909	
			1.914	
			1.925	
			2.497	

V^{5+} ions are located in the center of the VO_6 octahedra with similar V-O distances along the chains as observed in $VPO_4 \cdot H_2O$ [301], where the oxidation state is 3+, or in VPO_4F, where it is 4+ [279]. This indicates that the formation of short V=O (vanadyl type) and long V-O bonds along the chains, as it is the case for the three other structural hypotheses, strongly stabilizes the structure. Based on our theoretical study, the structure was refined (Figure 4.12) thanks to the Rietveld method in the space groups Cc or $P2_1/n$, leading to better results for the parameters refined using the Cc crystal structure (Table 4.5), in agreement with the theoretical phase stability. Cell parameters were refined to a = 7.2699(6) Å, b = 6.8773(4) Å, c = 7.2598(5) Å, β = 115.382(2)° (Vol = 327.93(4) $Å^3$) and the structure showed the expected alternated long and short V-O distances along the octahedral vanadium chains, with bond lengths of 2.51(2) Å and 1.59(2) Å, respectively. Small distortions are observed both for the in-plane V-O distances (between 1.85(2) Å and 1.93(3) Å) and for the P-O distances (1.55(2) Å, 1.56(4) Å, 1.55(3) Å and a shorter one of 1.48(4) Å, in agreement with the structure reported by Girgsdies et al. [293]). More recently, this result was confirmed by Chen et al. [302], further supporting the description of ϵ-VPO_4O

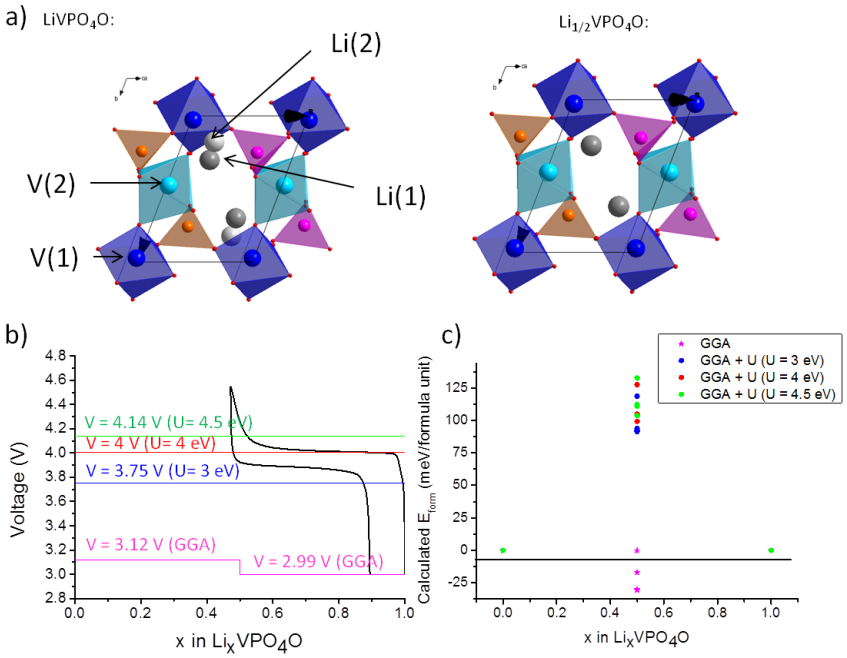

Figure 4.13: a) Crystal structure before relaxation used for DFT calculations. $LiVPO_4O$ from published experimental data (left) and $Li_{0.5}VPO_4O$ (right). $Li_{0.5}VPO_4O$ is obtained from $LiVPO_4O$ with different occupations of the Li1 and Li2 sites. The most stable structure is the one with the site Li1 only occupied. b) Various values of U used for GGA+U calculations applied on the 3d orbitals of V ions and resulting potentials. U = 4 eV represents the best choice. c) Formation energy for $Li_{0.5}VPO_4O$ for different U values. The phase would be stable with respect to $LiVPO_4O$ and VPO_4O only for U = 0.

in the monoclinic Cc space group.

Table 4.5: Refined parameters for VPO_4O. Comparison between Cc and $P2_1/n$ space groups.

$\epsilon - VPO_4O$	Cc	$P2_1/n$
χ^2, R_B, R_{wp}	2.83, 3.9%, 12.3%	3.57, 6.77%, 14.8%
a, b, c, (Å)	7.2699(6), 6.8773(4), 7.2598(5),	7.2684(6), 6.8772(4), 7.2605(6),
γ (°), Vol (Å^3)	115.382(2), 327.93(4).	115.384(3), 327.89(4).
V-O distances (Å)	1.85(2), 1.86(3), 1.86(2), 1.93(2), 1.59(2), 2.51(2).	1.83(3), 1.82(2), 1.88(1), 1.95(3), 1.58(2), 2.52(2).
Distortion	$41.95 \cdot 10^{-4}$	$48.07 \cdot 10^{-4}$
P-O distances (Å)	1.55(2), 1.56(3), 1.55(3), 1.48(2)	1.52(2), 1.63(3), 1.50(3), 1.60(2)
Distortion	$4.98 \cdot 10^{-4}$	$12.36 \cdot 10^{-4}$

4.4.4 Lithium insertion into $LiVPO_4O$ - Low voltage domain

We introduced in section 4.2.3 the complex behaviour of $LiVPO_4O$ during lithium insertion. A sequence of three reactions is observed:

$$LiV^{4+}PO_4O + \frac{1}{2}Li^+ + \frac{1}{2}e^- \Leftrightarrow Li_{1.5}V^{3.5+}PO_4O \tag{4.4}$$

$$Li_{1.5}V^{3.5+}PO_4O + \frac{1}{4}Li^+ + \frac{1}{4}e^- \Leftrightarrow Li_{1.75}V^{3.25+}PO_4O \tag{4.5}$$

$$Li_{1.75}V^{3.75+}PO_4O + \frac{1}{4}Li^+ + \frac{1}{4}e^- \Leftrightarrow Li_2V^{3+}PO_4O \tag{4.6}$$

According to the Gibbs phase rule, the first flat voltage-composition plateau (already shown in Figure 4.7) suggests a first order reaction, i.e. a two-phase reaction between the end members $LiVPO_4O$ and $Li_{1.5}VPO_4O$. This is strongly supported by the derivative curve $(dV/dx)^{-1}$, reported in green at the bottom of Figure 4.8 and in Figure 4.14, showing an intense narrow peak at 2.45 V. Further Li^+ insertion into $Li_{1.5}VPO_4O$ results in a feature that is not perfectly flat, therefore suggesting that a second order mechanism cannot be a priori ruled out. The insertion of the last 0.25 Li^+ proceeds again through a similar feature, thus suggesting again an analogous reaction between $Li_{1.75}VPO_4O$ and Li_2VPO_4O. It is worth mentioning that our electrochemical curve agrees well with the one reported by Allen et al.[274]. On the other hand, those reported by Harrison et al.[275] are similar in the $LiVPO_4O$ - $Li_{1.5}VPO_4O$ region, but they have a more sloping behaviour between $Li_{1.5}VPO_4O$ and Li_2VPO_4O. This can probably be explained by the different synthesis route used (microwave-assisted solvothermal method) which involves lower temperatures

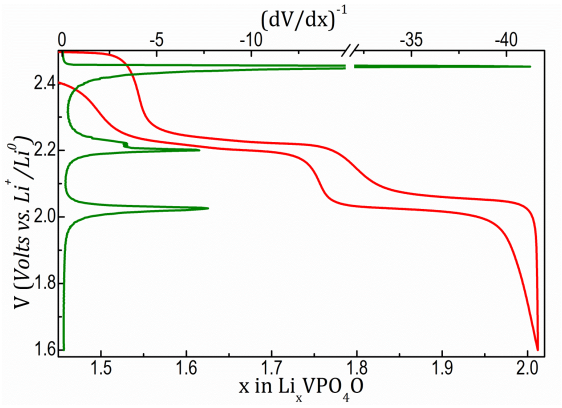

Figure 4.14: Galvanostatic cycling for a mixture of 80 wt% $LiVPO_4O$ and 20 wt% Csp (SPEX ball-milled for 30 minutes). Focus on the low voltage region between compositions $Li_{1.5}VPO_4O$ and Li_2VPO_4O.

and it is more likely to result in defects (their unit cell volume differs from ours by 1.2 $Å^3$).

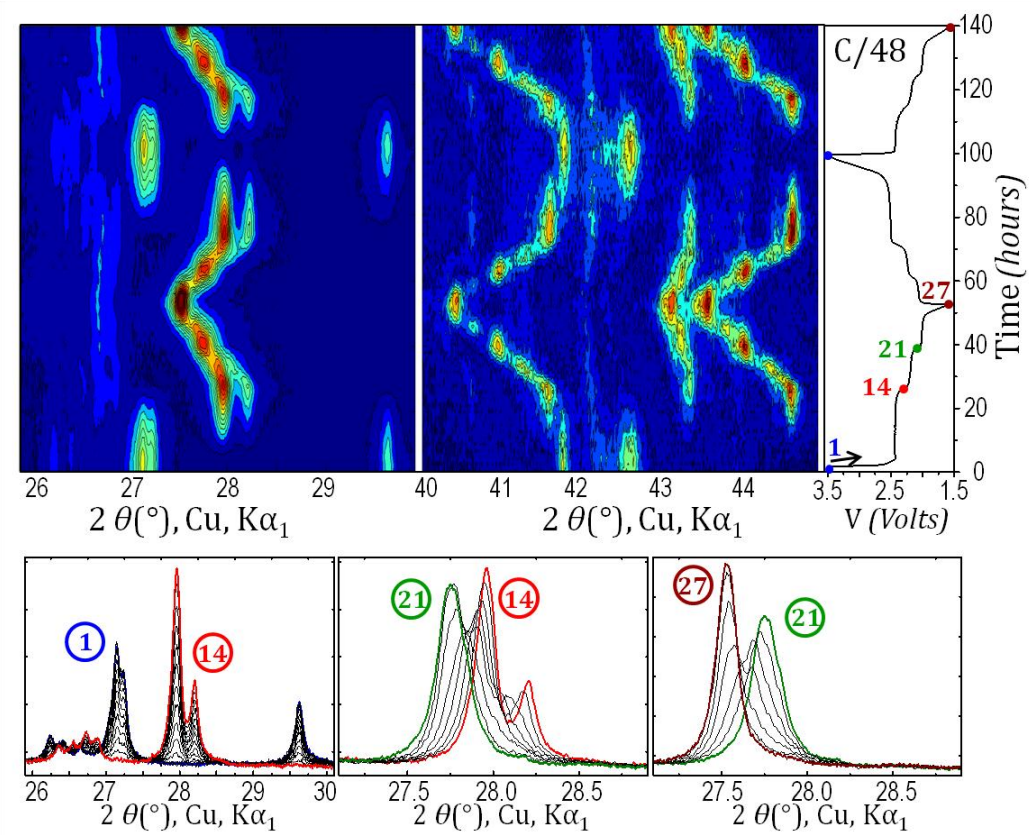

Figure 4.15: *Operando* X-ray diffraction measurement of $LiVPO_4O$ cycled at C/48 rate. The first cycle and a second discharge were recorded. (Top) Contour plot and electrochemical curve. (Bottom) An enlarged view of the [26-30°] or [27-29°] region of the first discharge where important compositions are highlighted (pristine $LiVPO_4O$ (pattern #1, blue), $Li_{1.5}VPO_4O$ (pattern #14, red), $Li_{1.75}VPO_4O$ (pattern #21, green) and Li_2VPO_4O (pattern #27, brown)).

In our case, *in situ* X-Ray diffraction during battery operation was chosen to carefully assess the validity of the biphasic reactions described above. It was performed on a X-Ray PANalytical diffractometer equipped with Cu-Kα_1 radiation, allowing high resolution data acquisition which is of key importance given the triclinic symmetry of the structures under investigation. A battery was cycled in a custom-made *in situ* cell with discharge, subsequent charge and a second final discharge of a $Li//LiVPO_4O$ cell at the rate of C/48. Every pattern was recorded in the [17° - 47°] region for two hours, corresponding 0.04 Li^+/pattern (= 2/48). Figure 4.15 shows a contour plot of the whole *operando* experiment in two selected regions [26° - 30°] and [40° - 45°], together with the electrochemical data on the right and a zoom of the phase transformations in the [26° - 30°] region at the bottom.

A highly reversible reaction could be achieved, with the full capacity of $LiVPO_4O$ reached during first discharge.

Concerning the phase diagram, a biphasic reaction between $LiVPO_4O$ and $Li_{1.5}VPO_4O$ could be easily observed, as expected from the derivative curve. In fact, every pattern in this region is clearly a linear combination of the two end members (patterns #1 and #14, respectively blue and red in Figure 4.15). From a first look at the diffraction patterns of Figure 4.15 the subsequent insertion mechanisms from $Li_{1.5}VPO_4O$ to $Li_{1.75}VPO_4O$ and from $Li_{1.75}VPO_4O$ to Li_2VPO_4O do not appear straightforward. As previously mentioned, both a solid solution and a series of two 2-phase reactions had to be considered. At first, a single-phase mechanism (solid solution) seems to be the preferred choice since an evolution of the cell parameters correlated to a shift of the Bragg positions is clear from the contour plot.

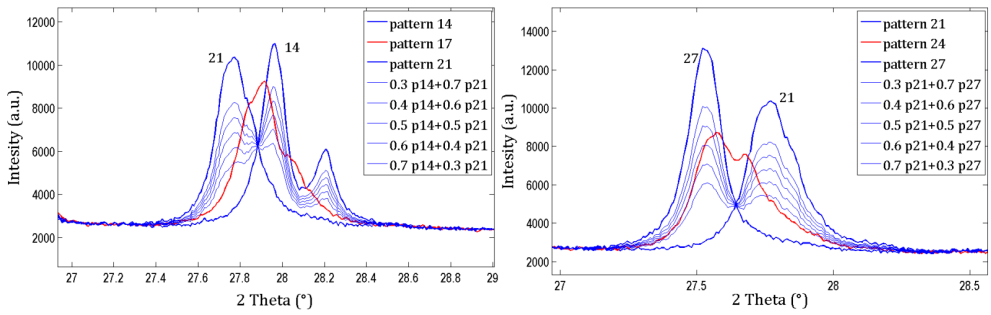

Figure 4.16: (Left) Patterns #14 and #21 are considered as extreme members of the biphasic reaction between $Li_{1.5}VPO_4O$ and $Li_{1.75}VPO_4O$. A perfect biphasic reaction is simulated as x·pattern #14 + (1-x)·pattern #21 (x = 0.3, 0.4, 0.5, 0.6, and 0.7). The simulations can be compared with the experimental pattern #17 (red), corresponding to a composition close to $Li_{1.6}VPO_4O$. (Right) Patterns #21 and #27 are considered as extreme members of the biphasic reaction between $Li_{1.75}VPO_4O$ and Li_2VPO_4O. A perfect biphasic reaction is simulated as x·pattern #21 + (1-x)·pattern #27 (x = 0.3, 0.4, 0.5, 0.6, and 0.7). The simulations can be compared with the experimental pattern #24 (red), corresponding to a composition close to $Li_{1.87}VPO_4O$.

Indeed, in the general case, a 2-phase reaction should not allow any important shift of the cell parameters. We therefore simulated the intermediate patterns as a linear combination of the end members (e.g. pattern #17 simulated as x · pattern #14 + (1-x) · pattern #21 and pattern #24 simulated as x · pattern #21 + (1-x) · pattern #27). As shown in Figure 4.16, the experimental patterns (#17 and #24) recorded at the middle of each "pseudo-plateau" cannot be fitted considering these linear combinations, which seems thus to exclude the straightforward two-phase reactions $Li_{1.5}VPO_4O$ - $Li_{1.75}VPO_4O$ and

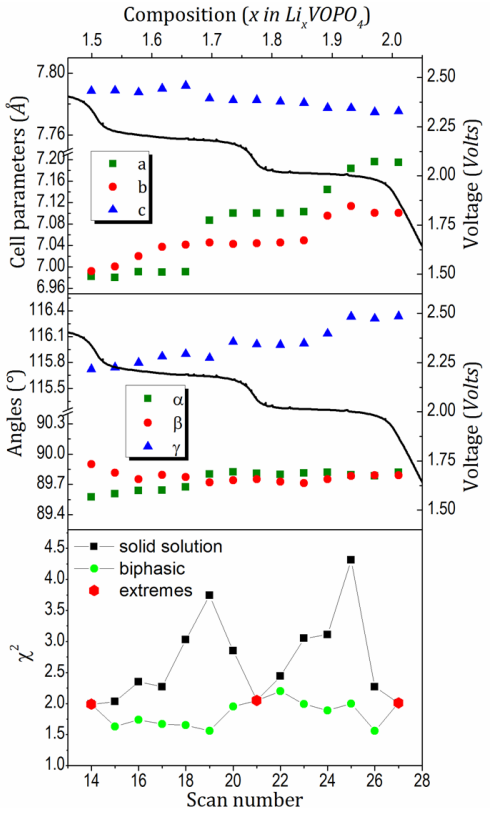

Figure 4.17: (Top and middle) Refined cell parameters (Le Bail fit) for a single phase solid solution between compositions $Li_{1.5}VPO_4O$ and Li_2VPO_4O. Error bars are within the symbols dimension. (Bottom) χ^2 parameters from the single-phase Le Bail fit of the XRPD scans from #14 to #27, compared to χ^2 for a sequence of two biphasic reactions. End members (in red) are $Li_{1.5}VPO_4O$, $Li_{1.75}VPO_4O$ and Li_2VPO_4O.

$Li_{1.75}VPO_4O$ - Li_2VPO_4O. Subsequently, we thus tried to refine all the patterns from #14 to #27 as single phases with variable cell parameters, using a Le Bail fit since the exact crystal structures are not known (many attempts have been done to chemically isolate the intermediate phases $Li_{1.5}VPO_4O$ and $Li_{1.75}VPO_4O$ to determine their crystal structure, but without success; in section 4.4.5 we observed them by *operando* synchrotron XRPD). The cell parameters obtained are plotted in Figure 4.17 and those determined for patterns #1, #14, #21, and #27 are reported in Table 4.6. The lattice parameters variation obtained considering the single-phase model is not fully convincing, since it is not smooth but rather step-like. This suggests the presence of a major phase that dominates the behavior and of a minor one that is almost unseen. Also, the evolution of χ^2 factors (bottom part of Figure 4.17) gives a useful indication since the "important" single-phase compositions (patterns #14, #21 and #27) show good fits while those intermediate between them correspond to significantly increased χ^2 values.

Table 4.6: Cell parameters of selected Li_xVPO_4O compositions, refined in the space group $P\bar{1}$. Vanadium chains run along b.

	a (Å)	b (Å)	c (Å)	α (°)	β (°)	γ (°)	V (Å^3)
$LiVPO_4O$ ref. [271]	6.7320(1)	7.1942(1)	7.9204(1)	89.843(1)	91.272(1)	116.886(4)	342.03(1)
$LiVPO_4O$ (*in situ*)	6.7341(4)	7.1959(5)	7.9177(4)	89.812(5)	91.277(5)	116.910(5)	342.04(3)
$Li_{1.5}VPO_4O$ (*in situ*)	6.9922(3)	6.9820(3)	7.7886(3)	90.099(6)	90.427(5)	115.722(4)	342.54(2)
$Li_{1.75}VPO_4O$ (*in situ*)	7.1002(4)	7.0443(3)	7.7826(4)	89.809(4)	89.753(5)	116.010(6)	349.82(3)
Li_2VPO_4O (*in situ*)	7.1948(6)	7.1009(7)	7.7753(7)	89.820(3)	89.791(4)	116.337(5)	356.00(6)
Li_2VPO_4O (chem.)	7.1989(4)	7.1012(3)	7.7771(3)	89.824(3)	89.812(3)	116.319(3)	356.36(2)

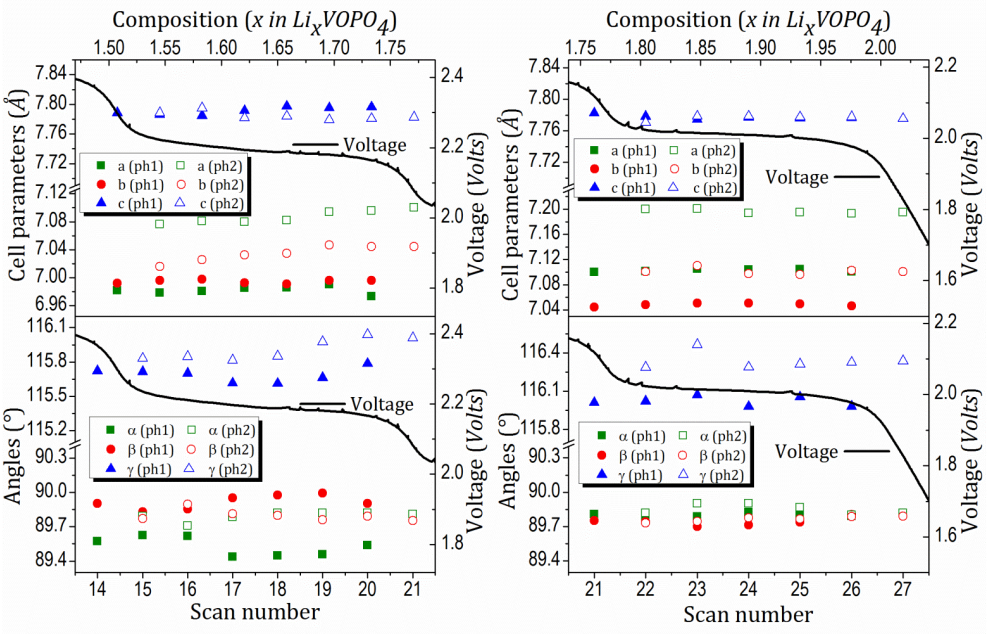

Figure 4.18: Refined cell parameters (Le Bail fit) for a sequence of two biphasic reactions between the compositions $Li_{1.5}VPO_4O$ and $Li_{1.75}VPO_4O$ (left) and between $Li_{1.75}VPO_4O$ and Li_2VPO_4O (right). Error bars are within the symbols dimension.

We therefore decided to carry on the investigation and to refine the patterns #14, #21 and #27 as single phases, while all intermediate compositions were refined with two phases for which the cell parameters were allowed to vary (the zero shift was always fixed thanks to a Beryllium diffraction peak used as reference). The result is shown in Figure 4.18. Despite the presence of two triclinic phases, it is remarkable that the cell parameters do not vary significantly. This is particularly true for a, b and c, while a certain variation of the angles is observed. Two main reasons can be adduced to justify this behavior. The first one is of experimental nature. Indeed, we cannot expect a perfect accuracy from the proposed Le Bail fit, since there are many Bragg positions composing every

apparent peak. As an example, the doublet in the [27.5°-28.5°] region (pattern #14, red in Figure 4.15) is actually composed of 6 different Bragg positions. When the subsequent patterns are considered and two phases are present, the number of Bragg positions in the same peak becomes 12. The second reason is physical and it deals with the fact that the experimental observation of an evolution of the cell parameters in a two phase reaction is not impossible, and has been recently reported for several systems ($NaFePO_4$ [60], $LiFePO_4$ [36], $LiMn_yFe_{1-y}PO_4$ [99], $Li_{1+x}Mn_{2-x}O_4$ [155]...). This can have different causes, like the presence of nanosized particles or important strains at the interface between the transforming phases. Once again, a look at the evolution of the χ^2 factor is relevant, not because of the lower obtained values which are somehow expected having doubled the amount of free parameters, but for the lack of a structure in the χ^2 distribution for the different patterns, which is approximately flat and satisfactory for all of them. Besides, Table 4.6 reveals another interesting fact. The unit cell volume changes only slightly between $LiVPO_4O$ and $Li_{1.5}VPO_4O$ ($\Delta V/V = 0.14\%$), while it changes significantly from $Li_{1.5}VPO_4O$ to Li_2VPO_4O (3.92%). This strong difference may be the explanation for such a dissimilar phase behavior between these composition ranges. The transition from $LiVPO_4O$ to $Li_{1.5}VPO_4O$ involves a very small volume change and it can therefore happen via a perfect first order reaction. On the contrary, the transitions from $Li_{1.5}VPO_4O$ to $Li_{1.75}VPO_4O$ and from $Li_{1.75}VPO_4O$ to Li_2VPO_4O involve a significant volume change (almost 2% for 0.25 lithium atoms) and they thus take place with significant strain in the material, determining a small but observable variation in the cell parameters.

4.4.5 The crystal structures of Li_xVPO_4O (x = 2, 1.75, 1.5)

x = 2

To the best of our knowledge, no detailed description of the crystal structure of Li_2VPO_4O has been reported in the literature so far, besides the values of the cell parameters [303]. We prepared Li_2VPO_4O through chemical reduction of $LiVPO_4O$ and measured the resulting powder on a PANalytical Empyrean X-Ray diffractometer and subsequently on the high resolution powder neutron diffractometer D2B at ILL. The patterns were indexed in the triclinic $P\bar{1}$ space group and the cell parameters retrieved are: a = 7.1989(4) Å, b = 7.1012(3) Å, c = 7.7771(3) Å, α = 89.824(3)°, β = 89.812(3)° and γ = 116.319(3)°. The resulting volume of the unit cell is 356.36(3) $Å^3$. A transformation a' = b, b' = a, c' = -c, α' = 180-β, β' = 180-α and $\gamma' = \gamma$ can be used to find a more standard triclinic setting, where

the cell parameters are a' = 7.1012(3) Å, b' = 7.1989(4), c' = 7.7771(3) Å, α' = 90.188(3)°, β' = 90.176(3)° and γ' = 116.319(4)°. The first setting will be used in the following to allow a better comparison with the structure of $LiVPO_4O$. The obtained parameters are not in good agreement with the previous report [303], but they are remarkably similar to those obtained from the end member of the *in situ* XRPD experiment described in the previous section (Table 4.6).

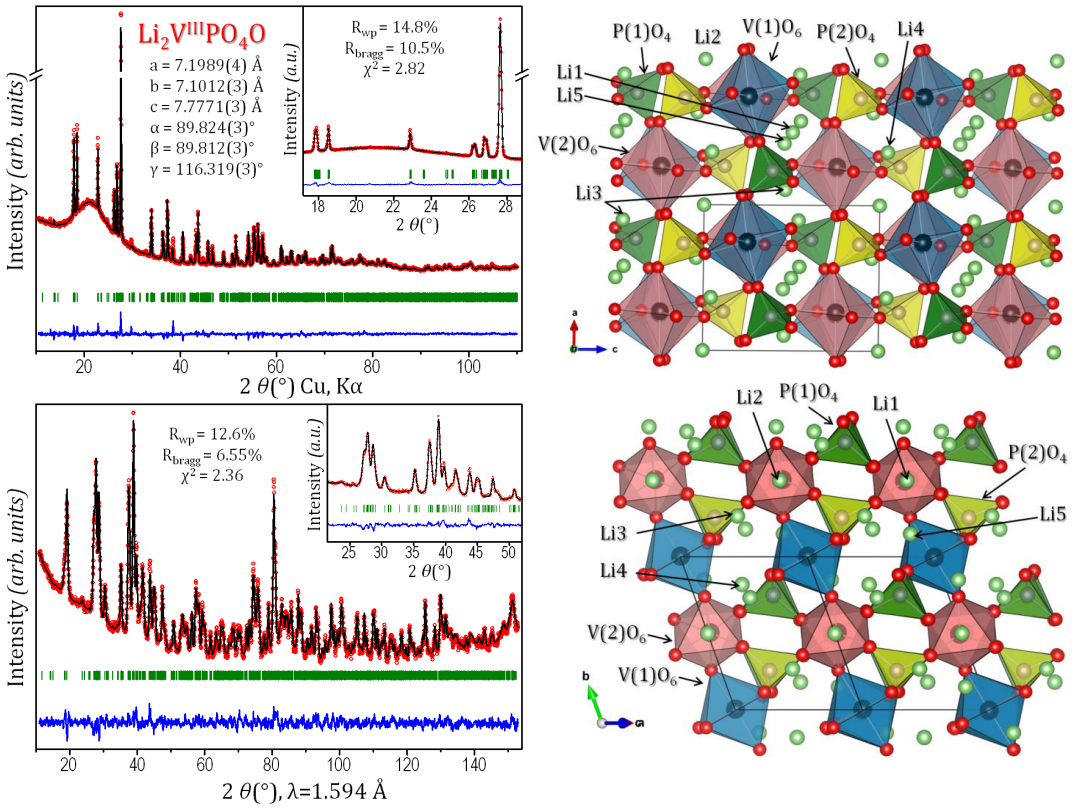

Figure 4.19: Left: (Top) XRPD measurement and Rietveld refinement of Li_2VPO_4O powder in a 0.3 mm diameter capillary. (Bottom) NPD measurement and Rietveld refinement of Li_2VPO_4O placed in a 6.5 mm diameter vanadium container. Right: Crystal structure of Li_2VPO_4O. Lithium positions are indicated.

As generally expected for lithium intercalation and vanadium reduction, the unit cell volume of Li_2VPO_4O (352.36(2) Å^3) is larger than the value obtained for $LiVPO_4O$ (342.03 (1) Å^3) and for VPO_4O (327.93(4) Å^3). In both cases the insertion of one lithium ion expands the unit cell by about 4% of its initial volume. The atomic coordinates of Li_2VPO_4O were subsequently located thanks to the FOX software [304] and the XRPD and NPD patterns refined by the Rietveld method. Li_2VPO_4O shows a double cell analogous to that of $LiVPO_4O$. Since the two different probes are sensitive to different structural parameters,

Table 4.7: Structural parameters obtained from Rietveld refinement of XRPD and Neutron diffraction data of Li_2VPO_4O. Parameters refined using XRPD data are in bold. Isotropic thermal displacement parameters were constrained to be equal for the same type of atom.

Li_2VPO_4O

S.G. $P\bar{1}$; Z=4

a = 7.1989(4) Å; b = 7.1012(3) Å; c = 7.7771(3) Å;
α = 89.824(3)°; β = 89.812(3)°; γ = 116.319(3)°.
V = 356.36 (3) Å^3; V/Z = 89.09 Å^3

XRPD: R_{wp} = 14.8%;
R_B = 10.5%; χ^2 = 2.82
NPD: R_{wp} = 12.6%;
R_B = 6.55%; χ^2 = 2.36

Atomic Parameters

Atoms	Wyckoff	Atomic Positions x/a	y/b	z/c	SOF	B_{iso}
V(1)	2i	**0.748(3)**	**-0.004(3)**	**-0.752(3)**	1	**1.5(2)**
V(2)	2i	**0.734(3)**	**-0.505(3)**	**-0.755(3)**	1	**2.5(2)**
P(1)	2i	0.24(1)	-0.248(9)	-0.612(8)	1	0.8(2)
P(2)	2i	0.27(1)	-0.743(9)	-0.885(8)	1	0.8(2)
O(1)	2i	0.563(5)	-0.910(5)	-0.310(4)	1	0.98(5)
O(2)	2i	0.07(1)	-0.359(9)	-0.755(6)	1	0.98(5)
O(3)	2i	0.721(7)	-0.591(8)	-0.499(6)	1	0.98(5)
O(4)	2i	0.161(8)	-0.117(7)	-0.496(7)	1	0.98(5)
O(5)	2i	0.232(9)	-0.259(8)	-0.152(7)	1	0.98(5)
O(6)	2i	0.064(5)	-0.883(5)	-0.784(4)	1	0.98(5)
O(7)	2i	0.230(7)	-0.588(8)	-0.993(6)	1	0.98(5)
O(8)	2i	0.728(8)	-0.260(8)	-0.652(7)	1	0.98(5)
O(9)	2i	0.57(1)	-0.354(9)	-0.259(6)	1	0.98(5)
O(10)	2i	0.337(8)	-0.877(7)	-0.008(7)	1	0.98(5)
Li(1)	1d	1/2	1/2	1/2	1	2.2(7)
Li(2)	1h	0	1/2	0	1	2.2(7)
Li(3)	2i	0.10(1)	0.27(1)	0.46(1)	1	2.2(7)
Li(4)	2i	0.36(1)	0.82(1)	0.04(1)	1	2.2(7)
Li(5)	2i	0.42(1)	0.15(1)	0.45(1)	1	2.2(7)

both patterns were exploited to obtain the final crystal structure, via successive refinement iterations between the X-Ray and neutron diffraction patterns. For instance, oxygen positions obtained from the X-Ray pattern are not accurate because of the high number of oxygen coordinates (30 independent parameters) and the limited sensitivity of X-Rays to light elements. The obtained results are shown in Figure 4.19, with the resulting representation of the crystal structure. The refined parameters are reported in Table 4.7 as obtained from the neutron diffraction data, with the exception of cell parameters, vanadium's fractional atomic coordinates and isotropic atomic displacement parameters. Bond

Table 4.8: Significant bond length distances of Li_2VPO_4O obtained from Rietveld refinement of XRPD and Neutron diffraction data. Only distances shorter than 2.5 Å are considered. V-O distances along the chains are highlighted in bold. Polyhedral distortion is calculated as $\Delta = 1/N \sum_i (d_i - \langle d \rangle / \langle d \rangle)^2$, bond valences as reported in [255].

Li_2VPO_4O

	V(1)	V(2)	P(1)	P(2)	Li(1)	Li(2)	Li(3)	Li(4)	Li(5)
Coord.	6	6	4	4	6	6	4	5	6
O(1)	2.09(4)	-	1.51(7)	-	-	-	-	2.17(7)	2.23(9) 2.09(9)
O(2)	-	2.17(6)	1.57(8)	-	-	2.11(5) x2	-	2.48(8)	-
O(3)	-	2.07(5)	1.57(9)	-	1.96(6) x2	-	2.10(9)	-	2.15(9)
O(4)	2.10(5)	-	1.55(9)	-	-	-	1.75(9)	-	2.03(9)
O(5)	**1.96(7)**	**1.94(7)**	-	-	-	2.13(5) x2	-	1.75(8)	-
O(6)	2.06(4)	-	-	1.56(6)	-	-	2.15(8)	-	-
O(7)	-	2.04(5)	-	1.50(9)	-	2.01(6) x2	-	-	-
O(8)	**1.92(7)**	**1.93(7)**	-	-	2.12(5) x2	-	1.93(9)	-	2.21(13)
O(9)	-	1.95(6)	-	1.56(8)	2.10(5) x2	-	-	-	2.07(10)
O(10)	2.03(5)	-	-	1.58(9)	-	-	-	2.29(9) 2.01(9)	-
Distor.($\cdot 10^{-4}$)	11.1	18.4	2.6	4.1	10.9	2.6	62.0	135	11.9
BVS	2.8(2)	2.9(2)	4.8(6)	4.8(5)	1.22(8)	1.13(7)	1.1(2)	1.0(1)	1.0(1)

length distances and polyhedral coordinations are reported in Table 4.8. Lithium's fractional atomic coordinates were determined thanks to Fourier difference maps, their location being not straightforward. Indeed, the first 4 lithium positions (Li1 and Li2, Wyckoff positions 1c and 1h, and Li3 and Li4, positions 2i) emerged quite clearly from the maps. The last site(s), required to respect the stoichiometry, was less easily detectable. Finally, the best solution was found from the map with the Li5 atom placed in a 2i site. As can be observed in Table 4.8, V and P environments are in line with those expected, although with significant error bars due to the large number of refined parameters; lithium local environments are also equally plausible, despite two short Li-O distances. No Li-Li distance shorter than 2.3 Å is observed. For all the cations (P^{5+}, V^{3+} and Li^+) the bond valences calculated are in very good agreement with those expected from the chemical formula Li_2VPO_4O. Regarding the vanadium environment, the $V(1)O_6$ and $V(2)O_6$ octahedra in Li_2VPO_4O can be compared to what is expected for $V^{3+}O_6$ polyhedra from the survey of Schindler et al.[281]. Indeed, the 3+ oxidation state in vanadium-centered octahedra is reported to result in an average bond length of 2.01 Å, with a maximum occurrence between 1.98 Å and 2.04 Å and extreme values of 1.88 Å and 2.16 Å. In our structure,

the refined values for Li_2VPO_4O give an average value of 2.03 Å for $V(1)O_6$ and of 2.02 Å for $V(2)O_6$, with all the V-O bond lengths in good agreement with the expected values. Note how the bonds along the chains are significantly shorter than the in-plane bonds in the octahedra.

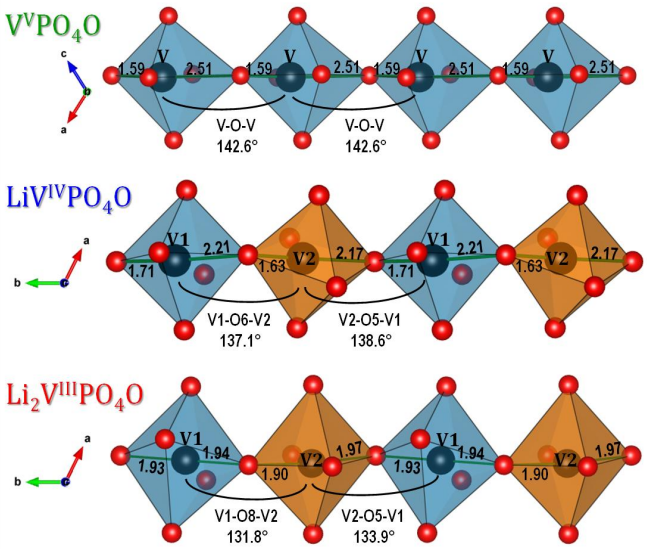

Figure 4.20: Octahedral chains of VPO_4O (top), $LiVPO_4O$ (middle) and Li_2VPO_4O (bottom), with V-O distances and V-O-V angles along the chains.

The V-O octahedral chains of the 3 end-members VPO_4O, $LiVPO_4O$ and Li_2VPO_4O are displayed in Figure 4.20. The general trend is a transition from long and short alternated V-O distances along the chains for V in the 5+ oxidation state (ionic radius 0.54 Å), to progressively more homogeneous ones while the oxidation state decreases to 4+ and then 3+ (ionic radii 0.58 Å and 0.64 Å respectively). The V-O-V angles, as well, diminish from high values (142.6°) to smaller ones (131-134°), while the octahedra show less and less distortions. Consequently and interestingly, the length of the chain diminishes on going from VPO_4O to $LiVPO_4O$ and to Li_2VPO_4O as witnessed by the strong contraction of the b lattice parameter from $LiVPO_4O$ (7.196 Å) to Li_2VPO_4O (7.101 Å) while the unit-cell volume increases (from 342.03 $Å^3$ for $LiVPO_4O$ to 356.44 $Å^3$ for Li_2VPO_4O). This fully supports XANES observations made by other groups[274,275], showing that lithiation of $LiVPO_4O$ progressively eliminates the shortest V=O bond.

x = 1.5 and x = 1.75

We determined the crystal structures of all the end members Li_xVPO_4O (x = 0, 1, 2), but the intermediate phases x = 1.5, 1.75 still remained unknown, except for the cell parameters that we retrieved from our *in situ* XRPD experiment (Table 4.6). Initial attempts to establish these two structures failed because of the difficulty at preparing samples for *ex situ* studies as was done for Li_2VPO_4O. We then decided to use *in situ* synchrotron XRPD to observe them in real time while crystallizing. We carried out our experiment at the MSPD beamline in ALBA, Barcelona. A battery was prepared with $LiVPO_4O$ as positive electrode (mixed with 18% Csp and 11% PTFE), in our custom setup for synchrotron XRPD measurements in transmission geometry [97]. The battery was then discharged slowly at C/32 rate. Due to the limited available beamtime, we did not follow the whole reaction *operando*, but we only put the battery in the beam when the key compositions (x = 1, 1.5, 1.75, 2) were almost formed. This way we were able to capture several 5-minutes diffraction scans of the pure intermediate phases.

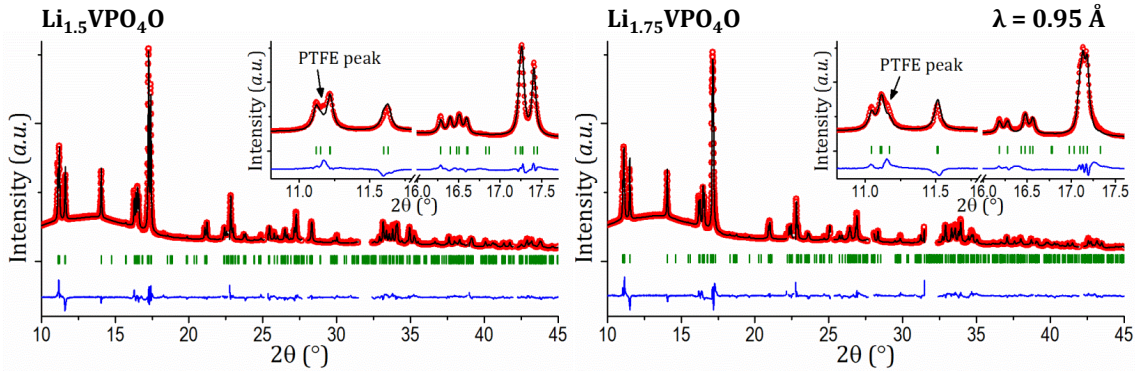

Figure 4.21: *In situ* Synchrotron XRPD measurement and Rietveld refinement of compositions $Li_{1.5}VPO_4O$ (top) and $Li_{1.5}VPO_4O$ (bottom), isolated during electrochemical discharge of $LiVPO_4O$. Most Bragg reflections originated by the experimental setup are easily excluded from the refinement, except for the binder PTFE that overlaps with important reflections of the phases of interest.

The obtained cell parameters are reported in Table 4.9 and Table 4.10. To be consistent with $LiVPO_4O$ and Li_2VPO_4O, all unit cells are set so that the vanadium octahedral chains run along the b axis. Given the good agreement with the cell parameters of Table 4.6, we pursued a structural determination. However, one should note that this is only a partial determination since, as previously mentioned, the triclinic unit cell contains several oxygen and lithium positions and thus the accuracy resulting from synchrotron XRPD measurements is limited. Thanks to the use of the FOX software and to subsequent Rietveld

Table 4.9: Structural parameters obtained from Rietveld refinement of *in situ* synchrotron XRPD data of $Li_{1.5}VPO_4O$. Isotropic thermal displacement parameters were constrained to be equal for the same type of atom. Soft constrains are used on P-O bonds (= 1.530 +/- 0.005).

$Li_{1.5}VPO_4O$

S.G. $P\bar{1}$; Z=4

a = 6.9930(2) Å; b = 6.9778(2) Å; c = 7.7921(2) Å; R_{wp} = 15.3%;
α = 90.133(2) °; β = 90.409(2) °; γ =115.727(2) ° R_B = 11.3%; χ^2 = 21.6
V = 342.52(3) Å^3; V/Z = 85.63 Å^3

Atomic Parameters						
Atoms	Wyckoff	Atomic Positions			SOF	B_{iso}
		x/a	y/b	z/c		
V(1)	2i	0.750(5)	0.992(5)	-0.236(3)	1	1.6(2)
V(2)	2i	0.753(5)	0.507(5)	-0.259(4)	1	1.6(2)
P(1)	2i	0.267(2)	0.766(2)	-0.102(2)	1	2.2(3)
P(2)	2i	0.221(2)	0.268(2)	-0.409(2)	1	2.2(3)
O(1)	2i	0.73(1)	0.24(2)	-0.34(1)	1	2.6(3)
O(2)	2i	0.22(1)	0.23(1)	-0.826(9)	1	2.6(3)
O(3)	2i	0.352(9)	0.632(9)	0.010(6)	1	2.6(3)
O(4)	2i	0.22(1)	0.939(9)	-0.006(6)	1	2.6(3)
O(5)	2i	0.068(6)	0.631(9)	-0.219(5)	1	2.6(3)
O(6)	2i	0.42(1)	0.83(1)	-0.260(6)	1	2.6(3)
O(7)	2i	0.145(9)	0.414(9)	-0.515(6)	1	2.6(3)
O(8)	2i	0.27(1)	0.103(9)	-0.515(6)	1	2.6(3)
O(9)	2i	0.09(1)	0.15(1)	-0.243(6)	1	2.6(3)
O(10)	2i	0.442(5)	0.410(9)	-0.322(6)	1	2.6(3)

refinement (Figure 4.21) we obtained the two structures nonetheless (except for the lithium sites). Their structural parameters are reported in Table 4.9 and Table 4.10, while bond-length distances are in Table 4.11. The 3D framework of $Li_{1.5}VPO_4O$ and $Li_{1.75}VPO_4O$ clearly resembles very much $LiVPO_4O$'s one. The observed decrease of the unit cell volume is in good agreement with vanadium's gradual reduction, as are the calculated vanadium bond-valence sum (BVS) values. In $Li_{1.5}VPO_4O$, the presence of two sites $V(1)^{3.8(5)+}$ and $V(2)^{3.2(3)+}$ suggests an alternation of V^{4+} and V^{3+} environments along the chains. In $Li_{1.75}VPO_4O$ V(1) still shows a slightly higher oxidation state than V(2): 3.4(3)+ vs. 3.1(3)+, giving on average exactly the expected 3.25+. The V-O bond-lengths along the chains offer less clear indications because of the significant error bars on oxygen positions; however one can observe that, in $Li_{1.5}VPO_4O$, V(1) possesses alternated long-short bonds, as is the case for V^{4+}, while V(2) has more homogeneous bonds, as for V^{3+}. This agrees

Table 4.10: Structural parameters obtained from Rietveld refinement of *in situ* synchrotron XRPD data of $Li_{1.75}VPO_4O$. Isotropic thermal displacement parameters were constrained to be equal for the same type of atom. Soft constrains are used on P-O bonds (=1.530 +/- 0.005).

$Li_{1.75}VPO_4O$

S.G. $P\bar{1}$; Z=4

a = 7.1019(3) Å; b = 7.0414(3) Å; c = 7.7926(3) Å; R_{wp} = 18.0%;
α = 89.815(3) °; β = 89.742(2) °; γ =116.015(3) ° R_B = 13.1%; χ^2 = 28.2
V = 350.19(3) Å^3; V/Z = 87.55 Å^3

Atomic Parameters

Atoms	Wyckoff	Atomic Positions			SOF	B_{iso}
		x/a	y/b	z/c		
V(1)	2i	0.750(5)	0.992(5)	-0.236(3)	1	1.6(2)
V(2)	2i	0.753(5)	0.507(5)	-0.259(4)	1	1.6(2)
P(1)	2i	0.267(2)	0.766(2)	-0.102(2)	1	2.2(3)
P(2)	2i	0.221(2)	0.268(2)	-0.409(2)	1	2.2(3)
O(1)	2i	0.73(1)	0.24(2)	-0.34(1)	1	2.6(3)
O(2)	2i	0.22(1)	0.23(1)	-0.826(9)	1	2.6(3)
O(3)	2i	0.352(9)	0.632(9)	0.010(6)	1	2.6(3)
O(4)	2i	0.22(1)	0.939(9)	-0.006(6)	1	2.6(3)
O(5)	2i	0.068(6)	0.631(9)	-0.219(5)	1	2.6(3)
O(6)	2i	0.42(1)	0.83(1)	-0.260(6)	1	2.6(3)
O(7)	2i	0.145(9)	0.414(9)	-0.515(6)	1	2.6(3)
O(8)	2i	0.27(1)	0.103(9)	-0.515(6)	1	2.6(3)
O(9)	2i	0.09(1)	0.15(1)	-0.243(6)	1	2.6(3)
O(10)	2i	0.442(5)	0.410(9)	-0.322(6)	1	2.6(3)

with the indication obtained by BVS. In $Li_{1.75}VPO_4O$ instead no conclusion can be drawn because both vanadium have long and short bonds and the octahedra are significantly more distorted (possibly because of inhomogeneous distribution of different octahedra). A few interesting remarks can be done on the evolution of the cell parameters during discharge: the biphasic reaction from $LiVPO_4O$ to $Li_{1.5}VPO_4O$ is quite peculiar because, although the two phases have similar unit cell volume, their cell parameters are significantly different. Contrary to what is expected, the crystallizing phase $Li_{1.5}VPO_4O$ has a shorter b axis length than $LiVPO_4O$, hence shorter octahedral chains. c is also slightly shorter, while a is much longer in $Li_{1.5}VPO_4O$. As for the angles, while α is poorly modified, both β and γ are decreased in $Li_{1.5}VPO_4O$. The newly forming phase thus privileges increased a and α parameters, indicating bigger distances between neighbouring chains, driven by lithium's insertions into the structure's tunnels (only partially compensated by the shorter

Table 4.11: Significant bond length distances of $Li_{1.5}VPO_4O$ and $Li_{1.75}VPO_4O$ obtained from Rietveld refinement of XRPD and Neutron diffraction data. V-O distances along the chains are highlighted in bold. Polyhedral distortion is calculated as $\Delta = 1/N \sum_i (d_i - \langle d \rangle / \langle d \rangle)^2$, bond valences as reported in [255].

$Li_{1.5}VPO_4O$	V(1)	V(2)	P(1)	P(2)	$Li_{1.75}VPO_4O$	V(1)	V(2)	P(1)	P(2)
O(1)	**1.98(12)**	**1.91(11)**	-	-		**1.67(9)**	**2.21(9)**	-	-
O(2)	**1.70(12)**	**1.89(11)**	-	-		**2.01(9)**	**1.73(9)**	-	-
O(3)	-	2.16(6)	1.57(7)	-		2.22(6)	-	1.57(6)	-
O(4)	1.93(5)	-	1.58(7)	-		2.24(5)	-	1.57(3)	-
O(5)	-	2.00(5)	1.58(4)	-		-	1.95(5)	1.56(3)	-
O(6)	2.09(8)	-	1.57(4)	-		-	2.00(6)	1.56(6)	-
O(7)	-	1.90(5)	-	1.57(7)		-	2.13(5)	-	1.56(6)
O(8)	2.03(5)	-	-	1.57(7)		-	2.11(5)	-	1.57(5)
O(9)	2.15(8)	-	-	1.59(5)		1.91(5)	-	-	1.57(6)
O(10)	-	2.03(5)	-	1.58(3)		1.99(5)	-	-	1.57(4)
BVS	3.8(5)	3.2(3)	4.5(4)	4.4(4)		3.4(3)	3.1(3)	4.6(3)	4.6(3)
Dist.($\cdot 10^{-4}$)	53.1	22.5	0.09	0.2		91.3	58.8	0.2	0.2

inter-chains distance along the c axis: Δa = 0.26 Å, Δc = - 0.13 Å). The strong decrease of b (Δb = - 0.23 Å) is instead surprising, as the opposite could be expected from vanadium's reduction. This is probably due to a change in the conformation of the chains, but a detailed analysis would require more precise knowledge of the V-O bond lengths and V-O-V angles along the chains. On the other hand, the reaction from $Li_{1.5}VPO_4O$ to $Li_{1.75}VPO_4O$ to Li_2VPO_4O follows a clear trend: b continuously increases and the same is true for a, while c remains almost constant. Regarding the three angles, they show small variations, except for γ which increases from 115.75° to 116.3°. Note that $Li_{1.5}VPO_4O$ is the only phase with both α and β slightly bigger than 90°, while they are slightly smaller in the other two phases. The insertion of 0.5 Li^+ into $Li_{1.5}VPO_4O$ in this case causes the expected gradual increase of the chains length, but also further increase of the tunnels size via an augmented a cell parameter; finally, the increase of γ probably relates to the variation of the chains conformation (i.e. the V-O-V angles which can also be modified). From this study we obtained a satisfactory but yet incomplete picture of these intermediate phases $Li_{1.5}VPO_4O$ and $Li_{1.5}VPO_4O$. They revealed to be quite tricky, because of the difficulty at isolating them *ex situ* and because of the triclinic nature of their unit cells and the light elements present. *In situ* NPD would be a desirable choice for a complementary experiment; however we had already attempted this experiment on $LiVPO_4O$, but without success mainly because of the difficulty to obtain a proper electrochemical behaviour from

200 mg-electrodes of $LiVPO_4O$, but also because of the limited angular resolution of NPD measurements and the limited intensity obtained from *operando* experiments, both real issues when the experiment is applied to a material with triclinic crystal structure.

4.5 Conclusions and perspectives

This chapter presented the electrochemical properties and structural modifications upon cycling of two vanadium phosphates of great interest for Li-ion batteries: $LiVPO_4F$ and $LiVPO_4O$. Both materials show energy densities among the highest achievable in polyanionic compounds, and moreover they have the ability to (de)intercalate two Li^+ cations per formula unit, which potentially doubles the available capacity. We specifically concentrated on the understanding of the structural modifications occurring upon Li^+ exchange, since this could be the key to allow the exploitation of the full potential of such materials. Our studies made combined use of *in situ* & *operando* XRPD, supported by *ex situ* neutron powder diffraction measurements for the precise determination of oxygen's and lithium's behaviour inside the triclinic structures of these materials. In the case of $LiVPO_4F$, we presented the reactions that bring the material to VPO_4F, through the extraction of Li^+ around 4.2 V vs. Li^+/Li: these are two biphasic processes, separated by the crystallization of the intermediate phase $Li_{0.67}VPO_4F$. At lower potential (1.8 V), $LiVPO_4F$ reacts to form Li_2VPO_4F following a single biphasic reaction.

Most of the work we carried out concerned $LiVPO_4O$, homeotypic to $LiVPO_4F$. In its high-voltage domain (Li^+ extraction at 3.95V vs. Li^+/Li) we demonstrated how particles size plays a crucial role during the electrochemical process: in fact, the big μm-size particles we obtain from the ceramic synthesis prevent reaching the theoretical capacity. We proved this by *in situ* XRPD; the study also indicated a Bragg peaks' broadening, showing how the material undergoes a form of "electrochemical grinding" upon prolonged cycling, which spontaneously improves the obtained capacity. The final member of such a reaction is ϵ-VPO_4O, which we confirmed to belong to the Cc space group. In the lower voltage region, lithiation of $LiVPO_4O$ can be achieved through a complex series of phase transformations: a first biphasic reaction at 2.5 V leading to $Li_{1.5}VPO_4O$; a second one at 2.2 V until composition $Li_{1.75}VPO_4O$, and a final one at 2 V to reach the end member Li_2VPO_4O. An insightful *operando* XRPD experiment was carried out using Cu Kα_1 radiation to take advantage of the best available angular resolution and well distinguish the Bragg reflections of the triclinic phases involved. It showed how the volume change between the

end members is a key parameter to determine the nature of the biphasic reaction observed: crystallographic phase transitions which involve small volume changes give rise to perfect biphasic reactions, while significant volume changes induce stress at the phases interface and a consequent variation of the cell parameters in the process.

The crystal structures of the above-mentioned phases were also determined for the first time: Li_2VPO_4O's structure was completely described in the $P\bar{1}$ space group thanks to a combined *ex situ* XRPD-NPD approach; interestingly, we noticed how vanadium's oxidation state in the real engine promoting the transformation of the octahedral chains: long-short alternated bonds were present along the chain in ϵ-VPO_4O, but as vanadium is reduced from 5+ to 4+ and then 3+, such V-O bonds become more regular and the octahedra less distorted. For the intermediate phases $Li_{1.5}VPO_4O$ and $Li_{1.75}VPO_4O$, which revealed to be more difficult to prepare for *ex situ* studies, *in situ* synchrotron XRPD was used to determine the structures, although the contribution of neutrons will still be needed in forthcoming studies to completely describe lithium's features. Further perspective work include the optimisation of $LiVPO_4O$'s particle size, since as discussed above this parameter is crucial to obtain full capacity both at high and low potential (in fact, long ball milling time are necessary at the moment). In the longer term, the goal is to achieve the functioning of Li_xVPO_4O in the full range $0 \leq x \leq 2$ while reducing the volume changes that would limit the use of this material on the two-cations intercalation reaction in real batteries. Finally, note that the tavorite crystal structure can accommodate several compositions, and among these several different polymorphs, possibly showing various degrees of electrochemical activity; therefore the research activity on materials belonging to this family will continue searching for new compositions with improved energy density and, possibly, able to exchange more than one Li^+/f.u..

Chapter 5

$Na_3V_2(PO_4)_2F_3$: a fluorophosphate for Na-ion batteries

5.1 Introduction

In the Introduction of this thesis it was discussed how Na-ion is one of the most promising candidates to replace Li-ion when looking for a lower-cost and abundant elements-based battery technology for storage grid applications. In this chapter we investigate a polyanionic material, $Na_3V_2(PO_4)_2F_3$, showing performances among the best ever achieved for a positive electrode for Na-ion batteries. This fluorophosphate also has an incredibly rich crystal chemistry, that we analyzed in details at different temperatures and different compositions upon Na^+ deintercalation, to provide a comprehensive phase diagram and understand its crystallographic transformations. $Na_3V_2^{III}(PO_4)_2F_3$ was first proposed by Barker et al.[305,306] as a positive electrode for Li-ion batteries vs. lithium or graphite to substitute the Na^+ cations for Li^+. It showed promising properties from the beginning, with a theoretical capacity of 128 mAh/g that could be experimentally obtained at an average potential of 3.95 V vs. Na^+/Na. More precisely, the extraction of 2 Na^+ ions has been demonstrated (Figure 5.1) following two main voltage-composition plateaus at about 3.7 V and 4.2 V vs. Na^+/Na, delivering ≈507 Wh/kg[305–307]. This value is comparable to commercial positive electrodes developed for Li-ion batteries such as $LiFePO_4$ (580 Wh/kg) and $LiMn_2O_4$ (480 Wh/kg). However this only includes the extraction/reinsertion of two sodium ions per formula unit. The extraction of the third one could increase the theoretical capacity up to a maximum value of 192.4 mAh/g, although this has not been proved to be possible in a Na-ion cell yet[75,308]. The deintercalation of the third sodium around 5

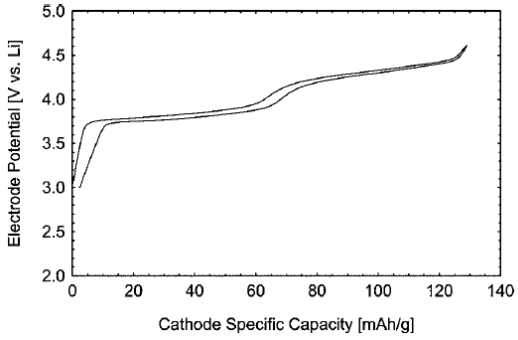

Figure 5.1: Voltage profile upon galvanostatic cycling of a typical Li//$Na_3V_2(PO_4)_2F_3$ cell between 3 - 4.6 V vs. Li^+/Li. Reprinted from [305].

V could lead to a huge energy density (> 800 Wh/kg), but this goal could not be easily achieved because of the high voltage involved, lying outside the stability window of available electrolytes [75]. The group of J.B. Goodenough [309] recently reported theoretical calculations showing that such a high voltage is due to the strong Coulombic attraction between Na^+ and the structure's anions. It was suggested that swapping the O and F anions to the less-electronegative Cl and Br ones could facilitate the extraction. It is worth mentioning again that $Na_3V_2(PO_4)_2F_3$ belongs to a family of compositions that can be written as $Na_3V_2O_{2\delta}(PO_4)_2F_{3-2\delta}$ $(0 \leq \delta \leq 1)$ [71,73,75,310]. Here, depending on δ, the oxidation state of vanadium varies between 3+ and 4+ with a concomitant modification of the physical properties and of the electrochemical signature of the material. In this family, $Na_3V_2^{III}(PO_4)_2F_3$ ($\delta = 0$) is one of the end members and it is the most interesting composition in terms of energy density. The crystal structure of $Na_3V_2(PO_4)_2F_3$ has been described in 1999 by Le Meins et al. [311], belonging to the tetragonal $P4_2/mnm$ space group. However this structure is in contrast with our recent observations [312], and in the next section we will thoroughly describe our new structural determination.

The fact that we found a new crystal structure for $Na_3V_2(PO_4)_2F_3$ is not completely surprising. In fact, despite recent published studies [308,315], some of the properties of $Na_3V_2(PO_4)_2F_3$ have not been observed in sufficient details yet: for instance, a close look at the literature reveals quite strong discrepancies [313] between the structural unit cell parameters of "$Na_3V_2(PO_4)_2F_3$", as gathered in Table 5.1. The reason for this is the versatility of vanadium towards oxidation/reduction and the concomitant existence of possible F/O mixing and substitution in the $Na_3V_2O_{2\delta}(PO_4)_2F_{3-2\delta}$ framework. Moreover, these stoichiometry issues may have profound impact on the electrochemical signature of these compositions, when used as positive electrodes in Na batteries, involving the V^{3+}/V^{4+}

Table 5.1: Space group and cell parameters of $Na_3V_2(PO_4)_2F_3$ (and other $Na_3V_2O_{2\delta}(PO_4)_2F_{3-2\delta}$ compositions) as gathered from the literature. # combined refinement.

Reference		Space group	a (Å)	b (Å)	c (Å)	Vol. (Å^3)	Announced composition
Hao [313]		$P4_2/mnm$	9.15	9.15	10.86	909.22	$Na_3V_2(PO_4)_2F_3$
Gover [306]		$P4_2/mnm$	9.0378(3)	9.0378(3)	10.7482(4)	877.94(6)	$Na_3V_2(PO_4)_2F_3$
Chihara [308]		$P4_2/mnm$	9.04	9.04	10.74	877.69	$Na_3V_2(PO_4)_2F_3$
Liu [314]		$P4_2/mnm$	9.04	9.04	10.735	877.5	$Na_3V_2(PO_4)_2F_3$
Shakoor [315]	XRD	$P4_2/mnm$	9.04(5)	9.04(5)	10.73(9)	876.9(4)	$Na_3V_2(PO_4)_2F_3$
	ND		9.034(3)	9.034(3)	10.740(8)	876.7(3)	
	DFT		9.034	9.034	10.679	871.5	
Le Meins [311]		$P4_2/mnm$	9.047(2)	9.047(2)	10.705(2)	876.2(3)	$Na_3V_2(PO_4)_2F_3$
Song [316]		$P4_2/mnm$	9.05	9.05	10.679	874.64	$Na_3V_2(PO_4)_2F_3$
Barker [305]		$P4_2/mnm$	9.0304(5)	9.0304(5)	10.6891(9)	871.68	$Na_3V_2(PO_4)_2F_3$
Serras [71]		$P4_2/mnm$	9.04258	9.04258	10.62738	869.0	$Na_3V^{III}_{0.4}(V^{IV}O)_{1.6}(PO_4)_2F_3$
Tsirlin [317]		$P4_2/mnm$	9.03051(2)	9.03051(2)	10.62002(3)	866.06	$Na_3(VO)_2(PO_4)_2F$
Our work	XRD	$P4_2/mnm$	9.0358(2)	9.0358(2)	10.7403(4)	876.90(4)	$Na_3V_2(PO_4)_2F_3$
	ND		9.0358(2)	9.0358(2)	10.7412(4)	876.98(5)	
	Synchro.		-	-	-	-	
Our work	XRD	Amam	9.0288(6)	9.0426(6)	10.7402(5)	876.88(9)	$Na_3V_2(PO_4)_2F_3$
	ND#		9.02847(3)	9.04444(3)	10.74666(6)	877.544(6)	
	Synchro.#		9.02847(3)	9.04444(3)	10.74666(6)	877.544(6)	

and/or the V^{4+}/V^{5+} redox couples. Contrary to the two ($\Delta V = 0.5$ V, Figure 5.1) or even three voltage domains previously reported upon Na^+ extraction [308,314–316], we found indeed that Na^+ extraction from stoichiometric $Na_3V^{III}_2(PO_4)_2F_3$ towards $Na_1V^{IV}_2(PO_4)_2F_3$ proceeded reversibly through four oxidation potential steps, as displayed in Figure 5.2 and as already reported by some of us in [75]. The relation between these features and the crystal structure of $Na_3V_2(PO_4)_2F_3$ will be discussed in the following: indeed, the precise mechanism associated with such a complex electrochemistry is described in section 5.3, where we investigate this by *in situ* / *operando* Synchrotron X-Ray powder diffraction.

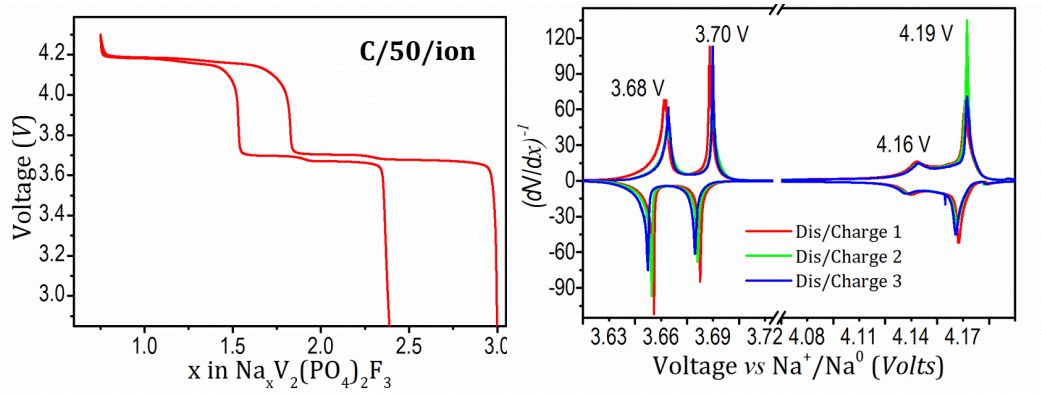

Figure 5.2: Galvanostatic cycling of a $Na_3V_2(PO_4)_2F_3$ // Na battery at C/50 rate per exchanged ion. Left: first cycle. Right: inverse derivative curve $(dV/dx)^{-1}$ for the first 3 cycles, showing the presence of four distinct electrochemical features.

5.1.1 Experimental

Characterization of $Na_3V_2(PO_4)_2F_3$

The static molar magnetic susceptibility of $Na_3V_2(PO_4)_2F_3$, ($\chi(T) = M(T)/H$ with H = 1 T as the magnetic field and M as the magnetization) was measured between 5 and 300 K using a SQUID magnetometer (Quantum Design). The zero-field cooled χ values were obtained by cooling the sample in zero field down to 5 K and then heating it under the measuring field. The diamagnetic contributions were corrected using the atomic values from Bain and Berry[318], yielding the final paramagnetic susceptibility χ_M.

High resolution scanning electron microscopy (SEM) analysis of metalized samples (Pd deposited) was performed using a Hitachi S-4500 microscope. Prior to the observation by electron microscopy, a suspension was obtained by grinding the material in hexane, a droplet of this suspension being deposited on a formvar carbon film supported on a copper grid. Electron diffraction experiments were carried out on many crystallites and very reproducible results were observed. The particles studied were chosen as isolated as possible. Electron diffraction patterns were obtained using a JEOL 2100. The electrochemical signature of the $Na_3V_2(PO_4)_2F_3$ active material was measured in Swagelok cells. The composite electrodes were prepared using 75 wt.% of active material, 12.5 wt.% of Carbon Super P and 12.5 wt.% of PVDF binder. Then the slurry of this mixture was cast on an Al foil with a 25 μm casting thickness and dried at 85 °C for 24 hours. A 1 M solution of $NaPF_6$ in PC (Aldrich) was used as electrolyte. Glass microfiber filters (Whatman) were used as separators and metallic sodium was used as negative electrode. During galvanostatic cycling the electrochemical

cell was charged and discharged at a current rate equivalent to C/50, meaning in the case of $Na_3V_2(PO_4)_2F_3$ the extraction/insertion of each Na^+ ion within 50 hours.

Diffraction data were collected on a number of instruments: laboratory X-Ray diffraction was performed on a PANalytical Empyrean diffractometer using Cu K$\alpha_{1,2}$, the powder being sealed in a 0.3 mm capillary used in Debye-Scherrer geometry. Synchrotron radiation XRPD data at room temperature were collected at the CRISTAL diffractometer of the SOLEIL synchrotron facility, at 0.6687 Å in the 5° - 50° 2θ angular range. High and low temperature measurements were performed at the MSPD beamline of the ALBA synchrotron facility (λ = 0.6198 Å and 0.6200 Å, respectively)[119]. Neutron diffraction data were acquired at the D2B high-resolution powder diffractometer of the ILL, at the wavelength of 1.594 Å, calibrated with a $Na_2Ca_3Al_2F_{14}$ (NACALF) reference. For more experimental information about the beamlines, see the Introduction. Diffraction data treatment and Rietveld refinements were performed using the FullProf Suite[177].

Operando synchrotron XRPD experiments

Electrodes were prepared by mixing $Na_3V_2(PO_4)_2F_3$ with Carbon Super P (Csp) as a conductive additive and Polyvinylidene fluoride (PVDF) as a binder (84:10:6 wt.%) and grinding them in a mortar until an homogeneous paste was obtained. Small pellets of ≈5 mm diameter and ≈300 μm thickness were used in our *in situ* cell for transmission experiments at synchrotron facilities[97]. The use of a binder is fundamental because it allows overcoming the problem of spatially-inhomogeneous electrodes observed while cycling in the *in situ* cell[98]. The active part of the cell is composed of layers of positive electrode, glass fiber separators (Whatman) wet with 1M $NaPF_6$ in EC:PC (1:1) electrolyte and sodium metal as a counter electrode. The stack is inserted between two Beryllium windows, acting as X-Ray-transparent current collectors. The internal pressure within the cell is applied through a spring to ensure optimal electrical contact.

Two batteries were prepared in two separate *in situ* cells. The first voltage-composition plateau was measured using a GITT (Galvanostatic Intermittent Titration Technique) protocol, for which steps of 5 minutes of charge and 5 minutes of relaxation are alternated. During charging steps, the current rate was set to be C/5 (extraction of 1 Na^+ ion in 5 hours in this case). Upon cycling, 5 minutes diffraction scans were continuously recorded during the 5' charge - 5' relaxation sequence. For the observation of the second voltage-composition plateau, the second cell was cycled off-line through the first voltage-composition plateau

and kept at the composition $Na_2V_2(PO_4)_2F_3$ until we could mount it on the instrument. Since in the first experiment we did not observe any significant evolution between subsequent scans recorded upon charge and relaxation, a continuous electrochemical cycling at C/5 rate was used (with 10 minutes relaxation times every 0.25 Na^+ exchange), while recording again diffraction scans continuously every 5 minutes.

Operando synchrotron radiation diffraction measurements were performed at the MSPD beamline[119] of the ALBA synchrotron. The experiment was carried out as described in the Introduction, in transmission geometry, at the operating wavelength of $\lambda = 0.9535(1)$ Å as refined using a NIST standard silicon sample (NIST SI640D). Powder diffraction patterns were collected using the MYTHEN detector. The full width at half maximum (FWHM) for representative peaks of the pristine phase is 0.022° at $2\theta = 17.15°$ (increasing to 0.04° towards the highest angles) and the signal-to-noise ratio for the most intense peak is ≈36. Table 5.5 (section 5.3) compares refinements outputs of the pristine phase from data collected in capillaries with actual results obtained using the *in situ* cell setup. Note that the use of the *in situ* cell only slightly increases the error bars, allowing refinements of all atomic parameters, including isotropic thermal factors B_{iso} (constraint to be equal for the same type of atoms) and site occupancy factors (SOFs) for sodium. However when performing Rietveld refinements on data collected using the *in situ* cell a few precautions have to be taken:

- The beam is going through all the layers stacked in the battery, generating Bragg peaks from sodium (often textured) and Beryllium (two windows displaced one with respect to the other). Detailed knowledge of the pristine phase allows eliminating the (narrow) 2θ regions where these peaks appear. In the following, Figure 5.3 shows the full measured 2θ range, indicating the position of the extra-Bragg peaks.

- Each layer suffers differently from X-Ray absorption. Beryllium is a light element and its absorption (0.24 cm^{-1}) can be neglected at this energy. Sodium metal is heavier but the absorption (24.9 cm^{-1}) can still be neglected as sodium is crossed before the sample. The absorption from the sample itself is important and it is taken into account using the correction factor for flat-plate samples in transmission geometry implemented in the Fullprof suite (approximately mt = 1, where m = 36.7 cm^{-1} is the absorption and t = 300 μm is the sample's thickness).

- Because the sample is enclosed in the *in situ* cell, hence not visible, it is impossible

to precisely position the sample in the center of the goniometer by standard optical alignment means. To correctly refine the data, both a zero-shift and a systematic shift ($\sin\theta$ dependence) correction are hence needed to compensate a possible misalignment of the sample. As a first step we thus used the pristine $Na_3V_2(PO_4)_2F_3$, whose unit cell parameters are well known, to determine zero-shift and systematic shift. As a second step we fixed these two parameters throughout all the subsequent refinements. Again, data treatment and Rietveld refinements [87] were performed using the Fullprof Suite [177].

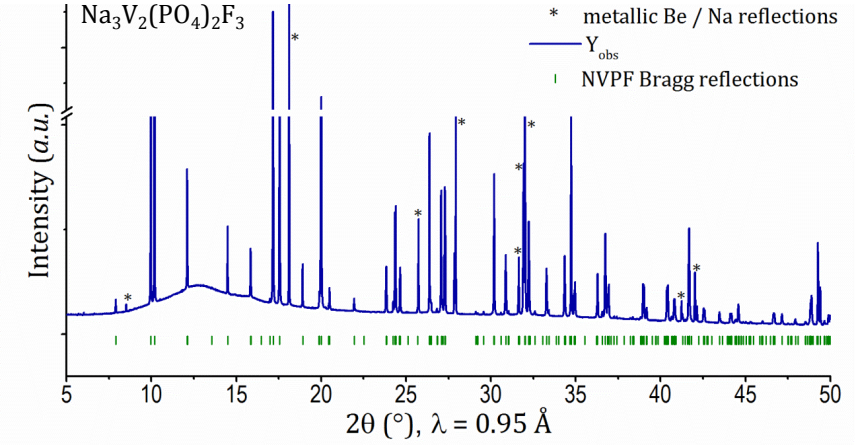

Figure 5.3: Whole angular range obtained from synchrotron radiation diffraction measurement of $Na_3V_2(PO_4)_2F_3$ *in situ* in our electrochemical cell. Extra Bragg reflections (from sodium and beryllium) are marked with an asterisk.

A sample of nominal composition $Na_2V_2(PO_4)_2F_3$ was also prepared *ex situ* by chemically oxidizing $Na_3V_2(PO_4)_2F_3$ with nitronium tetrafluoroborate (NO_2BF_4) in acetonitrile media. The resulting powder was washed, sealed in a 0.5 mm diameter capillary and then measured under the same experimental conditions.

5.1.2 Synthesis of $Na_3V_2(PO_4)_2F_3$

The synthesis of $Na_3V_2(PO_4)_2F_3$ was performed by Nicolas Brisset, Philippe Dagault and Gwenaël Lepage (ICMCB). It consists of two steps, following a procedure similar to the one patented by Barker et al. [272], where VPO_4 was used as an intermediate phase.

$$\frac{1}{2}V_2O_5 + (NH_4)_2HPO_4 + C_{sp} \rightarrow \frac{3}{2}H_2O + 2NH_3 + CO + c*VPO_4 \quad (5.1)$$

$$2c*VPO_4 + 3NaF \rightarrow Na_3V_2(PO_4)_2F_3 \quad (5.2)$$

The presence of Csp in reaction (1) (in the form of highly-divided soot) is necessary to allow for the carbothermal reduction of vanadium from 5+ to 3+. For reaction 5.1, the precursors V_2O_5, $(NH_4)_2HPO_4$ and Csp were mixed in a planetary grinder FRISTSCH Mono Mill for 12 hours at 400 rpm. The mixture was then pressed in a pellet and heated for 5 hours at 300 °C in an alumina crucible to evaporate possible ammonia residues. For homogenization the obtained product was milled again for 4 hours at the same speed and a pellet remade. This was finally heated at 800 °C for 5 hours to allow the carbothermal reduction and the formation of carbon coated VPO_4 (c-VPO_4).

For reaction 5.2, c-VPO_4 and NaF were mixed in a planetary grinder and then pressed in a pellet. This was placed in a gold tube (10 mm diameter) under argon. The tube was subsequently sealed and heated for 1 hour at 800 °C. Note that the oven was systematically pre-warmed and the chemicals were exposed to a steep temperature gradient. Finally, the tube was cooled at ambient temperature in about 15 minutes. The phase was obtained almost pure, with small amounts of Na_3VF_6 and $Na_5P_3O_{10}$ as impurities, subsequently eliminated by washing in water while stirring.

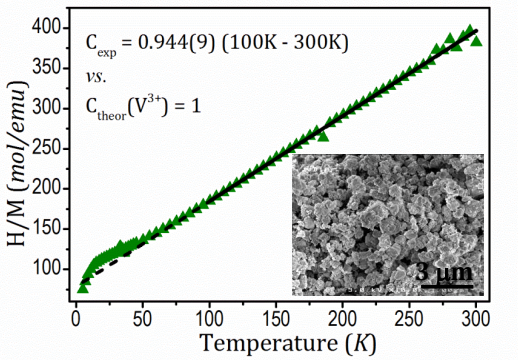

Figure 5.4: SQUID measurement of $Na_3V_2(PO_4)_2F_3$ between 5 K and 300 K. Inset: SEM image of metalized sample.

The resulting $Na_3V_2(PO_4)_2F_3$ powder is of high-purity and composed of 4-5 μm large particles aggregates, formed by the agglomeration of 100-300 nm smaller particles (Figure 5.4). The precise chemical composition of $Na_3V_2(PO_4)_2F_3$ was confirmed by means of an ICP-OES spectrometer (Varian 720-ES Optical Emission Spectrometer) after complete dissolution of the powder into a hydrochloric acid solution. Ratios of Na/V=1.55, Na/P=1.60 and V/P=1.03 were found, which agree rather well with the expected stoichiometry (1.50, 1.50 and 1.00, respectively). To further confirm the value found for the vanadium oxidation state we performed magnetic susceptibility measurements. Figure 5.4

reports the resulting $1/\chi_M$ versus temperature, showing a typical behavior of the Curie-Weiss law for paramagnetic materials. A linear fit of the data in the 100 - 300 K region leads to a value for the Curie constant of C = 0.944(9), in remarkable agreement with the previous report of Le Meins et al.[311] and with the approximate theoretical value of C = 1, obtained as χT=1/8 n(n+2), where n is the number of unpaired electrons, i.e. n=2 for V^{3+} which has $4s^0 3d^2$ electronic configuration. The antiferromagnetic behavior of the material is also described by a Néel temperature θ_N = 74 K.

It is worth mentioning that numerous other synthesis techniques can be used to prepare $Na_3V_2(PO_4)_2F_3$, as recently reported by different groups. Liu et al.[314] propose a two step process with intermediate c-VPO_4, but with different precursors in the first step: in particular, they use citric acid as both a chelating species and a carbon source. Song et al.[316] instead, make use of a single-step process based on CTR. Finally, Zhao et al.[319] propose a phase-transfer assisted solvothermal strategy to achieve low-temperature synthesis of $Na_3V_2(PO_4)_2F_3$.

5.2 Crystal structure of $Na_3V_2(PO_4)_2F_3$

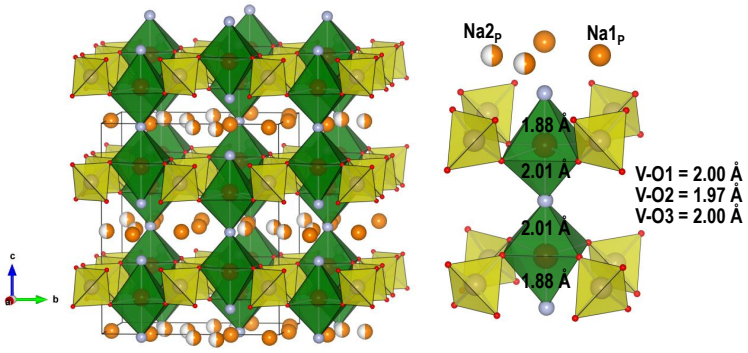

Figure 5.5: Crystal structure of $Na_3V_2(PO_4)_2F_3$ in the tetragonal space group $P4_2/mnm$ (ICSD 88808). Bi-octahedral $V_2O_8F_3$ (green) and PO_4 (yellow) building blocks are showed.

Based on single-crystal and powder X-Ray diffraction experiments, the crystal structure of $Na_3V_2(PO_4)_2F_3$ (Figure 5.5) was thought to be well-established since 1999. Le Meins et al.[311] initially described it using the tetragonal space group $P4_2/mnm$, with a distribution of Na^+ ions over 2 crystallographic sites: a first one, $Na1_P$, fully occupied and a second one, $Na2_P$, half-occupied only (here the subscript helps identifying the space group used, since several ones will be encountered in the following). The crystal structure of $Na_3V_2(PO_4)_2F_3$ highlights pairs of V^{3+} ions localized in bi-octahedral environments and surrounded by

four oxygen and two fluorine each, these fluorine being along the axis of the bi-octahedra. These $V_2O_8F_3$ have regular V-O and V-F bond lengths close to 2 Å and they are bridged by PO_4 tetrahedra, building a 3D framework with large tunnels along the [110] and [1-10] directions, where sodium ions are placed. This grants them a significant mobility and confers to $Na_3V_2(PO_4)_2F_3$ the ability to (de)intercalate sodium ions.

The same space group is used to describe the other members of the "solid solution" $Na_3V_2O_{2\delta}(PO_4)_2F_{3-2\delta}$. $V_2O_8F_3$ bi-octahedra become $V_2O_{8+2\delta}F_{3-2\delta}$ with 2δ vanadium ions present as vanadyl $(VO)^{2+}$ and the others (2-2δ) as V^{3+}. The V=O vanadyl type bonds are much shorter (≈1.6 Å) than V-F ones (≈2.1 Å). The end member δ =1, $Na_3V_2^{IV}O_2(PO_4)_2F$ (sometimes written as $Na_{1.5}V^{IV}OPO_4F_{0.5}$), can deliver a theoretical capacity of 156 mAh/g through two voltage-composition plateaus at 3.6 V and 4 V vs. Na^+/Na[317,320,321]. The crystal chemistry of this material was thoroughly studied by Tsirlin et al.[317], who proposed the existence of three different polymorphs with different space groups depending on the short, medium or long range ordering of sodium ions within the framework. The high temperature Na-disordered form (α phase) is described in the highly symmetric space group I4/mmm. At lower temperatures, Na becomes partially ordered in the β phase (298 K, space group $P4_2/mnm$) and almost completely ordered (γ phase) below 235 K ($P4_2/mbc$ space group).

5.2.1 Room temperature crystal structure

As we just discussed, the work of Le Meins et al.[311] assigned the tetragonal space group $P4_2/mnm$ to $Na_3V_2(PO_4)_2F_3$, used until now to describe the structure. However, close inspection of the published atomic coordinates points towards a very high (meaningless) value of the thermal parameter B_{iso} (Debye-Waller) on the Na(2) site (8.3 Å^2), occupied at 50%. The structure refinements of both neutron and laboratory X-Ray diffraction data, using the published structure of $Na_3V_2(PO_4)_2F_3$[311] as a starting model are plotted in Figure 5.6, showing a rather good agreement. In the light of this model, we fixed the occupancy factors at values of 1 and 1/2 on the two crystallographic Na(1) and Na(2) sites (both in 8i Wyckoff positions) respectively and confirmed, accordingly, an abnormally high thermal parameter value for sodium ions on the Na(2) site: 6.15 Å^2. Note that this site cannot be fully occupied as two equivalent positions generated by the mirror m perpendicular to [110] are too close (1.8 Å).

To gain further insight into the crystal structure of $Na_3V_2(PO_4)_2F_3$ (in particular in

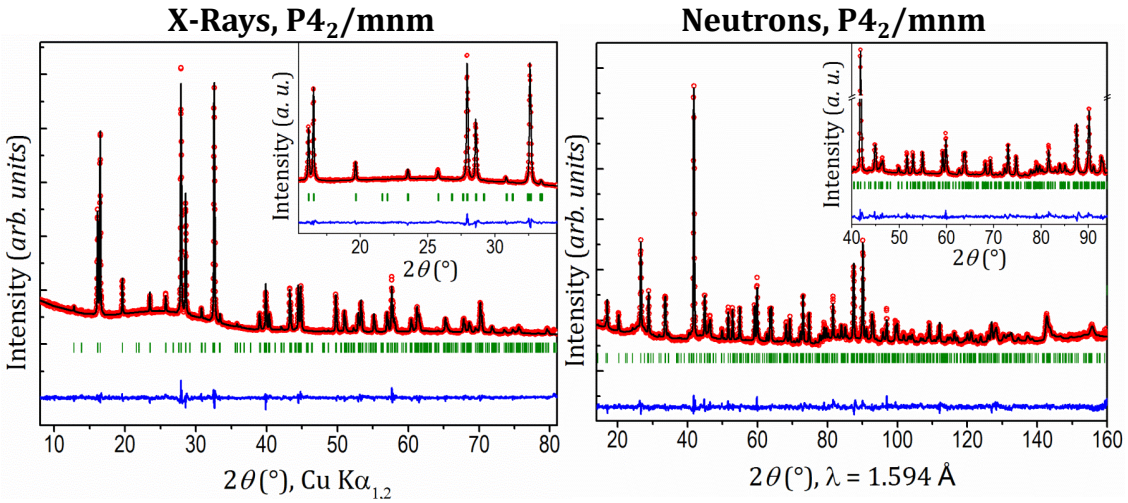

Figure 5.6: Rietveld refinement of $Na_3V_2(PO_4)_2F_3$ in the tetragonal space group $P4_2/mnm$ from XRPD on a laboratory diffractometer (left) and NPD (right) showing a good fit of the data.

the sodium ions distribution within the available crystallographic sites), we performed high angular resolution synchrotron radiation XRPD. Interestingly, we found that the indexation of the crystal structure of our $Na_3V_2(PO_4)_2F_3$ powder sample in the tetragonal space group $P4_2/mnm$ is not correct. Indeed, as Figure 5.7 shows, in-house X-ray diffraction generates diffraction peaks with rather large FWHMs ($> 0.1°$) from which $(h00)_{tetragonal}$ and $(0k0)_{tetragonal}$ reflections, for example, seem to be merged at the same 2θ angle. For a very subtle orthorhombic distortion, which appears to be the case here, high angular resolution synchrotron radiation diffraction (FWHM $\approx 0.005°$ for 2θ in the $0°$ - $25°$ angular

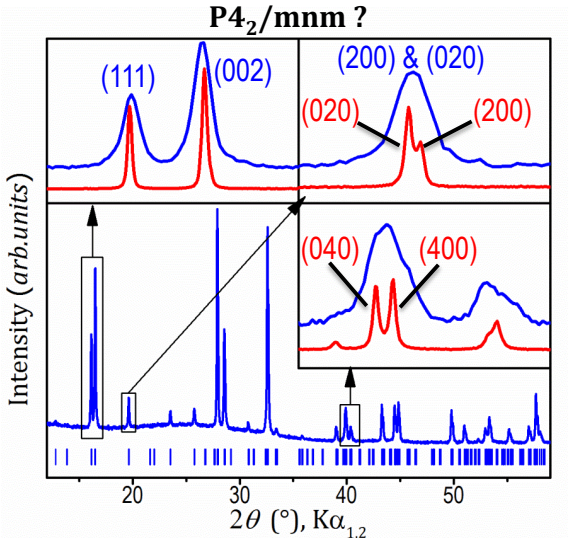

Figure 5.7: Comparison between X-Ray (blue) and synchrotron radiation (red) diffraction data of $Na_3V_2(PO_4)_2F_3$. The high resolution of synchrotron data allows to resolve the orthorhombic splitting.

range for the case of our measurement at SOLEIL) was essential for allowing us to refine the unit-cell parameters of $Na_3V_2(PO_4)_2F_3$. We chose the low-symmetry Pmmm space group to begin with, finding from Le Bail fit cell parameters values of a = 9.02837(3) Å, b = 9.04438(3) Å, c = 10.74643(3) Å, i.e. a b/a ratio of about 1.002 (Figure 5.8). Such a distortion had never been observed before because of a twofold reason. On one side, the synthesis conditions may surely play a role even if it appears to be a "general" property for the series of samples we have studied and obtained through the two-step solid state reaction described above. For instance, whatever the cooling rate (quenching in air, cooling at a controlled temperature rate ($< 2°C$/min) or cooling according to the furnace inertia) the orthorhombic distortion was always observed. As completely different synthesis routes are reported in literature (see the synthesis section 5.1.2) we cannot speculate whether they lead to orthorhombic distortion or not. On the other hand, we showed that extremely high angular resolution is required to observe the peaks' splitting. As most of the works recently reported on $Na_3V_2(PO_4)_2F_3$ did not focus on the structure but on syntheses and electrochemical performances, relying thus on laboratory powder X-Ray diffractometers only, these new features could not be observed. Even when synchrotron radiation sources are used, some choices of energy/detector (such as an image plate detector, for example) might not result in a sufficient angular resolution[322]. Having found the cell parameters, a suitable space group was searched for, since it was easily observed that Pmmm does not take into account many of the systematic extinctions. First, we observed that the obtained cell parameters are the only possible choice, i.e. none of the other possibilities reported in the literature for similar compounds could fit the data[317]. Indeed, cell parameters bigger by a factor $\sqrt{2}$ (with the cell rotated by 45°) would shift the (hh0) reflections, which are not splitted in the orthorhombic group, in the angular position of the (h00) - (0k0), where a splitting is needed to fit the data. Also, a cell smaller by a factor $\sqrt{2}$ (again with 45° rotation) would be incorrect, since the first peak in angular range (at 5.54°) could not be taken into account. Therefore we chose a combined approach using several indexing softwares (Dicvol, MacMaille, Fox), electron diffraction (performed by F. Weill at ICMCB) and crystallographic considerations to select the suitable space groups. We focused on non primitive cells since electron diffraction showed the existence of systematic extinctions in the whole reciprocal space. In particular, as shown in Figure 5.9a, with our choice of cell parameters (and therefore of orthorhombic setting) the only possible translation mode found from indexation is A. It can be observed that general (hkl) diffracted peak positions

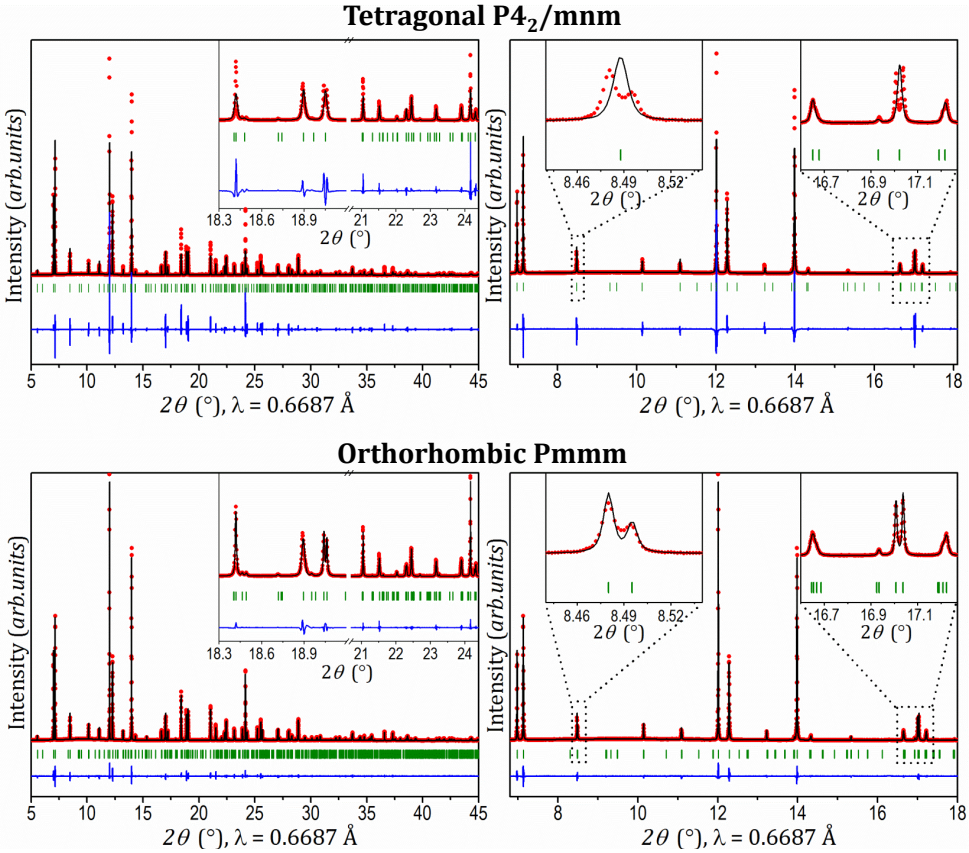

Figure 5.8: Le Bail fit of synchrotron radiation diffraction data in the $P4_2/mnm$ space group (top) and in the low-symmetry orthorhombic group Pmmm (bottom).

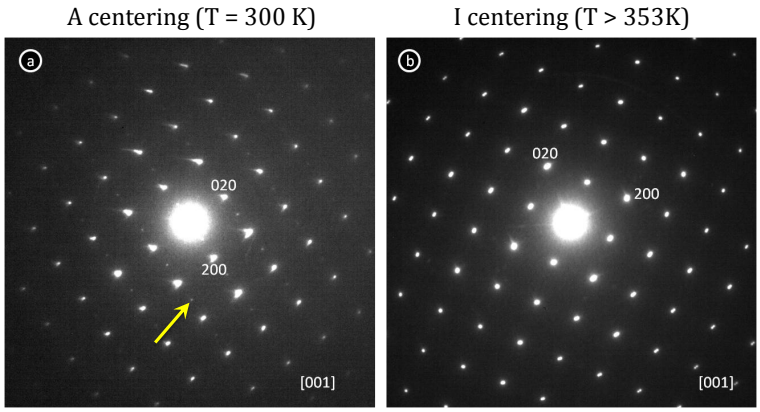

Figure 5.9: Electron diffraction data recorded with a) a room temperature specimen stage, showing the characteristic extinction corresponding to an A-centered Bravais lattice (weak reflections are indicated by the arrow) and b) with a specimen stage at 353 K. On this latter electron diffraction pattern, the systematic extinctions are consistent with an I-centered Bravais lattice.

respected k+l=2n. Moreover, an examination of systematic extinctions in the synchrotron radiation pattern revealed the following conditions for reflections to exist: for (h00), (0k0) and (00l), h = 2n, k = 2n and l = 2n; for (0kl), k+l = 2n; for (h0l) and (hk0), conditions were less clear due to peaks' vicinity, but we finally converged on h,l = 2n and k = 2n, respectively. Thanks to these considerations, the structure was subsequently refined for the best groups, namely Ama2 (n°40), Amam (n°63) and $A2_1am$ (n°36). The first is in its main setting, while the other two are Cmcm and $Cmc2_1$, both in their setting 4. It is crucial to note that Ama2 and $A2_1am$ are associated with the point group symmetry mm2-m2m-2mm, while Amam belongs to the mmm one, which allows its symmetry elements to be more similar to those obtained for $P4_2/mnm$.

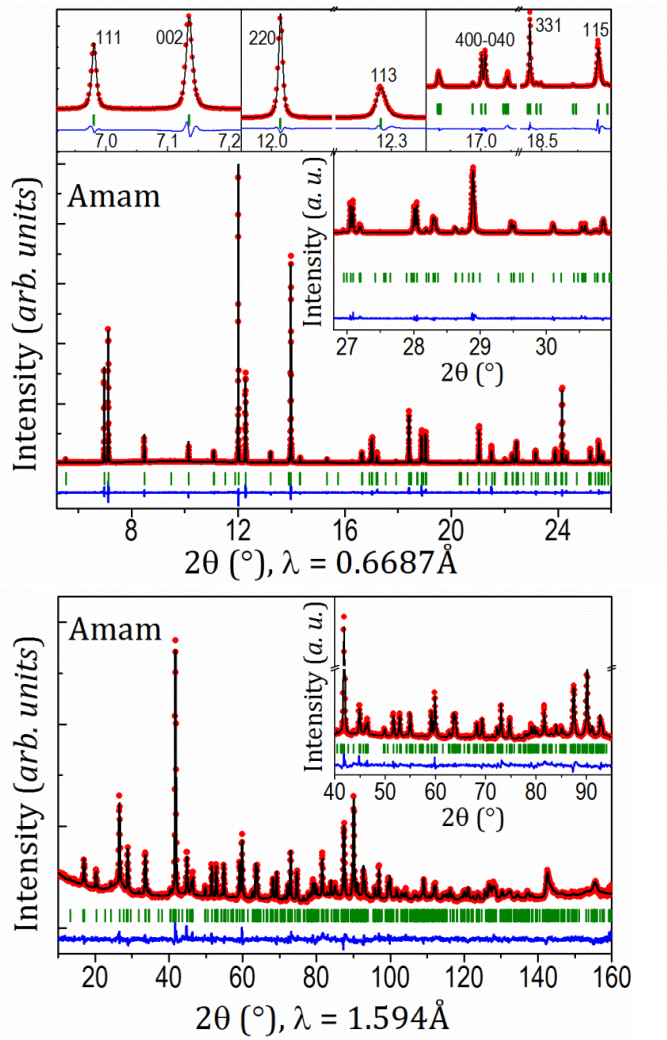

Figure 5.10: Combined Rietveld refinement of synchrotron radiation (top) and neutrons (bottom) diffraction data of $Na_3V_2(PO_4)_2F_3$ in the Amam space group. Insets zoom on significant peaks in the structure.

The structure was solved and the structural parameters refined using the Rietveld method. The results are shown in Figure 5.10, as obtained from combined structural refinements from synchrotron (top) and neutron (bottom) diffraction data with a relative weight of 50% for the two patterns. The refined parameters are reported in Table 5.2, while Table 5.3 reports bond-length distances and structural parameters. It is important to stress that the interatomic distances are in line with the expected values, and similar to those known from the "standard" model. The structural framework looks in fact identical to the one shown in Figure 5.5. For instance, we find tetrahedral distances P-O1 = 1.532(9) Å and P-O2 = 1.534(9) Å (Standard model: P1-O1 = 1.537 Å, P2-O2 = 1.533 Å and P2-O3 = 1.528 Å) and octahedral distances V-O1 = 2.006(9) Å, V-O2 = 1.965(9) Å, V-F1 = 1.981(2) Å and V-F2 = 1.968(6) Å (standard model: (V-O1 = 1.996 Å, V-O2 = 1.971 Å, V-F1 = 2.017 Å and V-F2 = 1.881 Å). The only difference that can be noted is a rather uniform V-F distance in our model, while in the "standard" one there are a shorter (1.881 Å) distance and a longer (2.017 Å) one. This shorter distance might in fact be an indication of the presence of oxygen in the bi-octahedra ($\delta \neq 0$ in $V_2O_{8+2\delta}F_{3-2\delta}$), leading to shorter vanadyl V=O bonds.

We confirmed that sodium is present in the unit cell of $Na_3V_2(PO_4)_2F_3$ in the planes at z = 0 and z = 1/2, as proposed by the "standard" model. However, due to the different symmetry elements in our unit cell, the Na ions distribution is modified. We found that sodium is distributed in 3 crystallographic sites, with partial site occupancy factors (SOFs) for 2 of them. Figure 5.11 shows the sodium distribution in the a-b plane. $Na1_A$ is placed in the center of a capped prism and when its SOF is refined it always leads to a value higher than 0.95, meaning that this site is essentially fully occupied. $Na2_A$ and $Na3_A$, instead, cannot be simultaneously occupied because of their vicinity ($Na2_A$ - $Na3_A$ = 0.93 Å). In good agreement with this, the independent simultaneous refinement of their SOFs leads to 0.68 and 0.28, meaning that either one or the other is always occupied. With respect to the surrounding environment, $Na2_A$ and $Na3_A$ are not equivalent since the first one occupies a capped prism, while the second one sits in a pyramidal site. However, none of them is in the center of the respective site, but the two positions are precisely divided by the face $F(2)_2O(2)_2$, representing the boundary between the polyhedra describing the two sites (Figure 5.10). The fact that $Na2_A$ is more occupied than $Na3_A$ is explained by the shorter $Na3_A$ - $Na3_A$ distance if compared to the $Na2_A$ - $Na2_A$ (2.87 Å vs. 3.87 Å), responsible for a stronger electrostatic repulsion. Moreover, the triangular-like distribution of sodium

Table 5.2: Structural parameters obtained from combined Rietveld refinement of synchrotron radiation and neutron diffraction data of $Na_3V_2(PO_4)_2F_3$.

$Na_3V_2(PO_4)_2F_3$

S.G. Amam; Z=4

a = 9.02847(3) Å;
b = 9.04444(3) Å;
c = 10.74666(6) Å;
V = 877.544(6) Å^3;
V/Z = 219.386 Å^3.

Synchrotron:
R_{wp} = 14.8%; R_B = 4.45%; χ^2 = 2.58.

Neutrons:
R_{wp} = 17.4%; R_B = 9.89%; χ^2 = 2.58.

Atomic Parameters

Atoms	Wyckoff	Atomic Positions			SOF	B_{iso}
		x/a	y/b	z/c		
V	8g	1/4	0.2536(5)	0.1844(2)	1	0.40(3)
P	8e	0	0	0.2472(6)	1	0.46(5)
O(1)	16h	0.0960(8)	0.0960(8)	0.1618(8)	1	0.9(2)
O(2)	16h	0.0943(8)	0.4038(8)	0.1659(8)	1	0.7(2)
F(1)	4c	1/4	0.253(2)	0	1	0.6(1)
F(2)	8g	1/4	0.756(1)	0.1325(5)	1	1.2(1)
Na(1)	4c	3/4	0.023(1)	0	1	2.3(3)
Na(2)	8f	0.536(1)	0.283(1)	0	0.65(3)	1.4(3)
Na(3)	8f	0.593(3)	0.364(4)	0	0.30(3)	3.1(9)

Table 5.3: Significant bond length distances (Å) of $Na_3V_2(PO_4)_2F_3$ obtained from Rietveld refinement of combined synchrotron radiation and neutron diffraction data. Distances shorter than 2.8 Å were considered. Polyhedral distortion is calculated as $\Delta = 1/N \sum_i (d_i - \langle d \rangle / \langle d \rangle)^2$, bond valences as reported in [255].

$Na_3V_2(PO_4)_2F_3$

	V	P	Na(1)	Na(2)	Na(3)
Coord.	6	4	7	7	6
O(1)	2.006(9) x2	1.532(9) x2	2.47(1) x4	2.70(1) x2	-
O(2)	1.965(9) x2	1.534(9) x2	-	2.40(1) x2	2.75(3) x2 2.48(2) x2
F(1)	1.981(2)	-	2.50(1)	2.59(1)	-
F(2)	1.968(6)	-	2.45(1) x2	2.43(1) x2	2.29(3) x2
Distor.($\cdot 10^{-4}$)	0.84	0.004	0.41	26.78	57.37
BVS	3.04(3)	5.02(6)	1.00(1)	0.92(1)	0.86(3)

cations can be regarded as the cause of the observed orthorhombic distortion, since such arrangement generates different electrostatic repulsion forces between the ions in the a and b directions, while in a square-like distribution as proposed in the standard model there

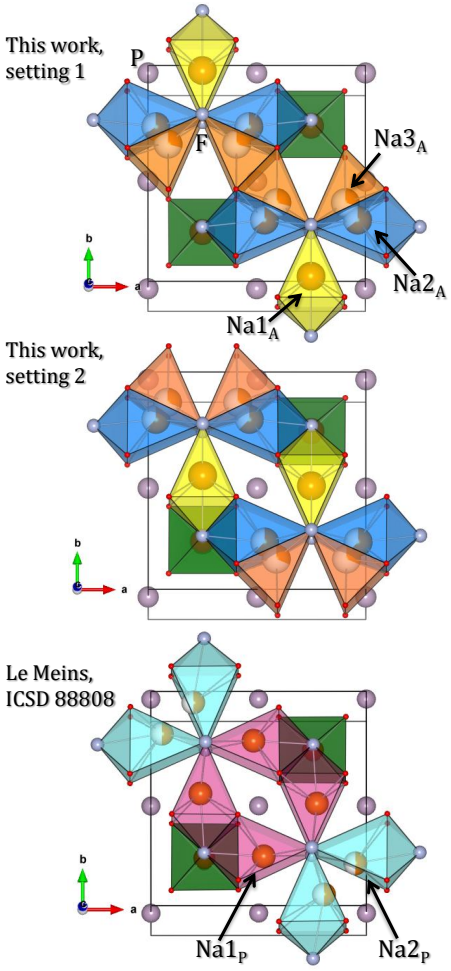

Figure 5.11: Distribution of sodium ions in the z = 0 plane in the structure of $Na_3V_2(PO_4)_2F_3$. Setting 1 (top) represents the result obtained in the refinement of Figure 5.10, setting 2 (middle) represents the alternative equivalent arrangement observed for sodium in the Amam space group. Bottom: compari-son with the sodium distribution present in literature.

is no reason to imagine such a distortion. Note that in this triangular arrangement the distances $Na1_A$ - $Na2_A$ and $Na1_A$ - $Na3_A$ are 3.04 Å and 3.39 Å respectively.

As a conclusive remark to complete the description of sodium ions distribution, we observed that reflections (hhl) where the contribution of h to dhhl is small with respect to the one of l (i.e. (002), (113), (006), (115) etc.) showed a marked asymmetry towards higher 2θ angles (insets in Figure 5.10), likely due to the occurrence of defects within the structure along the c axis. These defects can be related to stacking faults (or randomly distributed Na along c) or to a slight amount of vanadyl-type defects. Furthermore, the presence of disorder is supported by the fact that Fourier difference maps at the end of the refinements still show a small residual intensity present in the form of sodium ions rings (the same distribution as in the high-temperature phase). To support our conclusions

we verified if other configurations for sodium ions were possible. Indeed we observed that another possibility is to place the sodium atoms rotated by 180°, while leaving the rest of the structure unchanged. Figure 5.11 (middle) illustrates this distribution. We found that two symmetric distributions of the sodium ions could lead to the same fit of the data, leading to a maximal difference between the two of 50/50000 counts ($R_{bragg}1$ = 4.45%, $R_{bragg}2$ = 4.39%). However, the two descriptions could not coexist at the same time. In fact, considering two phases, one with the setting 1 and the other with the setting 2 for the sodium ions distribution, did not allow the software to converge because of the excessive similarity of the two phases, while placing all the sodium atoms from the two possible distributions in the structure together (6 crystallographic sites) leaving their occupancy unconstrained resulted in the Rietveld refinement converging towards one of the two single solutions. This is an important sign confirming that the triangular-like shape of the sodium distribution is really the cause for the orthorhombic distortion and that no other arrangement can lead to a good fit of our data. Moreover, we speculate that defects in the stacking along c of unit cells with the two different configurations of sodium are the cause for the asymmetric broadening of the reflections discussed above.

As previously stated, the correlation between the electrochemical data (Figure 5.2) and the sodium arrangement can be determined in details only by means of the *in situ* characterization we describe later on. Nevertheless, it is interesting to highlight that the separation between the first two voltage plateaus at 3.68 V and 3.7 V vs. Na^+/Na takes place at a composition $Na_xV_2(PO_4)_2F_3$ with x between 2.3 and 2.4, corresponding namely to the deintercalation of about the first 2/3 Na^+ ions over the 2 expected. Our determination of the crystal structure led us to propose three sodium sites for $Na_3V_2(PO_4)_2F_3$ with the following stoichiometry: $[Na1_A]_1[Na2_A]_{\approx 4/3}[Na3_A]_{\approx 2/3}$. $Na1_A$, fully occupied and in the center of the respective pyramidal site, reasonably seems to be the most stable one and it could be the sodium ion that has never been experimentally extracted, as it requires a too high potential. $Na2_A$ and $Na3_A$ might not be as stable, being out of the center of their respective sites and they can thus be deintercalated. It is interesting to point out that the deintercalation of the Na^+ ions occupying the $Na3_A$ crystallographic site could count for the 2/3 Na^+ ions deintercalated at 3.68 V. Our hypothesis is thus that the $Na3_A$ site is emptied first. No further hypothesis can be done at this stage, since the electrochemical behavior will strongly depend on a possible sodium rearrangement happening at this intermediate composition, $Na_{\approx 7/3}V_2(PO_4)_2F_3$, after the deintercalation of 2/3 Na^+ ions,

or afterwards at the composition $Na_2V_2(PO_4)_2F_3$. This discussion will be resumed and completed in section 5.3.

5.2.2 High Temperature (T > 300 K) crystal structure

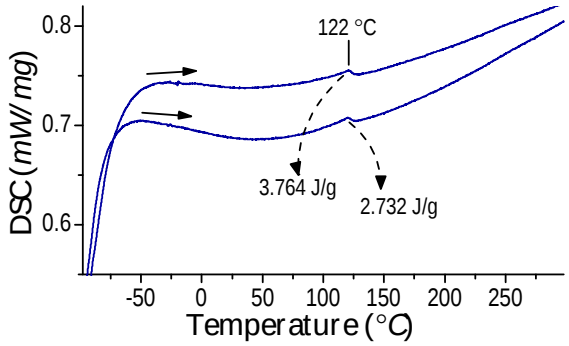

Figure 5.12: Differential scanning calorimetry of $Na_3V_2(PO_4)_2F_3$ (two repeated measurements) upon heating from -100 °C to 300 °C at 10 °C/min.

Since the $Na_3V_2O_2(PO_4)_2F$ system is reported to undergo an order-disorder transition at ≈500 K[317], Differential Scanning Calorimetry measurements were performed at 10°C/min under Ar and show indeed a similar transition for $Na_3V_2(PO_4)_2F_3$, completed at 395 K (Figure 5.12). The lower transition temperature suggests that $Na_3V_2(PO_4)_2F_3$ is more prone to sodium ions disordering than $Na_3V_2O_2(PO_4)_2F$. We hence decided to perform synchrotron radiation diffraction at temperatures of 300 K, 350 K and 400 K at the ALBA synchrotron facility. Thanks to these measurements (Figure 5.13) we could observe that the b cell parameter remains almost unchanged upon heating, while the a cell parameter converges to the value of b as the temperature increases, leading to a tetragonal symmetry confirmed also by the disappearance of many diffraction peaks. Furthermore, electron diffraction experiments were carried out (F. Weill, ICMCB) with the specimen stage at 353 K. Note that due to the heating effect of the electron beam, the actual temperature of the sample under investigation is higher. The obtained electron diffraction pattern (Figure 5.9b) can be indexed with a centered cell I. One notes in fact that the weak spots present at room temperature (Figure 5.9a) disappeared. The XRPD reflections of $Na_3V_2(PO_4)_2F_3$ at 400 K were subsequently indexed in the I4/mmm space group and the crystal structure refined with the Rietveld method. The obtained structural parameters are gathered in Table 5.4. The dimension of the unit cell is $\sqrt{2}$ times smaller than the one obtained at 298 K, namely a = b = 6.3927(1) Å and c = 10.756(1) Å (Volume V =

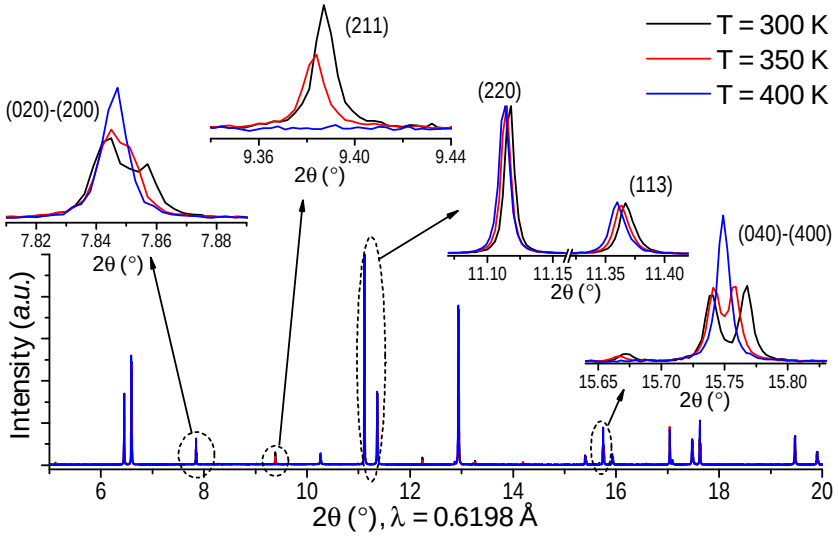

Figure 5.13: Synchrotron radiation XRPD of $Na_3V_2(PO_4)_2F_3$ at increasing temperatures from 300 K to 400 K.

439.558(3) Å^3). This is in line with the values observed for the high temperature phase of $Na_3V_2^{IV}O_2(PO_4)_2F$ by Tsirlin et al.[317] (a = b = 6.3956(1) Å, c = 10.6591(2) Å, V = 436.000(1) Å^3), the only dissimilarity being thus a shorter c axis in that case and hence a smaller unit cell volume. Note that this is expected in a V^{4+}-containing compound with respect to a V^{3+}-containing one.

Table 5.4: Structural parameters obtained from Rietveld refinement of synchrotron radiation diffraction data of $Na_3V_2(PO_4)_2F_3$ at T = 400 K.

$Na_3V_2(PO_4)_2F_3$ (T = 400 K)

S.G. I4/mmm; Z=2

a = b = 6.39271(3) Å;	R_B = 6.16%;
c = 10.75589(6) Å;	R_{wp} = 14.8%;
V = 877.544(6) Å^3; V/Z = 219.386 Å^3.	χ^2 = 2.58.

Atomic Parameters

Atoms	Wyckoff	Atomic Positions			SOF	B_{iso}
		x/a	y/b	z/c		
V	4e	0	0	0.1841(2)	1	0.67(6)
P	4d	1/2	0	0.25	1	0.75(8)
O	16n	0.3087(6)	0	0.1646(5)	1	1.1(1)
F(1)	2a	0	0	0	1	1.3(2)
F(2)	4e	0	0	0.3672(8)	1	1.7(2)
Na(1)	8h	0.277(1)	0.277(1)	0	0.45(3)	2.3(5)
Na(2)	16l	0.409(5)	0.225(4)	0	0.15(2)	2.6(9)

The general 3D framework is very similar in the two cases, the difference being that the $V_2O_{10}F$ bi-octahedra of $Na_3V_2O_2(PO_4)_2F$ are replaced by $V_2O_8F_3$ ones in $Na_3V_2(PO_4)_2F_3$, which are corner-sharing with PO_4 tetrahedra to build the stable open structure. In our work we observe interatomic distances P-O = 1.530(4) Å for the PO_4 tetrahedra and V^{III}-O = 1.985(4) Å, V^{III}-F(1) = 1.981(3) Å and V^{III}-F(2) = 1.97(1) Å for the VO_4F_2 octahedral units. This agrees well with the fact that V^{3+} in octahedral environment tends to induce homogeneous bond length distances, here close to 1.98 Å [10,95]. We expect therefore to observe a difference with $Na_3V_2^{IV}O_2(PO_4)_2F$, where the oxidation state 4+ of vanadium is more likely to induce long-short alternated distances for the out-of-plane bonds of the octahedra [281]. As a matter of fact, reported values for $Na_3V_2O_2(PO_4)_2F$ are V^{IV}-O(2) = 2.011(1) Å (in-plane), V^{IV}-O(1) = 1.626(3) Å (out-of-plane) and V^{IV}-F = 2.113(1) Å (while the reported P-O distance is 1.530(1) Å). Concerning sodium atoms, as in $Na_3V_2O_2(PO_4)_2F$ the increase of symmetry at high temperature is due to the loss of ordering between sodium ions in the a-b plane with respect to the room temperature phase, we could expect a similar behavior for $Na_3V_2(PO_4)_2F_3$.

As depicted in Figure 5.14, we observe that sodium ions are in fact disordered at 400 K and distributed in two crystallographic sites, building for symmetry constraints a "circle" around the fluorine atoms F(2) that are the extremes of the bi-octahedra (F(2) is however not in the plane z = 0 of the sodium ions, but above and below, at z = 0.3672(8)). In good agreement with the reported values for $Na_3V_2O_2(PO_4)_2F$, we find that the $Na1_I$ and $Na2_I$ sites are approximately half occupied (SOF = 0.45(3)) and 1/8 occupied (SOF = 0.15(2)), with still meaningful isotropic displacement parameters of 2.3(5) $Å^2$ and 2.6(9) $Å^2$, respectively. To conclude, the two compounds $Na_3V_2(PO_4)_2F_3$ and $Na_3V_2O_2(PO_4)_2F$ differ from the transition temperature between the room and high temperature phases (400 K vs. 500 K) and for their out-of-plane V-O or V-F distances in the octahedra. These are in particular homogeneous (V^{3+}) or alternated long-short (V^{4+}) distances, behavior caused by the different oxidation state of vanadium. On the other hand, the two high temperature phases have a strong similarity in terms of P-O bonds, in-plane V-O bonds and more importantly in the disordered circular arrangement of sodium cations in the a-b plane, which are the key factor driving symmetry changes for this class of materials.

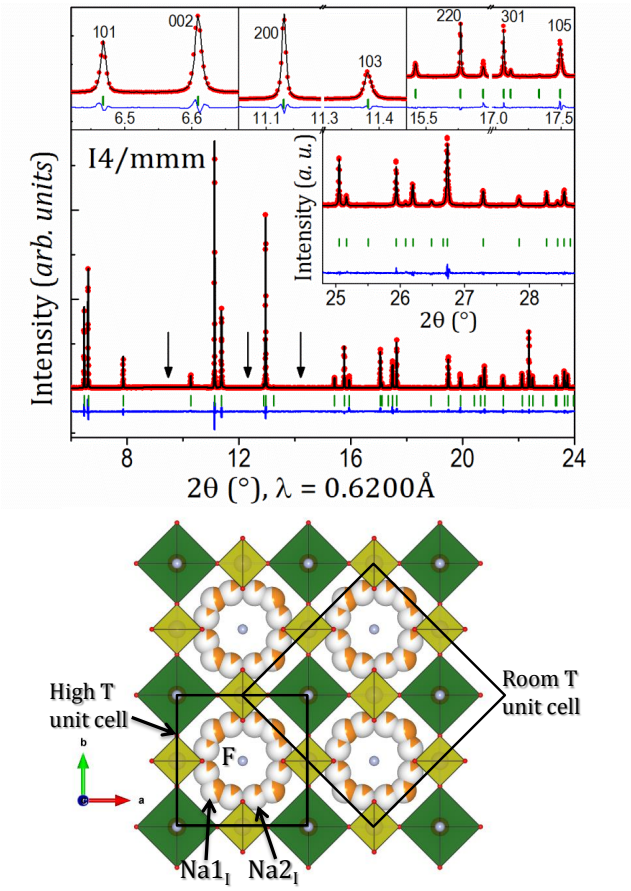

Figure 5.14: Top: Rietveld refinement of synchrotron radiation data for $Na_3V_2(PO_4)_2F_3$ at 400 K (high temperature phase, I4/mmm space group). Arrows indicate some of the extinct reflections with respect to the room temperature phase. Bottom: view along the [001] direction of the obtained crystal structure, showing the disordered distribution of sodium ions. The unit cells of the high T and room T phases are highlighted ($V_{roomT} = 2\ V_{highT}$).

5.2.3 Low Temperature (T < 300 K) crystal structure

To draw a more complete description of the phase diagram of $Na_3V_2(PO_4)_2F_3$ we carried out similar synchrotron radiation XRPD experiments upon cooling of the material, illustrated in Figure 5.15. We firstly note that the orthorhombic distortion is maintained and amplified. In fact we observe a variation of cell parameters, which tend to become smaller as expected from a temperature decrease. However not all of them change: it is clear from the behavior of Bragg reflections such as (011) or (040) that b and c remain rather constant, while a significantly decreases (see (400) constantly shifting to higher 2θ values). All the reflections present at room temperature are preserved while new ones appear concurrently: the transition begins at T = 200 K and these new reflections gain intensity as T decreases; the pattern at T = 100 K shows the most intense reflections.

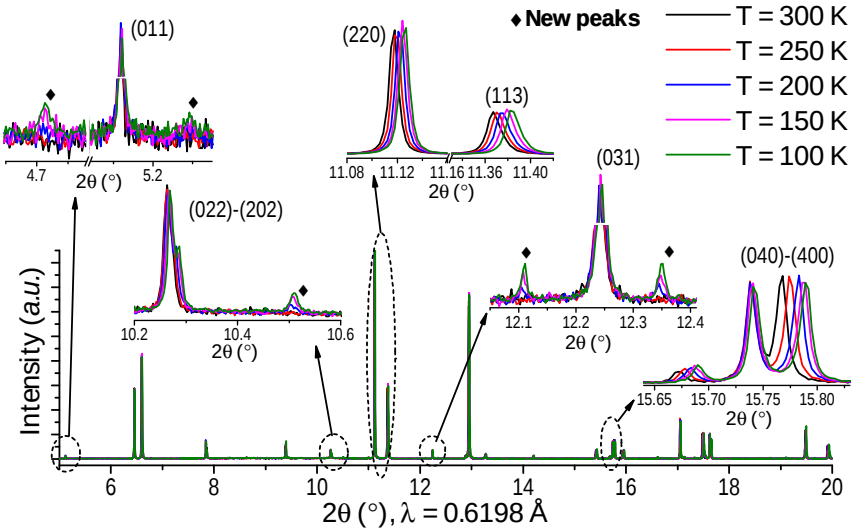

Figure 5.15: Synchrotron radiation XRPD of $Na_3V_2(PO_4)_2F_3$ at decreasing temperatures from 300K to 100 K.

The new Bragg peaks constitute a superstructure. They can indeed be indexed in a unit cell 3 times bigger in the [010] direction. The cell parameters obtained from Le Bail fit are: a = 9.016(1) Å, b = 27.127(1) Å, c = 10.729(1) Å. Therefore in this low temperature phase $Na_3V_2(PO_4)_2F_3$ maintains a constant value of c, while a decreases and b becomes 3 times bigger (b = 27.127(1) Å $= 3 \cdot 9.042$ Å $\approx$ 3 times b at T_{amb}). Such observations clearly suggest the presence of a superstructure due to sodium/vacancy ordering in the a-b plane. A detailed description of this ordering has not been found yet due to the complexity of the large unit cell (V = 2623.98(3) $Å^3$), while electron diffraction did not provide conclusive results because of the material's instability under the beam at low temperature. Note that, as described previously in this chapter, $Na_3(V^{IV}O)_2(PO_4)_2F$ also shows phase transformations upon heating and cooling [317]. At high temperature, the same space group (I4/mmm) is applicable to both materials because in both cases sodium ions are disordered. However, at room temperature $Na_3V_2(PO_4)_2F_3$ shows an orthorhombic distortion that has not been reported for $Na_3(V^{IV}O)_2(PO_4)_2F$ up to date. The latter also shows a low temperature form, found to belong to the $P4_2/mbc$ tetragonal space group at 235 K and with a unit cell two times bigger than the room temperature one (a' = b' $\approx a\sqrt{2}$); however the authors needed a second high-T-like (Na disordered) phase to properly fit their data, leaving some doubts about their structural description. For this reason, and because inconsistent with our observation of b becoming 3 times longer, we did not consider their structural model for $Na_3V_2(PO_4)_2F_3$.

5.3 Phase diagram of $Na_3V_2(PO_4)_2F_3$ upon Na^+ extraction: *in situ* synchrotron radiation XRPD

Two outcomes of the previous section - a crystal structure different from the previously accepted one (recalled in Figure 5.16a-b) and fine details in the electrochemical data (Figure 5.2) - contrast quite strongly with the available literature on the extraction of sodium from $Na_3V_2(PO_4)_2F_3$. In fact the reaction mechanism upon Na^+ extraction to yield $NaV_2(PO_4)_2F_3$ (deintercalation of two sodium ions) has been often described as a solid solution based on *ex situ* and *in situ* X-Ray diffraction and more recently on ab-initio calculations and NMR experiments[308,314,315,323–325]. In other words, every composition x in $Na_xV_2(PO_4)_2F_3$ ($3 \leq x \leq 1$) ever observed has been simply described in the $P4_2/mnm$ space group, the only one known up to now. We stress that here (and in the following) we will be referring to the phases $Na_xV_2(PO_4)_2F_3$ ($1 \leq x \leq 3$) and not to $Na_3V_2O_{2\delta}(PO_4)_2F_{3-2\delta}$ ($0 \leq \delta \leq 1$). Possible reasons at the origin of these discrepancies are (i) the lack of sufficient angular resolution of diffraction data and (ii) differences in the actual stoichiometry of the pristine samples. In particular the control of the O/F ratio is not straightforward

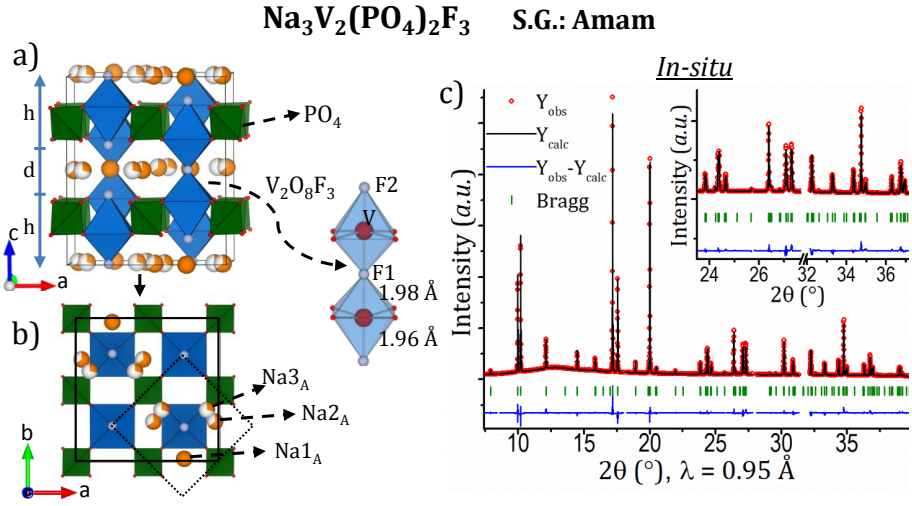

Figure 5.16: a) Crystal structure of $Na_3V_2(PO_4)_2F_3$ in the recently proposed Amam space group, showing $V_2O_8F_3$ bi-octahedra, PO_4 tetrahedra and the three different sites for sodium. The c axis is such that c = 2h+d where h is the height of an octahedron and d the height of sodium tunnels. b) top view displaying the a-b plane in the case of room temperature unit cell (solid line indicates the associated space group Amam, dotted line indicates the unit cell observed at high temperature (400K), in the space group I4/mmm). Orange spheres represent fully occupied Na sites, white/orange spheres partially occupied ones. c) Rietveld refinement of the structure of $Na_3V_2(PO_4)_2F_3$ from data collected using our *in situ* custom cell in transmission geometry.

Table 5.5: Comparison between Rietveld refinement obtained for $Na_3V_2(PO_4)_2F_3$ in a capillary in Debye-Scherrer geometry (black, top lines) and for the same material measured *in situ* in transmission in our electrochemical cell (blue, bottom lines).

$Na_3V_2(PO_4)_2F_3$

Our work ([312]) vs. **refined *in situ***

S.G. Amam; Z=4

a = 9.02847(3) Å; **a = 9.0262(2) Å;**
b = 9.04444(3) Å; **b = 9.0418(2) Å;**
c = 10.74666(6) Å; **c = 10.7434(3) Å;**
V = 877.544(6) Å^3; **V = 876.80(1) Å^3**
V/Z = 219.20(1) Å^3; **V/Z = 219.386 Å^3.**

Synchrotron: R_{wp} = 14.8%; R_B = 4.45%; χ^2 = 2.58.
Neutrons: R_{wp} = 17.4%; R_B = 9.89%; χ^2 = 2.58.
Synchro. *in situ*: R_{wp} = 11.4%; R_B = 6.36%; χ^2 = 18.1.

Atoms	Wyckoff	Atomic Positions x/a	y/b	z/c	SOF	B_{iso}
V	8g	1/4	0.2536(5)	0.1844(2)	1	0.40(3)
			0.2529(9)	**0.1848(3)**		**1.36(8)**
P	8e	0	0	0.2472(6)	1	0.46(5)
				0.244(1)		**1.6(1)**
O(1)	16h	0.0960(8)	0.0960(8)	0.1618(8)	1	0.9(2)
		0.096(1)	**0.097(1)**	**0.159(1)**		**1.2(1)**
O(2)	16h	0.0943(8)	0.4038(8)	0.1659(8)	1	0.7(2)
		0.091(1)	**0.404(1)**	**0.164(1)**		**1.2(1)**
F(1)	4c	1/4	0.253(2)	0	1	0.6(1)
			0.253(2)			**1.4(1)**
F(2)	8g	1/4	0.756(1)	0.1325(5)	1	1.2(1)
			0.756(2)	**0.1349(6)**		**1.4(1)**
Na(1)	4c	3/4	0.023(1)	0	1	2.3(3)
			0.024(2)			**3.8**
Na(2)	8f	0.536(1)	0.283(1)	0	0.65(3)	1.4(3)
		0.538(2)	**0.289(2)**		**0.8(1)**	**3.8**
Na(3)	8f	0.593(3)	0.364(4)	0	0.30(3)	3.1(9)
		0.623(5)	**0.393(6)**		**0.2(1)**	**3.8**

and can result in additional electrochemical features around 3.6 V vs. Na^+/Na, related with mixed valence phases of the family $Na_3V_2O_{2\delta}(PO_4)_2F_{3-2\delta}$ (the operating voltage decreases as δ increases). Moreover recently published *in situ* studies showed that for the two compositions $\delta = 1$ and $\delta = 0.8$, which are still supposed to belong to the tetragonal $P4_2/mnm$ space group, the sodium extraction mechanism is far from being a simple solid solution[74,326,327]. The $\delta = 0.8$ sample ($V^{3.8+}$) revealed for the first time a biphasic reaction during the lower voltage-composition plateau, while the biggest part of the charging process was modeled as a solid solution[74,326]. The V^{4+} extreme member ($Na_3V_2O_2(PO_4)_2F$,

$\delta = 1$) showed instead a sequence of two biphasic reactions upon extraction of the first sodium (hence with observation of an intermediate phase), followed by a long solid solution region and finally another biphasic reaction at the end of charge[327]. These observations are actually not surprising since Na-intercalation compounds exhibit a strong tendency to form intermediate phases[57,328]. For the reasons described above we decided to study the extraction of sodium from $Na_3V_2(PO_4)_2F_3$ ($\delta = 0$) by means of *operando* diffraction experiments[329]. Given the complexity of the reactions involved and considering the small orthorhombic distortion of $Na_3V_2(PO_4)_2F_3$, it appears clearly that high angular resolution (comparable to the one that can be obtained for standard synchrotron measurements in capillaries) is a mandatory requirement for this kind of experiments. We achieved this goal using both the MSPD beamline[119] at ALBA synchrotron and the electrochemical cell for *in situ* XRD and XAS measurements in transmission geometry described in the introduction[97,98]. The electrochemical extraction of Na^+ from $Na_3V_2(PO_4)_2F_3$ was fol-

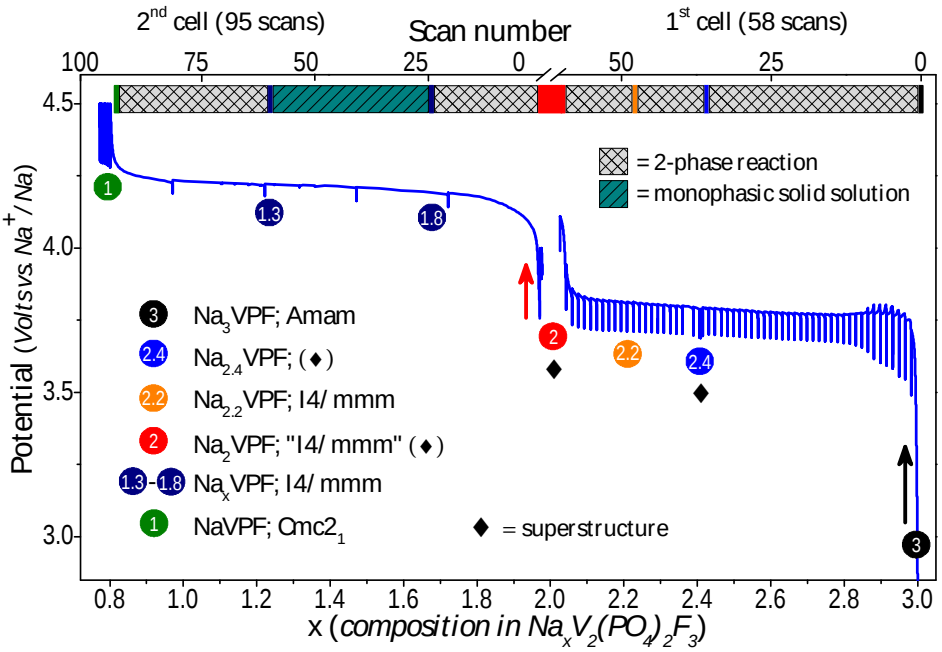

Figure 5.17: Potential-composition electrochemical curves obtained upon Na^+ extraction from Na_3VPF. The first cell was cycled (GITT) between the compositions Na_3VPF and Na_2VPF while recording 58 5-minutes diffraction scans; the second one (galvanostatic cycling) between the compositions Na_2VPF and NaVPF while recording 95 5-minutes scans. Significant single-phase compositions are highlighted by colored circles. For the 1^{st} cell they are obtained by the electrochemistry. Cycling of the 2^{nd} cell resulted in $\Delta x > 1$ because of electrolyte oxidation, hence in this case reported compositions are those obtained from Rietveld refinement. Top line describes the nature of the observed deintercalation mechanism.

lowed in real time and several phase transitions were identified upon cycling, often involving ordering/disordering phenomena within the sodium ions sub-lattice. The extremely good angular resolution and high intensity offered on the MSPD beamline (Figure 5.3) allowed to follow the reaction with unprecedented details, making full structural Rietveld refinements possible (Figure 5.16c) and even a first-time crystal structure determination for the end member $NaV_2(PO_4)_2F_3$ directly from *in situ* (*operando*) diffraction data.

As previously described (Figure 5.2), sodium ions are extracted from the framework of $Na_3V_2(PO_4)_2F_3$ through two different voltage regions, a lower one around 3.7 V vs. Na^+/Na and a higher one around 4.2 V vs. Na^+/Na. Given the incredibly rich phase diagram found and analyzed in this study (Figure 5.17) and for sake of clarity, the two voltage domains are discussed separately. Additionally, each definite $Na_xV_2(PO_4)_2F_3$ composition will be labeled as Na_xVPF in the following.

5.3.1 $Na_3V_2(PO_4)_2F_3$ - $Na_2V_2(PO_4)_2F_3$ system (3.7 V vs. Na^+/Na)

Figure 5.18 shows the XRPD patterns recorded during GITT relaxation intervals, upon extraction of sodium from Na_3VPF until the composition Na_2VPF is reached at the end of the first voltage-composition domain. Note the very high quality of the diffracted data, in terms of both angular and intensity resolution, essential for identifying tricky phenomena occurring in this system. It immediately appears that no continuous shifts in diffracted peak positions occur during this first electrochemical region: those of the pristine phase Na_3VPF lose intensity right away, while new ones start growing. Specific compositions and their corresponding XRPD patterns are highlighted with colored circles indicating the amount of Na/f.u. (determined from electrochemistry in this case, as described in the Experimental section). These are $Na_{2.4}V_2(PO_4)_2F_3$ ($Na_{2.4}$VPF), $Na_{2.2}V_2(PO_4)_2F_3$ ($Na_{2.2}$VPF) and $Na_2V_2(PO_4)_2F_3$ (Na_2VPF), corresponding to new single phases found in this sub-system and they are discussed in the following. Besides the obvious correlated appearances/disappearances of these phases (Figure 5.18), a peculiar attention was paid to reflections of weaker intensities (Figure 5.18b) which usually act as indicators of the presence/absence of sodium/vacancy ordering within the framework. As described for example for Na_3VPF in the transition from 298 K (orthorhombic Amam) to 400K (tetragonal I4/mmm)[312]), sodium ions disorder upon heating and adopt a "circular" arrangement above fluorine anions, inducing the material to adopt a more symmetrical space group and thus to lose several weak reflections.

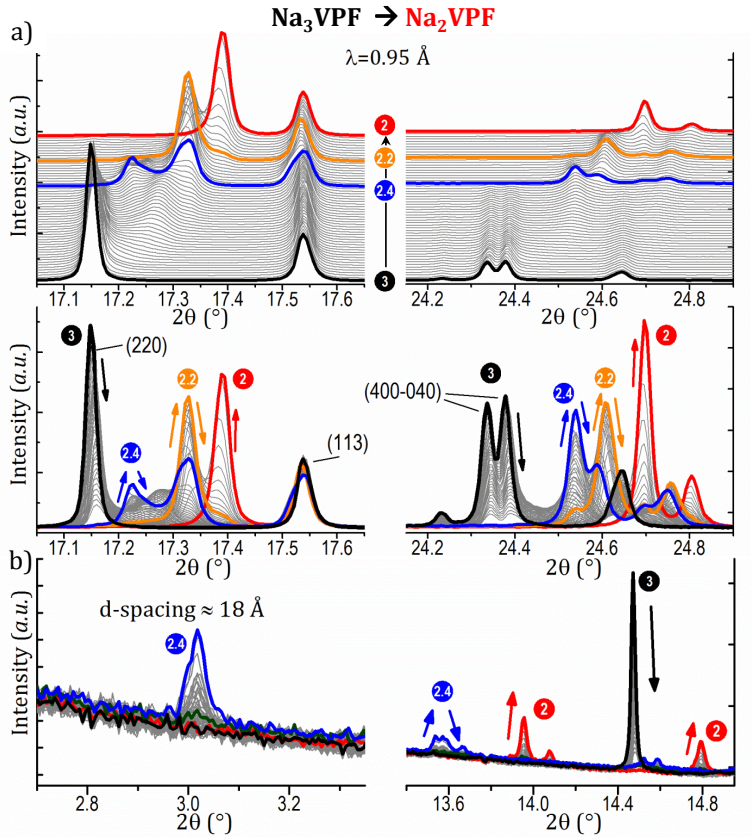

Figure 5.18: Different angular domains observed during the extraction of 1 Na^+ from Na_3VPF (black curve). Several single-phase compositions are formed through biphasic domains, namely $Na_{2.4}VPF$ (blue), $Na_{2.2}VPF$ (orange) and Na_2VPF (red). a) 17°-17.7° (left) and 24.1°-24.9° (right) angular domains. Peaks are indexed for the Na_3VPF phase. b) 2.7°-3.3° and 13.5°-14.9° angular domains (weak peaks related to sodium ordering).

The detailed evolution of specific Bragg peaks in the two-phase region Na_3VPF - $Na_{2.4}VPF$ is depicted in Figure 5.19. From the very beginning of the Na^+ extraction, large "shoulders" appear on the right side of the reflections of Na_3VPF, progressively revealing an internal structure, where at least three distinct diffraction peaks can be noticed (scan #30). These reflections remain broad, indicating that the reaction crosses different intermediate states (probably metastable) where sodium partially orders on the short-medium range only, until reaching the composition $Na_{2.4}VPF$. A close examination of the data reveals as well the appearance of additional weak-intensity diffraction peaks for $Na_{2.4}VPF$, in particular at a 2θ value of 3° ($d_{hkl} \approx 18$ Å, shown on Figure 5.18b) which suggests a doubling of the unit cell (superstructure) in the a or b directions (or both) due to Na^+/vacancy and/or V^{3+}/V^{4+} possible ordering. Considering that the values of a and b were 9.026 Å and 9.042 Å respectively in the Na_3VPF pristine phase (Table 5.6), the d-spacing of 18

Å (2 × 9 Å) in $Na_{2.4}$VPF is consistent with the oxidation of vanadium from V^{3+} to "$V^{3.3+}$" (shorter in-plane bonds). However no complete indexation was found for this phase because a simple doubling of any of the unit cell parameters could not explain all observed reflections. We believe this composition is in fact not fully "stabilized" and that it still contains domains which have not reached complete ordering.

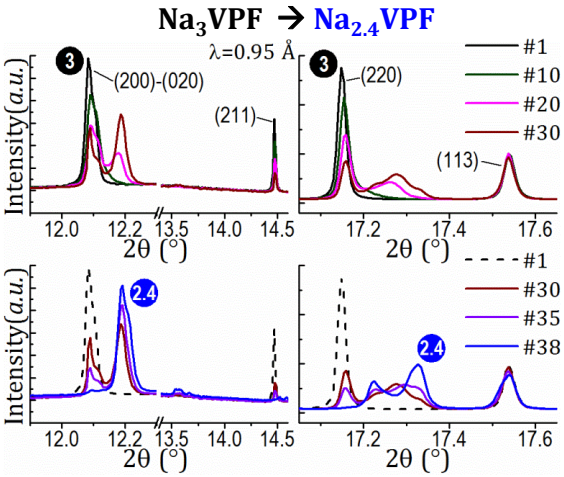

Figure 5.19: Detailed view of the initial stages of sodium deintercalation. Selected patterns from #1 (Na_3VPF) to #38 ($Na_{2.4}$VPF) are presented in the 11.9°-14.55° and 17°-17.7° angular domains. A complex behavior can be noticed in the structured shape of the peaks (200)-(020) and (220). Other peaks as (211) disappear (effect of sodium disordering), while some are almost unaffected (113).

Table 5.6: Compositions obtained upon Na^+ extraction from Na_3VPF. Space groups, cell parameters and volumes are reported. # The actual space group of composition Na_2VPF in its superstructural arrangement is not known, so the low-symmetry space group Pmmm is used to index all observed reflections.

Composition	S.G.	a (Å)	b (Å)	c (Å)	Vol. (Å^3)	V/Z (Å^3)
$Na_3V_2(PO_4)_2F_3$ (ref. [312])	Amam	9.02847(3)	9.04444(3)	10.74666(6)	877.544(6)	219.386(6)
$Na_3V_2(PO_4)_2F_3$ (*in situ*)	Amam	9.0262(1)	9.0418(2)	10.7434(3)	876.80(1)	219.20(1)
$Na_{2.4}V_2(PO_4)_2F_3$	Structure not determined					
$Na_{2.2}V_2(PO_4)_2F_3$	I4/mmm	6.3244(1)	6.3244(1)	10.7837(3)	431.33(1)	215.66(1)
$Na_2V_2(PO_4)_2F_3$	I4/mmm (#)	6.3021(1)	6.3021(1)	10.7933(2)	428.67(1)	214.34(1)
	Pmmm (#)	25.221(1)	12.599(1)	21.586(1)	6859.42(3)	214.36(3)
$Na_{1.8}V_2(PO_4)_2F_3$ (solid	I4/mmm	6.2800(1)	6.2800(1)	10.8493(3)	427.88(1)	213.94(1)
$Na_{1.3}V_2(PO_4)_2F_3$ solut.)		6.2481(1)	6.2481(1)	10.9222(2)	426.39(1)	213.19(1)
$NaV_2(PO_4)_2F_3$	$Cmc2_1$	8.7822(3)	8.7962(3)	11.0015(2)	849.86(1)	212.47(1)

Once the $Na_{2.4}$VPF composition is reached, the deintercalation reaction proceeds again

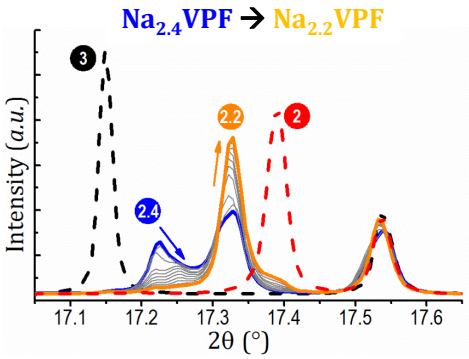

Figure 5.20: Detailed view of the biphasic reaction between scans #38 ($Na_{2.4}VPF$) and #47 ($Na_{2.2}VPF$). At this composition only two peaks at 17.33° and 17.54 ° remain, characteristic of the I4/mmm space group.

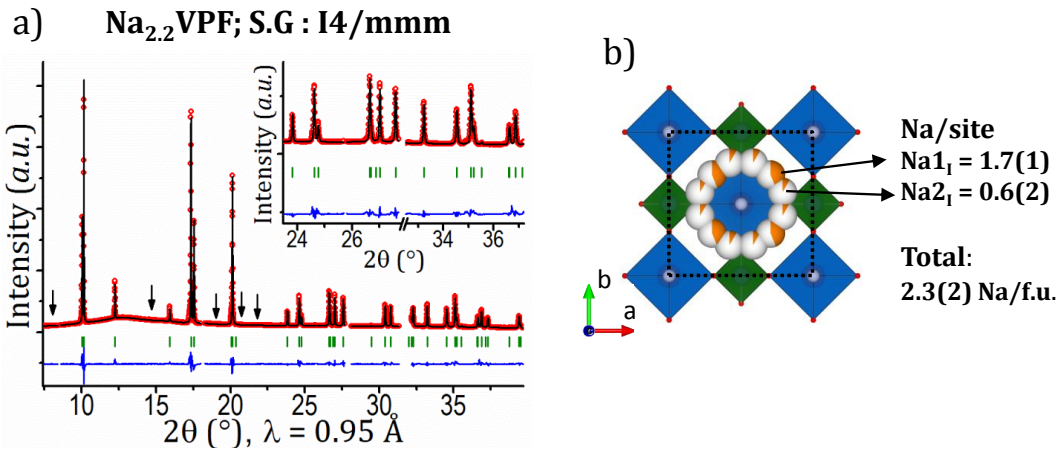

Figure 5.21: a) Rietveld refinement of the intermediate phase $Na_{2.2}VPF$. Missing reflections related to sodium ordering in Na_3VPF (S.G: Amam) are indicated by arrows. b) Crystal structure of $N_{2.2}VPF$, refined in the I4/mmm space group. Two sites $Na1_I$ and $Na2_I$ are present for sodium. Their occupancy is refined and related sodium amount is reported.

as a biphasic one (Figure 5.18 and Figure 5.20) towards a newly isolated single phase, $Na_{2.2}VPF$. This phase is interesting as it shows no extra weak reflections (loss of the superstructure observed for $Na_{2.4}VPF$) and displays a rather "simple" XRPD pattern: the characteristic peaks of the orthorhombic Na_3VPF due to Na^+ ordering are absent in $Na_{2.2}VPF$, fully indexed using the I4/mmm space group. Overall, from Na_3VPF to $Na_{2.2}VPF$ (passing through $Na_{2.4}VPF$), the unit cell volume decreases from V/Z = 219.39(1) $Å^3$ to V/Z = 215.66(1) $Å^3$ which appears somewhat small ($\Delta V/V$ = -1.7%) since a strong anisotropy in lattice parameters variations occurs: $\Delta a/a$ = -0.92%; $\Delta b/b$ = -1.10%; $\Delta c/c$ = +0.38% (Table 5.6). The crystal structure of $Na_{2.2}VPF$ was refined by the Rietveld method (Figure 5.21). Sodium ions adopt a disordered arrangement, and Fourier difference maps (re-

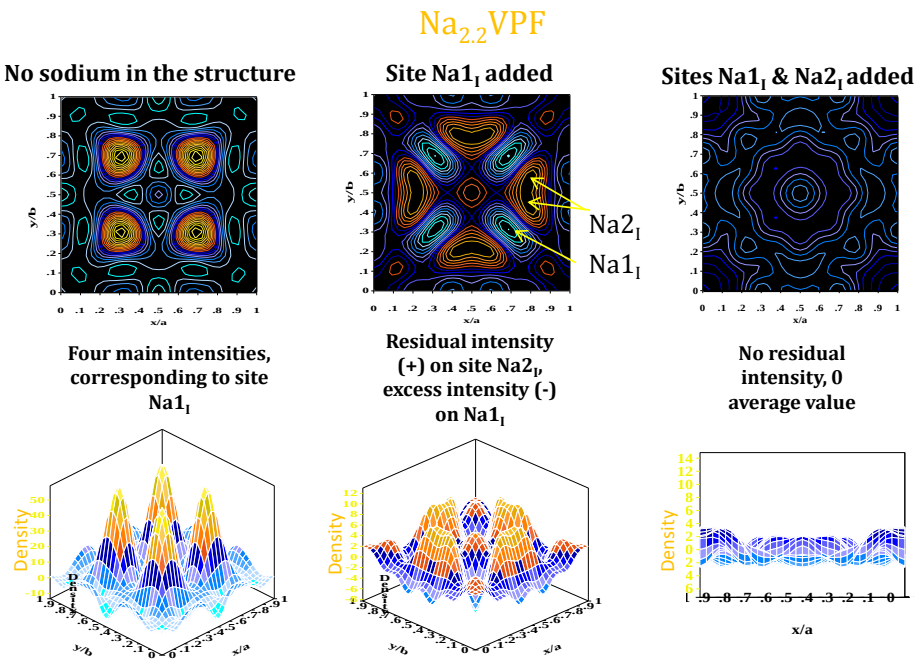

Figure 5.22: Fourier difference map obtained after Rietveld refinement of diffraction data at composition $Na_{2.2}VPF$. Top: structural model for refinement not including any sodium. Middle: structural model with $Na1_I$ site only included. Bottom: structural model with $Na1_I$ and $Na2_I$ included.

ported in Figure 5.22) reveal that both $Na1_I$ and $Na2_I$ sodium positions are occupied, leading to a refined composition of x = 2.3(2), in good agreement with the electrochemical data (x = 2.2). These refinements show, interestingly, that the above mentioned variation of the cell parameter c (between Na_3VPF and $Na_{2.2}VPF$) is opposite to the shortening of the V-F bond lengths along the F-V-F-V-F chain in the bi-octahedra (Table 5.7): V-F1 decreases from 1.981(2) Å to 1.953(5) Å and V-F2 decreases from 1.968(6) Å to 1.91(1) Å, as expected for the oxidation of vanadium. Considering the model used in ref.[322] (c ≈ 2h+d with h = height of an octahedron and d = height of sodium's tunnels, Figure 5.16a), we notice a significant increase in the value of d. In fact, d varies from 2.86(1) Å for the pristine Na_3VPF phase to 3.06(1) Å for $Na_{2.2}VPF$. The increase in the value of c is mainly due to the increased electrostatic repulsion between subsequent bi-octahedra, caused by a smaller global screening effect of sodium.

The final reaction observed in the 3.7 V vs. Na region is again a biphasic one. The XRPD peaks of $Na_{2.2}VPF$ disappear while new peaks belonging to the Na_2VPF end-member appear (Figure 5.18). A first look at the 24°-25° 2θ region shows that the splitted (400) and (040) peaks of Na_3VPF are again merged into one single peak in Na_2VPF, suggesting a tetragonal space group. A more detailed look reveals however that this phase

Table 5.7: Bond-lengths and sodium content per formula unit obtained from Rietveld refinement of selected deintercalated phases observed *in situ* during Na^+ extraction from Na_3VPF.

Composition	Refined Na/f.u.	V-F1 (Å)	V-F2 (Å)	V-O1 (Å)	V-O2 (Å)
$Na_3V_2(PO_4)_2F_3$ (ref. [312])	2.9(2)	1.981(2)	1.968(6)	2.006(9)	1.965(9)
$Na_3V_2(PO_4)_2F_3$ (*in situ*)	3.0(2)	1.985(3)	1.938(9)	2.00(1)	2.00(1)
$Na_{2.2}V_2(PO_4)_2F_3$	2.3(2)	1.953(5)	1.91(1)	1.954(6)	1.954(6)
$Na_2V_2(PO_4)_2F_3$ (I4/mmm)	2.05(7)	1.947(4)	1.88(1)	1.946(6)	1.946(6)
$Na_{1.8}V_2(PO_4)_2F_3$ (solid	1.85(7)	1.932(5)	1.92(1)	1.926(9)	1.926(9)
$Na_{1.3}V_2(PO_4)_2F_3$ solut.)	1.31(6)	1.938(4)	1.87(1)	1.942(6)	1.942(6)
$NaV_2(PO_4)_2F_3$	0.88(9)	V1: 2.00(9)	V1-F3: 1.67(4)	V1-O1: 1.86(6)	V1-O2: 1.89(6)
		V2: 1.88(9)	V2-F2: 2.02(3)	V2-O3: 1.92(6)	V2-O4: 2.09(5)

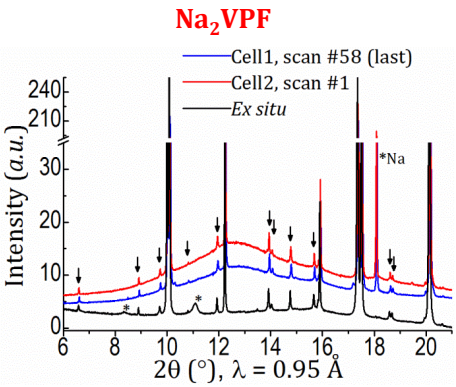

Figure 5.23: Comparison of composition Na_2VPF obtained by *ex situ* chemical oxidation (black), *in situ* in the first electrochemical cell (blue, after diffraction measurements across the low-voltage-composition plateau) and *in situ* in the second electrochemical cell (red, before diffraction measurements across the high-voltage-composition plateau). The same Bragg reflections are observed. An asterisk marks peaks not belonging to phase Na_2VPF (originating from sodium metal in the *in situ* experiments; from an impurity left as residue of the chemical preparation in the *ex situ* sample).

generates many extra weak reflections that can be observed in the 13.4°-15° (Figure 5.18b) and 6°-21° (Figure 5.23) 2θ domains. Neglecting the weakest peaks, the reflections can be indexed with an "average" cell using the high-symmetry I4/mmm space group (a=6.3021(1) Å, c=10.7933(2) Å). At present, a complete indexation of the XRD pattern for Na_2VPF could be found only for a huge superstructure cell of a' = 25.221(1) Å, b' = 12.599(1) Å and c' = 21.586(1) Å (Figure 5.24), i.e. with a' = 4a, b' = 2b, c' = 2c (Vsupercell = 16×Vsubcell) with respect to the cell parameters of $Na_{2.2}VPF$. Such a large unit cell can be

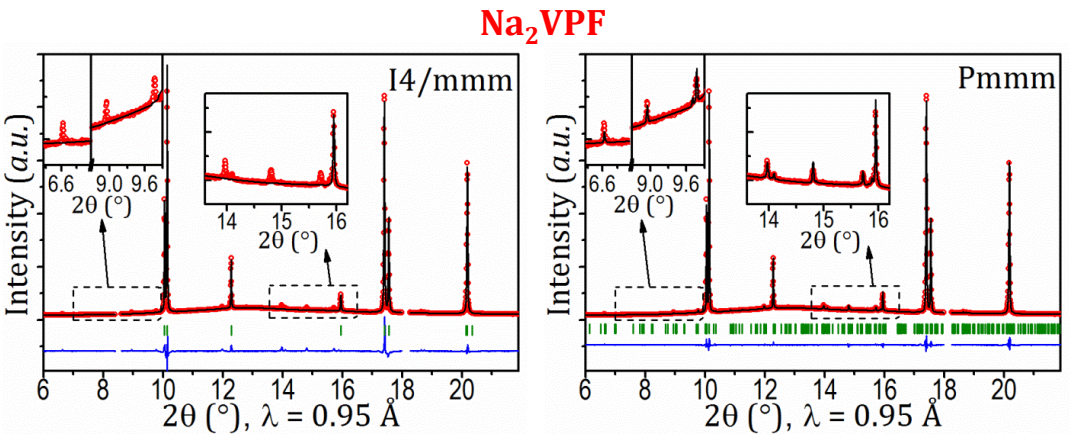

Figure 5.24: Left: Rietveld refinement of the "average" structure of Na_2VPF in the I4/mmm space group. Right: full pattern matching of the superstructure observed, taking into account all Bragg peaks.

explained assuming that not only sodium ions adopt some sort of ordering, but vanadium cations do the same (V^{3+} and V^{4+}) as the average oxidation state of V within Na_2VPF is $V^{3.5+}$. To verify the reproducibility of our *in situ* data we prepared Na_2VPF *ex situ* (Figure 5.23), by chemical oxidation of Na_3VPF, yielding a powder with very similar unit-cell parameters and superstructure reflections. At present, and in the following of the paper, we treated Na_2VPF in the "average" tetragonal unit cell, which gives meaningful results (parameters reported in Table 5.6 and Table 5.7). Importantly, Fourier difference maps (Figure 5.25) do not show any intensity on the $Na2_I$ site, leaving only the square-like distribution generated by the $Na1_I$ site (its occupancy can be refined to give 2.05(6) Na/f.u., Figure 5.25). This is however only an "average" distribution and several first principle calculations[74,309,315,322] predicted that instead of 4 half-occupied positions (generated by the same crystallographic site) it is favorable for sodium to arrange in 2 fully occupied positions (trans arrangement), alternated so as to minimize the electrostatic repulsion. The fact that we observe a superstructure is in good agreement with these studies and the actual structure determination of Na_2VPF will possibly confirm them. We are confident that our observation of a large unit cell combining different types of orderings will stimulate further research especially in terms of DFT and ab-initio calculations, in order to propose an adequate crystal structure for Na_2VPF.

A close look at the correspondence between the electrochemical and diffraction data reveals a somewhat puzzling behavior. As can be seen in the inverse derivative curve of Figure 5.2, the Na^+ extraction from Na_3VPF to Na_2VPF seems to be composed of two

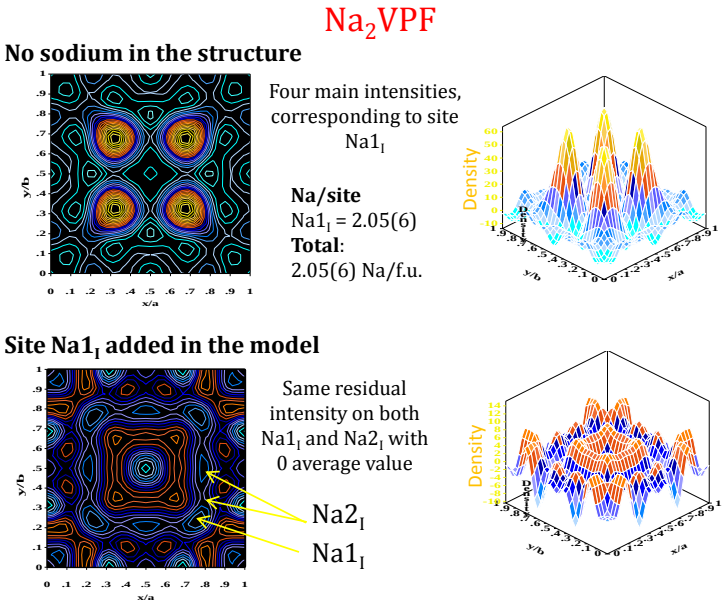

Figure 5.25: Fourier difference maps obtained after Rietveld refinement of diffraction data at composition Na_2VPF. Top: structural model for refinement not including any sodium. Bottom: structural model with $Na1_I$ site only included.

features at 3.68 V and 3.70 V vs. Na^+/Na (i.e. separated by only 20 mV), suggesting a sequence of two biphasic reactions with an intermediate phase around the composition $Na_{\approx 2.4}V_2(PO_4)_2F_3$. At the end of section 5.2.1 we made the hypothesis that this intermediate phase could actually be $Na_{7/3}V_2(PO_4)_2F_3$, crystallized following the extraction of the first 2/3 Na/f.u., namely that the $Na3_A$ site was emptied first. However our structural data recorded *in situ* point towards three biphasic reactions Na_3VPF - $Na_{2.4}VPF$, $Na_{2.4}VPF$ - $Na_{2.2}VPF$ and $Na_{2.2}VPF$ - Na_2VPF. Hence our hypothesis must be rejected, in favor of multiple biphasic reactions caused by the several stable configurations for sodium ions in the structure. A similar case of electrochemistry / diffraction "disagreement" (or "difference in sensitivity") was recently reported for the Na^+ extraction from $NaFePO_4$, towards an intermediate phase $Na_{2/3}FePO_4$. This intermediate phase is observed by diffraction both upon charge and subsequent discharge, while it is hardly expected from the shape of the voltage-composition electrochemical curve on discharge. This asymmetry phenomenon was tentatively attributed by the authors to different lattice mismatches [58,60,330]. In our case the two compositions $Na_{2.4}VPF$ and $Na_{2.2}VPF$ are so close to each other in energy that they cannot be differentiated from their electrochemical (voltage) signature, even at extremely relaxed GITT conditions (see Figure 5.26). The $Na_{2.4}VPF$ composition is able to stabilize a long range order (2/3 V^{3+}, 1/3 V^{4+} for example) suppressed in $Na_{2.2}VPF$,

even if local orders might be maintained.

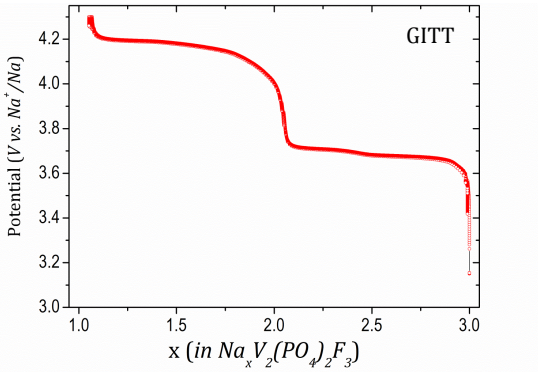

Figure 5.26: GITT of $Na_3V_2(PO_4)_2F_3$. Charge at C/100 for 30 minutes, relaxation until dV/dt < 4mV/h. Electrode mass ≈20 mg.

5.3.2 $Na_2V_2(PO_4)_2F_3$ - $NaV_2(PO_4)_2F_3$ system (4.2 V vs. Na^+/Na)

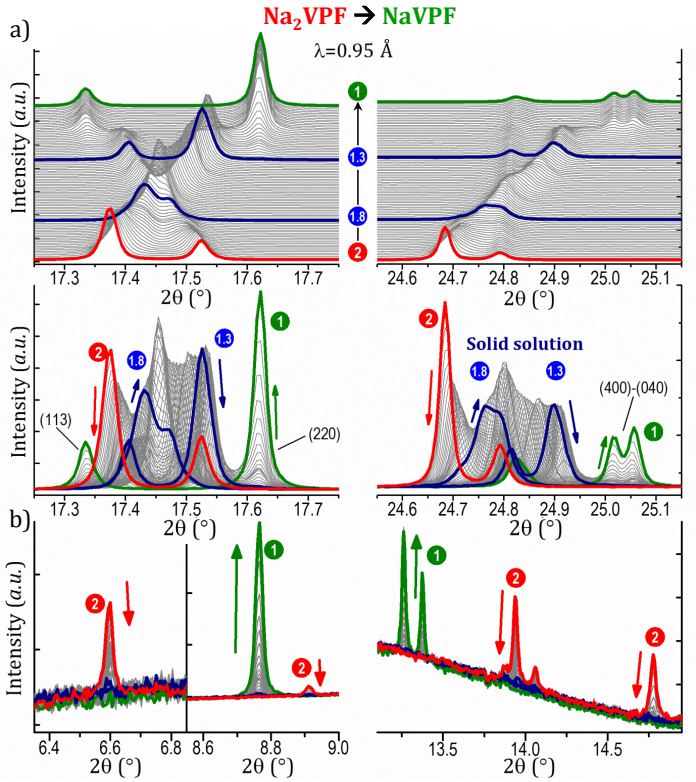

Figure 5.27: Different angular domains observed during the extraction of 1 Na^+ from Na_2VPF (red curve). Na_2VPF disappears through a biphasic reaction, then a solid solution is present between $Na_{1.8}VPF$ and $Na_{1.3}VPF$ (both in dark blue); finally Na1VPF (green curve) crystallizes through a biphasic reaction. a) 17.25°-17.75° (left) and 24.55°-25.15° (right) angular domains. Peaks are indexed for the NaVPF phase. b) 6.4°-6.8°, 8.6°-9.0° and 12.9°-14.9° angular domains (weak peaks related to sodium ordering).

To study the higher voltage domain, i.e. the extraction of sodium from Na_2VPF to NaVPF, a second electrochemical cell was cycled off-line until the Na_2VPF composition was reached and then placed in the beam. The evolution of Bragg's reflections when Na^+ is extracted from Na_2VPF is shown in Figure 5.27. The diffraction peaks of the pristine phase Na_2VPF lose intensity right away (red curve), while new ones start growing. Specific compositions and their corresponding XRPD patterns are highlighted again with colored circles indicating the amount of Na/f.u. (determined from XRPD in this case, since from galvanostatic cycling we notice that the theoretical capacity $\Delta x = 1$ is exceeded because of partial electrolyte oxidation). We discuss in the following the new single phases found in this sub-system, which are $Na_2V_2(PO_4)_2F_3$ (Na_2VPF), $Na_xV_2(PO_4)_2F_3$ (Na_xVPF, $1.8 < x < 1.3$) and $NaV_2(PO_4)_2F_3$ (NaVPF).

In the early stage of Na^+ extraction from Na_2VPF, the weakest diffraction peaks disappear, most likely because of sodium and vanadium cations disordering in the structure (Figure 5.27b). The $(dV/dx)^{-1}$ shoulder at 4.16 V vs. Na^+/Na (Figure 5.2) corresponds to a biphasic first order reaction that could be easily mistaken for a second order one due to the extreme vicinity of the disappearing peaks of Na_2VPF with those of the growing phase $Na_{\approx 1.8}$VPF. However a few reflections are lost in the process, leaving no doubt about the reaction mechanism. Interestingly, in the Na_2VPF - $Na_{1.8}$VPF miscibility gap, the cell parameters of both phases continue to vary (results from Rietveld refinement in Figure 5.28a), although this would be in principle thermodynamically forbidden (in equilibrium conditions a biphasic reaction implies that the two phases, the sodium-rich and the sodium-poor, change in relative weight but not in the amount of sodium in every phase, thus keeping constant cell parameters). This is directly observable in Figure 5.27, where the diffracted reflections from Na_2VPF (in red) lose intensity but also shift concurrently (although in absolute values the variation of cell parameters during that 2-phase region is only of 0.01 Å to 0.02 Å). Such a behavior has been recently reported for several materials as an effect induced by particle size, strains and high-rate (non-equilibrium) cycling conditions[95,99,100,314,331]. In our case the battery charged rather slowly (C/5 per Na^+) and the volume change from Na_2VPF to $Na_{1.8}$VPF is only $\Delta V/V$ = -0.2%. At present we do not have any obvious hypothesis to explain this puzzling lattice parameters' variation within a biphasic electrochemical process.

The single phase $Na_{1.8}$VPF is sodium-disordered and undergoes a solid solution reaction upon further Na^+ extraction within the Na_xVPF ($1.8 < x < 1.3$) composition range. All

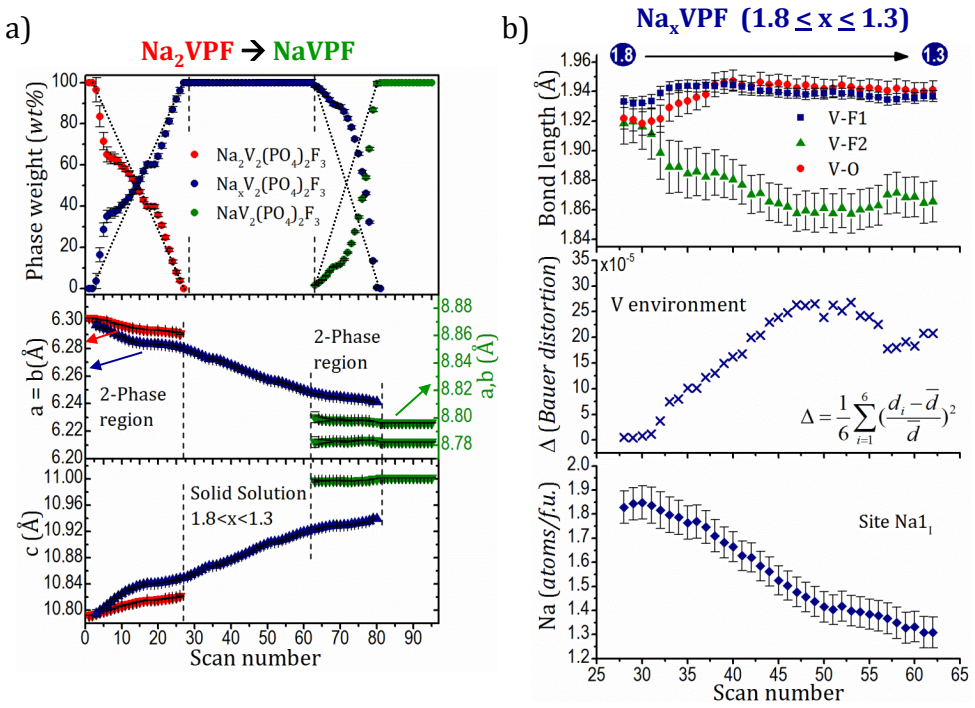

Figure 5.28: a) Parameters obtained from Rietveld refinement during the high-voltage-composition plateau (electrode reacting from composition Na_2VPF to NaVPF). Unit cell parameters of the different phases and relative percentage in weight are presented. All the phases were described in the space group I4/mmm, except NaVPF in $Cmc2_1$. b) Parameters obtained from Rietveld refinement (S.G. I4/mmm) during the solid solution reaction occurring in Na_xVPF ($1.8 < x < 1.3$). Top: vanadium's bond lengths obtained from refinement of fractional atomic coordinates. Middle: Bauer distortion calculated for VO_4F_2 octahedra. Bottom: amount of sodium per f.u. obtained from the refined site occupancy factor in site $Na1_I$.

reflections can be indexed using the I4/mmm space group. A sequential Rietveld refinement procedure was undertaken (Figure 5.28). The a and b lattice parameters continuously decrease from 6.2800(1) Å to 6.2481(1) Å, while c increases (more significantly) from 10.8493(3) Å to 10.9222(2) Å, leading to characteristic Bragg peaks crossings (see 17.4°-17.6° 2θ region in Figure 5.27). All fractional atomic coordinates and the site occupancy factor (SOF) for sodium in the $Na1_I$ site were refined (Figure 5.28b). SOF is a particularly useful parameter because it offers a direct observation of the amount of sodium present in the unit cell. The total number of Na^+ within the $Na1_I$ equivalent crystallographic positions decreases from 1.85(7) for $Na_{1.8}$VPF to 1.31(6) Na/f.u. for $Na_{1.3}$VPF. The V-F bond lengths vary anisotropically (1.932(5) Å to 1.938(4) Å for V-F1, 1.92(1) Å to 1.87(1) Å for V-F2) as often encountered during vanadium oxidation [10,95], while V-O increases slightly from 1.926(9) Å to 1.942(9) Å (Table 5.7). It is interesting to observe the distortion

of vanadium's octahedral environment (Figure 5.28b), which increases by a factor 30 during this solid solution process, mainly due to the continuous shortening of the V-F2 bond.

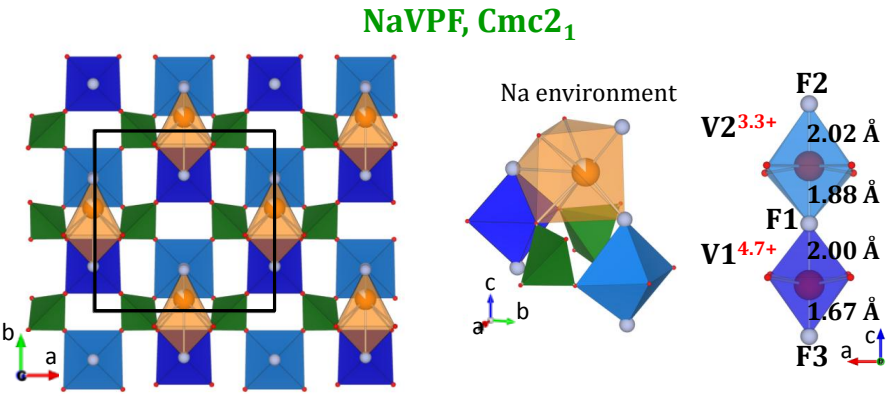

Figure 5.29: Structure of NaVPF (full composition $NaV_2(PO_4)_2F_3$) in the $Cmc2_1$ space group. Two different environments for vanadium cations are observed (dark and light blue), suggesting a V^{3+}-V^{5+} pair (oxidation state from BVS calculations is displayed). Environment of sodium in a capped prism is also reported.

The end of charge occurs through a biphasic reaction between $Na_{1.3}$VPF and NaVPF at 4.19 V vs. Na^+/Na (Figure 5.2). Extra reflections at low 2θ angles indicate the formation of a new sodium-ordered phase, NaVPF (Figure 5.27b). The reaction between $Na_{1.3}$VPF and NaVPF is peculiar because it shows a delay. NaVPF starts forming promptly, but its crystallization is not evolving linearly. A possible explanation is that this phase nucleates in the form of stable small domains spread in the sample, making it hardly detectable by diffraction. As the process goes on, the domains either grow and/or coalesce until a long range NaVPF crystalline structure is observed. This process can be understood in view of the proposed NaVPF crystal structure as will be discussed with more details at the end of the next paragraph. The diffraction pattern of the obtained NaVPF phase does not correspond to any of those previously encountered. Cell parameters reveal a certain similarity with the pristine phase because of a subtle orthorhombic distortion: a = 8.7822(3) Å, b = 8.7962(3) Å, c = 11.0015(2) Å that can be noticed in the right part of Figure 5.28 (in green, peaks (400) and (040)). This indicates an extremely small volume change $\Delta V/V$ = 3% along the overall charge of the material (Table 5.6). Systematic extinctions reveal a C-centered space group for the crystal structure of NaVPF and the space groups showing the best results from profile-matching are Cmcm, $Cmc2_1$ and C2cm in setting 1. A structural determination in space groups Cmcm and C2cm was attempted without success, while

$Cmc2_1$ (a subgroup of Cmcm) allowed us to obtain a structure related to the pristine one, showing V bi-octahedra and PO_4 tetrahedra. This description requires a shift of the unit cell origin of (1/4, 0, 0) with respect to the pristine one, placing V in two different 4a Wyckoff positions and generating two different V environments (Figure 5.29). Rietveld refinement (reported with relative Fourier maps in Figure 5.30) indeed showed that the two vanadium belonging to the same bi-octahedron have different environments: bond-valence sum calculations clearly differentiates them as a V^{3+}-V^{5+} -type pair (+4.7(3) for V1 and +3.3(2) for V2) rather than a V^{4+}-V^{4+} one.

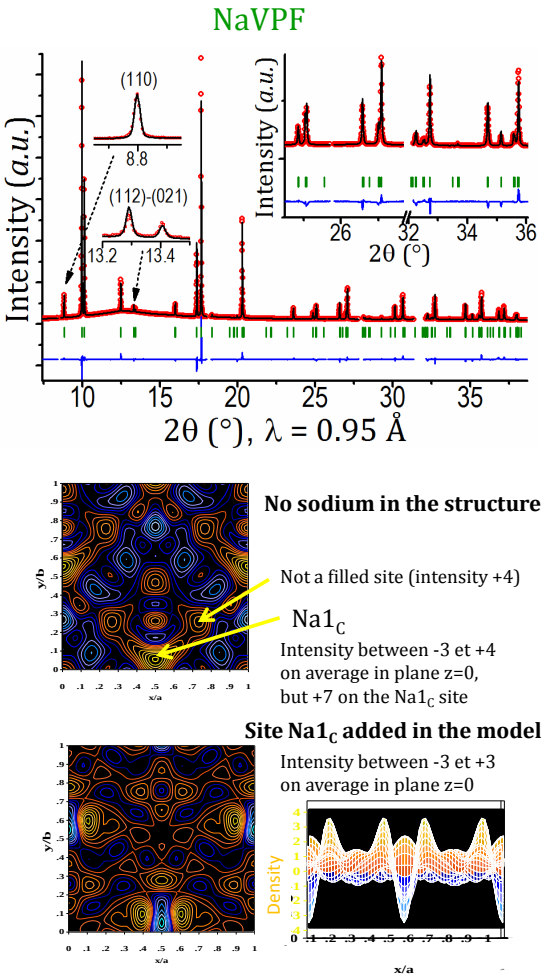

Figure 5.30: Top: Rietveld refinement of the structure of NaVPF in the $Cmc2_1$ space group. (110), (112) and (021) peaks are evidenced because they are characteristics of this crystal structure only. Bottom: Fourier difference map obtained after Rietveld refinement of diffraction data, using a structural model not including any sodium.

More than two oxidation states of vanadium have already been shown to coexist in the same material and vanadium's disproportionation is an occurring reaction ($2V^{4+} \rightarrow$

Table 5.8: Structural parameters obtained from Rietveld refinement of *in situ* synchrotron radiation data for fully charged NaVPF, in the space group $Cmc2_1$. Because of the floating origin of this space group, z/c of V1 is not refined.

$NaV_2(PO_4)_2F_3$

S.G. $Cmc2_1$; Z=4

a = 8.7822(3) Å;
b = 8.7961(3) Å; R_{wp} = 14.8%;
c = 11.0015(2) Å; R_B = 4.45%;
V = 849.86(1) Å^3; χ^2 = 2.58.
V/Z = 212.47(1) Å^3.

Atomic Parameters

Atoms	Wyckoff	Atomic Positions			SOF	B_{iso}#
		x/a	y/b	z/c		
V1	4a	1/2	0.248(4)	0.338(-)	1	0.63
V2	4a	0	0.251(3)	0.1908(7)	1	0.63
P##	8	0.244(2)	0.501(3)	0.276(1)	1	0.96
O1	8	0.357(5)	0.098(6)	0.368(3)	1	1.07
O2	8	0.347(7)	0.397(7)	0.361(3)	1	1.07
O3	8	0.157(7)	0.100(7)	0.193(3)	1	1.07
O4	8	0.163(5)	0.423(5)	0.170(2)	1	1.07
F(1)	4a	1/2	0.247(6)	0.520(6)	1	0.59
F(2)	4a	1/2	0.24(1)	0.875(2)	1	0.59
F(3)	4a	1/2	0.232(8)	0.187(3)	1	0.59
Na(2)	4a	1/2	0.071(2)	0.025(8)	0.88(9)	3.0

refined in the final stages of refinement and then fixed

soft constraints used on P-O distances (P-O = 1.54 Å+/- 0.02 Å)

V^{3+} + V^{5+}). As an example, it was found for $Li_{1+x}V_3O_8$ that upon reduction (Li insertion) the signature of V^{3+} can coexist with the V^{4+} and V^{5+} ones[332]. In the same way, the coexistence of V^{3+} and V^{5+} has also been observed using XANES spectroscopy for $NaV_2^{4.8+}O_{1.6}(PO_4)_2F_{1.4}$, obtained by sodium deintercalation from the pristine compound $Na_3V_2^{4.8+}O_{1.6}(PO_4)_2F_{1.4}$[310]: the signature of V^{3+} is reported to be present with those of V^{4+} and V^{5+}. The authors proposed that the small amount of V^{3+} present in the pristine material would not be involved in the redox processes, but considering our results obtained for $NaV_2^{IV}(PO_4)_2F_3$, it could also be that V^{3+} is oxidized to V^{4+} and it subsequently undergoes disproportionation. In our case, a 50%-50% V^{3+}-V^{4+} ordered composition was most likely formed upon Na^+ extraction towards Na_2VPF. Upon further oxidation, tetragonal symmetry suggests that only one site of V is present in the solid solution domain. When the final biphasic reaction takes place, either every vanadium has $3d^14s^0$ electronic

structure (i.e. one unpaired electron) or they are distributed 50%-50% $3d^24s^0$ and $3d^04s^0$ (i.e. one vanadium with no unpaired electron and one with a pair). It seems in our case that this charge distribution is energetically favorable, especially in a system where the two vanadium environments share one corner.

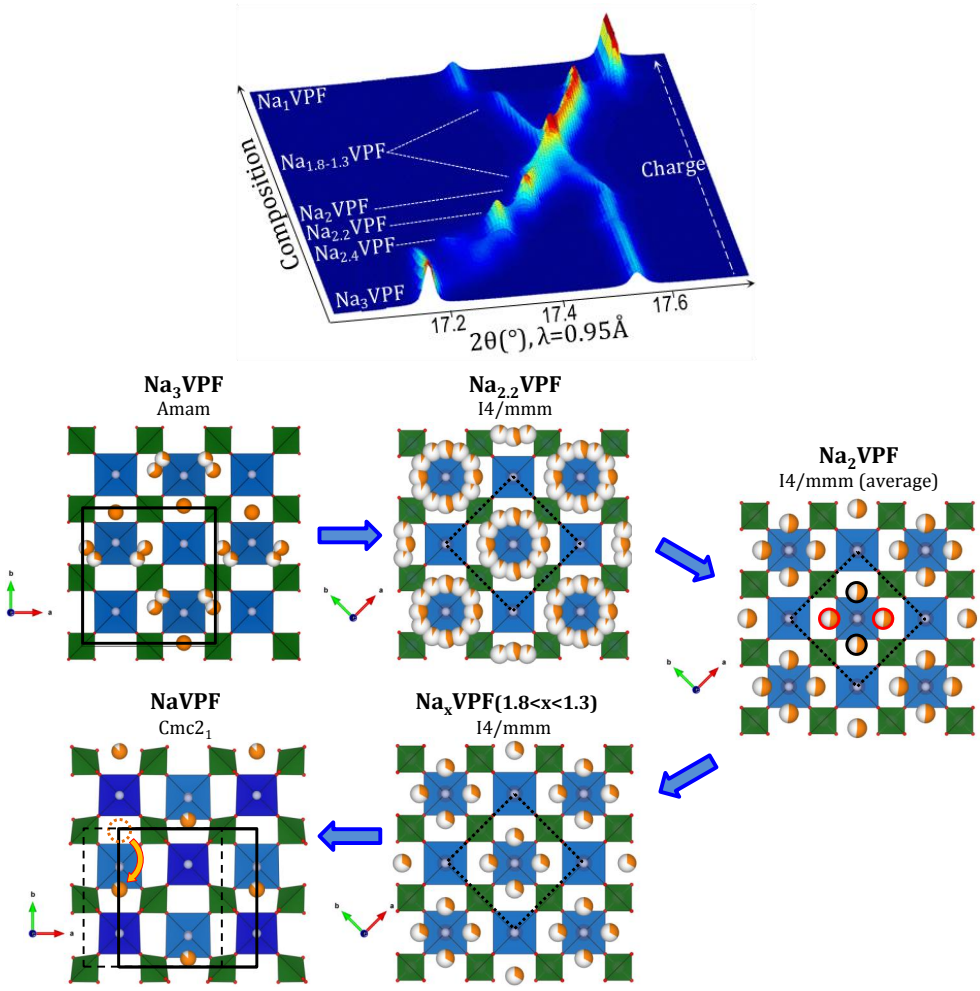

Figure 5.31: Top: Tridimensional view of the 2 Na^+ extraction from Na_3VPF (complete charge). Bottom: sodium distribution obtained from Rietveld refinement of the different phases observed upon sodium extraction from Na_3VPF. Although a superstructure was observed for phase Na_2VPF, only the average structure was determined, thus the red/black circles indicate that only two positions out of four are expected to be occupied. For NaVPF, an orange dotted circle shows the second sodium site $Na1_A$ which is filled in the structure of Na_3VPF (dashed cell), while it is now empty.

Table 5.8 gathers all the structural information related to NaVPF obtained from Rietveld refinement. The V1-O distances are significantly shorter than the V2-O ones and the V1-F3 bond-length is rather short (but already observed for other V^{5+}-F containing compounds[333]). Our conclusions on the V^{5+}/V^{3+} disproportionation in NaVPF are based,

noticeably, on structural refinements from *in situ* XRPD data and will deserve supporting electronic structure calculations and oxidation-sensitive analysis techniques (XAS for example). Regarding sodium ions, we found them placed in a single fully occupied site $Na1_C$, partially corresponding to the $Na1_A$ site of the pristine material. Its environment is a capped prism, composed of 4 oxygen and 3 fluorine atoms. Local charge compensation results in longer $Na1_C$-$V1^{4.7+}$ bond-length (3.48(3) Å) than $Na1_C$-$V2^{3.3+}$ (3.35(3) Å). A strong difference is noticed with respect to Na_3VPF: in both cases the plane z = 0 hosts two Na1 sites, but looking at the two arrangements (Figure 5.31) we notice that for NaVPF one of the two Na1 positions is on the opposite side of the fluorine atom F1, with respect to the Na_3VPF case. This partially explains the need for a different space group (together with the fact that two V environments are present in NaVPF). To highlight the main crystal structure modifications observed upon sodium extraction from Na_3VPF, Figure 5.31 gives special emphasis to sodium rearrangement inside the unit cell. In the light of this, the biphasic transition between $Na_{1.3}$VPF and NaVPF discussed above can be understood as follows: during the solid solution Na_xVPF ($1.8 < x < 1.3$) the vanadium polyhedral distortion increases significantly. At composition $Na_{1.3}$VPF, the sodium- and vanadium oxidation- disordered space group I4/mmm is not energetically favorable anymore, and vanadium undergoes disproportionation. The 4 ≈1/4-filled sites stop being equivalent and sodium ions converge on a single site in a bigger unit cell. This ordering happens on several small domains, underestimated by diffraction methods and separated by larger ones which remain disordered. Only when the ordered domains coalesce, diffraction is able to properly quantify them.

5.4 From $Na_3V_2(PO_4)_2F_3$ to $Ag_3V_2(PO_4)_2F_3$: Na^+/Ag^+ ion exchange

Our *operando* experiment on Na_3VPF as well as the remarkable properties of this material upon Na^+ extraction / insertion at high rates[75] strongly suggest facile ion transport properties of the Na^+ cations. This opens up several possibilities of ion exchange to prepare new compositions for different purposes and silver-containing compounds can be of interest for a few niche but important applications. The Ag^+ cation is slightly bigger than Na^+ (1.29 Å vs. 1.16 Å) but it is also well-known to be more polarisable due to its electronic configuration $5s^0 4d^{10}$. This fact allows substitution of these cations within similar

frameworks[334,335]. The compounds investigated in the literature include open structures of NASICON-type such as $Ag_{1+x}Zr_{2-x}M_x(PO_4)_3$ (M = Sc, Fe[336]), $AgTaMP_3O_{12}$ (M = Al, Ga, In, Cr, Fe and Y)[337], $AgSbMP_3O_{12}$ (M = Al, Ga, Fe and Cr)[338] and other structural families such as $(Ag_{1-x}Na_x)_2$-$FeMn_2(PO_4)_3$[339], $Ag_2VP_2O_8$[340], $AgRu_2(P_2O_7)_2$[341] and $Ag_{7-x}Na_xFe_3(X_2O_7)_4$ (X = P, As)[334,335]. The high ionic conductivity of these ceramics can be exploited in devices such as membranes, fuel cells and gas sensors[342,343]. Other potential applications include low thermal expansion materials[344], hosts for radioactive waste[345], catalyst supports[346], ion exchangers[347] and insertion/extraction reactions[348]. Here we report on our preliminary study to obtain a new silver fluorophosphate $Ag_3V_2^{III}(PO_4)_2F_3$ prepared through ion exchange from the sodium analogous $Na_3V_2^{III}(PO_4)_2F_3$ (Na_3VPF). For the preparation, carried out by Fabien Lalère in LRCS, as-synthesized Na_3VPF powder was stirred during several hours in a saturated solution of $AgNO_3$ to exchange sodium ions by silver ions. The resulting powder was washed several times with water and then acetone, and dried at 50°C under vacuum to be characterized and eventually put back into the $AgNO_3$ solution to carry on the ion exchange as much as needed (to displace the equilibrium) to get the desired $Ag_3V_2(PO_4)_2F_3$ phase.

Table 5.9: Ion exchange as a function of elapsed time. Cell parameters obtained from LeBail fit of XRPD data are reported. The last column shows the silver amount measured via MEB-EDX (except for t=15min because of the insufficient amount of material recovered).

Time	a (Å)	b (Å)	c (Å)	V/Z (Å^3)	a/b	x in $Na_{3-x}Ag_xV_2(PO_4)_2F_3$
0	9.028(3)	9.042(3)	10.741(3)	219.2	0.998	0
15 min	9.043(3)	9.037(3)	10.767(3)	220.0	1.000	unknown
20 hrs	9.075(3)	9.035(3)	10.916(3)	223.8	1.004	2.4
60 hrs	9.082(2)	9.028(2)	10.945(2)	224.3	1.006	2.8

Figure 5.32 and Table 5.9 show the ion exchange evolution over time. Note that after 15 min Bragg peaks are in similar positions but with modified intensity, indicative of the initial substitution of Ag for Na. After 20 hours the diffraction pattern is clearly modified from the pristine one, as the reflections significantly change position and intensity, while after 60 hours they show only slight changes. These first observations suggest a solid solution domain present close to the extremes of $Na_{3-x}Ag_xV_2(PO_4)_2F_3$, but they are not sufficient to support the total absence of a miscibility gap.

As measured from MEB-EDX after 60 hours we obtained $Ag_{2.70}Na_{0.38}V_2(PO_4)_2F_3$, still containing sodium but significantly Ag-rich, and the compound will be referred to as

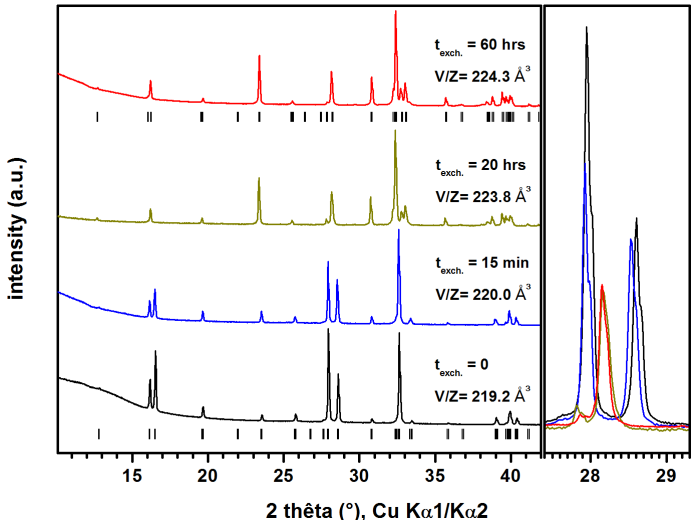

Figure 5.32: Evolution of the XRPD diffraction patterns of $Na_3V_2(PO_4)_2F_3$ as the Ag^+/Na^+ ion exchange proceeds. The different position of the (111) and (002) peaks are highlighted on the right.

Ag_3VPF for brevity in the following. Since the material's diffraction patterns were clearly modified from the pristine ones, we proceeded to make a new structural determination. The measurements were carried out at MSPD (ALBA) and on the D2B (ILL) diffractometer, in the high-resolution mode as described previously (see the Introduction). A complete structural Rietveld refinement was carried out on the two combined data set (Figure 5.33). A first look at the synchrotron XRPD pattern shows modified angular positions for Bragg reflections, although the most important differences are found on the reflections' intensities, as expected by the much higher atomic weight of silver with respect to sodium. The

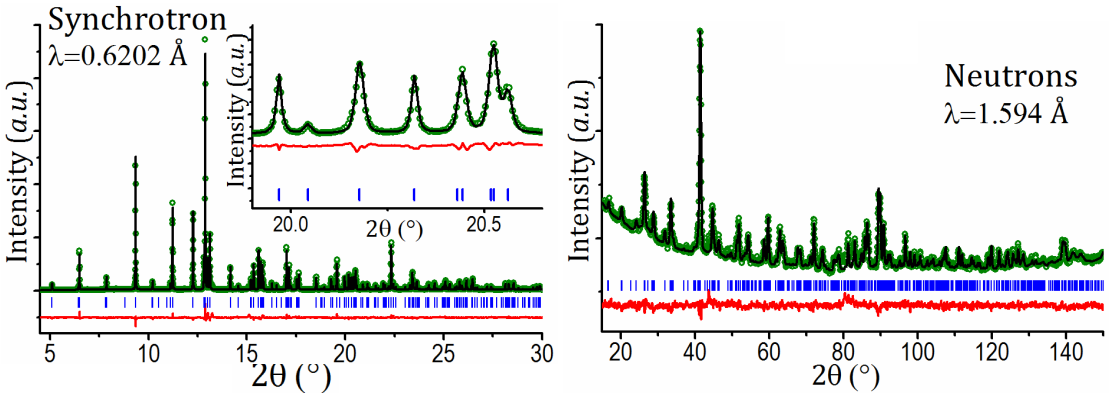

Figure 5.33: Combined Rietveld refinement of synchrotron XRPD and NPD of Ag_3VPF. Measured data are shown as green dots, Rietveld fit as a black line, their difference as a red line and Bragg positions as blue marks.

indexation quickly revealed the compatibility of such Bragg positions with the space group Amam of Na_3VPF [312]. As all peaks are properly indexed, no doubt is left about the presence of a single phase after our ionic exchange. As previously discussed, the parent compound has the peculiarity of an extremely small orthorhombic distortion in the ab plane (Table 5.9). The distortion is found to significantly increase in Ag_3VPF , where a = 9.0843(1) Å and b = 9.0303(1) Å (b < a now and a/b = 1.006). This implies that while the b unit cell parameter slightly decreases, a strongly increases. The c axis lengthens as well, from c = 10.741(3) Å to c = 10.9942(1) Å. It is interesting to note that this is a direct confirmation of the Amam space group's exactitude for Na_3VPF. The Ag/Na substitution respects the same symmetry constrains and this space group can be more clearly and undoubtedly confirmed in reason of the presence of Ag, which has two effects: it distorts more the (a,b) plane, making the Bragg peaks' splitting easier to observe; and it

Table 5.10: Structural parameters obtained from combined Rietveld refinement of synchrotron XRPD and neutrons diffraction data of Ag_3VPF.

$Ag_{2.70}Na_{0.38}V_2(PO_4)_2F_3$ (Ag_3VPF)

S.G. Amam; Z=4

Combined: $\chi^2 = 6.56$.

a = 9.0843(1) Å;

b = 9.0303(1) Å;

c = 10.9442(1) Å;

V = 897.796(1) Å^3;

V/Z = 224.449(1) Å^3.

Synchrotron:

R_{wp} = 16.7%; R_B = 7.88%.

Neutrons:

R_{wp} = 18.9%; R_B = 12.6%.

Atomic Parameters

Atoms	Wyckoff	Atomic Positions			SOF	B_{iso}#
		x/a	y/b	z/c		
V1	8g	1/4	0.2525(6)	0.1820(4)	1	0.5(1)
P1	8e	0	0	0.2396(9)	1	0.7(1)
O1	16h	0.099(1)	0.094(1)	0.156(1)	1	0.7(2)
O2	16h	0.093(1)	0.402(1)	0.175(1)	1	0.7(2)
F1	4c	1/4	0.265(2)	0	1	0.8(3)
F2	8g	1/4	0.742(2)	0.140(1)	1	1.0(3)
Ag1	4c	1/4	0.9610(5)	0	0.92(1)	2.1(1)
Ag2	8f	0.9598(7)	0.792(1)	1/2	0.51(6)	1.2(2)
Ag3	8f	0.942(1)	0.856(2)	1/2	0.38(6)	1.6(3)
Na1	4c	1/4	0.9610(5)	0	0.08(1)	2.1(1)
Na2	8f	0.9598(7)	0.792(1)	1/2	0.15(3)	1.2(2)

Total amount of Na (0.38) is set to the value found by MEB-EDX.

Na3 SOF is found slightly negative, thus it is set to 0.

is a stronger scatterer of X-Rays (Z = 47 vs. Z=11 for Na), thus dominating the intensity of reflections and leaving no doubt about its position in the structure.

Based on the combined Rietveld refinement of diffraction patterns (Figure 5.33 and Table 5.10), the crystal structure of Ag_3VPF was obtained and it is shown in Figure 5.34. The basic structural framework of Na_3VPF, consisting of $V_2O_8F_3$ bi-octahedra, is preserved. Such bioctahedral environments are bridged by corner-sharing PO_4 tetrahedra, building a stable structure where large tunnels are present along the [110] and [1-10] directions. These are responsible for the facile sodium extraction from Na_3VPF and for its promising electrochemical activity as a positive electrode for Na-ion batteries, but also for the relative ease of ion exchange with silver without consequent disruption of the 3D framework of the material.

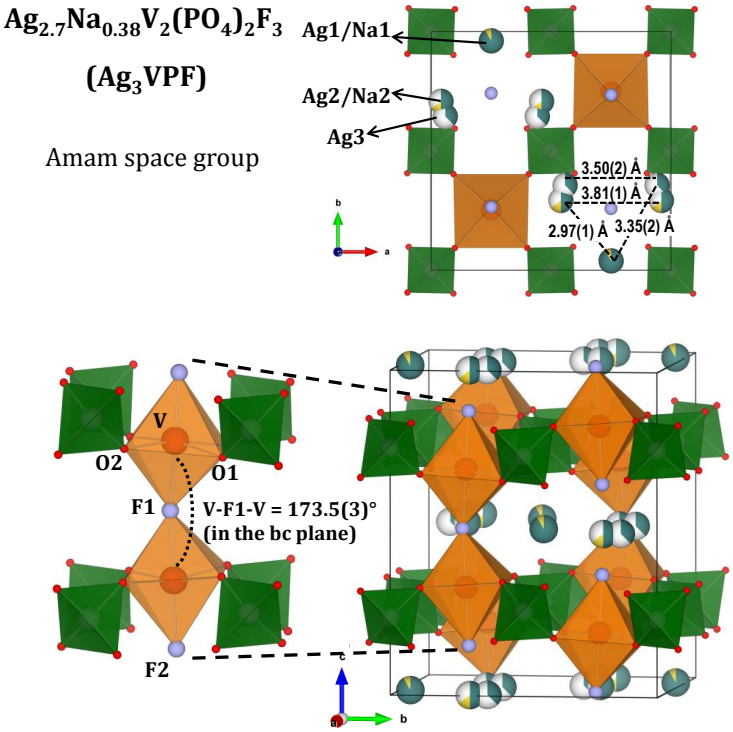

Figure 5.34: Crystal structure of Ag_3VPF obtained by ion exchange with Na_3VPF. The space group Amam is retained, but a more pronounced orthorhombic distortion is induced.

Table 5.11 and Table 5.12 report all significant structural information on PO_4 tetrahedra and VO_4F_2 octahedra, respectively. The most important differences between the parent structural framework and the one obtained after Ag/Na ion exchange can be summarized as follows:

- more pronounced orthorhombic distortion and longer c axis, as discussed above.

- bond-length distances within the octahedra and tetrahedra are in general poorly affected: P-O distances in PO_4 and V-O ones in VO_4F_2 are barely modified, while a small difference is found for V-F bonds: V-F1 increases from 1.98 Å to 1.995(5) Å and V-F2 decreases from 1.97 Å to 1.95(1) Å.
- the angle between the two octahedra, given by V-F1-V, decreases from an almost straight one in Na_3VPF (179.5(2)°) to a significantly bent one (173.5(3)°). The bending completely happens in the (b,c) plane, since x/a is fixed by symmetry to be 1/4 for V and F1. It is interesting to note that such bending does not correlate to a bigger value of the b cell parameters (on the contrary, b slightly decreases), while, on the other hand, a and c increase.

Table 5.11: Significant bond-length distances (Å) (upper right part), angles (°) (down left part), polyhedral distortion and Bond-Valence Sum calculations for PO_4 tetrahedra in Ag_3VPF.

***PO*$_4$**	O(1)	O(1)	O(2)	O(2)
O(1)	**1.54(1)**	2.47(2)	2.55(2)	2.54(2)
O(1)	106.8(3)	**1.54(1)**	2.54(2)	2.55(2)
O(2)	111.7(3)	110.8(2)	**1.54(1)**	2.45(2)
O(2)	110.8(2)	111.7(3)	105.2(3)	**1.54(1)**

Distortion $\Delta = 0.11{\cdot}10^{-5}$, BVS = +4.94(9)

Table 5.12: Significant bond-length distances (Å) (upper right part), angles (°) (down left part), polyhedral distortion and Bond-Valence Sum calculations for VO_4F_2 octahedra in Ag_3VPF.

***VO*$_4$*F*$_2$**	O(1)	O(1)	O(2)	O(2)	F(1)	F(2)
O(1)	**2.01(1)**	2.74(1)	2.80(2)	3.95(2)	2.68(1)	2.94(2)
O(1)	86.2(2)	**2.01(1)**	3.95(2)	2.80(2)	2.68(1)	2.94(2)
O(2)	89.5(1)	169.1(2)	**1.96(1)**	2.85(2)	2.69(2)	2.87(2)
O(2)	169.1(2)	89.5(1)	92.9(2)	**1.96(1)**	2.69(2)	2.87(2)
F(1)	84.1(1)	84.1(1)	85.5(1)	85.5(1)	**1.995(5)**	3.95(2)
F(2)	96.1(2)	96.1(2)	94.3(2)	94.3(2)	179.7(2)	**1.95(1)**

Distortion $\Delta = 1.174{\cdot}10^{-a}$, BVS = +3.04(4)

The increase of the unit cell can be explained by steric effects of the bigger Ag^+ ions with respect to Na^+. As reviewed by Shannon[349], effective ionic radii for 6-coordinated Na^+ and Ag^+ are 1.02 Å and 1.15 Å, respectively (If classical crystal ionic radii are used, the two values become 1.16 Å and 1.29 Å, the difference being the choice of the radius of

oxygen r(O^{2-})). Regardless of the choice, in both cases a difference of 0.13 Å is present, whose effects have been described above. It is important to mention that, although Ag^+ is bigger and somehow distorts the structure of Na_3VPF, it is also sufficiently polarisable (due to the high number of electrons, $5s^0 4d^{10}$) not to demand a symmetry modification of the structure.

In Na_3VPF, sodium ions are found in the plane z = 0 and z = 1/2, distributed on a "triangular" arrangement of three crystallographic sites $Na1_A$, $Na2_A$ and $Na3_A$. The first one is fully occupied, while $Na2_A$ and $Na3_A$ have partial occupancy, respectively, close to 2/3 and 1/3. We found, surprisingly, that Ag^+ ions place themselves on the exact same sites of Na^+ ions in Na_3VPF. Even relative occupations are similar (Table 5.10). Figure 5.34 also gathers Na^+ and Ag^+ distributions in the z = 0 plane with the relative inter-cationic distances. Since from MEB-EDX it is found that the ion exchange is not complete (about 0.38 Na/f.u. remaining) we used this information during Rietveld refinement to localize sodium by constraining the total Na amount to 0.38. We observe that the remaning Na^+ cations are localized in $Na1_A$ (0.08(1) / f.u.) and $Na2_A$ (0.30(3) / f.u.) sites, but not in the $Na3_A$ one, where the site occupancy factor (SOF) converged to a negligible (slightly negative) value. We can conclude that Ag-Ag distances are very similar to Na-Na ones in Na_3VPF, except for Ag3-Ag3 which are farther away (Na3-Na3 = 2.84 Å in Na_3VPF whereas Ag3-Ag3 = 3.50 Å).

5.5 Conclusions and perspectives

In this work we showed how the use of high resolution techniques led to new insight on $Na_3V_2(PO_4)_2F_3$, a material previously thought to be well-known from the crystal structure and electrochemical points of view, but with a significant amount of discrepancies found throughout the literature, which we believe to be the result of a partial substitution of oxygen for fluorine. Since the fully disordered sodium distribution is obtained at lower temperature for $Na_3V_2(PO_4)_2F_3$ than for $Na_3V_2O_2(PO_4)_2F$ ($\Delta T = 100°C$), it is reasonable to expect higher ionic conductivity for the fluorine-rich phase. As a result, it appears that the O/F ratio could be a very critical parameter. Its control will allow getting the optimized composition and thus the material with the most attractive electrochemical properties for Na-ion batteries. For the actual composition $Na_3V_2(PO_4)_2F_3$ (Na_3VPF), slow galvanostatic cycling showed the presence of four distinct electrochemical features, an original electrochemical signature for Na_3VPF that we have reported for the first time[75].

More importantly, synchrotron radiation powder diffraction data revealed a small but significant orthorhombic distortion in Na_3VPF (b/a=1.002). This led to an indexation in the Amam space group and to a new structure preserving the framework but strongly impacting the sodium distribution in the planes. This arrangement is the most interesting aspect of Na_3VPF because it derives from a totally disordered one at high temperature to a partially ordered one at ambient temperature. The precise origin of such residual disorder is a challenging problem, currently under investigation. High angular and intensity resolution synchrotron radiation XRPD was then used to study the structural evolution of Na_3VPF upon Na^+ extraction in details. The sodium deintercalation reaction, generally reported to be a simple solid solution, reveals instead an extremely complicated phase transformations sequence. The two voltage domains around 3.7 V and 4.2 V vs. Na^+/Na have been analyzed separately. The lower voltage region never proceeds through a solid solution. Instead it reveals three biphasic reactions involving two intermediate phases, $Na_{2.4}VPF$ and $Na_{2.2}VPF$. The latter displays the same structure as the high-temperature form of Na_3VPF, crystallizing in the tetragonal space group I4/mmm due to Na^+ disordering. The former stabilizes instead an ordering on a longer range, up to a ≈18 Å d-spacing, suggesting a superstructural arrangement. At the end of the first voltage-composition plateau, the phase Na_2VPF is obtained, revealing another possible superstructure due to sodium ordering and/or charge ordering. The higher voltage region shows a biphasic reaction upon which Na_2VPF disappears and subsequently a wide solid solution of compositions Na_xVPF ($1.8 < x < 1.3$), again sodium-disordered. Thanks to the high quality of these synchrotron data we could follow the reaction in detail and observe the structural modifications (e.g. cell parameters, bond lengths, polyhedral distortion...) and sodium extraction (namely sodium's site occupancy factor) in real time. The end-member NaVPF is finally attained through another biphasic reaction. The structure of this composition is different than those previously encountered and a structural determination was carried out for the first time directly on data collected *operando*. It revealed a $Cmc2_1$ space group, leading to a fully occupied sodium site and most importantly and unexpectedly to two different vanadium environments (a V^{3+}-V^{5+} couple in every bi-octahedron). The extremely small volume change observed from Na_3VPF to NaVPF, along the overall charge, further qualifies Na_3VPF as a material of choice for long term cycling stability. These *in situ* measurements demonstrate how obtaining good angular resolution and high intensity data is crucial because, delivering more detailed information, it can radically change the understanding of a given electrode's

behavior. Our study proves how even resolving weak Bragg reflections can be a key element because it allows, for example, distinguishing among sodium ordered and sodium disordered structures. This is important as it paves the way to direct observation of fine reaction pathways and thus to a more exact knowledge of electrode materials' properties. Finally, we began to study the ion exchange of Na^+ in Na_3VPF with other cations, exploiting its high ionic conductivity. In particular we report here the exchange with Ag^+, since materials for silver intercalation are used for interesting applications. We show how we can obtain almost pure Ag_3VPF ($Ag_{2.70}Na_{0.38}V_2(PO_4)_2F_3$) and how it preserves the crystal structure of Na_3VPF, although with modified cell parameters. Interestingly, even the positions of Ag^+ cations are those who were occupied by Na^+, producing further evidence of the correctness of our structural determination on Na_3VPF. Several studies are envisaged to complete those reported here. Firstly, a direct measurement of the ionic conductivity of Na_3VPF, which could not be completed in time because of technical issues, and the growth of Na_3VPF single crystals, to confirm our structure and to facilitate ionic conductivity measurements. Secondly, the phase diagram of Na_3VPF is still far from being totally understood. The superstructures encountered at compositions $Na_{2.4}VPF$ and Na_2VPF still need to be explained. Here the help of electron diffraction will probably be of key importance, once the phases are stabilized under the beam. Moreover, temperature-controlled studies at key compositions such as Na_2VPF or NaVPF are currently in the making, to get further insights into Na^+ diffusion into the VPF framework. Finally, note that our study of Na_3VPF demonstrates the potentialities of *operando* synchrotron radiation XRPD studies to understand reaction processes in electrode materials. This is complementary to *operando* NPD and they can be both used, depending on the properties under investigation, to get detailed insights through the Rietveld method. Countless materials could then beneficiate from these advanced characterization techniques, as we plan to do with those we believe to be more significant for the Li-ion and Na-ion technology.

Conclusion

The central idea of this thesis has been the application of the *operando* methodology to a variety of electrode materials for alkali intercalation-based battery technologies, i.e. Li-ion and Na-ion. Strong motivation for conducting such studies is the belief that the improvement of batteries performances is directly related to a deep understanding of their functioning. In this respect, *operando* studies are the best choice to observe Li^+ or Na^+ (de)intercalation reactions in real time and to obtain detailed information about such processes. Given the crystalline nature of most electrode materials, the characterization technique of choice for determining their structure and structural modifications upon cycling is diffraction. Electrode materials contain heavy transition metals and light cations (Li, Na) and anions (O, F...), thus rarely a single probe is able to observe all of them: combined studies are required. During our diffraction experiments we then tried to exploit several different probes and to take advantage of their combined use to obtain a maximum of details: neutrons, in particular, are sensitive to lithium and oxygen, key elements in battery electrodes, while X-Rays give precise information on transition metals and cell parameters. Synchrotron radiation was also used, as it offers unrivaled angular and time resolution, crucial for *operando* experiments.

These studies require appropriate setups to be carried out: the electrochemical cells needed must be able to combine good electrochemical properties with the specific requirements of the characterization techniques of choice. Often contrasting, these requirements make setups design quite tricky. In our research groups two of such cells were developed for *in situ*/*operando* XRPD and synchrotron XRPD studies, so that they could be extensively used in this thesis. Then, a large part of the PhD project has been the development of a complementary cell for *in situ*/*operando* neutron powder diffraction. Given the significant issues that such experiments present, special precautions had to be taken in the design, like the use of "neutron-transparent" (Ti,Zr) alloy for cell manufacture and of deuterated elec-

trolytes. Chapter 2 specifically describes the issues/drawbacks of *in situ* NPD diffraction and the electrochemical cells developed in the literature and by us to achieve such a goal. All the separate contributions and possible scattering events were considered and discussed and our first successful *operando* study on $LiFePO_4$ was described. We demonstrated how we could obtain detailed structural information even during an *operando* experiment (the charge, or delithiation to composition $FePO_4$) and subsequently use this awareness to carry out new studies on challenging materials belonging to the spinel crystal family. In Chapter 3 we studied in detail the (de)lithiation of materials of strong relevance for applications: three samples in the family $Li_{1+x}Mn_{2-x}O_4$ (x = 0, x = 0.05 and x = 0.10) and a high-voltage spinel $LiNi_{0.4}Mn_{1.6}O_4$. Our experiments and analysis revealed several insights on the phase diagram and (de)lithiation processes of these materials when they are cycled in a battery. Importantly, we confirmed that *operando* NPD allows us to be sensitive not only to cell parameters, phase fractions and fractional atomic coordinates, but also to more elusive (but carrying much information) parameters as atomic displacement parameters and lithium's site occupancy factors. Therefore we could observe and explain new features of the electrochemical reactions, as for example the voltage-dependent rate of delithiation in $Li_{1.10}Mn_{1.90}O_4$ or the distortion occurring on isolated Ni^{3+} cations upon charge of $LiNi_{0.4}Mn_{1.6}O_4$. Our results confirmed the feasibility and the richness of information attainable from *in situ* NPD; the technique will then continue to be exploited to study new interesting materials, both in our group and for the whole scientific community since the (Ti,Zr) *in situ* cell will remain available at ILL. In our specific case, we also envisage to widen the application range of such experiments: new materials will be studied, mostly among polyanionic phosphates; new cells will be designed, with the goal of allowing also electrochemical cycling at high temperature (for application in all-solid-state batteries); and new electrolytes will be developed to cut the cost of experiments.

When they are not the main characterization technique used, neutrons can be a valuable tool to support (less expensive) XRPD studies, as in the case of $LiVPO_4O$. We reported our study on such a material in Chapter 4, where the phase diagram and phase transformations observed on both lithiation and delithiation are described in detail. This Tavorite compound, already part of the PhD of a previous student in our group, is of great interest as it offers good gravimetric energy density and the ability to exchange 2 Li^+/f.u., possibly doubling the available capacity. We combined electrochemical characterizations, revealing the importance of controlling particle size to obtain good cyclability, with structural studies

analyzing in-depth the mechanisms of lithium extraction/insertion. Here we showed the strength and richness of the *operando* diffraction approach, even when laboratory diffractometers are used instead of large-scale instruments. Complex series of phase transition could be followed in real time and the effect of strains induced by the volume change between different phases was highlighted. Neutrons were still used as a complement in this study, specifically to determine detailed crystal structures when significant amounts of light elements are present in the stoichiometry. In the light of the phase transformations thoroughly described in this work, improvement of the electrochemical performances and rate capabilities will possibly be achieved in future studies. To complete the range of large scale instruments represented in this thesis, synchrotron radiation was also used for selected studies requiring extremely high angular and intensity resolution. Here, synchrotron XRPD was mainly employed for experiments concerning $Na_3V_2(PO_4)_2F_3$, a greatly promising material for next-generation Na-ion batteries. The compound was revisited, since it was indexed in a new orthorhombic space group and a new crystal structure was determined, with corrected positions of Na^+ in the unit cell. Moreover, *operando* synchrotron XRPD showed an incredibly rich phase diagram upon sodium extraction, resulting from different possible sodium and/or vanadium orderings. Such ordering/disordering phenomena, occurring at different compositions and temperatures in $Na_xV_2(PO_4)_2F_3$ and detailed in Chapter 5, are the reason for the several phase transitions that the material exhibits, inducing space group modifications and even the creation of superstructures. Synchrotron radiation XRPD also helped complementing other studies spread through this thesis; one in particular deserves to be mentioned, namely the first-time observation of the intermediate phase $Li_{0.5}Mn_2O_4$ during charge of $LiMn_2O_4$. This material has been studied for 30 years and the two separated electrochemical regions observed during its charge are well-known. However, the cause of such a separation had only been conjectured to be an ordered phase, without any experimental proof. We could finally show that it is due to a cooperative cation charge ordering and lithium/vacancy ordering occurring in $Li_{0.5}Mn^{3+}_{0.5}Mn^{4+}_{1.5}O_4$, reducing the phase symmetry from $Fd\bar{3}m$ to $P2_13$. This observation fully validated the precious contribution of high-resolution *operando* synchrotron radiation to the study of battery materials.

In conclusion, this thesis attempted at exploiting a maximum of diffraction techniques, *ex situ*, *in situ* and *operando*, using X-Rays, synchrotron radiation and neutrons as probes, to obtain in turn a picture as complete as possible on electrode materials as they transform inside a battery. Our approach based on combined use of different techniques revealed to

be extremely useful to obtain complementary insights and to reveal the interconnection between crystal structures and electrochemical properties present in these materials. We are hopeful that deeper understanding will be of primary importance to improve their performances or to develop in the future new electrode materials with better electrochemical properties for next-generation battery systems.

Acknowledgements

These three amazing years of PhD have been an extremely formative experience from the scientific and personal point of view and there are many people I need to thank for it. Firstly, my supervisors Laurence, Emmanuelle and Christian.

They have been great teachers, those I needed to tackle a subject new to me and to like it, a lot. Not only that, they have also been models and friends. We made a very efficient team and working together was always a pleasure. I will never forget our fruitful beamtimes, when we multi-tasked among experiments, data analysis and, while waiting the measurements, we planned and even wrote papers. I also want to thank François Fauth, who gave me the possibility to start a new series of synchrotron experiments and taught me a lot; I am proud to be the first user that brought *in situ* XRPD experiments on batteries to MSPD.

This thesis would not have been possible without the support of many other people that helped me overcoming any issue; for this I need to thank, at ILL, Ludovic Gendrin, Jean-Luc Laborier, Thomas Hansen, Alain Daramsey and Alain Bertoni. At LRCS, Jean-Bernard Leriche, Mathieu Morcrette and Jean-Noël Chotard. At ICMCB, Philippe Dagault, Eric Lebraud, Stan Pechev, Cathy Denage. For useful scientific discussion I also want to thank Juan Rodriguez-Carvajal, Michel Ménétrier, Dany Carlier.

Three years of PhD do not pass without making many friends, especially while often traveling among different labs. These are the people who shared most every-day moments, extra coffees to keep working long enough, tough moments while facing scientific issues...and finally beers to forget them. So although they won't probably read this, it's a pleasure to mention all of them: Francesco, Federica, Yuri, Giacomo, Alessio, Ernesto, Pippo, Daria, Annalisa, Valentino, Elodie, Cedric, Stephane, Vincent, Manu, Laurent, Florian, Laura, Thibault, Sylvain, Fabien, Yue, Lionel, Amina, Hania, Robin, Wan-Si, Huikyong, Liang, Michal...and if I forgot someone, I hope they will forgive me.

Finally I want to thank my family, for being the constant presence that, regardless the

physical distance, followed each of my steps, giving me strength and always supporting me. And last but not least, my wife Camilla, for sharing with me this path and sometimes the weight of difficult scientific days.

Bibliography

[1] Michael M. Lee, Joel Teuscher, Tsutomu Miyasaka, Takurou N. Murakami, and Henry J. Snaith. Efficient hybrid solar cells based on meso-superstructured organometal halide perovskites. *Science*, 338(6107):643–647, 2012. 2

[2] Mingzhen Liu, Michael B. Johnston, and Henry J. Snaith. Efficient planar heterojunction perovskite solar cells by vapour deposition. *Nature*, 501(7467):395–398, 2013. 2

[3] Zhenguo Yang, Jianlu Zhang, Michael C. W. Kintner-Meyer, Xiaochuan Lu, Daiwon Choi, John P. Lemmon, and Jun Liu. Electrochemical energy storage for green grid. *Chemical Reviews*, 111(5):3577–3613, 2011. 2, 14

[4] Bruno Scrosati and Jurgen Garche. Lithium batteries: Status, prospects and future. *Journal of Power Sources*, 195(9):2419–2430, 2010. 3, 65

[5] Jean-Marcel Ateba Mba. *New Transition Metal Fluorophosphates as Positive Electrode Materials for Li-ion Batteries*. PhD thesis, 2013. 6, 30, 101, 104, 107, 108, 111, 112

[6] M. S. Whittingham. Electrical energy storage and intercalation chemistry. *Science*, 192(4244):1126–1127, 1976. 6

[7] K. Mizushima, P. C. Jones, P. J. Wiseman, and J. B. Goodenough. Li_xCoO_2 ($0 < x < 1$): A new cathode material for batteries of high energy density. *Materials Research Bulletin*, 15(6):783–789, 1980. 7, 10

[8] J. B. Goodenough and Y. Kim. Challenges for Rechargeable Li Batteries. *Chemistry of Materials*, 22(3):587–603, 2010. 8, 12, 15, 65

[9] M. S. Whittingham. Lithium batteries and cathode materials. *Chemical Reviews*, 104(10):4271–4301, 2004. 10, 15

[10] Christian Masquelier and Laurence Croguennec. Polyanionic (Phosphates, Silicates, Sulfates) Frameworks as Electrode Materials for Rechargeable Li (or Na) Batteries. *Chemical Reviews*, 113(8):6552–6591, 2013. 11, 13, 16, 101, 157, 173

[11] M. Stanley Whittingham. Ultimate limits to intercalation reactions for lithium batteries. *Chemical Reviews*, 114(23):11414–11443, 2014. 15, 101

[12] Laurence Croguennec and M. Rosa Palacin. Recent achievements on inorganic electrode materials for lithium-ion batteries. *Journal of the American Chemical Society*, 137(9):3140–3156, 2015. 10, 15, 93

[13] J. N. Reimers and J. R. Dahn. Electrochemical and insitu x-ray-diffraction studies of lithium intercalation in lixcoo2. *Journal of The Electrochemical Society*, 139(8):2091–2097, 1992. 10

[14] Kyu Tae Lee, Sookyung Jeong, and Jaephil Cho. Roles of surface chemistry on safety and electrochemistry in lithium ion batteries. *Accounts of Chemical Research*, 46(5):1161–1170, 2013. PMID: 22509931. 10

[15] M. Guilmard, C. Pouillerie, L. Croguennec, and C. Delmas. Structural and electrochemical properties of $LiNi_{0.70}Co_{0.15}Al_{0.15}O_2$. *Solid State Ionics*, 160(1â2):39–50, 2003. 11

[16] M. Guilmard, A. Rougier, M. Grüne, L. Croguennec, and C. Delmas. Effects of aluminum on the structural and electrochemical properties of $LiNiO_2$. *Journal of Power Sources*, 115(2):305–314, 2003. 11

[17] T. Ohzuku and Y. Makimura. Layered lithium insertion material of $LiCo_{1/3}Ni_{1/3}Mn_{1/3}O_2$ for lithium ion batteries. *Chemistry Letters*, (7):642–643, 2001. 11

[18] Christopher S. Johnson, Jeom-Soo Kim, A. Jeremy Kropf, Arthur J. Kahaian, John T. Vaughey, Linda M. L. Fransson, Kristina Edstrom, and Michael M. Thackeray. Structural characterization of Layered $Li_xNi_{0.5}Mn_{0.5}O_2$ ($0 \leq x \leq 2$) Oxide Electrodes for Li Batteries. *Chemistry of Materials*, 15(12):2313–2322, 2003. 11

[19] Z. H. Lu, D. D. MacNeil, and J. R. Dahn. Layered cathode materials $LiNi_xLi_{(1/3-2x/3)}Mn_{(2/3-x/3)}O_2$ for lithium-ion batteries. *Electrochemical and Solid State Letters*, 4(11):A191–A194, 2001. 11

[20] M. M. Thackeray, W. I. F. David, P. G. Bruce, and J. B. Goodenough. Lithium insertion into manganese spinels. *Materials Research Bulletin*, 18(4):461–472, 1983. 11, 60, 62, 63, 64

[21] M. M. Thackeray, P. J. Johnson, L. A. de Picciotto, P. G. Bruce, and J. B. Goodenough. Electrochemical extraction of lithium from $LiMn_2O_4$. *Materials Research Bulletin*, 19(2):179–187, 1984. 63

[22] Goodenough, J. B., Thackeray, M. M., David, W. I. F., Bruce, and P. G. *Lithium insertion/extraction reactions with manganese oxides*, volume 21. Gauthier-Villars, Paris, FRANCE, 1984. 11, 62, 63, 79

[23] M. M. Thackeray. Manganese oxides for lithium batteries. *Progress in Solid State Chemistry*, 25(1-2):1–71, 1997. 11, 47, 63, 64, 67, 69

[24] Yuan Gao, K. Myrtle, Meijie Zhang, J. N. Reimers, and J. R. Dahn. Valence band of $LiNi_{0.5}Mn_{1.5}O_4$ and its effects on the voltage profiles of $LiNi_{0.5}Mn_{1.5}O_4$/li electrochemical cells. *Physical Review B*, 54(23):16670–16675, 1996. 11, 91

[25] K. Amine, H. Tukamoto, H. Yasuda, and Y. Fujita. A new three-volt spinel $Li_{1+x}Mn_{1.5}Ni_{0.5}O_4$ for secondary lithium batteries. *Journal of The Electrochemical Society*, 143(5):1607–1613, 1996. 11, 65, 91

[26] A. Manthiram and J. B. Goodenough. Lithium insertion into $Fe_2(MO_4)_3$ frameworks: Comparison of M = W with M = Mo. *Journal of Solid State Chemistry*, 71(2):349–360, 1987. 12

[27] A. Manthiram and J. B. Goodenough. Lithium insertion into $Fe_2(SO_4)_3$ frameworks. *Journal of Power Sources*, 26(3â4):403–408, 1989. 12

[28] A. K. Padhi, K. S. Nanjundaswamy, and J. B. Goodenough. Phospho-olivines as positive-electrode materials for rechargeable lithium batteries. *Journal of The Electrochemical Society*, 144(4):1188–1194, 1997. 12, 47

[29] A. K. Padhi, K. S. Nanjundaswamy, C. Masquelier, S. Okada, and J. B. Goodenough. Effect of Structure on the Fe^{3+}/Fe^{2+} Redox Couple in Iron Phosphates. *Journal of The Electrochemical Society*, 144(5):1609–1613, 1997. 12

[30] Masao Yonemura, Atsuo Yamada, Yuki Takei, Noriyuki Sonoyama, and Ryoji Kanno. Comparative kinetic study of olivine Li_xMPO_4 (M = Fe, Mn). *Journal of The Electrochemical Society*, 151(9):A1352–A1356, 2004. 12

[31] A. Yamada, S. C. Chung, and K. Hinokuma. Optimized $LiFePO_4$ for lithium battery cathodes. *Journal of The Electrochemical Society*, 148(3):A224–A229, 2001. 12

[32] Byoungwoo Kang and Gerbrand Ceder. Battery materials for ultrafast charging and discharging. *Nature*, 458(7235):190–193, 2009. 12

[33] C. Delacourt, P. Poizot, J. M. Tarascon, and C. Masquelier. The existence of a temperature-driven solid solution in Li_xFePO_4 for $0 \leq x \leq 1$. *Nature Materials*, 4(3):254–260, 2005. 12, 18, 47

[34] A. Yamada, H. Koizumi, S. I. Nishimura, N. Sonoyama, R. Kanno, M. Yonemura, T. Nakamura, and Y. Kobayashi. Room-temperature miscibility gap in Li_xFePO_4. *Nature Materials*, 5(5):357–360, 2006. 47, 54

[35] Rahul Malik, Aziz Abdellahi, and Gerbrand Ceder. A critical review of the li insertion mechanisms in $LiFePO_4$ electrodes. *Journal of The Electrochemical Society*, 160(5):A3179–A3197, 2013. 18

[36] Hao Liu, Fiona C. Strobridge, Olaf J. Borkiewicz, Kamila M. Wiaderek, Karena W. Chapman, Peter J. Chupas, and Clare P. Grey. Capturing metastable structures during high-rate cycling of $LiFePO_4$ nanoparticle electrodes. *Science*, 344(6191), 2014. 12, 25, 126

[37] J. B. Goodenough, H. Y. P. Hong, and J. A. Kafalas. Fast Na^+-ion transport in skeleton structures. *Materials Research Bulletin*, 11(2):203–220, 1976. 13

[38] Zhengliang Gong and Yong Yang. Recent advances in the research of polyanion-type cathode materials for li-ion batteries. *Energy & Environmental Science*, 4(9):3223–3242, 2011. 13

[39] J. M. Tarascon and M. Armand. Issues and challenges facing rechargeable lithium batteries. *Nature*, 414(6861):359–367, 2001. 13, 15, 65

[40] Ralf Wagner, Nina Preschitschek, Stefano Passerini, Jens Leker, and Martin Winter. Current research trends and prospects among the various materials and designs used

in lithium-based batteries. *Journal of Applied Electrochemistry*, 43(5):481–496, 2013. 13

[41] Dave Andre, Sung-Jin Kim, Peter Lamp, Simon Franz Lux, Filippo Maglia, Odysseas Paschos, and Barbara Stiaszny. Future generations of cathode materials: an automotive industry perspective. *Journal of Materials Chemistry A*, 3(13):6709–6732, 2015. 14

[42] Evan M. Erickson, Chandan Ghanty, and Doron Aurbach. New horizons for conventional lithium ion battery technology. *The Journal of Physical Chemistry Letters*, 5(19):3313–3324, 2014. 14

[43] John B. Goodenough. Cathode materials: A personal perspective. *Journal of Power Sources*, 174(2):996–1000, 2007. 15

[44] Brian L. Ellis, Kyu Tae Lee, and Linda F. Nazar. Positive Electrode Materials for Li-Ion and Li-Batteries. *Chemistry of Materials*, 22(3):691–714, 2010.

[45] J. W. Fergus. Recent developments in cathode materials for lithium ion batteries. *Journal of Power Sources*, 195(4):939–954, 2010. 15

[46] Rangeet Bhattacharyya, Baris Key, Hailong Chen, Adam S. Best, Anthony F. Hollenkamp, and Clare P. Grey. In situ nmr observation of the formation of metallic lithium microstructures in lithium batteries. *Nat Mater*, 9(6):504–510, 2010. 15

[47] Katherine J. Harry, Daniel T. Hallinan, Dilworth Y. Parkinson, Alastair A. MacDowell, and Nitash P. Balsara. Detection of subsurface structures underneath dendrites formed on cycled lithium metal electrodes. *Nat Mater*, 13(1):69–73, 2014. 15

[48] Jordi Cabana, Laure Monconduit, Dominique Larcher, and M. Rosa Palacin. Beyond intercalation-based li-ion batteries: The state of the art and challenges of electrode materials reacting through conversion reactions. *Advanced Materials*, 22(35):E170–E192, 2010. 15

[49] Jean-Marie Tarascon. Is lithium the new gold? *Nat Chem*, 2(6):510–510, 2010. 15

[50] BL Ellis, WRM Makahnouk, Y Makimura, K Toghill, and LF Nazar. A multifunctional 3.5 v iron-based phosphate cathode for rechargeable batteries. *Nature Materials*, 6(10):749–753, 2007. 15

[51] C. Wadia, P. Albertus, and V. Srinivasan. Resource constraints on the battery energy storage potential for grid and transportation applications. *Journal of Power Sources*, 196(3):1593–1598, 2011. 15

[52] Veronica Palomares, Montse Casas-Cabanas, Elizabeth Castillo-Martinez, Man H. Han, and Teofilo Rojo. Update on na-based battery materials. a growing research path. *Energy & Environmental Science*, 6(8):2312–2337, 2013. 15

[53] Veronica Palomares, Paula Serras, Irune Villaluenga, Karina B. Hueso, Javier Carretero-Gonzalez, and Teofilo Rojo. Na-ion batteries, recent advances and present challenges to become low cost energy storage systems. *Energy & Environmental Science*, 5(3):5884–5901, 2012. 15

[54] Brian L. Ellis and Linda F. Nazar. Sodium and sodium-ion energy storage batteries. *Current Opinion in Solid State and Materials Science*, 16(4):168–177, 2012. 16

[55] S. Komaba, C. Takei, T. Nakayama, A. Ogata, and N. Yabuuchi. Electrochemical intercalation activity of layered $NaCrO_2$ vs. $LiCrO_2$. *Electrochemistry Communications*, 12(3):355–358, 2010. 16

[56] J. J. Braconnier, C. Delmas, C. Fouassier, and P. Hagenmuller. Electrochemical behavior of the phases Na_xCoO_2. *Materials Research Bulletin*, 15(12):1797–1804, 1980. 16

[57] R. Berthelot, D. Carlier, and C. Delmas. Electrochemical investigation of the P2-Na_xCoO_2 phase diagram. *Nat Mater*, 10(1):74–80, 2011. 16, 162

[58] P. Moreau, D. Guyomard, J. Gaubicher, and F. Boucher. Structure and stability of sodium intercalated phases in olivine $FePO_4$. *Chemistry of Materials*, 22(14):4126–4128, 2010. 16, 170

[59] M. Casas-Cabanas, V. V. Roddatis, D. Saurel, P. Kubiak, J. Carretero-Gonzalez, V. Palomares, P. Serras, and T. Rojo. Crystal chemistry of na insertion/deinsertion in $FePO_4$-$NaFePO_4$. *Journal of Materials Chemistry*, 22(34):17421–17423, 2012. 112

[60] J. Gaubicher, F. Boucher, P. Moreau, M. Cuisinier, P. Soudan, E. Elkaim, and D. Guyomard. Abnormal operando structural behavior of sodium battery material: Influence of dynamic on phase diagram of Na_xFePO_4. *Electrochemistry Communications*, 38(0):104–106, 2014. 16, 126, 170

[61] J. Barker, M. Y. Saidi, and J. L. Swoyer. A sodium-ion cell based on the fluorophosphate compound $NaVPO_4F$. *Electrochemical and Solid State Letters*, 6(1):A1–A4, 2003. 16

[62] J. Barker, M. Y. Saidi, and J. L. Swoyer. A comparative investigation of the li insertion properties of the novel fluorophosphate phases, $NaVPO_4F$ and $LiVPO_4F$. *Journal of The Electrochemical Society*, 151(10):A1670–A1677, 2004.

[63] J. Q. Zhao, J. P. He, X. C. Ding, J. H. Zhou, Y. O. Ma, S. C. Wu, and R. M. Huang. A novel sol-gel synthesis route to $NaVPO_4F$ as cathode material for hybrid lithium ion batteries. *Journal of Power Sources*, 195(19):6854–6859, 2010. 16

[64] Zelang Jian, Liang Zhao, Huilin Pan, Yong-Sheng Hu, Hong Li, Wen Chen, and Liquan Chen. Carbon coated $Na_3V_2(PO_4)_3$ as novel electrode material for sodium ion batteries. *Electrochemistry Communications*, 14(1):86–89, 2012. 16

[65] Yasushi Uebou, Toshiyasu Kiyabu, Shigeto Okada, and Jun-ichi Yamaki. Electrochemical sodium insertion into the 3D-framework of $Na_3M_2(PO_4)_3$ (M= Fe, V). *Reports of Institute of Advanced Material Study, Kyushu University*, 16:1–5, 2002.

[66] Kuppan Saravanan, Chad W. Mason, Ashish Rudola, Kim Hai Wong, and Palani Balaya. The first report on excellent cycling stability and superior rate capability of $Na_3V_2(PO_4)_3$ for sodium ion batteries. *Advanced Energy Materials*, 3(4):444–450, 2013. 16

[67] D. A. Stevens and J. R. Dahn. High capacity anode materials for rechargeable sodium-ion batteries. *Journal of The Electrochemical Society*, 147(4):1271–1273, 2000. 16

[68] P. Senguttuvan, G. Rousse, V. Seznec, J. M. Tarascon, and M. R. Palacin. $Na_2Ti_3O_7$: Lowest voltage ever reported oxide insertion electrode for sodium ion batteries. *Chemistry of Materials*, 23(18):4109–4111, 2011.

[69] P. Senguttuvan, G. Rousse, M. E. Arroyo y de Dompablo, Herve Vezin, J. M. Tarascon, and M. R. Palacin. Low-Potential Sodium Insertion in a NASICON-Type Structure through the Ti(III)/Ti(II) Redox Couple. *Journal of the American Chemical Society*, 135(10):3897–3903, 2013. 16

[70] Brian L Ellis, WR Michael Makahnouk, WN Rowan-Weetaluktuk, DH Ryan, and Linda F Nazar. Crystal structure and electrochemical properties of A_2MPO_4F Fluo-

rophosphates (A= Na, Li; M= Fe, Mn, Co, Ni). *Chemistry of Materials*, 22(3):1059–1070, 2009. 16

[71] Paula Serras, Veronica Palomares, Aintzane Goni, Izaskun Gil de Muro, Pierre Kubiak, Luis Lezama, and Teofilo Rojo. High voltage cathode materials for Na-ion batteries of general formula $Na_3V_2O_{2x}(PO_4)_2F_{3-2x}$. *Journal of Materials Chemistry*, 22(41):22301–22308, 2012. 16, 138, 139

[72] Paula Serras, Veronica Palomares, Aintzane Goni, Pierre Kubiak, and Teofilo Rojo. Electrochemical performance of mixed valence $Na_3V_2O_{2x}(PO_4)_2F_{3-2x}$/C as cathode for sodium-ion batteries. *Journal of Power Sources*, 241(0):56–60, 2013.

[73] Young-Uk Park, Dong-Hwa Seo, Byoungkook Kim, Kun-Pyo Hong, Hyungsub Kim, Seongsu Lee, Rana A Shakoor, Keiichi Miyasaka, Jean-Marie Tarascon, and Kisuk Kang. Tailoring a fluorophosphate as a novel 4 v cathode for lithium-ion batteries. *Scientific Reports*, 2, 2012. 138

[74] Young-Uk Park, Dong-Hwa Seo, Hyung-Soon Kwon, Byoungkook Kim, Jongsoon Kim, Haegyeom Kim, Inkyung Kim, Han-Ill Yoo, and Kisuk Kang. A new high-energy cathode for a na-ion battery with ultrahigh stability. *Journal of the American Chemical Society*, 135(37):13870–13878, 2013. 161, 169

[75] Alexandre Ponrouch, Remi Dedryvere, Damien Monti, Atif E. Demet, Jean Marcel Ateba Mba, Laurence Croguennec, Christian Masquelier, Patrik Johansson, and M. Rosa Palacin. Towards high energy density sodium ion batteries through electrolyte optimization. *Energy & Environmental Science*, 6(8):2361–2369, 2013. 16, 137, 138, 139, 178, 184

[76] John Muldoon, Claudiu B. Bucur, and Thomas Gregory. Quest for nonaqueous multivalent secondary batteries: Magnesium and beyond. *Chemical Reviews*, 2014. 17

[77] Yanguang Li, Ming Gong, Yongye Liang, Ju Feng, Ji-Eun Kim, Hailiang Wang, Guosong Hong, Bo Zhang, and Hongjie Dai. Advanced zinc-air batteries based on high-performance hybrid electrocatalysts. *Nat Commun*, 4:1805, 2013. 17

[78] Meng-Chang Lin, Ming Gong, Bingan Lu, Yingpeng Wu, Di-Yan Wang, Mingyun Guan, Michael Angell, Changxin Chen, Jiang Yang, Bing-Joe Hwang, and Hongjie

Dai. An ultrafast rechargeable aluminium-ion battery. *Nature*, 520(7547):324–328, 2015. 17

[79] Arumugam Manthiram, Yongzhu Fu, Sheng-Heng Chung, Chenxi Zu, and Yu-Sheng Su. Rechargeable lithiumâsulfur batteries. *Chemical Reviews*, 2014. 17

[80] Alan C. Luntz and Bryan D. McCloskey. Nonaqueous LiâAir batteries: A status report. *Chemical Reviews*, 2014. 17

[81] R. Van Noorden. A better battery. *Nature*, 507(7490):26–28, 2014. 17

[82] Venkat Srinivasan and John Newman. Existence of path-dependence in the $LiFePO_4$ electrode. *Electrochemical and Solid-State Letters*, 9(3):A110–A114, 2006. 18

[83] C. Delmas, M. Maccario, L. Croguennec, F. Le Cras, and F. Weill. Lithium deintercalation in $LiFePO_4$ nanoparticles via a domino-cascade model. *Nat Mater*, 7(8):665–671, 2008. 18, 56

[84] N. Meethong, H. Y. S Huang, S. A Speakman, W. C Carter, and Y. M. Chiang. Strain accommodation during phase transformations in olivine-based cathodes as a materials selection criterion for high-power rechargeable batteries. *Advanced Functional Materials*, 17(7):1115–1123, 2007. 18

[85] C. Delmas, M. Menetrier, L. Croguennec, S. Levasseur, J. P. Peres, C. Pouillerie, G. Prado, L. Fournes, and F. Weill. Lithium batteries: a new tool in solid state chemistry. *International Journal of Inorganic Materials*, 1(1):11–19, 1999. 19

[86] John Meurig Thomas. Centenary: The birth of x-ray crystallography. *Nature*, 491(7423):186–187, 2012. 10.1038/491186a. 20

[87] H. M. Rietveld. A profile refinement method for nuclear and magnetic structures. *Journal of Applied Crystallography*, 2:65, 1969. 22, 50, 114, 143

[88] H. Schober. An introduction to the theory of nuclear neutron scattering in condensed matter. *Journal of Neutron Research*, 17(3-4), 2014. 23

[89] G. E. Bacon. *Neutron Diffraction, 3rd edition.* Clarendon Press, United Kingdom, 1975. 23

[90] J. R. Dahn, M. A. Py, and R. R. Haering. In situ x-ray diffraction experiments on lithium intercalation compounds. *Canadian Journal of Physics*, 60(3):307–313, 1982. 25

[91] J. R. Dahn and R. R. Haering. Anomalous bragg peak widths in Li_xTiS_2. *Solid State Communications*, 40(3):245–248, 1981.

[92] T. Gustafsson, J. O. Thomas, R. Koksbang, and G. C. Farrington. The polymer battery as an environment for in situ x-ray diffraction studies of solid-state electrochemical processes. *Electrochimica Acta*, 37(9):1639–1643, 1992.

[93] A. S. Andersson, B. Kalska, L. Haggstrom, and J. O. Thomas. Lithium extraction/insertion in $LiFePO_4$: an x-ray diffraction and mossbauer spectroscopy study. *Solid State Ionics*, 130(1-2):41–52, 2000.

[94] M. Morcrette, Y. Chabre, G. Vaughan, G. Amatucci, J. B. Leriche, S. Patoux, C. Masquelier, and J. M. Tarascon. In situ x-ray diffraction techniques as a powerful tool to study battery electrode materials. *Electrochimica Acta*, 47(19):3137–3149, 2002.

[95] M. Bianchini, J. M. Ateba-Mba, P. Dagault, E. Bogdan, D. Carlier, E. Suard, C. Masquelier, and L. Croguennec. Multiple phases in the ϵ-VPO_4O - $LiVPO_4O$-Li_2VPO_4O system: a combined solid state electrochemistry and diffraction structural study. *Journal of Materials Chemistry A*, 2(26):10182–10192, 2014. 25, 108, 111, 157, 172, 173

[96] V. R. Albertini, P. Perfetti, F. Ronci, P. Reale, and B. Scrosati. In situ studies of electrodic materials in li-ion cells upon cycling performed by very-high-energy x-ray diffraction. *Applied Physics Letters*, 79(1):27–29, 2001. 25

[97] J. B. Leriche, S. Hamelet, J. Shu, M. Morcrette, C. Masquelier, G. Ouvrard, M. Zerrouki, P. Soudan, S. Belin, E. Elkaim, and F. Baudelet. An electrochemical cell for operando study of lithium batteries using synchrotron radiation. *Journal of The Electrochemical Society*, 157(5):A606–A610, 2010. 26, 82, 114, 131, 141, 162

[98] G. Ouvrard, M. Zerrouki, P. Soudan, B. Lestriez, C. Masquelier, M. Morcrette, S. Hamelet, S. Belin, A. M. Flank, and F. Baudelet. Heterogeneous behaviour of the lithium battery composite electrode $LiFePO_4$. *Journal of Power Sources*, 229:16–21, 2013. 114, 141, 162

[99] D. B. Ravnsbaek, K. Xiang, W. Xing, O. J. Borkiewicz, K. M. Wiaderek, P. Gionet, K. W. Chapman, P. J. Chupas, and Y. M. Chiang. Extended solid solutions and coherent transformations in nanoscale olivine cathodes. *Nano Letters*, 14(3):1484–1491, 2014. 126, 172

[100] Xiaoyu Zhang, Martijn van Hulzen, Deepak P. Singh, Alex Brownrigg, Jonathan P. Wright, Niels H. van Dijk, and Marnix Wagemaker. Rate-induced solubility and suppression of the first-order phase transition in olivine $LiFePO_4$. *Nano Letters*, 14(5):2279–2285, 2014. 25, 172

[101] W. W. Huang and R. Frech. In situ raman spectroscopic studies of electrochemical intercalation in $Li_xMn_2O_4$-based cathodes. *Journal of Power Sources*, 81:616–620, 1999. 25

[102] Yuki Orikasa, Takehiro Maeda, Yukinori Koyama, Haruno Murayama, Katsutoshi Fukuda, Hajime Tanida, Hajime Arai, Eiichiro Matsubara, Yoshiharu Uchimoto, and Zempachi Ogumi. Transient phase change in two phase reaction between $LiFePO_4$ and $FePO_4$ under battery operation. *Chemistry of Materials*, 25(7):1032–1039, 2013. 26, 47

[103] O. J. Borkiewicz, B. Shyam, K. M. Wiaderek, C. Kurtz, P. J. Chupas, and K. W. Chapman. The ampix electrochemical cell: a versatile apparatus for in situ x-ray scattering and spectroscopic measurements. *Journal of Applied Crystallography*, 45:1261–1269, 2012. 26

[104] H. Koga, L. Croguennec, M. Menetrier, P. Mannessiez, F. Weill, C. Delmas, and S. Belin. Operando x-ray absorption study of the redox processes involved upon cycling of the li-rich layered oxide $Li_{1.20}Mn_{0.54}Co_{0.13}Ni_{0.13}O_2$ in li ion batteries. *The Journal of Physical Chemistry C*, 118(11):5700–5709, 2014. 26

[105] Michel Letellier, Frederic Chevallier, and FranÃ§ois Beguin. In situ 7li nmr during lithium electrochemical insertion into graphite and a carbon/carbon composite. *Journal of Physics and Chemistry of Solids*, 67(5â6):1228–1232, 2006. 26

[106] Baris Key, Rangeet Bhattacharyya, Mathieu Morcrette, Vincent SezneÌc, Jean-Marie Tarascon, and Clare P. Grey. Real-Time NMR Investigations of Structural Changes in Silicon Electrodes for Lithium-Ion Batteries. *Journal of the American Chemical Society*, 131(26):9239–9249, 2009. 26

[107] C. M. Ionica-Bousquet, P. E. Lippens, L. Aldon, J. Olivier-Fourcade, and J. C. Jumas. In situ 119Sn Mossbauer Effect Study of Li-$CoSn_2$ electrochemical system. *Chemistry of Materials*, 18(26):6442–6447, 2006. 26

[108] Jean-Claude Jumas, MoulayTahar Sougrati, Alexis Perea, Laurent Aldon, and Josette Olivier-Fourcade. Combined operando studies of new electrode materials for li-ion batteries. *Hyperfine Interactions*, 217(1-3):107–115, 2013.

[109] Alexis Perea, Moulay T. Sougrati, Costana M. Ionica-Bousquet, Bernard Fraisse, Cecile Tessier, Laurent Aldon, and Jean-Claude Jumas. Operando Fe-57 Mossbauer and XRD investigation of $Li_xMn_yFe_{1-y}PO_4$/C composites (y=0; 0.25). *RSC Advances*, 2(5):2080–2086, 2012.

[110] Alexis Perea, Moulay T. Sougrati, Costana M. Ionica-Bousquet, Bernard Fraisse, Cecile Tessier, Laurent Aldon, and Jean-Claude Jumas. Operando Fe-57 Mossbauer and XRD investigation of $Li_xMn_yFe_{1-y}PO_4$/C composites (y=0.50; 0.75). *RSC Advances*, 2(25):9517–9524, 2012.

[111] R. A. Dunlap, Ou Mao, and J. R. Dahn. Application of in situ mossbauer effect methods for the study of electrochemical reactions in lithium-ion battery electrode materials. *Physical Review B*, 59(5):3494–3500, 1999. 26

[112] Jiajun Wang, Yu-chen Karen Chen-Wiegart, and Jun Wang. In operando tracking phase transformation evolution of lithium iron phosphate with hard x-ray microscopy. *Nat Commun*, 5, 2014. 26

[113] Nils Ohmer, Bernhard Fenk, Dominik Samuelis, Chia-Chin Chen, Joachim Maier, Markus Weigand, Eberhard Goering, and Gisela Schutz. Phase evolution in single-crystalline $LiFePO_4$ followed by in situ scanning x-ray microscopy of a micrometre-sized battery. *Nat Commun*, 6, 2015. 26

[114] J. Y. Huang, L. Zhong, C. M. Wang, J. P. Sullivan, W. Xu, L. Q. Zhang, S. X. Mao, N. S. Hudak, X. H. Liu, A. Subramanian, H. Y. Fan, L. A. Qi, A. Kushima, and J. Li. In situ observation of the electrochemical lithiation of a single SnO_2 nanowire electrode. *Science*, 330(6010):1515–1520, 2010. 26

[115] Junjie Niu, Akihiro Kushima, Xiaofeng Qian, Liang Qi, Kai Xiang, Yet-Ming Chiang, and Ju Li. In situ observation of random solid solution zone in $LiFePO_4$ electrode. *Nano Letters*, 14(7):4005–4010, 2014. 26

[116] B. Jerliu, L. Dorrer, E. Huger, G. Borchardt, R. Steitz, U. Geckle, V. Oberst, M. Bruns, O. Schneider, and H. Schmidt. Neutron reflectometry studies on the lithiation of amorphous silicon electrodes in lithium-ion batteries. *Physical Chemistry Chemical Physics*, 15(20):7777–7784, 2013. 26

[117] Martin Ebner, Federica Marone, Marco Stampanoni, and Vanessa Wood. Visualization and quantification of electrochemical and mechanical degradation in li ion batteries. *Science*, 342(6159):716–720, 2013. 26

[118] P. P. R. M. L. Harks, F. M. Mulder, and P. H. L. Notten. In situ methods for Li-ion battery research: A review of recent developments. *Journal of Power Sources*, 288(0):92–105, 2015. 26

[119] F. Fauth, I. Peral, C. Popescu, and M. Knapp. The new material science powder diffraction beamline at alba synchrotron. *Powder Diffraction*, 28(S2):S360–S370, 2013. 29, 82, 141, 142, 162

[120] Abderrahim Aatiq, Michel Menetrier, Laurence Croguennec, Emmanuelle Suard, and Claude Delmas. On the structure of $Li_3Ti_2(PO_4)_3$. *Journal of Materials Chemistry*, 12(10):2971–2978, 2002. 34

[121] A.J. Dianoux and G.H. Lander. *Neutron Data Booklet*. Old City, Institut Laue-Langevin, Grenoble, 2001. 34, 43, 44, 45

[122] L. Croguennec, E. Suard, P. Willmann, and C. Delmas. Structural and electrochemical characterization of the $LiNi_{1-y}Ti_yO_2$ electrode materials obtained by direct solid-state reactions. *Chemistry of Materials*, 14(5):2149–2157, 2002. 34

[123] O. Bergstom, A. M. Andersson, K. Edstrom, and T. Gustafsson. A neutron diffraction cell for studying lithium-insertion processes in electrode materials. *Journal of Applied Crystallography*, 31:823–825, 1998. 36, 39

[124] H. Berg and J. O. Thomas. Neutron diffraction study of electrochemically delithiated $LiMn_2O_4$ spinel. *Solid State Ionics*, 126(3-4):227–234, 1999. 77

[125] H. Berg, H. Rundlov, and J. O. Thomas. The $LiMn_2O_4$ to lambda-MnO_2 phase transition studied by in situ neutron diffraction. *Solid State Ionics*, 144(1-2):65–69, 2001. 36, 39, 77

[126] F. Rosciano, M. Holzapfel, W. Scheifele, and P. Novak. A novel electrochemical cell for in situ neutron diffraction studies of electrode materials for lithium-ion batteries. *Journal of Applied Crystallography*, 41:690–694, 2008. 36, 39

[127] J. F. Colin, V. Godbole, and P. Novak. In situ neutron diffraction study of li insertion in $Li_4Ti_5O_{12}$. *Electrochemistry Communications*, 12(6):804–807, 2010. 36, 39

[128] M. A. Rodriguez, D. Ingersoll, and D. H. Doughty. Quantitative analysis of li contents in Li_xCoO_2 cathodes via rietveld refinement. *Powder Diffraction*, 18(2):135–139, 2003. 36

[129] Mark A. Rodriguez, David Ingersoll, Sven C. Vogel, and Darrick J. Williams. Simultaneous in situ neutron diffraction studies of the anode and cathode in a lithium-ion cell. *Electrochemical and Solid-State Letters*, 7(1):A8–A10, 2004. 39

[130] Mark A. Rodriguez, Mark H. Van Benthem, David Ingersoll, Sven C. Vogel, and Helmut M. Reiche. In situ analysis of $LiFePO_4$ batteries: Signal extraction by multivariate analysis. *Powder Diffraction*, 25(Special Issue 02):143–148, 2010. 39

[131] N. Sharma, V. K. Peterson, M. M. Elcombe, M. Avdeev, A. J. Studer, N. Blagojevic, R. Yusoff, and N. Kamarulzaman. Structural changes in a commercial lithium-ion battery during electrochemical cycling: An in situ neutron diffraction study. *Journal of Power Sources*, 195(24):8258–8266, 2010. 39

[132] N. Sharma and V. K. Peterson. In situ neutron powder diffraction studies of lithium-ion batteries. *Journal of Solid State Electrochemistry*, 16(5):1849–1856, 2012. 39

[133] A. Senyshyn, M. J. Muhlbauer, K. Nikolowski, T. Pirling, and H. Ehrenberg. In-operando neutron scattering studies on Li-ion batteries. *Journal of Power Sources*, 203:126–129, 2012. 39

[134] X. L. Wang, K. An, L. Cai, Z. L. Feng, S. E. Nagler, C. Daniel, K. J. Rhodes, A. D. Stoica, H. D. Skorpenske, C. D. Liang, W. Zhang, J. Kim, Y. Qi, and S. J. Harris. Visualizing the chemistry and structure dynamics in lithium-ion batteries by in-situ neutron diffraction. *Scientific Reports*, 2, 2012. 39

[135] O. Dolotko, A. Senyshyn, M. J. Muhlbauer, K. Nikolowski, F. Scheiba, and H. Ehrenberg. Fatigue process in li-ion cells: An in situ combined neutron diffraction and elec-

trochemical study. *Journal of The Electrochemical Society*, 159(12):A2082–A2088, 2012. 39

[136] Lu Cai, Ke An, Zhili Feng, Chengdu Liang, and Stephen J. Harris. In-situ observation of inhomogeneous degradation in large format li-ion cells by neutron diffraction. *Journal of Power Sources*, 236(0):163–168, 2013. 36, 39

[137] Neeraj Sharma and Vanessa K. Peterson. Current-dependent electrode lattice fluctuations and anode phase evolution in a lithium-ion battery investigated by in situ neutron diffraction. *Electrochimica Acta*, 101(0):79–85, 2013. 39

[138] Neeraj Sharma and Vanessa K. Peterson. Overcharging a lithium-ion battery: Effect on the Li_xC_6 negative electrode determined by in situ neutron diffraction. *Journal of Power Sources*, 244(0):695–701, 2013. 39

[139] A. Senyshyn, O. Dolotko, M. J. Muhlbauer, K. Nikolowski, H. Fuess, and H. Ehrenberg. Lithium intercalation into graphitic carbons revisited: Experimental evidence for twisted bilayer behavior. *Journal of The Electrochemical Society*, 160(5):A3198–A3205, 2013. 36, 39

[140] N. Sharma, G. D. Du, A. J. Studer, Z. P. Guo, and V. K. Peterson. In-situ neutron diffraction study of the MoS_2 anode using a custom-built Li-ion battery. *Solid State Ionics*, 199:37–43, 2011. 37, 39

[141] N. Sharma, M. V. Reddy, G. D. Du, S. Adams, B. V. R. Chowdari, Z. P. Guo, and V. K. Peterson. Time-Dependent in-Situ Neutron Diffraction Investigation of a $Li(Co_{0.16}Mn_{1.84})O_4$ Cathode. *Journal of Physical Chemistry C*, 115(43):21473–21480, 2011. 39

[142] G. D. Du, N. Sharma, V. K. Peterson, J. A. Kimpton, D. Z. Jia, and Z. P. Guo. Br-doped $Li_4Ti_5O_{12}$ and Composite TiO_2 anodes for li-ion batteries: Synchrotron x-ray and in situ neutron diffraction studies. *Advanced Functional Materials*, 21(20):3990–3997, 2011. 39

[143] N. Sharma, X. W. Guo, G. D. Du, Z. P. Guo, J. Z. Wang, Z. X. Wang, and V. K. Peterson. Direct evidence of concurrent solid-solution and two-phase reactions and the nonequilibrium structural evolution of $LiFePO_4$. *Journal of the American Chemical Society*, 134(18):7867–7873, 2012. 39

[144] N. Sharma, D. H. Yu, Y. S. Zhu, Y. P. Wu, and V. K. Peterson. Non-equilibrium Structural Evolution of the Lithium-Rich $Li_{1+y}Mn_2O_4$ Cathode within a Battery. *Chemistry of Materials*, 25(5):754–760, 2013. 37, 39, 69

[145] M. Roberts, J. J. Biendicho, S. Hull, P. Beran, T. Gustafsson, G. Svensson, and K. Edstrom. Design of a new lithium ion battery test cell for in-situ neutron diffraction measurements. *Journal of Power Sources*, 226:249–255, 2013. 37, 39, 46

[146] Haodong Liu, Christopher R. Fell, Ke An, Lu Cai, and Ying Shirley Meng. In-situ neutron diffraction study of the $xLi_2MnO_3\cdot$ (1-x)$LiMO_2$ (x = 0, 0.5; M = Ni, Mn, Co) layered oxide compounds during electrochemical cycling. *Journal of Power Sources*, 240(0):772–778, 2013. 37, 39

[147] V. A. Godbole, M. Hess, C. Villevieille, H. Kaiser, J. F. Colin, and P. Novak. Circular in situ neutron powder diffraction cell for study of reaction mechanism in electrode materials for li-ion batteries. *RSC Advances*, 3(3):757–763, 2013. 37, 39, 45

[148] M. Bianchini, J. B. Leriche, J.-L. Laborier, L. Gendrin, E. Suard, L. Croguennec, and C. Masquelier. A new null matrix electrochemical cell for rietveld refinements of in-situ or operando neutron powder diffraction data. *Journal of The Electrochemical Society*, 160(11):A2176–A2183, 2013. 37, 39, 66

[149] B. Vadlamani, K. An, M. Jagannathan, and K. S. Ravi Chandran. An in-situ electrochemical cell for neutron diffraction studies of phase transitions in small volume electrodes of li-ion batteries. *Journal of The Electrochemical Society*, 161(10):A1731–A1741, 2014. 37, 39, 58

[150] Wei Kong Pang, Vanessa K. Peterson, Neeraj Sharma, Je-Jang Shiu, and She-huang Wu. Lithium migration in $Li_4Ti_5O_{12}$ studied using in situ neutron powder diffraction. *Chemistry of Materials*, 26(7):2318–2326, 2014. 38, 39

[151] Wei Kong Pang and Vanessa K. Peterson. A custom battery for operando neutron powder diffraction studies of electrode structure. *Journal of Applied Crystallography*, 48(1):280–290, 2015. 38, 39, 45, 58

[152] Chih-Wei Hu, Neeraj Sharma, Ching-Yu Chiang, Hui-Chia Su, Vanessa K. Peterson, Han-Wei Hsieh, Yu-Fang Lin, Wu-Ching Chou, Bor-Yuan Shew, and Chih-Hao

Lee. Real-time investigation of the structural evolution of electrodes in a commercial lithium-ion battery containing a V-added $LiFePO_4$ cathode using in-situ neutron powder diffraction. *Journal of Power Sources*, 244(0):158–163, 2013. 39

[153] Moshiul Alam, Tracey Hanley, Wei Kong Pang, Vanessa K. Peterson, and Neeraj Sharma. Comparison of the so-called cgr and ncr cathodes in commercial lithium-ion batteries using in situ neutron powder diffraction. *Powder Diffraction*, 29(SupplementS1):S35–S39, 2014. 39

[154] Wei Kong Pang, Moshiul Alam, Vanessa K. Peterson, and Neeraj Sharma. Structural evolution of electrodes in the NCR and CGR cathode-containing commercial lithium-ion batteries cycled between 3.0 and 4.5 V: An operando neutron powder-diffraction study. *Journal of Materials Research*, FirstView:1–8, 2014. 39, 58

[155] Matteo Bianchini, Emmanuelle Suard, Laurence Croguennec, and Christian Masquelier. Li-Rich $Li_{1+x}Mn_{2-x}O_4$ Spinel Electrode Materials: An Operando Neutron Diffraction Study during Li+ Extraction/Insertion. *The Journal of Physical Chemistry C*, 118(45):25947–25955, 2014. 39, 64, 126

[156] Jordi Jacas Biendicho, Matthew Roberts, Colin Offer, Dag Noreus, Erika Widenkvist, Ronald I. Smith, Gunnar Svensson, Kristina Edstrom, Stefan T. Norberg, Sten G. Eriksson, and Stephen Hull. New in-situ neutron diffraction cell for electrode materials. *Journal of Power Sources*, (0), 2014. 39, 58

[157] I. A. Bobrikov, A. M. Balagurov, Chih-Wei Hu, Chih-Hao Lee, Tsan-Yao Chen, Sangaa Deleg, and D. A. Balagurov. Structural evolution in $LiFePO_4$-based battery materials: In-situ and ex-situ time-of-flight neutron diffraction study. *Journal of Power Sources*, 258(0):356–364, 2014. 39, 58

[158] William R. Brant, Siegbert Schmid, Guodong Du, Helen E. A. Brand, Wei Kong Pang, Vanessa K. Peterson, Zaiping Guo, and Neeraj Sharma. In situ neutron powder diffraction using custom-made lithium-ion batteries. *JoVE*, (93):e52284, 2014. 39

[159] O. Dolotko, A. Senyshyn, M. J. Muhlbauer, K. Nikolowski, and H. Ehrenberg. Understanding structural changes in NMC Li-ion cells by in situ neutron diffraction. *Journal of Power Sources*, 255(0):197–203, 2014. 39, 58

[160] Wei Kong Pang, Vanessa K. Peterson, Neeraj Sharma, Je-Jang Shiu, and She-huang

Wu. Structure of the $Li_4Ti_5O_{12}$ anode during charge-discharge cycling. *Powder Diffraction*, 29(SupplementS1):S59–S63, 2014. 39

[161] Wei Kong Pang, Neeraj Sharma, Vanessa K. Peterson, Je-Jang Shiu, and She-huang Wu. In-situ neutron diffraction study of the simultaneous structural evolution of a $LiNi_{0.5}Mn_{1.5}O_4$ cathode and a $Li_4Ti_5O_{12}$ anode in a $LiNi_{0.5}Mn_{1.5}O_4$-$Li_4Ti_5O_{12}$ full cell. *Journal of Power Sources*, 246(0):464–472, 2014. 39, 58

[162] Wei Kong Pang, Sujith Kalluri, Vanessa K. Peterson, Shi Xue Dou, and Zaiping Guo. Electrochemistry and structure of the cobalt-free $Li_{1+x}MO_2$ (M = Li, Ni, Mn, Fe) composite cathode. *Physical Chemistry Chemical Physics*, 16(46):25377–25385, 2014. 39

[163] A. Senyshyn, M. J. Muhlbauer, O. Dolotko, M. Hofmann, T. Pirling, and H. Ehrenberg. Spatially resolved in operando neutron scattering studies on li-ion batteries. *Journal of Power Sources*, 245(0):678–683, 2014. 39

[164] Veronika Zinth, Christian von Luders, Michael Hofmann, Johannes Hattendorff, Irmgard Buchberger, Simon Erhard, Joana Rebelo-Kornmeier, Andreas Jossen, and Ralph Gilles. Lithium plating in lithium-ion batteries at sub-ambient temperatures investigated by in situ neutron diffraction. *Journal of Power Sources*, 271(0):152–159, 2014. 39, 58

[165] A. Senyshyn, M. J. Muhlbauer, O. Dolotko, and H. Ehrenberg. Low-temperature performance of li-ion batteries: The behavior of lithiated graphite. *Journal of Power Sources*, 282(0):235–240, 2015. 39

[166] A. V. Dobromyslov and N. I. Taluts. Structure studies of quenched and tempered ZrTi alloys. *Fizika Metallov I Metallovedenie*, 63(1):127–132, 1987. 41

[167] J. L. Murray. The Ti-Zr (Titanium-Zirconium) system. *Bulletin of Alloy Phase Diagrams*, 2(2):197–201, 1981.

[168] Toshio Doi, Humihiko Ishida, and Tadashi Umezawa. Study of Nb-Zr-Ti phase diagram. *JAP INST METALS J*, 30(2):139–145, 1966.

[169] S. S. Sidhu, LeRoy Heaton, D. D. Zauberis, and F. P. Campos. Neutron diffraction study of titaniumâzirconium system. *Journal of Applied Physics*, 27(9):1040–1042, 1956. 42

[170] Grenoble Institut Laue-Langevin. TiZr Null Matrix Alloy. `https://www.ill.eu/fr/instruments-support/sample-environment/equipment/high-pressures/tizr-null-matrix-alloy/`. 41, 43

[171] R. Petibon, Jing Li, Neeraj Sharma, Wei Kong Pang, Vanessa K. Peterson, and J. R. Dahn. The use of deuterated ethyl acetate in highly concentrated electrolyte as a low-cost solvent for in situ neutron diffraction measurements of li-ion battery electrodes. *Electrochimica Acta*, 174:417–423, 2015. 46, 58

[172] G. Rousse, J. Rodriguez-Carvajal, S. Patoux, and C. Masquelier. Magnetic structures of the triphylite $LiFePO_4$ and of its delithiated form $FePO_4$. *Chemistry of Materials*, 15(21):4082–4090, 2003. 47

[173] A. S. Andersson and J. O. Thomas. The source of first-cycle capacity loss in LiFePO4. *Journal of Power Sources*, 97â98(0):498–502, 2001. 47, 56

[174] P. Gibot, M. Casas-Cabanas, L. Laffont, S. Levasseur, P. Carlach, S. Hamelet, J. M. Tarascon, and C. Masquelier. Room-temperature single-phase Li insertion/extraction in nanoscale Li_xFePO_4. *Nature Materials*, 7(9):741–747, 2008. 47

[175] C. Delacourt, J. Rodriguez-Carvajal, B. Schmitt, J. M. Tarascon, and C. Masquelier. Crystal chemistry of the olivine-type Li_xFePO_4 system ($0 \leq x \leq 1$) between 25 and 370 degrees c. *Solid State Sciences*, 7(12):1506–1516, 2005. 47

[176] Atsuo Yamada, Hiroshi Koizumi, Noriyuki Sonoyama, and Ryoji Kanno. Phase change in Li_xFePO_4. *Electrochemical and Solid-State Letters*, 8(8):A409–A413, 2005. 49

[177] J. Rodriguez-Carvajal. Recent advances in magnetic-structure determination by neutron powder diffraction. *Physica B*, 192(1-2):55–69, 1993. 50, 66, 114, 141, 143

[178] X. Orlhac, C. Fillet, P. Deniard, A. M. Dulac, and R. Brec. Determination of the crystallized fractions of a largely amorphous multiphase material by the rietveld method. *Journal of Applied Crystallography*, 34(2):114–118, 2001. 56

[179] Ralph Walter Graystone Wyckoff. *Crystal structures*. Krieger, 1964. 59

[180] Mineralogy Database. Spinel, 2000. 59

[181] W. H. Bragg. The structure of magnetite and the spinels. *Nature*, 95:561–561, 1915. 60

[182] W. H. Bragg. The structure of the spinel group of crystals. *Philosophical Magazine Series 6*, 30(176):305–315, 1915.

[183] S. Nishikawa. *Proc. Tokyo Math. Phys. Soc.*, 8:199, 1915. 60

[184] T. F. W. Barth and E. Posnjak. Spinel structures with and without variate atom equipoints. *Zeitschrift fur Kristallographie*, 82(5/6):325–341, 1932. 60, 62, 86

[185] E. J. W. Verwey and E. L. Heilmann. Physical properties and cation arrangement of oxides with spinel structures i. cation arrangement in spinels. *The Journal of Chemical Physics*, 15(4):174–180, 1947. 60

[186] G. Bacon. A neutron-diffraction study of magnesium aluminium oxide. *Acta Crystallographica*, 5(5):684–686, 1952. 61

[187] Jeremy K. Burdett, Geoffrey D. Price, and Sarah L. Price. Role of the crystal-field theory in determining the structures of spinels. *Journal of the American Chemical Society*, 104(1):92–95, 1982. 61

[188] J. B. Goodenough and A. L. Loeb. Theory of ionic ordering, crystal distortion, and magnetic exchange due to covalent forces in spinels. *Physical Review*, 98(2):391–408, 1955. 62

[189] M. M. Thackeray and J. Coetzer. A preliminary investigation of the electrochemical performance of α-Fe_2O_3 and Fe_3O_4 cathodes in high-temperature cells. *Materials Research Bulletin*, 16(5):591–597, 1981. 62

[190] M. M. Thackeray, W. I. F. David, and J. B. Goodenough. Structural characterization of the lithiated iron oxides $Li_xFe_3O_4$ and $Li_xFe_2O_3$ ($0leqxleq2$). *Materials Research Bulletin*, 17(6):785–793, 1982. 62

[191] D. G. Wickham and W. J. Croft. Crystallographic and magnetic properties of several spinels containing trivalent manganese. *Journal of Physics and Chemistry of Solids*, 7(4):351–360, 1958. 62

[192] T. Ohzuku, M. Kitagawa, and T. Hirai. Electrochemistry of manganese-dioxide in lithium nonaqueous cell. x-ray diffractional study on the reduction of spinel-related

manganese-dioxide. *Journal of The Electrochemical Society*, 137(3):769–775, 1990. 63, 65

[193] W. I. F. David, M. M. Thackeray, L. A. Depicciotto, and J. B. Goodenough. Structure refinement of the spinel-related phases $Li_2Mn_2O_4$ and $Li_{0.2}Mn_2O_4$. *Journal of Solid State Chemistry*, 67(2):316–323, 1987. 63

[194] J. C. Hunter. Preparation of a new crystal form of manganese dioxide lambda MnO_2. *Journal of Solid State Chemistry*, 39(2):142–147, 1981. 63, 77, 80

[195] M. M. Thackeray, A. de Kock, M. H. Rossouw, D. Liles, R. Bittihn, and D. Hoge. Spinel electrodes from the Li-Mn-O system for rechargeable lithium battery applications. *Journal of The Electrochemical Society*, 139(2):363–366, 1992. 63, 64

[196] W. Liu, K. Kowal, and G. C. Farrington. Mechanism of the electrochemical insertion of lithium into $LiMn_2O_4$ spinels. *Journal of The Electrochemical Society*, 145(2):459–465, 1998. 64, 65, 79

[197] C. Baehtz, T. Buhrmester, N. N. Bramnik, K. Nikolowski, and H. Ehrenberg. Design and performance of an electrochemical in-situ cell for high resolution full-pattern x-ray powder diffraction. *Solid State Ionics*, 176(17-18):1647–1652, 2005. 64, 65, 77, 79, 95

[198] A. Van der Ven, C. Marianetti, D. Morgan, and G. Ceder. Phase transformations and volume changes in spinel $Li_xMn_2O_4$. *Solid State Ionics*, 135(1â4):21–32, 2000. 64, 79, 89, 90

[199] J. M. Tarascon and D. Guyomard. Li metal-free rechargeable batteries based on $Li_{1+x}Mn_2O_4$ cathodes ($0 \leq x \leq 1$) and carbon anodes. *Journal of The Electrochemical Society*, 138(10):2864–2868, 1991. 64

[200] J. M. Tarascon, E. Wang, F. K. Shokoohi, W. R. McKinnon, and S. Colson. The spinel phase of $LiMn_2O_4$ as a cathode in secondary lithium cells. *Journal of The Electrochemical Society*, 138(10):2859–2864, 1991.

[201] Dominique Guyomard and Jean-Marie Tarascon. High-voltage-stable electrolytes for $Li_{1+x}Mn_2O_4$/carbon secondary batteries, 1993.

[202] J. M. Tarascon and D. Guyomard. The $Li_{1+x}Mn_2O_4$/C rocking-chair system: a review. *Electrochimica Acta*, 38(9):1221–1231, 1993. 64

[203] J. M. Tarascon, W. R. McKinnon, F. Coowar, T. N. Bowmer, G. Amatucci, and D. Guyomard. Synthesis conditions and oxygen stoichiometry effects on li insertion into the spinel $LiMn_2O_4$. *Journal of The Electrochemical Society*, 141(6):1421–1431, 1994. 64

[204] D. Guyomard and J. M. Tarascon. The carbon/$Li_{1+x}Mn_2O_4$ system. *Solid State Ionics*, 69(3â4):222–237, 1994.

[205] J. M. Tarascon, F. Coowar, G. Amatuci, F. K. Shokoohi, and D. G. Guyomard. The $Li_{1+x}Mn_2O_4$/C system materials and electrochemical aspects. *Journal of Power Sources*, 54(1):103–108, 1995. 64

[206] Yuan Gao and J. R. Dahn. Synthesis and characterization of $Li_{1+x}Mn_{2-x}O_4$ for LiâIon Battery Applications. *Journal of The Electrochemical Society*, 143(1):100–114, 1996.

[207] W. Liu, G. C. Farrington, F. Chaput, and B. Dunn. Synthesis and electrochemical studies of spinel phase $LiMn_2O_4$ cathode materials prepared by the pechini process. *Journal of The Electrochemical Society*, 143(3):879–884, 1996.

[208] Y. Y. Xia and M. Yoshio. An investigation of lithium ion insertion into spinel structure li-mn-o compounds. *Journal of The Electrochemical Society*, 143(3):825–833, 1996. 64

[209] G. Rousse, C. Masquelier, J. Rodriguez-Carvajal, E. Elkaim, J. P. Lauriat, and J. L. Martinez. X-ray study of the spinel $LiMn_2O_4$ at low temperatures. *Chemistry of Materials*, 11(12):3629–3635, 1999. 64, 69

[210] G Rousse, C Masquelier, J Rodriguez-Carvajal, and M Hervieu. Cubic orthorhombic transition in the stoichiometric spinel $LiMn_2O_4$. *Electrochemical and Solid-State Letters*, 2(1):6–8, 1999.

[211] J. Rodriguez-Carvajal, G. Rousse, C. Masquelier, and M. Hervieu. Electronic crystallization in a lithium battery material: Columnar ordering of electrons and holes in the spinel $LiMn_2O_4$. *Physical Review Letters*, 81(21):4660–4663, 1998. 69

[212] S. Mukerjee, T. R. Thurston, N. M. Jisrawi, X. Q. Yang, J. McBreen, M. L. Daroux, and X. K. Xing. Structural evolution of $Li_xMn_2O_4$ in lithium-ion battery cells mea-

sured in situ using synchrotron X-ray diffraction techniques. *Journal of The Electrochemical Society*, 145(2):466–472, 1998. 65

[213] T. R. Thurston, N. M. Jisrawi, S. Mukerjee, X. Q. Yang, J. McBreen, M. L. Daroux, and X. K. Xing. Synchrotron x-ray diffraction studies of the structural properties of electrode materials in operating battery cells. *Applied Physics Letters*, 69(2):194–196, 1996.

[214] Ryoji Kanno, Atsuro Kondo, Masao Yonemura, Richard Gover, Yoji Kawamoto, Mitsuharu Tabuchi, Takashi Kamiyama, Fujio Izumi, Christian Masquelier, and Gwenaelle Rousse. The relationships between phases and structures of lithium manganese spinels. *Journal of Power Sources*, 81â82(0):542–546, 1999. 64, 67

[215] M. Yonemura, A. Yamada, H. Kobayashi, M. Tabuchi, T. Kamiyama, Y. Kawamoto, and R. Kanno. Synthesis, structure, and phase relationship in lithium manganese oxide spinel. *Journal of Materials Chemistry*, 14(13):1948–1958, 2004. 64

[216] D. K. Kim, P. Muralidharan, H. W. Lee, R. Ruffo, Y. Yang, C. K. Chan, H. Peng, R. A. Huggins, and Y. Cui. Spinel $LiMn_2O_4$ nanorods as lithium ion battery cathodes. *Nano Letters*, 8(11):3948–3952, 2008. 64

[217] E. Hosono, T. Kudo, I. Honma, H. Matsuda, and H. S. Zhou. Synthesis of single crystalline spinel $LiMn_2O_4$ nanowires for a lithium ion battery with high power density. *Nano Letters*, 9(3):1045–1051, 2009. 64

[218] Nissan. Leaf. `http://www.nissan.co.za/~/media/Files/Nissan/Asia%20Pacific/NSA/e-brochure/Leaf%20Brochure_OCT2013SML`, 2010. 64

[219] M. R. Palacin, Y. Chabre, L. Dupont, M. Hervieu, P. Strobel, G. Rousse, C. Masquelier, M. Anne, G. G. Amatucci, and J. M. Tarascon. On the origin of the 3.3 and 4.5 v steps observed in $LiMn_2O_4$-based spinels. *Journal of The Electrochemical Society*, 147(3):845–853, 2000. 64

[220] MR Palacin, G Rousse, M Morcrette, L Dupont, C Masquelier, Y Chabre, M Hervieu, and JM Tarascon. On the role of defects in decreasing the extra 3.3/3.95 and 4.5 v redox steps in li-mn-o spinels. *Journal of Power Sources*, 97:398–401, 2001.

[221] L. Dupont, M. Hervieu, G. Rousse, C. Masquelier, M. R. Palacin, Y. Chabre, and J. M. Tarascon. Tem studies: The key for understanding the origin of the 3.3 v and

4.5 v steps observed in $LiMn_2O_4$-based spinels. *Journal of Solid State Chemistry*, 155(2):394–408, 2000. 64

[222] C. Masquelier, M. Tabuchi, K. Ado, R. Kanno, Y. Kobayashi, Y. Maki, O. Nakamura, and J. B. Goodenough. Chemical and magnetic characterization of spinel materials in the $LiMn_2O_4$-$Li_2Mn_4O_9$-$Li_4Mn_5O_{12}$ system. *Journal of Solid State Chemistry*, 123(2):255–266, 1996. 64, 66, 67

[223] Atsuo Yamada, Kaoru Miura, Koichiro Hinokuma, and Masahiro Tanaka. Synthesis and structural aspects of $LiMn_2O_{4+-\delta}$ as a cathode for rechargeable lithium batteries. *Journal of The Electrochemical Society*, 142(7):2149–2156, 1995.

[224] Yongyao Xia, Tetsuo Sakai, Takuya Fujieda, X. Q. Yang, X. Sun, Z. F. Ma, J. McBreen, and Masaki Yoshio. Correlating capacity fading and structural changes in $Li_{1+y}Mn_{2-2y}O_{4-\delta}$ spinel cathode materials: A systematic study on the effects of li/mn ratio and oxygen deficiency. *Journal of The Electrochemical Society*, 148(7):A723–A729, 2001. 64

[225] D. H. Jang, Y. J. Shin, and S. M. Oh. Dissolution of spinel oxides and capacity losses in 4V $Li/Li_xMn_2O_4$ coils. *Journal of The Electrochemical Society*, 143(7):2204–2211, 1996.

[226] Y. Y. Xia, Y. H. Zhou, and M. Yoshio. Capacity fading on cycling of 4 V $Li/LiMn_2O_4$ cells. *Journal of The Electrochemical Society*, 144(8):2593–2600, 1997. 64

[227] R. J. Gummow, A. Dekock, and M. M. Thackeray. Improved capacity retention in rechargeable 4v lithium/lithium manganese oxide (spinel) cells. *Solid State Ionics*, 69(1):59–67, 1994. 64

[228] Jaephil Cho and Michael M. Thackeray. Structural changes of $LiMn_2O_4$ spinel electrodes during electrochemical cycling. *Journal of The Electrochemical Society*, 146(10):3577–3581, 1999.

[229] G. G. Amatucci, N. Pereira, T. Zheng, and J.-M. Tarascon. Failure mechanism and improvement of the elevated temperature cycling of $LiMn_2O_4$ compounds through the use of the $LiAl_xMn_{2-x}O_{4-z}F_z$ solid solution. *Journal of The Electrochemical Society*, 148(2):A171–A182, 2001.

[230] J.-S. Kim, J. T. Vaughey, C. S. Johnson, and M. M. Thackeray. Significance of the Tetrahedral A Site on the Electrochemical Performance of Substituted $Li_{1.05}M_{0.05}Mn_{1.90}O_4$ Spinel Electrodes (M = Li, Mg, Zn, Al) in Lithium Cells. *Journal of The Electrochemical Society*, 150(11):A1498–A1502, 2003. 64, 65, 73

[231] C. Sigala, D. Guyomard, A. Verbaere, Y. Piffard, and M. Tournoux. Positive electrode materials with high operating voltage for lithium batteries: $LiCr_yMn_{2-y}O_4$ ($0 \leq y \leq 1$). *Solid State Ionics*, 81(3â4):167–170, 1995.

[232] K. Amine, H. Tukamoto, H. Yasuda, and Y. Fujita. Preparation and electrochemical investigation of $LiMn_{2-x}Me_xO_4$ (Me: Ni, Fe, and x = 0.5, 1) cathode materials for secondary lithium batteries. *Journal of Power Sources*, 68(2):604–608, 1997. 91

[233] Q. M. Zhong, A. Bonakdarpour, M. J. Zhang, Y. Gao, and J. R. Dahn. Synthesis and electrochemistry of $LiNi_xMn_{2-x}O_4$. *Journal of The Electrochemical Society*, 144(1):205–213, 1997. 91

[234] X. L. Wu and S. B. Kim. Improvement of electrochemical properties of $LiNi_{0.5}Mn_{1.5}O_4$ spinel. *Journal of Power Sources*, 109(1):53–57, 2002.

[235] G. Q. Liu, W. S. Yuan, G. Y. Liu, and Y. W. Tian. The electrochemical properties of $LiNi_{0.5}Mn_{1.2}Ti_{0.3}O_4$ compound. *Journal of Alloys and Compounds*, 484(1-2):567–569, 2009.

[236] Si Hyoung Oh, Kyung Yoon Chung, Sang Hoon Jeon, Chang Sam Kim, Won Il Cho, and Byung Won Cho. Structural and electrochemical investigations on the $LiNi_{0.5-x}Mn_{1.5-y}M_{x+y}O_4$ (M = Cr, Al, Zr) compound for 5 V cathode material. *Journal of Alloys and Compounds*, 469(1â2):244–250, 2009.

[237] S. Patoux, L. Sannier, H. Lignier, Y. Reynier, C. Bourbon, S. Jouanneau, F. Le Cras, and S. Martinet. High voltage nickel manganese spinel oxides for li-ion batteries. *Electrochimica Acta*, 53(12):4137–4145, 2008. 65, 91, 92, 93

[238] Sebastien Patoux, Lise Daniel, Carole Bourbon, Helene Lignier, Carole Pagano, Frederic Le Cras, Severine Jouanneau, and Sebastien Martinet. High voltage spinel oxides for li-ion batteries: From the material research to the application. *Journal of Power Sources*, 189(1):344–352, 2009. 65, 92

[239] L. P. Wang, H. Li, X. J. Huang, and E. Baudrin. A comparative study of $Fd\bar{3}m$ and $P4_332$ $LiNi_{0.5}Mn_{1.5}O_4$. *Solid State Ionics*, 193(1):32–38, 2011. 87, 91

[240] D. Mikhailova, A. Thomas, S. Oswald, W. Gruner, N. N. Bramnik, A. A. Tsirlin, D. M. Trots, A. Senyshyn, J. Eckert, and H. Ehrenberg. Structural changes in the $LiCrMnO_4$ Cathode Material during Electrochemical Li extraction and insertion. *Journal of The Electrochemical Society*, 160(5):A3082–A3089, 2013.

[241] Hugues Duncan, Bin Hai, Michal Leskes, Clare P. Grey, and Guoying Chen. Relationships between Mn3+ Content, Structural Ordering, Phase Transformation, and Kinetic Properties in $LiNi_xMn_{2-x}O_4$ cathode materials. *Chemistry of Materials*, 26(18):5374–5382, 2014. 91, 92, 93

[242] Murat Yavuz, Nilufer Kiziltas-Yavuz, Aiswarya Bhaskar, Marco Scheuermann, Sylvio Indris, Francois Fauth, Michael Knapp, and Helmut Ehrenberg. Influence of iron on the structural evolution of $LiNi_{0.4}Fe_{0.2}Mn_{1.4}O_4$ during electrochemical cycling investigated by in situ powder diffraction and spectroscopic methods. *Zeitschrift Fur Anorganische Und Allgemeine Chemie*, 640(15):3118–3126, 2014.

[243] Kuppan Saravanan, Angelique Jarry, Robert Kostecki, and Guoying Chen. A study of room-temperature $Li_xMn_{1.5}Ni_{0.5}O_4$ solid solutions. *Sci. Rep.*, 5, 2015. 65, 93

[244] R. Dedryvere, D. Foix, S. Franger, S. Patoux, L. Daniel, and D. Gonbeau. Electrode/electrolyte interface reactivity in high-voltage spinel $LiMn_{1.6}Ni_{0.4}O_4/Li_4Ti_5O_{12}$ lithium-ion battery. *The Journal of Physical Chemistry C*, 114(24):10999–11008, 2010. 65, 92

[245] Zhongli Wang, Nicolas Dupre, Anne-Claire Gaillot, Bernard Lestriez, Jean-Frederic Martin, Lise Daniel, Sebastien Patoux, and Dominique Guyomard. CMC as a binder in $LiNi_{0.4}Mn_{1.6}O_4$ 5 V cathodes and their electrochemical performance for Li-ion batteries. *Electrochimica Acta*, 62(0):77–83, 2012. 65, 92

[246] A. Mosbah, A. Verbaere, and M. Tournoux. Phases Li_xMnO_2-λ rattachees au type spinelle. *Materials Research Bulletin*, 18(11):1375–1381, 1983. 68

[247] G. Blasse. The structure of some new mixed metal oxides containing lithium. *Journal of Inorganic and Nuclear Chemistry*, 25(6):743–744, 1963. 68

[248] H. Berg, E. M Kelder, and J. O. Thomas. Neutron diffraction study of stoichiometric spinel $Li_{1+x}Mn_{2-x}O_4$ showing octahedral 16c-site li-occupation. *Journal of Materials Chemistry*, 9(2):427–429, 1999. 69

[249] L. N. Zhou, M. Leskes, A. J. Ilott, N. M. Trease, and C. P. Grey. Paramagnetic electrodes and bulk magnetic susceptibility effects in the in situ NMR studies of batteries: Application to $Li_{1.08}Mn_{1.92}O_4$ spinels. *Journal of Magnetic Resonance*, 234:44–57, 2013. 75

[250] M. Wagemaker, D. R Simon, E. M Kelder, J. Schoonman, C. Ringpfeil, U. Haake, D. Lutzenkirchen-Hecht, R. Frahm, and F. âM Mulder. A kinetic two-phase and equilibrium solid solution in spinel $Li_{4+x}Ti_5O_{12}$. *Advanced Materials*, 18(23):3169–3173, 2006. 77

[251] R. A. Young and A. Sakthivel. Bimodal distributions of profile-broadening effects in rietveld refinement. *Journal of Applied Crystallography*, 21(5):416–425, 1988. 83

[252] J. H. Kim, S. T. Myung, C. S. Yoon, S. G. Kang, and Y. K. Sun. Comparative study of $LiNi_{0.5}Mn_{1.5}O_4$-delta and $LiNi_{0.5}Mn_{1.5}O_4$ cathodes having two crystallographic structures: $Fd\bar{3}m$ $p4_332$. *Chemistry of Materials*, 16(5):906–914, 2004. 87, 91

[253] N. Amdouni, K. Zaghib, F. Gendron, A. Mauger, and C. M. Julien. Structure and insertion properties of disordered and ordered $LiMn_{1.5}Ni_{0.5}O_4$ spinels prepared by wet chemistry. *Ionics*, 12(2):117–126, 2006. 87

[254] D Gryffroy, RE Vandenberghe, and E Legrand. A neutron diffraction study of some spinel compounds containing octahedral ni and mn at a 1:3 ratio. In *Materials Science Forum*, volume 79, pages 785–790. Trans Tech Publ. 87, 91

[255] ID Brown and D Altermatt. Bond-valence parameters obtained from a systematic analysis of the inorganic crystal structure database. *Acta Crystallographica Section B: Structural Science*, 41(4):244–247, 1985. 88, 129, 134, 152

[256] A. N. Mansour, L. Croguennec, and C. Delmas. A unique structure of Ni(III) in $LiNi_{0.3}Co_{0.7}O_2$ Without Jahn-Teller Distortion. *Electrochemical and Solid-State Letters*, 8(10):A544–A548, 2005. 90

[257] M. Kunduraci and G. G. Amatucci. Synthesis and characterization of nanostructured

4.7V $Li_xMn_{1.5}Ni_{0.5}O_4$ spinels for high-power lithium-ion batteries. *Journal of The Electrochemical Society*, 153(7):A1345–A1352, 2006. 91

[258] M. Kunduraci and G. G. Amatucci. The effect of particle size and morphology on the rate capability of 4.7V $Li_xMn_{1.5+\delta}Ni_{0.5-\delta}O_4$ spinel lithium-ion battery cathodes. *Electrochimica Acta*, 53(12):4193–4199, 2008.

[259] Eunseok Lee and Kristin A. Persson. Revealing the coupled cation interactions behind the electrochemical profile of $Li_xNi_{0.5}Mn_{1.5}O_4$. *Energy & Environmental Science*, 5(3):6047–6051, 2012. 91

[260] Hajime Arai, Kenji Sato, Yuki Orikasa, Haruno Murayama, Ikuma Takahashi, Yukinori Koyama, Yoshiharu Uchimoto, and Zempachi Ogumi. Phase transition kinetics of LiNi0.5Mn1.5O4 electrodes studied by in situ x-ray absorption near-edge structure and x-ray diffraction analysis. *Journal of Materials Chemistry A*, 1(35):10442–10449, 2013. 93

[261] S. Martinez, I. Sobrados, D. Tonti, J. M. Amarilla, and J. Sanz. Chemical vs. electrochemical extraction of lithium from the Li-excess $Li_{1.10}Mn_{1.90}O_4$ spinel followed by NMR and DRX techniques. *Physical Chemistry Chemical Physics*, 2014. 95

[262] A. Rougier, C. Delmas, and A. V. Chadwick. Non-cooperative Jahn-Teller effect in $LiNiO_2$: An EXAFS study. *Solid State Communications*, 94(2):123–127, 1995. 96

[263] Won-Sub Yoon, Clare P. Grey, Mahalingam Balasubramanian, Xiao-Qing Yang, and James McBreen. In situ x-ray absorption spectroscopic study on $LiNi_{0.5}Mn_{0.5}O_2$ cathode material during electrochemical cycling. *Chemistry of Materials*, 15(16):3161–3169, 2003. 96

[264] E.T. Filho. Estudos brasileiros de geologia. *Fundacao Getrilio Varpas*, 1946. 102

[265] M.L. Lindberg and W.T. Pecora. Tavorite and barbozalite, 2 new phostate minerals from minas-gerais, brazil. *American Mineralogist*, 40((11-2)):952–966, 1955. 102

[266] A.D. Cloizeaux. On a new locality of amblygonite and on montebrasite, a new hydrated aluminium and lithium phosphate. 1874. 102

[267] N. Marx, L. Croguennec, D. Carlier, A. Wattiaux, F. Le Cras, E. Suard, and C. Delmas. The structure of tavorite $LiFePO_4(OH)$ from diffraction and gga plus

u studies and its preliminary electrochemical characterization. *Dalton Transactions*, 39(21):5108–5116, 2010. 103

[268] V.I. Simonov and N.V. Belov. The crystal structure of amblygonite. *Doklady Akademii Nauk Sssr*, 119(2):354–356, 1958. 102, 103, 106

[269] G. Rousse and J. M. Tarascon. Sulfate-based polyanionic compounds for li-ion batteries: Synthesis, crystal chemistry, and electrochemistry aspects. *Chemistry of Materials*, 26(1):394–406, 2014. 103

[270] A. Groat Lee, C. Chakoumakos Bryan, H. Brouwer Darren, M. Hoffman Christina, A. Fyfe Colin, Heiko Morell, and J. Schultz Arthur. The amblygonite ($LiAlPO_4F$)-montebrasite ($LiAlPO_4OH$) solid solution: A combined powder and single-crystal neutron diffraction and solid-state 6Li MAS, CP MAS, and REDOR NMR study, 2003. 103

[271] Jean-Marcel Ateba Mba, Christian Masquelier, Emmanuelle Suard, and Laurence Croguennec. Synthesis and crystallographic study of homeotypic $LiVPO_4F$ and $LiVPO_4O$. *Chemistry of Materials*, 24(6):1223–1234, 2012. 103, 104, 106, 107, 108, 109, 110, 111, 112, 125

[272] Jeremy Barker, M Yazid Saidi, and Jeffrey Swoyer. Lithium metal fluorophosphate materials and preparation thereof, 2002. 104, 143

[273] J. Barker, M. Y. Saidi, and J. L. Swoyer. Electrochemical insertion properties of the novel lithium vanadium fluorophosphate, $LiVPO_4F$â. *Journal of The Electrochemical Society*, 150(10):A1394–A1398, 2003. 104, 108

[274] Chris J. Allen, Qingying Jia, C. N. Chinnasamy, Sanjeev Mukerjee, and K. M. Abraham. Synthesis, structure and electrochemistry of lithium vanadium phosphate cathode materials. *Journal of The Electrochemical Society*, 158(12):A1250–A1259, 2011. 105, 110, 121, 130

[275] Katharine L. Harrison, Craig A. Bridges, Carlo U. Segre, C. Daniel Varnado, Danielle Applestone, Christopher W. Bielawski, Mariappan Parans Paranthaman, and Arumugam Manthiram. Chemical and electrochemical lithiation of $LiVOPO_4$ cathodes for lithium-ion batteries. *Chemistry of Materials*, 2014. 121, 130

[276] C. Ling, R. G. Zhang, and F. Mizuno. Phase stability and its impact on the electrochemical performance of $VOPO_4$ and $LiVOPO_4$. *Journal of Materials Chemistry A*, 2(31):12330–12339, 2014. 105, 117

[277] A. Shahul Hameed, Mangayarkarasi Nagarathinam, M. V. Reddy, B. V. R. Chowdari, and Jagadese J. Vittal. Synthesis and electrochemical studies of layer-structured metastable α_I-$LiVOPO_4$. *Journal of Materials Chemistry*, 22(15):7206–7213, 2012. 105

[278] J. Gaubicher, T. Le Mercier, Y. Chabre, J. Angenault, and M. Quarton. Li/β-$VOPO_4$: A New 4 V System for Lithium Batteries. *Journal of The Electrochemical Society*, 146(12):4375–4379, 1999. 105

[279] Brian L Ellis, TN Ramesh, Linda JM Davis, Gillian R Goward, and Linda F Nazar. Structure and electrochemistry of two-electron redox couples in lithium metal fluorophosphates based on the tavorite structure. *Chemistry of Materials*, 23(23):5138–5148, 2011. 106, 112, 113, 118, 119

[280] A. V. Lavrov, V. P. Nikolaev, G. G. Sadikov, and M. A. Poraikoshits. Synthesis and crystal-structure of mixed vanadyl and lithium ortho-phosphate, $LiVOPO_4$. *Doklady Akademii Nauk Sssr*, 266(2):343–346, 1982. 107

[281] M. Schindler, F. C. Hawthorne, and W. H. Baur. Crystal chemical aspects of vanadium:â polyhedral geometries, characteristic bond valences, and polymerization of (von) polyhedra. *Chemistry of Materials*, 12(5):1248–1259, 2000. 108, 129, 157

[282] J. Barker, R. K. B. Gover, P. Burns, A. Bryan, M. Y. Saidi, and J. L. Swoyer. Structural and electrochemical properties of lithium vanadium fluorophosphate, $LiVPO_4F$. *Journal of Power Sources*, 146(1â2):516–520, 2005. 108

[283] B. M. Azmi, T. Ishihara, H. Nishiguchi, and Y. Takita. Cathodic performance of $LiVOPO_4$ prepared by impregnation method for li ion secondary battery. *Electrochemistry*, 71(12):1108–1110, 2003. 110

[284] Bustam M Azmi, Tatsumi Ishihara, Hiroyasu Nishiguchi, and Yusaku Takita. $LiVOPO_4$ as a new cathode materials for li-ion rechargeable battery. *Journal of Power Sources*, 146(1):525–528, 2005. 110, 117

[285] Yong Yang, Haisheng Fang, Jing Zheng, Liping Li, Guangshe Li, and Guofeng Yan. Towards the understanding of poor electrochemical activity of triclinic $LiVOPO_4$: Experimental characterization and theoretical investigations. *Solid State Sciences*, 10(10):1292–1298, 2008. 110

[286] Jean-Marcel Ateba Mba, Laurence Croguennec, Nor Irwin Basir, Jerry Barker, and Christian Masquelier. Lithium insertion or extraction from/into tavorite-type $LiVPO_4F$: An in situ X-ray diffraction study. *Journal of The Electrochemical Society*, 159(8):A1171–A1175, 2012. 112, 113

[287] D Larcher, C Masquelier, D Bonnin, Y Chabre, V Masson, J-B Leriche, and J-M Tarascon. Effect of particle size on lithium intercalation into α-Fe_2O_3. *Journal of The Electrochemical Society*, 150(1):A133–A139, 2003. 114

[288] John P Perdew, Kieron Burke, and Matthias Ernzerhof. Generalized gradient approximation made simple. *Physical Review Letters*, 77(18):3865, 1996. 114

[289] G Kresse and D Joubert. From ultrasoft pseudopotentials to the projector augmented-wave method. *Physical Review B*, 59(3):1758, 1999. 114

[290] Georg Kresse and Jurgen Furthmuller. Efficient iterative schemes for ab initio total-energy calculations using a plane-wave basis set. *Physical Review B*, 54(16):11169, 1996. 114

[291] Vladimir I Anisimov, Jan Zaanen, and Ole K Andersen. Band theory and mott insulators: Hubbard u instead of stoner i. *Physical Review B*, 44(3):943, 1991. 114

[292] AI Liechtenstein, VI Anisimov, and J Zaanen. Density-functional theory and strong interactions: Orbital ordering in mott-hubbard insulators. *Physical Review B*, 52(8):R5467, 1995. 114

[293] F. Girgsdies, W. S. Dong, J. K. Bartley, G. J. Hutchings, R. Schlogl, and T. Ressler. The crystal structure of ϵ-$VOPO_4$. *Solid State Sciences*, 8(7):807–812, 2006. 117, 118, 119

[294] Frank Girgsdies, Matthias Schneider, Angelika Bruckner, Thorsten Ressler, and Robert Schlogl. The crystal structure of δ-$VOPO_4$ and its relationship to ω-$VOPO_4$. *Solid State Sciences*, 11(7):1258 – 1264, 2009. 117

[295] Z. G. Li, R. L. Harlow, N. Herron, H. S. Horowitz, and E. M. McCarron. Unit cell information for δ- and γ-$VOPO_4$. *Journal of Catalysis*, 171(2):506–508, 1997. ISI Document Delivery No.: YD852 Times Cited: 14 Cited Reference Count: 10 Li, ZG Harlow, RL Herron, N Horowitz, HS McCarron, EM Academic press inc jnl-comp subscriptions San diego. 117

[296] R Gopal and Ca Calvo. Crystal structure of βvpo$_5$. *Journal of Solid State Chemistry*, 5(3):432–435, 1972. 117

[297] M. Tachez, F. Theobald, and E. Bordes. A structural explanation for the polymorphism of the α form of anhydrous vanadyl phosphate. *Journal of Solid State Chemistry*, 40(3):280 – 283, 1981. 117

[298] Byron Jordan and Crispin Calvo. Crystal structure of α-vpo$_5$. *Canadian Journal of Chemistry*, 51(16):2621–2625, 1973. 117

[299] T. A. Kerr, J. Gaubicher, and L. F. Nazar. Highly reversible Li Insertion at 4 V in ϵâVOPO$_4$/αâLiVOPO$_4$ Cathodes. *Electrochemical and Solid-State Letters*, 3(10):460–462, 2000. 117, 118

[300] Yanning Song, Peter Y Zavalij, and M Stanley Whittingham. ϵ-$VOPO_4$: Electrochemical synthesis and enhanced cathode behavior. *Journal of The Electrochemical Society*, 152(4):A721–A728, 2005. 117

[301] JT Vaughey, William TA Harrison, Allan J Jacobson, David P Goshorn, and Jack W Johnson. Synthesis, structure, and properties of two new vanadium (iii) phosphates: Vpo$_4$·h$_2$o and v1. 23 (po4)(oh) 0.69 (h2o) 0.31. cntdot. 0.33 h2o. *Inorganic Chemistry*, 33(11):2481–2487, 1994. 119

[302] Zehua Chen, Qiyuan Chen, Liquan Chen, Ruibo Zhang, Hui Zhou, Natasha A. Chernova, and M. Stanley Whittingham. Electrochemical behavior of nanostructured ϵ-$VOPO_4$ over two redox plateaus. *Journal of The Electrochemical Society*, 160(10):A1777–A1780, 2013. 119

[303] M Stanley Whittingham, Yanning Song, Samuel Lutta, Peter Y Zavalij, and Natasha A Chernova. Some transition metal (oxy) phosphates and vanadium oxides for lithium batteries. *Journal of Materials Chemistry*, 15(33):3362–3379, 2005. 126, 127

[304] R. Cerny and V. Favre-Nicolin. Fox: A friendly tool to solve nonmolecular structures from powder diffraction. *Powder Diffraction*, 20(4):359–365, 2005. 127

[305] J. Barker, R. K.B. Gover, P. Burns, and A. J. Bryan. Hybrid-ion: A lithium-ion cell based on a sodium insertion material. *Electrochemical and Solid-State Letters*, 9(4):A190–A192, 2006. 137, 138, 139

[306] R. K. B. Gover, A. Bryan, P. Burns, and J. Barker. The electrochemical insertion properties of sodium vanadium fluorophosphate, $Na_3V_2(PO_4)_2F_3$. *Solid State Ionics*, 177(17â18):1495–1500, 2006. 137, 139

[307] J. Barker, R. K. B. Gover, P. Burns, and A. J. Bryan. $Li_{4/3}Ti_{5/3}O_4$ parallel to $Na_3V_2(PO_4)_2F3$: An example of a hybrid-ion cell using a non-graphitic anode. *Journal of The Electrochemical Society*, 154(9):A882–A887, 2007. 137

[308] Kuniko Chihara, Ayuko Kitajou, Irina D. Gocheva, Shigeto Okada, and Jun-ichi Yamaki. Cathode properties of $Na_3M_2(PO_4)_2F_3$ (M = Ti, Fe, V) for sodium-ion batteries. *Journal of Power Sources*, 227:80–85, 2013. 137, 138, 139, 160

[309] Maowen Xu, Penghao Xiao, Shannon Stauffer, Jie Song, Graeme Henkelman, and John B. Goodenough. Theoretical and experimental study of vanadium-based fluorophosphate cathodes for rechargeable batteries. *Chemistry of Materials*, 2014. 138, 169

[310] P. Serras, V. Palomares, J. Alonso, N. Sharma, J. M. L. del Amo, P. Kubiak, M. L. Fdez-Gubieda, and T. Rojo. Electrochemical Na Extraction/Insertion of $Na_3V_2O_{2x}(PO_4)_2F_{3-2x}$. *Chemistry of Materials*, 25(24):4917–4925, 2013. 138, 176

[311] J. M. Le Meins, M. P. Crosnier-Lopez, A. Hemon-Ribaud, and G. Courbion. Phase Transitions in the $Na_3M_2(PO_4)_2F_3$ Family (M=Al3+, V3+, Cr3+, Fe3+, Ga3+): Synthesis, Thermal, Structural, and Magnetic Studies. *Journal of Solid State Chemistry*, 148(2):260–277, 1999. 138, 139, 145, 146

[312] M. Bianchini, N. Brisset, F. Fauth, F. Weill, E. Elkaim, E. Suard, C. Masquelier, and L. Croguennec. $Na_3V_2(PO_4)_2F_3$ revisited: A high-resolution diffraction study. *Chemistry of Materials*, 26(14):4238–4247, 2014. 138, 161, 163, 165, 168, 181

[313] GONG ZhengLiang WEN Wen TAN Shi HAO XiaoGang, LIU ZiGeng and YANG Yong. In situ XRD and solid state NMR characterization of $Na_3V_2(PO_4)_2F_3$ as

cathode material for lithium-ion batteries. *Scientia Sinica Chimica*, 42(1):38–46, 2012. 138, 139

[314] Zigeng Liu, Yan-Yan Hu, Matthew T. Dunstan, Hua Huo, Xiaogang Hao, Huan Zou, Guiming Zhong, Yong Yang, and Clare P. Grey. Local structure and dynamics in the na ion battery positive electrode material $Na_3V_2(PO_4)_2F_3$. *Chemistry of Materials*, 26(8):2513–2521, 2014. 139, 145, 160, 172

[315] RA Shakoor, Dong-Hwa Seo, Hyungsub Kim, Young-Uk Park, Jongsoon Kim, Sung-Wook Kim, Hyeokjo Gwon, Seongsu Lee, and Kisuk Kang. A combined first principles and experimental study on $Na_3V_2(PO_4)_2F_3$ for rechargeable na batteries. *Journal of Materials Chemistry*, 22(38):20535–20541, 2012. 138, 139, 160, 169

[316] Weixin Song, Xiaobo Ji, Zhengping Wu, Yirong Zhu, Fangqian Li, Yinpeng Yao, and Craig E Banks. Multifunctional dual $Na_3V_2(PO_4)_2F_3$ cathode for both lithium-ion and sodium-ion batteries. *RSC Advances*, 4(22):11375–11383, 2014. 139, 145

[317] A. A. Tsirlin, R. Nath, A. M. Abakumov, Y. Furukawa, D. C. Johnston, M. Hemmida, H. A. Krug von Nidda, A. Loidl, C. Geibel, and H. Rosner. Phase separation and frustrated square lattice magnetism of $Na_{1.5}VOPO_4F_{0.5}$. *Physical Review B*, 84(1):014429, 2011. 139, 146, 148, 155, 156, 159

[318] Gordon A Bain and John F Berry. Diamagnetic corrections and pascal's constants. *Journal of Chemical Education*, 85(4):532, 2008. 140

[319] Junmei Zhao, Linqin Mu, Yuruo Qi, Yong-Sheng Hu, Huizhou Liu, and Sheng Dai. A phase-transfer assisted solvo-thermal strategy for low-temperature synthesis of $Na_3(VO_{1-x}PO_4)_2F_{1+2x}$ cathodes for sodium-ion batteries. *Chemical Communications*, 51(33):7160–7163, 2015. 145

[320] Werner Massa, Olga V. Yakubovich, and Olga V. Dimitrova. Crystal structure of a new sodium vanadyl(IV) fluoride phosphate $Na_3V_2O_2F(PO_4)_2$. *Solid State Sciences*, 4(4):495–501, 2002. 146

[321] F. Sauvage, E. Quarez, J. M. Tarascon, and E. Baudrin. Crystal structure and electrochemical properties vs. Na+ of the sodium fluorophosphate $Na_{1.5}VOPO_4F_{0.5}$. *Solid State Sciences*, 8(10):1215–1221, 2006. 146

[322] Young-Uk Park, Dong-Hwa Seo, Hyungsub Kim, Jongsoon Kim, Seongsu Lee, Byoungkook Kim, and Kisuk Kang. A family of high-performance cathode materials for Na-ion Batteries, $Na_3(VO_{1-x}PO_4)_2F_{1+2x}$ $(0 \leq x \leq 1)$: combined first-principles and experimental study. *Advanced Functional Materials*, 24(29):4603–4614, 2014. 148, 167, 169

[323] Weixin Song, Xiaoyu Cao, Zhengping Wu, Jun Chen, Yirong Zhu, Hongshuai Hou, Qing Lan, and Xiaobo Ji. Investigation of the sodium ion pathway and cathode behavior in $Na_3V_2(PO_4)_2F_3$ combined via a first principles calculation. *Langmuir*, 30(41):12438–12446, 2014. 160

[324] Weixin Song, Xiaobo Ji, Zhengping Wu, Yingchang Yang, Zhou Zhou, Fangqian Li, Qiyuan Chen, and Craig E. Banks. Exploration of ion migration mechanism and diffusion capability for $Na_3V_2(PO_4)_2F_3$ cathode utilized in rechargeable sodium-ion batteries. *Journal of Power Sources*, 256(0):258–263, 2014.

[325] Weixin Song, Xiaobo Ji, Jun Chen, Zhengping Wu, Yirong Zhu, Kefen Ye, Hongshuai Hou, Mingjun Jing, and Craig E. Banks. Mechanistic investigation of ion migration in $Na_3V_2(PO_4)_2F_3$ hybrid-ion batteries. *Physical Chemistry Chemical Physics*, 17(1):159–165, 2015. 160

[326] Paula Serras, Veronica Palomares, Teofilo Rojo, Helen E. A. Brand, and Neeraj Sharma. Structural evolution of high energy density V3+/V4+ mixed valent $Na_3V_2O_{2x}(PO_4)_2F_{3-2x}$ (x = 0.8) sodium vanadium fluorophosphate using in situ synchrotron X-ray powder diffraction. *Journal of Materials Chemistry A*, 2(21):7766–7779, 2014. 161

[327] Neeraj Sharma, Paula Serras, Veronica Palomares, Helen E. A. Brand, Javier Alonso, Pierre Kubiak, M. Luisa Fdez-Gubieda, and TeÃ³filo Rojo. Sodium Distribution and Reaction Mechanisms of a $Na_3V_2O_2(PO_4)_2F$ Electrode during Use in a Sodium-Ion Battery. *Chemistry of Materials*, 26(11):3391–3402, 2014. 161, 162

[328] Ying S. Meng, Yoyo Hinuma, and Gerbrand Ceder. An investigation of the sodium patterning in $Na_xCoO_2(0.5<x<1)$ by density functional theory methods. *The Journal of Chemical Physics*, 128(10):–, 2008. 162

[329] M. Bianchini, F. Fauth, N. Brisset, F. Weill, E. Suard, C. Masquelier, and L. Croguennec. Comprehensive investigation of the $Na_3V_2(PO_4)_2F_3$-$NaV_2(PO_4)_2F_3$ system by

operando high resolution synchrotron x-ray diffraction. *Chemistry of Materials*, 27(8):3009–3020, 2015. 162

[330] Florent Boucher, Joël Gaubicher, Marine Cuisinier, Dominique Guyomard, and Philippe Moreau. Elucidation of the $Na_{2/3}FePO_4$ and $Li_{2/3}FePO_4$ intermediate superstructure revealing a pseudouniform ordering in 2d. *Journal of the American Chemical Society*, 2014. 170

[331] Montserrat Galceran, Damien Saurel, Begona Acebedo, Vladimir V. Roddatis, Egoitz Martin, Teofilo Rojo, and Montse Casas-Cabanas. The mechanism of $NaFePO_4$ (de)sodiation determined by in situ X-ray diffraction. *Physical Chemistry Chemical Physics*, 16(19):8837–8842, 2014. 172

[332] Florent Boucher, Nelly Bourgeon, Karl Delbe, Philippe Moreau, Dominique Guyomard, and Guy Ouvrard. Study of $Li_{1+x}V_3O_8$ by band structure calculations and spectroscopies. *Journal of Physics and Chemistry of Solids*, 67(5â6):1238–1242, 2006. 176

[333] Benkic, P., Golic, L., Koller, J., Zemva, and B. *Crystal structure of $(Xe_2F_{11}+)(VF_6)$*, volume 46. Slovenian Chemical Society, Ljubljana, Slovenie, 1999. 177

[334] Eric Quarez, Olivier Mentre, Yassine Oumellal, and Christian Masquelier. Crystal structures of new silver ion conductors $Ag_7Fe_3(X_2O_7)_4$ (X = P, As). *New Journal of Chemistry*, 33(5):998–1005, 2009. 179

[335] Eric Quarez, Olivier Mentre, Karim Djellab, and Christian Masquelier. Crystal structures and sodium/silver distributions within the ionic conductors $Na_5Ag_2Fe_3(As_2O_7)_4$ and $Na_2Ag_5Fe_3(P_2O_7)_4$. *New Journal of Chemistry*, 34(2):287–293, 2010. 179

[336] J. Angenault, J. C. Couturier, and M. Quarton. Ionic conductivity of solid solutions $Ag_{1+x}Zr_{2-x}M_x(PO_4)_3$ with MIII = Sc, Fe. *Materials Research Bulletin*, 24:789–794, 1989. 179

[337] K. Koteswararao, G. Rambabu, M. Raghavender, G. Prasad, G. Kumar, and M. Vithal. Preparation, characterization and impedance study of AgTaMPO (M=Al, Ga, In, Cr, Fe and Y). *Solid State Ionics*, 176(37-38):2701–2710, 2005. 179

[338] G. Rambabu, N. Anantharamulu, K. Koteswara Rao, G. Prasad, and M. Vithal.

Powder x-ray diffraction, infrared and conductivity studies of $AgSbMP_3O_{12}$ (M=Al, Ga, Fe and Cr). *Materials Research Bulletin*, 43(6):1509–1518, 2008. 179

[339] A. Daidouh, C. Durio, C. Pico, M.L. Veiga, N. Chouaibi, and A. Ouassini. Structural and electrical study of the alluaudites $(Ag_{1-x}Na_x)_2FeMn_2(PO_4)_3$ (x = 0, 0.5 and 1). *Solid State Sciences*, 4:541–548, 2002. 179

[340] A. Daidouh, M.L. veiga, and C. Pico. Structure characterization and ionic conductivity of $Ag_2VP_2O_8$. *Journal of Solid State Chemistry*, 130:28–34, 1997. 179

[341] Hiroshi Fukuoka, Hideyuki Matsunaga, and Shoji Yamanaka. Crystal structure and ionic conductivity of ruthenium diphosphate $ARu_2(P_2O_7)_2$, A=Li, Na, and Ag, with a tunnel structure. *Materials Research Bulletin*, 38(6):991–1001, 2003. 179

[342] Michel Meunier, Ricardo Izquierdo, Lahcen Hasnaoui, Eric Quenneville, Dentcho Ivanov, FranÃ§ois Girard, Arthur Yelon, and Michael Paleologou. Pulsed laser deposition of superionic ceramic thin films: deposition and applications in electrochemistry. *Applied Surface Science*, 127-129:466–470, 1998. 179

[343] R. Collongues, A. Kahn, and D. Michel. Superionic conducting oxides. *Annual Review of Materials Science*, 9:123–150, 1979. 179

[344] James Alamo and Rustum Roy. Crystal chemistry of the $NaZr_2(PO_4)_3$, NZP or CTP, structure family. *Journal of Materials Science*, 21(2):444–450, 1986. 179

[345] Rustum Roy, E. R. Vance, and James Alamo. Nzp, a new radiophase for ceramic nuclear waste forms. *Materials Research Bulletin*, 17:585–589, 1982. 179

[346] A Serghini, M Kacimi, M Ziyad, and R Brochu. Decompotion of 2-butanol over nasicon zirconium-copper phosphates. *JOURNAL DE CHIMIE PHYSIQUE ET DE PHYSICO-CHIMIE BIOLOGIQUE*, 85(4):499–504, 1988. 179

[347] Naohiro Hirose and Jun Kuwano. Ion-exchange properties of NASICON-type phosphates with the frameworks $Ti_2(PO_4)_3$ and $Ti_{1.7}Al_{0.3}(PO_4)_3$. *Journal of Materials Chemistry*, 4:9–12, 1994. 179

[348] Kevin Kirshenbaum, David C. Bock, Chia-Ying Lee, Zhong Zhong, Kenneth J. Takeuchi, Amy C. Marschilok, and Esther S. Takeuchi. In situ visualization of $Li/Ag_2VP_2O_8$ batteries revealing rate-dependent discharge mechanism. *Science*, 347(6218):149–154, 2015. 179

[349] R. Shannon. Revised effective ionic radii and systematic studies of interatomic distances in halides and chalcogenides. *Acta Crystallographica Section A*, 32(5):751–767, 1976. 183